Synthesis and multinuclear magnetic resonance studies of some nitrogen-containing ceramic phases

Matthew J. Leach

Synthesis and Multinuclear Magnetic Resonance Studies of some Nitrogen-containing Ceramic Phases

by

Matthew J. Leach B. A.

A Thesis submitted in partial fulfilment
of the requirements for the degree of
Doctor of Philosophy

Department of Chemistry

The University of Durham
1990

Memorandum

The research presented in this Thesis has been carried out at the Department of Chemistry of the University of Durham, and the Department of Mechanical, Materials and Manufacturing Engineering (Wolfson Laboratory) of the University of Newcastle upon Tyne, between October 1987 and September 1990. It is the original work of the author unless stated otherwise. None of this work has been submitted for any other degree.

To Alison

Abstract

Synthesis and Multinuclear Magnetic Resonance Studies of some Nitrogen-containing Ceramic Phases

by

Matthew J. Leach

This Thesis describes the synthesis of a range of sialon ceramic phases, and their characterisation using multinuclear magnetic resonance and powder X-ray diffraction.

Silicon–29 and aluminium–27 MAS NMR spectroscopies have been used in the past on a range of inorganic systems, with considerable success. In this study, they were applied to phases in M–Si–Al–O–N systems, with M=La, Y, Li, Mg and Ca, leading to an improved understanding of the factors affecting chemical shifts and other NMR parameters.

It was found that some structural information on, for example, O/N ordering was not available from ^{29}Si and ^{27}Al NMR, but could be obtained from studies of other nuclei. Nitrogen–15 and oxygen–17 were selected for further study. The low natural abundances of these nuclei meant that isotopically enriched materials had to be prepared. The synthesis of α–$Si_3^{15}N_4$, $Mg^{17}O$ and $Si^{17}O_2$, and of enriched sialon materials is described, and also ^{15}N and ^{17}O MAS NMR studies of many sialon phases. In particular, the ^{15}N and ^{29}Si spectra of lanthanum new phase, a phase of previously unknown structure, were combined with a Patterson map from powder XRD data to allow the crystal structure of this phase to be determined.

Finally, the feasibility of using other nuclei to study ceramic structures has been investigated, and ^{9}Be, ^{7}Li and ^{139}La NMR spectra of several phases are reported.

Acknowledgements

Many people have helped me in the work described below, and I can mention only a few here. First and foremost, I would like to thank my supervisors, Professor Robin Harris and Dr. Derek Thompson for help, guidance and many useful discussions. I also express my gratitude to Dr. Killian O'Reilly and others at Daresbury, who helped with acquisition and processing of powder XRD data.

Dr. David Apperley (UDIRL) has imparted much of his wisdom on NMR of ceramics and also on use of the VXR spectrometer, and I thank him for all his help. I also thank all those in the Chemistry department who have helped with tips on NMR.

At Newcastle, many people have helped initiate me into the ways of materials science, in particular Drs. Kath Liddell, Piotr Korgul, Yibing Cheng and Bob Oscroft. I thank Phil Wilson for the considerable effort which he put into building the nitridation rig, and also Dave Robinson and Richard Baron for numerous smaller jobs.

Finally, I would like to thank all those at Durham and Newcastle who have helped make my three years so enjoyable, especially Anita, Xiao Ping, and Jim Song, of those not already mentioned; and of course Alison for all her support and for providing a totally non-NMR environment to go home to!

Abbreviations

$^{v}/_{o}$	Percent by volume
$^{a}/_{o}$	percent by atoms
$^{m}/_{o}$	percent by moles
$^{w}/_{o}$	percent by weight
IPA	isopropyl alcohol
Et	C_2H_5
Ln	any lanthanide
PSCR	Paulings Second Crystal Rule
sialon	any ceramic material containing Si, Al, O and N
□	vacancy
n.n.	nearest neighbour
n.n.n	next nearest neighbour
$\mathbf{I}$	nuclear spin
$\mathbf{B}_o$	static magnetic field
$\mathbf{B}_1$	perturbing magnetic field
η	asymmetry
δ_X	chemical shift of X
δ_X^{200}	observed chemical shift in 4.7 T field
δ_X^{300}	observed chemical shift in 7.1 T field
LAB	laboratory frame
ROF	rotating frame
PAS	principal axis system
FT	Fourier transformation
FWHH	full width at half height
ssb	spinning sideband

Key to synthesis table

B	ball-milled in IPA
A	mixed in agate pestle and mortar in IPA
AH	mixed in agate pestle and mortar in hydrocarbon
D	dry mixed in Al_2O_3 cylinder on Glen-Creston mill
C	carbon furnace
M	muffle furnace (in air)
W	tungsten furnace
V	vertical tube furnace
G	glass melting induction furnace
H	hot press

XRD

s	strong
m	medium
w	weak
v	very
tr	trace

NMR parameters

SF	spectrometer frequency
PA	pulse angle
NT	number of transients
RD	recycle delay
ST	single transient after long delay
SR	spin rate
AF	apodisation constant
LB	linebroadening parameter
*	spinning side band
sh	shoulder

Contents

Chapter I

Introduction

1.1 Introduction

The human race has used traditional clay ceramics for thousands of years for many purposes, such as building and cooking. They are virtually unsurpassed in their ability to withstand heat and chemical attack, and are also strong and cheap. The twentieth century has seen many improvements in ceramic technology, including the development of new ceramic materials for structural, mechanical, electronic and optical applications. The area of high temperature engineering ceramics has received particular attention,[1,2] with ZrO_2,[3] SiC,[4] and Si_3N_4 being the most promising parent materials. It is on silicon nitride and the sialons (an acronym for Si+Al+O+N containing ceramics) that the work described in this Thesis will concentrate.

Two major problems have hindered the use of sialons in engineering applications: fabrication difficulties and the brittleness commonly associated with all ceramics. In an attempt to overcome these problems, a great deal of research has been done on elucidating the solid-state chemistry of the systems and phases encountered in these materials. The work described in this Thesis is one small part of that effort.

Many techniques have been used in the quest for structural information on nitrogen ceramic phases, most notably x-ray diffraction (XRD) and transmission electron microscopy (TEM), but neither of these techniques is particularly suited to looking at short-range order and local chemical environment. Solid-state NMR using magic-angle spinning has proved a valuable technique for studying the short-range structure of silicates and zeolites,[5] and it became clear in the early Eighties that it could also be used productively in the study of ceramics. Around 25 research papers applying solid-state NMR to engineering ceramic systems had already been published when the work described in this Thesis was started, and many more have

been published since then; testimony to the many unresolved issues pertaining to the structure of ceramic phases, and the usefulness of NMR in addressing many of these issues.

1.2 Organisation of this Thesis

A multinuclear, multitechnique approach has been taken in this Thesis. It therefore proved convenient to organise results in terms of the type of material studied rather than the nucleus observed. This has many advantages concerned with a unified approach to structural elucidation which will become apparent, but also some disadvantages where common themes can be discerned which are independent of the material studied. There will therefore be an unusually large number of cross-references throughout the text, which are inevitable. Some of the main ideas will also be tied up in the final chapter (**Chapter 10**), in which each of the main nuclei studied will be reviewed in turn. The remainder of the Thesis is organised as follows:

Chapter 2 contains a review of the theory of solid-state NMR, with particular reference to the factors affecting chemical shift, the problems associated with observing quadrupolar nuclei, and relaxation and linewidth effects likely to be encountered in ceramic materials. A brief review of powder XRD and Rietveld profile refinement is also included.

Chapter 3 is a comprehensive literature review divided into two sections. In the first, the structures of silicon nitrides, Si–Al–O–N and M–Si–Al–O–N phases will be reviewed. In the second, the NMR literature of relevance to the remainder of the Thesis will be considered, with particular emphasis on ^{29}Si chemical shifts in silicates and ^{17}O studies of metal oxides and silicates.

Chapter 4 contains essential experimental details on synthetic, NMR and XRD studies undertaken.

Chapter 5 describes in detail the preparation of isotopically enriched α–$Si_3^{15}N_4$, $Mg^{17}O$ and $Si^{17}O_2$, and also considers the NMR spectra of these and closely related materials, including not only ^{15}N and ^{17}O spectra, but also ^{29}Si spectra of unenriched and enriched materials.

Chapter 6 describes a comprehensive multinuclear magnetic resonance study of the Y–Si–Al–O–N and La–Si–Al–O–N systems, observing ^{29}Si, ^{27}Al, ^{17}O, ^{15}N and ^{139}La. Many structural conclusions are reached, and those on the lanthanum new phase, combined with high-resolution powder XRD data allow the structure of this phase to be determined.

Chapter 7 is concerned with a multinuclear study of phases with the wurtzite structure.

Chapter 8 contains NMR and powder XRD data on a range of α'– and β'–sialons. A series of correlations between chemical shift and unit cell parameters is presented together with likely explanations.

Chapter 9 describes a multinuclear study of Si–Al–O–N and Mg–Si–Al–O–N polytypoid phases. The complexities of the structures of these phases make structural conclusions difficult to reach. A ^{9}Be study of a series of Be–Si–O–N phases is also described.

REFERENCES

1. Steinberg, M. A. *Sci. Am.* **255**, 58–64 (1986).
2. Bowen, H. K. *Sci. Am.* **255**, 146–154 (1986).
3. Stevens, R. S. *An Introduction to Zirconia*; Magnesium Elektron, 1986.
4. *Ceramics for High Performanc Applications II*; Burke, J. J.; Lenoe, E. N.; Katz, R. N. Eds.; Brook-Hill, Chestnut Hill: Mass. 1978.
5. Engelhardt, G.; Michel, D. *High Resolution Solid-State NMR of Silicates and Zeolites*; Wiley: Chichester, U.K. 1987.

Figure 2.1.1 The basic NMR experiment.

(a) Precession of magnetic moments about B_Z in the LAB

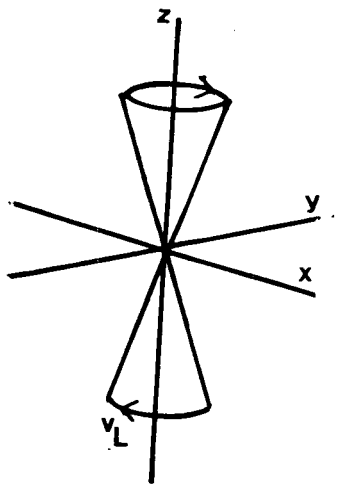

(b) Equilibrium magnetisation in the ROF

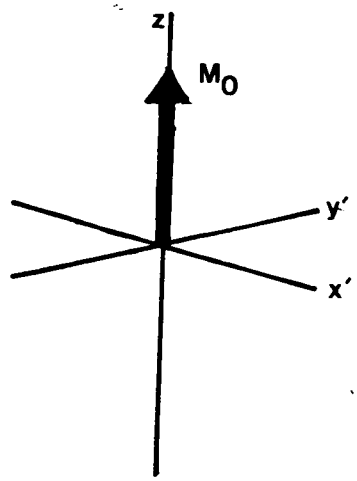

(c) Effect of $\mathbf{B}_1$ in ROF

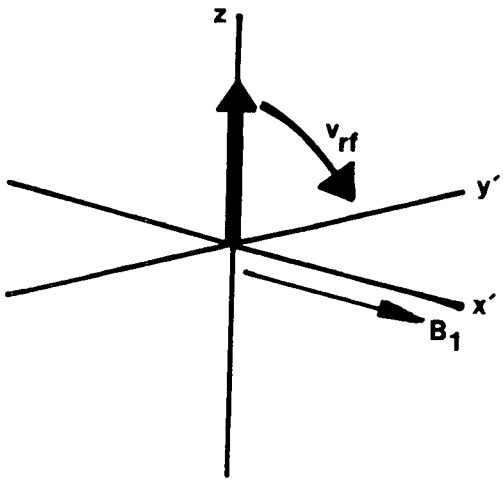

(d) Return to equilibrium in the ROF after $\pi/2$ pulse

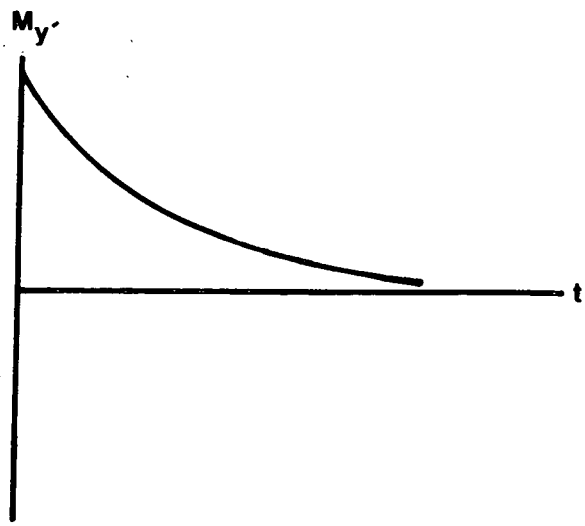

Chapter II

The Theory of Nuclear Magnetic Resonance Spectroscopy and Powder Diffraction.

2.1 Theory of Nuclear Magnetic Resonance Spectroscopy

2.1.1 The Basic NMR Experiment for a Spin-1/2 Nucleus

If an isolated spin-1/2 nucleus is placed in a static magnetic field, $\mathbf{B_0}$, then it is well known[1] that the Zeeman interaction causes the nucleus to be in one of only two states, corresponding to $m_I = \pm\frac{1}{2}$. In either of these two states, the nuclear magnetic moment **precesses** around the $\mathbf{B_0}$ field axis (from henceforward defined as B_z) at a frequency ν_L, the **Larmor frequency** (Figure 2.1.1a). For an ensemble of nuclei, a Boltzmann distribution of moments between the two states will occur at equilibrium, and the sample will possess an overall magnetisation M_0 (Figure 2.1.1b). If a perturbing magnetic field, $\mathbf{B_1}$, oscillating at the Larmor frequency is applied in the xy plane, then transitions will be induced between the two states due to mixing of the states. This is most simply considered in the **rotating frame** (ROF), in which the x' and y' axes rotate at the frequency of $\mathbf{B_1}$, ν_1, about z, with respect to the laboratory frame (LAB). $\mathbf{B_1}$ can then be thought of as acting along the x'-axis of the ROF, and the bulk magnetisation then precesses around $\mathbf{B_1}$ at a rate ν_{rf} (Figure 2.1.1c). If a $\pi/2$ pulse is applied along x', and the system is allowed to return to equilibrium, a **Free Induction Decay** (FID) (Figure 2.1.1d) can be recorded by monitoring magnetisation in the $x'y'$ plane of the ROF: **Fourier Transformation** (FT) of the FID allows the precise value(s) of ν_L to be determined.

According to approximations such as the Born-Oppenheimer approximation,[2] it is possible to write a nuclear spin hamiltonian, H_N independently of the atomic or molecular hamiltonian. The levels of Figure 2.1.1a are then the solutions of the equation:

$$H_Z \mid \psi >= E_Z \mid \psi > \qquad (2.1.1)$$

where the Zeeman hamiltonian is given by the equation:[3]

$$H_Z = -\gamma\hbar\mathbf{I}.\mathbf{B_0} \tag{2.1.2}$$

In real systems, the total spin hamiltonian is made up not only of the Zeeman hamiltonian, but also other hamiltonians due to a range of interactions. If, as is virtually always the case, the Zeeman interaction is of by far the largest magnitude, then the total spin hamiltonian can be written as a simple sum. For systems considered in this Thesis, the expression is:

$$H_N = H_Z + H_{rf} + H_D + H_S + H_Q \tag{2.1.3}$$

where H_{rf} represents the effect of the radiofrequency perturbation by $\mathbf{B_1}$, H_D the effect of direct dipole-dipole coupling with other magnetic nuclei, H_S the effect of shielding of the nucleus by electrons, and H_Q the effect of quadrupole coupling for $I > \frac{1}{2}$ nuclei (Indirect, or J-coupling is frequently negligible in solid samples). The effect of the non-Zeeman hamiltonians on the system can then be treated using first, and sometimes second order perturbation theory. H_Z and H_{rf} are termed external hamiltonians, because the interactions which they represent are with externally applied fields and can be controlled by the experimentalist. The remaining hamiltonians of Equation 2.1.3 are termed internal hamiltonians.

2.1.2 Internal Hamiltonians

All three internal hamiltonians can be written in the form[4]

$$\hbar^{-1}H_\lambda = c_\lambda\mathbf{I}.\mathbf{R}_\lambda.\mathbf{A}_\lambda \tag{2.1.4}$$

as the coupling of two vectors, at least one of which is the nuclear spin operator of the nucleus in question. $\mathbf{R}_\lambda$ is a coupling tensor. The quantities c_λ, $\mathbf{R}_\lambda$ and $\mathbf{A}_\lambda$ are listed for the three cases in Table 2.1.1.

The tensor $\mathbf{R}_\lambda$ in Equation 2.1.4, represented by a three-by-three matrix, can normally be transformed to its principal axis system (PAS), in which it is diagonal, by means of a suitable similarity transform. Three physically significant quantities can be defined in terms of the diagonal components in the PAS (R_{XX}, R_{YY}, R_{ZZ}):

$$\text{isotropic average :} \qquad R_{iso} = \frac{1}{3}\text{tr}\mathbf{R}_\lambda$$

$$\text{anisotropy :} \qquad \delta\mathbf{R} = R_{ZZ} - R_{iso} \tag{2.1.5}$$

$$\text{asymmetry :} \qquad \eta_R = \frac{R_{XX} - R_{YY}}{\delta\mathbf{R}}$$

The axes of the PAS are defined such that

$$| R_{ZZ} - R_{iso} | \geq | R_{YY} - R_{iso} | \geq | R_{XX} - R_{iso} | \tag{2.1.6}$$

Table 2.1.2 lists R_{iso}, $\delta\mathbf{R}$ and η_R for the internal hamiltonians.

Table 2.1.1 Internal hamiltonians

λ	c_λ	$\mathbf{R}_\lambda$	$\mathbf{A}_\lambda$
D	$-2\gamma_1\gamma_2\hbar\frac{\mu_0}{4\pi}$	$\mathbf{D}$	$\mathbf{I_2}$
S	γ_1	σ	$\mathbf{B_0}$
Q	$\frac{eQ}{2I(2I-1)\hbar}$	$e\mathbf{q}$	$\mathbf{I_1}$

Table 2.1.2 Values of PAS tensor components

λ	R_{iso}	$\delta\mathbf{R}$	η_R
D	0	$\frac{1}{r^3}$	0
S	σ	$\sigma_{ZZ} - \sigma$	$\frac{\sigma_{XX}-\sigma_{YY}}{\sigma_{ZZ}-\sigma}$
Q	0	eq_{ZZ}	$\frac{q_{XX}-q_{YY}}{q_{ZZ}}$

It is often convenient to describe the interaction hamiltonian in terms of irreducible tensor operators: dyadic products, T_{lm}; and tensor components A_{lm}, in spherical coordinates:[5]

$$-\hbar H_\lambda = c_\lambda \sum_{l=0,2} \sum_{m=-l}^{l} (-1)^m A_{lm} T_{l-m} \tag{2.1.7}$$

This is particularly useful when rotation of samples is being considered. The values of A_{lm} and T_{l-m} are listed in References 3 and 5. Changes in axis system (eg from ROF to PAS) can then be described by use of Wigner rotation matrices:[5]

$$A'_{lm} = \sum_{m'=-l}^{l} D^l_{m'm}(\alpha, \beta, \gamma) A_{lm} \tag{2.1.8}$$

2.1.3 Dipolar Interactions

Equation 2.1.4 can be expressed in the LAB by use of Equations 2.1.7 and 2.1.8 for two coupled spin-1/2 nuclei:[6]

$$H_D = \frac{\gamma_i \gamma_j \hbar^2}{r_{ij}^3} \left(\frac{\mu_0}{4\pi}\right)(A + B + C + D + E + F) \tag{2.1.9}$$

$$\begin{aligned}
A &= (1 - 3\cos^2\theta) I_{zi} I_{zj} \\
B &= -\frac{1}{4}(1 - 3\cos^2\theta)[I_i^+ I_j^- + I_i^- I_j^+] \\
C &= -\frac{3}{2}\sin\theta\cos\theta e^{-i\phi}[I_{zi} I_j^+ + I_i^+ I_{zj}] \\
D &= -\frac{3}{2}\sin\theta\cos\theta e^{i\phi}[I_{zi} I_j^- + I_i^- I_{zj}] \\
E &= -\frac{3}{4}\sin^2\theta e^{-2i\theta}[I_i^+ I_j^+] \\
F &= -\frac{3}{4}\sin^2\theta e^{2i\theta}[I_i^- I_j^-]
\end{aligned} \tag{2.1.10}$$

Only the secular terms, A and B involve $\Delta M_I = 0$, and thus only these terms contribute in first order to the perturbation of the Zeeman levels.

In the solution state, molecules are rapidly tumbling, and the values of θ and ϕ thus vary randomly. It can easily be shown[7] that all six terms of Equation 2.1.9 then average to zero, and H_D has no overall effect on the appearance of the spectrum. If similarly narrow lines are required from solid-state samples, then rapid spinning about an angle of 54.7^o to the field axis can be shown to average the effect of the terms A and B in Equation 2.1.9 and hence H_D, to zero[8] (Magic Angle Spinning), with the following provisos:

(i) If the spin rate, ν_{MAS}, is not much greater than the dipolar linewidth, and the line is inhomogeneously broadened[9] (i.e. heteronuclear coupling), then rotational echoes are formed in the FID at intervals equal to the rotor period. In the transformed spectrum, these appear as **spinning side-bands** (ssb), at intervals of ν_{MAS} from the centreband. The position of the centreband can easily be determined by recording spectra at different spin rates.

(ii) If the $\mathbf{I}_1$ nucleus is coupled not to a second spin-1/2 nucleus, but to a nucleus with $I > \frac{1}{2}$, then magic-angle spinning does not fully average the interaction because the quadrupolar interaction (*vide infra*) causes the quadrupolar nucleus not to be in purely Zeeman states,[10] and the z-axes of the Zeeman PAS and ROF for this nucleus no longer coincide. This leads to non-secular terms in Equations like 2.1.9 which depend on the value of χ_Q of the quadrupolar nucleus. Spinning at the magic-angle no longer fully averages the effect of H_D, leading to residual linewidth (or occasionally a resolvable splitting in the line[10]).

(iii) In cases where heteronuclear coupling is strong, it is often more effective to decouple spectra by irradiation of the heteronucleus.

2.1.4 Shielding Interactions

This is caused by the interaction of local magnetic fields generated by the electrons in the sample with the nuclei under investigation.[11] Table 2.1.2 shows that, unlike H_D, H_S is not traceless, and thus this hamiltonian has a significant effect on spectra, even in the solution state, where angle dependence averaging can occur.

The angle dependence of $\delta\sigma$ for an axially symmetric ($\eta_S = 0$) shielding hamil-

tonian is identical to that given for H_D in Equations 2.1.9 and 2.1.10. It is thus clear that the effect of MAS will be identical if only the secular parts of the hamiltonian are considered, again an excellent assumption. Broadening due to shielding anisotropy (SA) is inhomogeneous, and thus spinning side-bands can be observed if $\nu_{MAS} \leq \delta\sigma$. It can also be shown[12] that if $\eta_S \neq 0$, MAS still averages out this interaction, and narrow lines can be seen in the spectrum.

The expectation value of the isotropic part of the shielding tensor is generally quoted with respect to a standard reference material:

$$(\delta/ppm) = (\sigma_{iso}(REF) - \sigma_{iso}) \times 10^6 \tag{2.1.11}$$

where δ is the **chemical shift**.

Factors affecting chemical shift

Pople[13] has determined that in many instances, the isotropic shielding constant, σ, for an atom can be written as the sum of two terms: a diamagnetic and a paramagnetic term.

$$\sigma = \sigma_d + \sigma_p \tag{2.1.12}$$

The diamagnetic term results from the spatial distribution of the electrons, and the paramagnetic term from their orbital angular momentum. s–electrons, and p– (and d–) electrons in closed shells, thus contribute only to σ_d, whilst p–electrons in open shells contribute to both σ_d and σ_p.

Explicit calculation of these quantities is possible,[14] but requires detailed knowledge of the atomic orbitals around the nucleus in question, particularly in the case of σ_p.

For nuclei such as ^{1}H, ^{7}Li, ^{9}Be and ^{23}Na, in which electrons are present only in orbitals with zero angular momentum, σ_d is dominant, and a small shift range is observed. For nuclei such as ^{13}C, ^{15}N, ^{17}O, ^{27}Al and ^{29}Si, electrons are present in p–orbitals, and it is found that the contribution from σ_p is dominant, resulting in a much larger shift range.

Jameson and Gutowsky[15] have shown that σ_p can be approximated from a known set of atomic orbitals for main group elements using the expression

$$\sigma_p = \frac{-\mu_0 e^2 \hbar^2}{6\pi m^2 \Delta E} \langle r^{-3} \rangle_p P_u \tag{2.1.13}$$

where ΔE is an average excitation energy, $\langle r^{-3} \rangle_p$ is the expectation value of r^{-3} for the valence p–electrons, and P_u is a term which reflects the charge distribution and asymmetry of the p–electrons.

Many authors have attempted to use this equation to estimate σ_p,[16] but for the majority of systems, the calculations are very approximate. The equation is relevant, however, in emphasizing the importance of the electron density and distribution around the atom of interest. Most attempts at calculating shielding tensor components from structural variables have relied on semi-empirical methods, and correlations of chemical shift with variables which Equation 2.1.13 predicts should occur. Details of such investigations for ^{29}Si will be given in the next chapter.

2.1.5 Quadrupolar Interactions

For nuclei with $I > 1/2$, coupling between the magnetic dipole and electric quadrupole moments is often very strong, and the interaction needs to be treated by both first and second order perturbation theory. Indeed, in some instances, $\mid H_Q \mid > \mid H_Z \mid$, and perturbation theory is no longer suitable. For all systems investigated in this work, $\mid H_Z \mid \gg \mid H_Q \mid$, and only this case will be considered below.

The first order contribution to the energy of the Zeeman state comes from the secular part of the interaction hamiltonian. This includes terms of identical angular dependence to A and B in Equation 2.1.10 for $\eta_Q = 0$. It is fully averaged by MAS (even if $\eta_Q \neq 0$). For a nucleus of spin I, the first order energy shift of the $\mid I, m_I >$ level is given by[3]

$$E_m^{(1)} = \frac{1}{4} h \nu_Q [m^2 - \frac{1}{3} I(I+1)](3\cos^2\theta - 1 + \eta_Q \sin^2\theta \cos 2\phi) \tag{2.1.14}$$

$$\nu_Q = \frac{3e^2 qQ}{2I(2I-1)h} \tag{2.1.15}$$

Figure 2.1.2 Schematic first order powder pattern for a spin–3/2 nucleus.

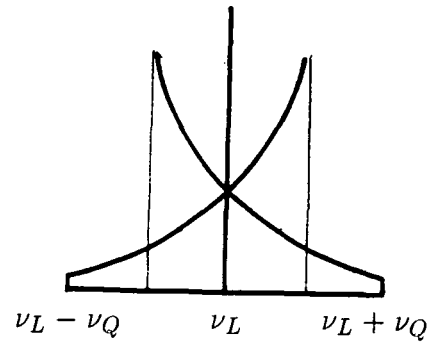

Figure 2.1.3 Schematic second order quadrupolar powder pattern for the $|\frac{3}{2}, \frac{1}{2} > \rightarrow |\frac{3}{2}, -\frac{1}{2} >$ transition.

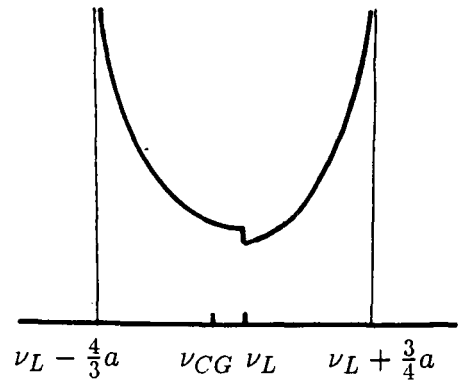

The term e^2qQ/h is often referred to as the quadrupole coupling constant, and is given the symbol χ_Q. The most important point to glean from Equation 2.1.14 is that the energy shift for the $\mid I, \frac{1}{2} > \rightarrow \mid I, -\frac{1}{2} >$ transition is always zero, and thus the central transition for a spin-n/2 nucleus is unperturbed by the first order interaction. No transition is unaffected in the case of a nucleus with integral spin. In the solid state it is thus much easier to obtain spectra of spin-n/2 nuclei.

The first order powder pattern for a typical spin-3/2 nucleus is shown in Figure 2.1.2. As mentioned above, this interaction is fully averaged by MAS, and, since broadening due to this interaction is inhomogeneous, the powder pattern is split into spinning side-bands if, as is almost invariably the case, $\nu_{MAS} \leq \nu_Q$.

The intensity of a given line in the spectrum of a spin-n/2 nucleus depends upon whether it is made up from one, or more than one transition, and therefore care needs to be taken when spectra are to be interpreted quantitatively. For an $\mid I, m_I > \rightarrow \mid I, m_I - 1 >$transition, the relative intensity is given by[3]

$$Int = \frac{3}{2}\frac{I(I+1) - m(m-1)}{I(I+1)(2I+1)} \tag{2.1.16}$$

relative to an intensity of one for $\chi_Q = 0$, the situation where the energies of all the possible transitions are equal.

There is often a contribution to the energy of a particular state from the non-secular part of the interaction hamiltonian. This second-order coupling does affect the $\mid I, \frac{1}{2} > \rightarrow \mid -\frac{1}{2} >$ transition. The shift in energy of the $\mid I, m_I >$ level due to the coupling is given for $\eta_Q = 0$ by[3]

$$E_m^{(2)} = \frac{-h\nu_Q^2 m}{32\nu_L}([4I(I+1) + 8m^2 + 1]\frac{9}{16}\sin^2 2\theta + [2I(I+1) - 2m^2 - 1]\frac{9}{16}\sin^4\theta) \tag{2.1.17}$$

The effect of this energy shift is seen most clearly on the $\mid I, \frac{1}{2} > \rightarrow \mid I, -\frac{1}{2} >$ transition, because if the quadrupole coupling is large enough to affect this transition, then all of the other transitions will be significantly broadened by the first order interaction. The second order powder pattern for a $\mid \frac{3}{2}, \frac{1}{2} > \rightarrow \mid \frac{3}{2}, -\frac{1}{2} >$

transition is shown in Figure 2.1.3. The shift of the centre of gravity of the $| I, \frac{1}{2} > \rightarrow | I, -\frac{1}{2} >$ transition with respect to ν_L, $\Delta\nu$, is given by

$$\Delta\nu = \nu_{CG} - \nu_L = -\frac{\nu_Q^2}{30\nu_L}[I(I+1) - \frac{3}{4}](1 + \frac{1}{3}\eta^2) \qquad (2.1.18)$$

The angle dependence of the energy shift in Equation 2.1.17 is not the same as for treatments by first order perturbation theory, and the interaction can thus not be wholly averaged by MAS, and is only scaled. It is possible to calculate the MAS lineshape using Equation 2.1.17, and analogous expressions for $\eta_Q \neq 0$ by considering the effect of making the angles time-dependent, and summing over time.[17,18] This is most easily achieved by use of computer programs capable of rapid and lengthy summations. An important result is that the centre of gravity of the $| I, \frac{1}{2} > \rightarrow | I, -\frac{1}{2} >$ transition as given by Equation 2.1.18 is unchanged under magic-angle spinning.

The different angle dependence of $E_m^{(2)}$ suggests that spinning the sample at an angle other than 54.7^o to B_Z would more fully average the second order quadrupolar interaction. Ganapathy *et al.*[16] have shown that by spinning the sample at angles of *ca.* either 75^o or 36^o to B_Z minimises the effect of the second order interaction. This technique, variable angle spinning (VAS) NMR can, in favourable cases narrow the linewidth by a factor of two or more over MAS. Unfortunately, the sample is of course no longer being spun at the magic angle, and thus broadening due to shielding anisotropy and dipolar coupling is no longer fully averaged.

There have been two recent ingenious attempts to overcome this problem:

(i) Dynamic angle spinning (DAS) NMR,[20,21] in which the angle of spinning is mechanically altered during acquisition of the FID.

(ii) Double rotation (DOR) NMR,[21,22] in which, by use of a 'rotor-within-a-rotor', the sample is spun at two axes (54.7^o and 30.6^o) simultaneously.

Determination of χ_Q and η_Q

It is often important and useful to determine the values of χ_Q and η_Q. They are needed to calculate the isotropic chemical shift (Equation 2.1.18), and can also

provide chemical information on site symmetry in their own right. Several methods have been used, and the three most useful are:

(i) If the quadrupole coupling is the dominant line-broadening mechanism, then it is often possible to compare observed and calculated spectra, either static (first or second order) or with MAS (second order), and hence deduce χ_Q and η_Q. If the major lineshape features cannot be resolved, then a rough estimate of χ_Q can be obtained from the linewidth under MAS conditions.

(ii) Equation 2.1.18 demonstrates the dependence of $\Delta\nu$ on the Larmor frequency, and hence B_0. If ν_{CG} is measured at more than one static field strength, then the true chemical shift can be determined from Equation 2.1.18. If $\eta_Q \sim 0$, then only two measurements are required, but if $\eta_Q > 0$, more than two readings are needed. This method is most accurate for large values of χ_Q.

(iii) The two-dimensional nutation spectrum[23] can be used to determine χ_Q and η_Q to a high degree of accuracy, but is not suitable if lines are broadened significantly by the effect of the other internal hamiltonians or by chemical shift dispersion.

None of these methods is ideal if spectra are broadened by other interactions, as is generally the case in the samples studied in this thesis, and thus it has often proved difficult to obtain accurate values of χ_Q, and especially η_Q.

2.1.6 Relaxation and Linewidth Effects

Relaxation can be characterised in most systems by two parameters: the spin-lattice (longitudinal) relaxation time, T_1, and the spin-spin (transverse) relaxation time, T_2. T_1 relaxation involves the growth or decay of magnetisation parallel to B_Z, and T_2 relaxation the decay of magnetisation in the xy-plane of the LAB.

Spin-lattice relaxation is caused by the presence of local, randomly fluctuating magnetic fields with a component modulating at the Larmor frequency of the relaxing nucleus.[24] These fluctuations are generally caused by molecular motion. If no motion is present, as in ceramic samples, then T_1 times tend to be very long. Residual T_1 relaxation must occur in these cases, but the mechanism is not known. This matter will be discussed further in later chapters.

Homonuclear spin diffusion is often important in limiting values of T_1 in solids. Homonuclear dipolar coupling between nuclei can allow flip-flop transitions to occur, which are efficient because they are energy conserving. This allows relaxation to be transferred from nuclei where it is more rapid (e.g. at surfaces) to nuclei where it is less rapid.

Spin-lattice relaxation of quadrupolar nuclei is invariably found to be more rapid than for spin-1/2 nuclei. The quadrupolar interaction allows for much more efficient transfer of energy to the lattice than any other interaction, although a modulation of electric field gradient is still required.

Spin-spin relaxation[24] is caused by fluctuating magnetic fields at very low (or zero) frequencies. Thus, in systems such as ceramics in which there is no motion, it is found that $T_2 \ll T_1$.

The precise causes of linewidth in MAS NMR spectra of solids are not always clear, but the following are thought to be important (in addition to instrumental factors):

(i) Natural linewidth. This is caused by T_1 relaxation which leads to non-negligible linewidths because of lifetime broadening. The magnitude of this effect is given by the expression $(\pi T_1)^{-1}$.

(ii) Broadening due to $\mathbf{B}_0$ inhomogeneity. This is not a relaxation phenomenon, and it can be removed by use of a spin-echo pulse sequence.

(iii) Broadening due to isotropic chemical shift dispersion. This is caused by structural disorder, surface effects, and the presence of solid solutions. It is particularly important in the examination of glasses.

(iv) Broadening due to the incomplete averaging of second order interactions, notably the quadrupolar interaction (Section 2.1.5), and dipole-quadrupole coupling (Section 2.1.3).

(v) Broadening due to the presence of paramagnetic impurities[25,26] in the sample: caused by the effect on T_2, and by second order magnetic susceptibility anisotropy broadening. Spinning side-band manifolds can also be enhanced by the presence

of paramagnetic impurities,[25] and this is thought to be due to the larger first order magnetic susceptibility anisotropy broadening.

2.2 Theory of Powder Diffraction

The theory of powder diffraction has been well described.[27] The aim of this short section is to briefly emphasise points of relevance later in this Thesis, and describe the Rietveld Profile Refinement method for crystal structure determination.

Diffraction lines are observed when the Bragg condition is satisfied:

$$\lambda = 2d_{hkl} \sin\theta \tag{2.2.1}$$

where θ is the angle between the incident x-ray beam and the (hkl) plane. The intensity of a particular reflection is found to be related to the square of the modulus of the structure factor, $\mid F(hkl) \mid^2$, of the plane, where

$$F(hkl) = \sum_{1}^{N} f_n \exp 2\pi i(hx_n + ky_n + lz_n) \tag{2.2.2}$$

f_n is the atomic scattering factor of the nth atom, at a position (x_n, y_n, z_n) in the unit cell, and can be determined from standard tables.[28]

It is clear from Equation 2.2.2 that the intensity of a given reflection will be dominated by the effect of heavy atoms such as lanthanum, which have large atomic scattering factors. This can make determination of light atom positions very difficult. It can also be difficult to distinguish atoms such as Si and Al, and O and N, which possess very similar scattering factors.

Fourier transformation of an indexed powder pattern gives a Patterson map:[29]

$$P(\mathbf{r}) = \sum_{h,k,l} I_{hkl} \exp\{-2\pi i(hx + ky + lz)\} \tag{2.2.3}$$

A peak in the Patterson map at a position $\mathbf{r}_1$ corresponds to an interatomic vector $\mathbf{r}_1$ within the crystal structure; the intensity of the peak is proportional to the product of the atomic scattering factors of the two linked atoms.

Rietveld Profile Refinement[30,31]

A powder XRD diffractogram can be described as a series of profile points, $x(\theta)$. Rietveld profile refinement involves a least squares fitting of calculated and experimental values of the profile points. The calculated profile, $y(\theta)$ is given by:

$$y(\theta) = \sum_{patterns} \sum_{hkl} C(hkl). \mid F(hkl) \mid^2 .PSF(\theta, hkl) + B(\theta) \qquad (2.2.4)$$

where $C(hkl)$ is a modifying term taking into account factors such as Lorentz polarisation, $PSF(\theta, hkl)$ is the peak shape function of the (hkl) reflection at θ, and $B(\theta)$ is the background count at θ.

Various peak shape functions have been used. Most common for synchrotron XRD data is the pseudo-Voigt:

$$PSF(\theta) = n.L(\theta) + (1 - n).G(\theta) \qquad (2.2.5)$$

where $L(\theta)$ and $G(\theta)$ are Lorentzian and Gaussian peak shape functions. The linewidth of these two components is found to vary with θ_{hkl}, and thus a linewidth function, $H(hkl)$ is defined:

$$H(hkl) = \sqrt{U \tan^2 \theta_{hkl} + V \tan \theta_{hkl} + W} \qquad (2.2.6)$$

The following parameters are always varied in a refinement:

1. S: the overall scale factor.
2. Z: the zeropoint error in θ
3. U, V, W, n: the linewidth parameters,
4. $a, b, c, \alpha, \beta, \gamma$: unit cell dimensions
5. Trial atomic coordinates, isotropic temperature factors and site occupation factors.

Other parameters, such as anisotropic temperature factors can also be varied, but those listed above are normally sufficient.

The goodness of a particular fit is measured by the profile R-factor:

$$R_{wp} = \{\sum w_\theta [x(\theta) - c'y(\theta)]^2 / \sum w_\theta y(\theta)^2\}^{\frac{1}{2}} \qquad (2.2.7)$$

where w_θ is a weighting factor, generally equal to $(\frac{1}{y(\theta)})$, and c' is the scale factor. This value can be compared with the expected R-value, R_E:

$$R_E = [(N - P + C)/\sum w_\theta y(\theta)^2]^{\frac{1}{2}} \qquad (2.2.8)$$

where N is the number of profile points, P the number of parameters, and C the number of constraints.

The refinement in fact involves the minimisation of χ^2:

$$\chi^2 = (\frac{R_{wp}}{R_E})^2 \qquad (2.2.9)$$

For a good fit, $\chi^2 \sim 1$.

Standard R-indices (R_I and R_F) can also be determined from the observed and calculated profiles to allow comparisons with refinements by other methods.

REFERENCES

1. Abragam, A. *Principles of Magnetic Resonance*; Oxford University Press: Oxford, U.K. 1961.
2. Atkins, P. W. *Molecular Quantum Mechanics*; Oxford University Press: Oxford, U.K. 1983.
3. Engelhardt, G.; Michel, D. *High Resolution Solid-state NMR of Silicates and Zeolites*; Wiley: Chichester, U.K. 1987. Chapter 2.
4. Harris, R. K. *Nuclear Magnetic Resonance Spectroscopy*; Longman: Harlow, U.K. 1983. Appendix 4.
5. Haeberlen, U. *High-Resolution NMR in Solids, Selective Averaging*; Academic Press: London, UK, 1976.
6. Reference 1; Chapter 4.
7. Reference 4; Chapter 4.
8. Andrew, E. R. *Prog. NMR Spectrosc.* **8**, 1–39 (1971).
9. Inhomogeneous or heterogeneous broadening is caused by the presence of spin isochromats precessing at different and discrete frequencies.
10. Böhm, J.; Fenzke, D.; Pfeifer, H. *J. Magn. Reson.* **55**, 197–204 (1983).

11. Pople, J. A.; Schneider, W. G.; Bernstein, H. J. *High Resolution Nuclear Magnetic Resonance*; McGraw Hill: New York, 1959.

12. Gerstein, B. C.; Dybowski, C. R. *Transient Techniques in NMR of Solids*; Academic Press: Orlando, Florida, 1985. Chapter 6.

13. Pople, J. A. *Discuss. Faraday Soc.* **34**, 7–14 (1964).

14. Webb, G. A. *NMR and the Periodic Table*; Harris, R. K.; Mann, B. E. Ed.; Academic Press: London, U.K. 1978. Chapter 3, and references therein.

15. Jameson, C. J.; Gutowsky, H. S. *J. Chem. Phys.* **40**, 1714–1724 (1964).

16. See for example the discussion on ^{29}Si chemical shifts in Chapter 4 of Reference 3.

17. Müller, Von D. *Annal. der Physik (Leipzig)* **39**, 451–460 (1982).

18. Samoson, A.; Kundla, E.; Lippmaa, E. *J. Magn. Reson.* **49**, 350–357 (1982).

19. Ganapathy, S.; Schramm, S.; Oldfield, E. *J. Chem. Phys.* **77**, 4360–4365 (1982).

20. Mueller, K. T.; Sun, B. Q.; Chingos, G. C.; Zwanziger, J. W.; Terao, T.; Pines, A. *J. Magn. Reson.* **86**, 470–487 (1990).

21. Chmelka, B. F.; Mueller, K. T.; Pines, A.; Stebbins, J.; Wu, Y.; Zwanziger, J. W. *Nature* **339**, 42–43 (1989).

22. Samoson, A.; Lippmaa, E.; Pines, A. *Mol. Phys.* **65**, 1013–1018 (1988).

23. Samoson, A.; Lippmaa, E. *Phys. Rev. B.* **28**, 6567–6570 (1982).

24. Freeman, R. *A Handbook of Nuclear Magnetic Resonance*; Longman: Harlow, U.K. 1988.

25. Oldfield, E.; Kinsey, R. A.; Smith, K. A.; Nichole, J. A.; Kirkpatrick, R. J. *J. Magn. Reson.* **51**, 325–329 (1983).

26. Grimmer, A-R.; v Lampe, F.; Mägi, M.; Lippmaa, E. *Z. Chem.* **23**, 343–344 (1983).

27. McKie, D.; McKie, C. *Essentials of Crystallography*; Blackwell: Oxford, U.K. 1986. Chapter 7.

28. *International Tables for X-ray Crystallography, Volume 3*; Kynoch Press, Birmingham, 1962.

29. Patterson, A. L. *Z. Krist.* **90**, 517–542 (1935).

30. Rietveld, H. M. *J. Appl. Crystallogr.* **2**, 65–71 (1969).

31. Fitch, A. N.; Murray, A. D. *Manual for Multipattern Rietveld Refinement Program*; PDPL, Daresbury Laboratory , 1989.

Chapter III

Previous Investigations

3.1 Structures of Nitrogen Ceramic Phases

3.1.1 Introduction

Silicon nitride was identified as a material for high-temperature engineering applications several decades ago.[1] It combines high strength, excellent thermal shock resistance, low specific gravity, low coefficient of thermal expansion and thermal stability up to 1800^oC. It cannot, however, be densified in the pure form either by hot-pressing or by pressureless sintering, because no liquid phase is present, even at the decomposition temperature. A liquid phase aids densification because the solid phase can dissolve in it and then be reprecipitated, allowing much more rapid mass transfer than by self-diffusivity in the solid.[2]

Many metal oxides have been investigated as densification agents for silicon nitride. These oxides react with the surface silica layer present on silicon nitride[3] to give a metal silicate liquid in which silicon nitride is somewhat soluble, and allows densification. When the sintered silicon nitride is cooled, the silicate liquid forms grain boundary glassy and crystalline phases which often contain small amounts of nitrogen. These phases have the effect of impairing the strength, creep resistance and oxidation resistance of the silicon nitride, and thus there is intense interest in their structures.

Most main group and lanthanide oxides, plus ZrO_2 and ThO_2 have been used as densification agents in recent years, and the M–Si–O–N systems of these metals have been studied to identify the phases which occur and to determine their structures. In particular, a large number of phases occur in the quaternary Si–Al–O–N system, and more recently there has been considerable interest[4] in some of these phases too for engineering applications. Transition metal oxides have not proved useful as densification agents, because of their tendency to form interstitial nitrides and silicides.

Figure 3.1.1 The crystal structure of β–Si_3N_4, projected along **c**. The z coordinates of the Si atoms (only) are given as $100z/c$.

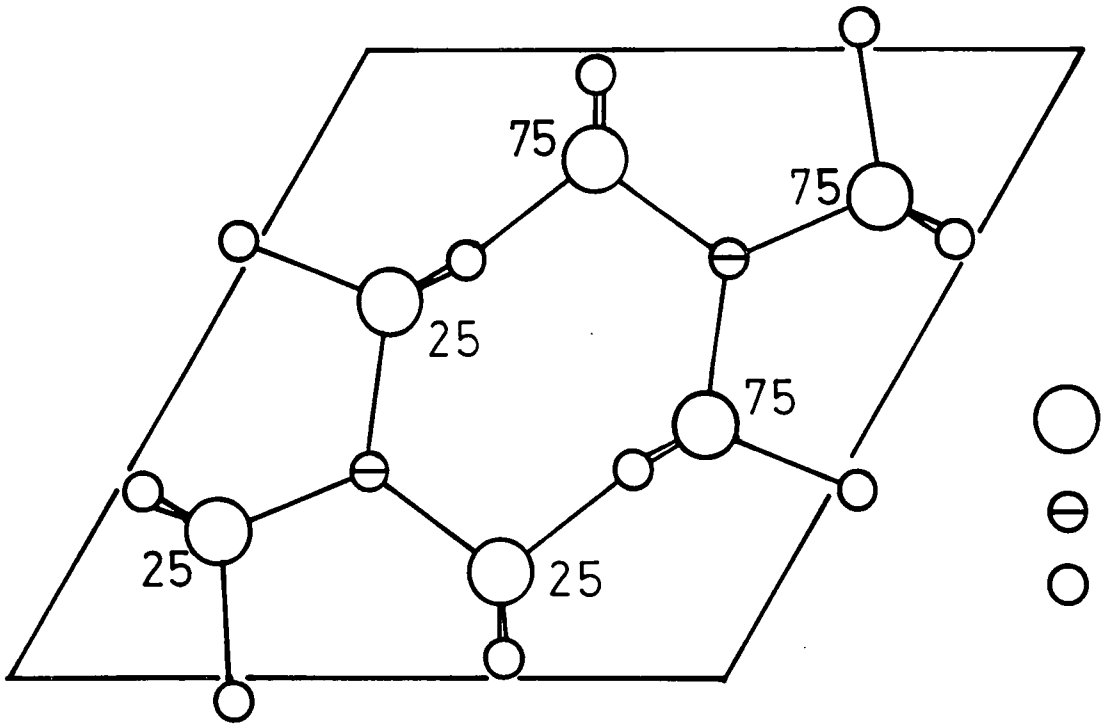

Figure 3.1.2 Schematic diagram of the crystal structure of Si_2N_2O.

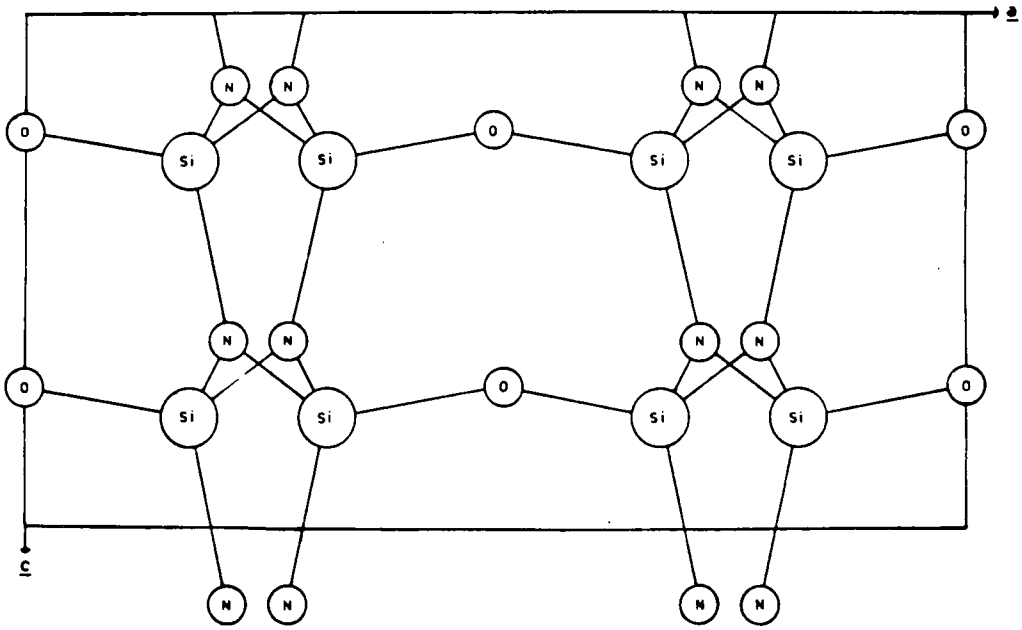

The remainder of this section consists of a description of the crystal structures of many of the phases encountered in M–Si–(Al)–O–N systems. Phase relationships will be represented using reciprocal salt diagrams, and the construction and interpretation of these diagrams is described in Appendix A.

3.1.2 Simple Binary Nitrides and Oxynitrides

Nitrogen can form a wide range of ionic, covalent and metallic compounds with metals.[5,6] Phases in the Si–Al–O–N system contain nitrogen in a covalent environment in which it is three or four coordinated (except in X-phase) to a metal. If more electropositive metals are introduced, then the bonding is found to become more ionic, and the nitrogen coordination number increases.

Silicon nitride was discovered in 1857,[7] but it was not until 1958 that Turkdogan *et al.*[8] and Hardie and Jack[9] established that it occurs in two hexagonal polymorphs: α–Si_3N_4 and β–Si_3N_4. There were many early determinations of the crystal structures of these two polymorphs,[9–12] often from powder patterns, but more reliable, single crystal determinations have now been published.

Grün[13] has determined the structure of β–Si_3N_4, shown in Figure 3.1.1. The Si and N environments are listed in Table 3.1.1. There is one silicon environment, in which the coordination is [SiN_4], and two nitrogen environments in which coordination is [NSi_3], and approximately planar.

Table 3.1.1 Silicon and nitrogen environments in silicon nitrides

	Si atom	site	ratio	N atom	site	ratio
α–Si_3N_4	Si(1)	6(c)	1	N(1)*	2(a)	1
	Si(2)	6(c)	1	N(2)*	2(b)	1
				N(3)†	6(c)	3
				N(4)†	6(c)	3
β–Si_3N_4	Si	6(c)		N(1)*	2(b)	1
				N(2)†	6(c)	

*on threefold axis; †not on threefold axis.

Figure 3.1.3 Behaviour diagram for the Si–Al–O–N system at $1700^{o}C$.[3]

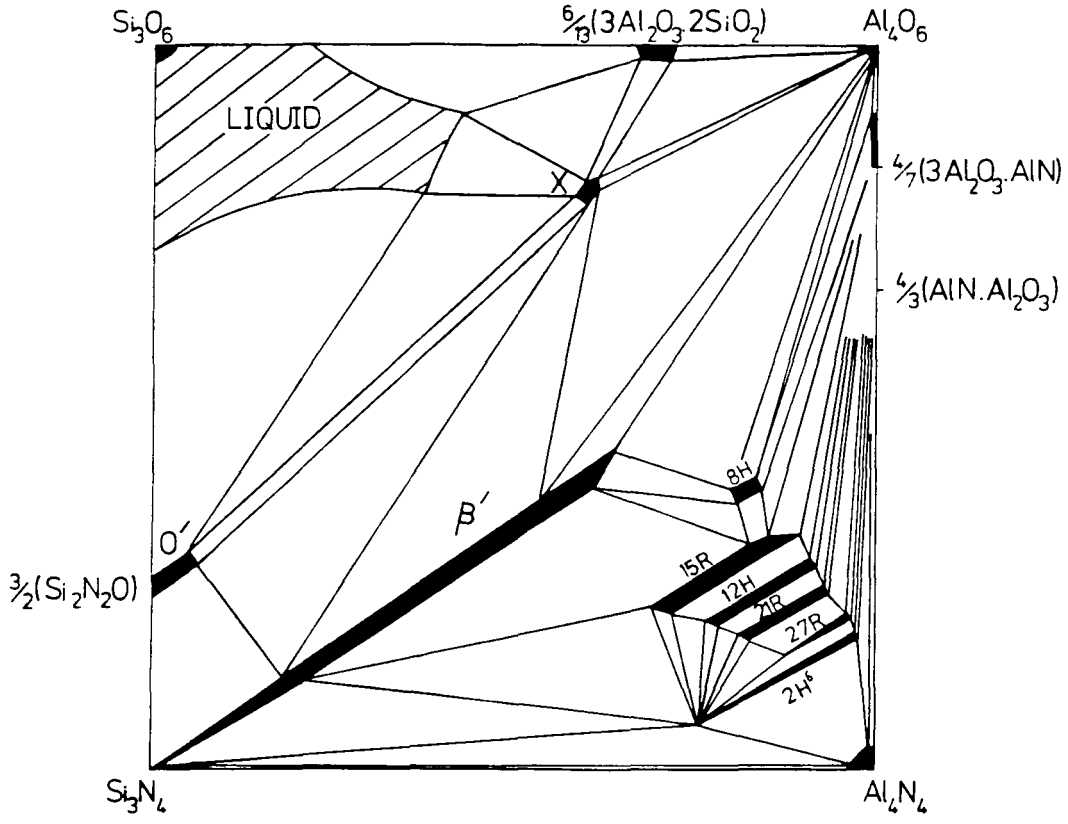

The structure of α–Si_3N_4 is more complicated. The unit cell is of double the volume of β–Si_3N_4 ($a_\alpha \approx a_\beta$, $c_\alpha \approx 2c_\beta$). Marchand *et al.*[14] and Kato *et al.*[15] have determined the structures of single crystal α–Si_3N_4, with reasonable agreement. The structure is found to be closely related to that of β–Si_3N_4. The top half of the cell is related to the bottom half (which is roughly isostructural with β–Si_3N_4) by reflection through a plane parallel to **c**, followed by translation by $c/2$. Distortions of bond lengths and angles mean that the symmetry of this transformation is not preserved, and each Si and N environment in β–Si_3N_4 thus gives rise to two in α–Si_3N_4 (Table 3.1.1).

There has been considerable controversy as to whether α–Si_3N_4 is stabilised by small amounts of oxygen.[11] Jack[16] has proposed that the structure can incorporate small numbers of Si^{3+} ions in the large interstices present in the structure, and suggests that the observed variations in measured unit cell dimensions of α–Si_3N_4 samples is due to a range of compositions $Si^{3+}_{0.3}Si^{4+}_{11.8}N^{3-}_{16}$ — $Si^{3+}_{0.3}Si^{4+}_{11.8}O^{2-}_{0.5}N^{3-}_{15.5}$.

Silicon also forms an oxynitride, Si_2N_2O. The structure of this phase[17] consists of layers of composition (SiN) bridged by two-coordinate oxygen atoms. Coordination environments (all equivalent in each case) are [$SiON_3$], [NSi_3] and [OSi_2].

Aluminium nitride crystallises in the wurtzite structure, in which Al is coordinated to four nitrogen atoms, and nitrogen to four silicon atoms. Only one type of each environment is found. Aluminium also forms a series of oxynitride phases,[18] which are not discussed here.

3.1.3 The Si–Al–O–N System

Early phase diagrams of the Si–Al–O–N system[19–21] showed considerable discrepancies. The presently accepted diagram at 1700^oC is shown in Figure 3.1.3. Four important structure types can be identified which contain significant amounts of nitrogen.

(i)β'–sialon

Isomorphous substitution of (AlO) for (SiN) can often occur in nitrogen ceramic phases, and the extent of this substitution is particularly large in β–Si_3N_4, where approximately two-thirds of the silicon can be replaced by aluminium, to

give a limiting composition $Si_2Al_4O_4N_4$.[20] There is a continuous range of homogeneity between these two compositions, represented by the general formula $Si_{6-Z}Al_ZO_ZN_{8-Z}$. The homogeneity range perpendicular to the line of constant M:X ratio is found to be negligible.

Slasor[22] has shown that the Z value of a particular β'–sialon can be determined from accurate measurements of the unit cell dimensions:

$$Z_a = (a - 7.6023)/0.030 \qquad (3.1.1)$$

$$Z_c = (c - 2.9060)/0.027$$

The major unresolved issue in the structure of β'–sialon is the ordering of (Si/Al) and (O/N) atoms on the metal and non-metal sites. Gillott *et al.*[23] and van Dijen *et al.*[24] have studied a series of β'–sialons by powder neutron diffraction. They conclude that oxygen atoms are more likely to occupy N 2(b) sites than would be expected from a random distribution. In Z=4 β'–sialon for example, Gillott *et al.* determine that the N 2(b) sites are 75% occupied by oxygen rather than the 50% predicted for a random distribution. They also conclude that there are a small number of vacant metal sites, a conclusion not supported by van Dijen.

(ii) O′–sialon

A similar, though less extensive isomorphous substitution is found to occur in Si_2N_2O,[25] to give a phase of general formula $Si_{2-x}Al_xO_{1+x}N_{2-x}$, where $x \leq 0.15$.

(iii) Sialon X–phase

Two polymorphs of this phase are known to exist: low–X and high–X, with a composition approximately $Si_3Al_6O_{12}N_2$. Low–X has a triclinic unit cell, and a structure similar to that of mullite.[26]

(iv) Sialon polytypoids

These are six structurally related AlN rich phases observed in the Si–Al–O–N system.[19,27] Polytypes are solids of identical composition which differ only in the way in which layers of the structure are stacked; polytypoids are similar to

Figure 3.1.4 Crystal structure of 15R sialon as determined by (a) Thompson,[30] and (b) Bando *et al.*[29]

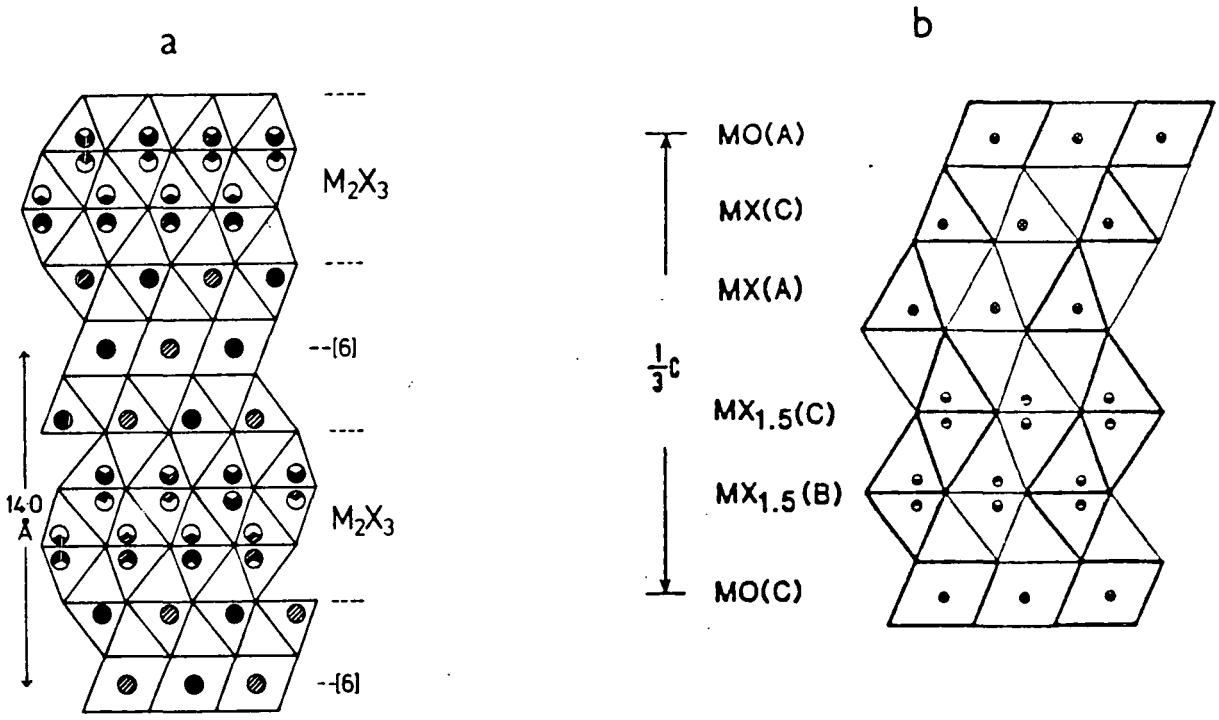

Table 3.1.2 The six Si–Al–O–N polytypoids[28]

Ramsdell symbol	M:X	Layers per block	a/Å	c/Å	Interlayer spacing/Å
8H	4:5	4	2.988	23.02	2.88
15R	5:6	5	3.010	41.81	2.79
12H	6:7	6	3.029	32.91	2.74
21R	7:8	7	3.048	57.19	2.72
27R	9:10	9	3.059	71.98	2.67
2Hδ	11:12	11	3.079	5.30	2.65
2H (AlN)	1:1	1	3.114	4.99	2.49

polytypes, except that the composition varies systematically between the phases. The compositions of the six sialon polytypoids are listed in Table 3.1.2. Hexagonal structures (H) consist of two symmetry-related blocks in the unit cell, whilst rhombohedral structures (R) contain three such blocks. Structure determinations[28,29] on the sialon polytypoids indicate that they are made up of layers of composition MX interspersed with layers of composition MX_2. Figure 3.1.4 shows the structure of 15R sialon, as determined by Thompson[30] and Bando *et al.*[29] Both structures contain layers in which a metal is six-coordinate (MX), four-coordinate (MX); plus layers made up of two edge-sharing tetrahedra in which one metal atom is distributed between two possible sites (MX_2). They differ in the stacking order of these layers (see Figure). The structures of 8H[30] and 12H[29] polytypes have also been determined, and show similar structural features. The determination by Bando *et al.* again showed that the layers with octahedral metal, and of composition MX_2 are adjacent.

The structural techniques used in the determinations described above are incapable of determining (Si/Al) and (O/N) distributions on M and X sites, but it is assumed that aluminium occupies all of the six-coordinate sites, as six-coordinate silicon is uncommon; and that oxygen will preferentially coordinate aluminium, and nitrogen silicon.

Polytypoid structures also occur in M–Si–Al–O–N systems,[28] and some of these

Figure 3.1.5 Generalised α'–sialon structure, after Patience.[78] Dotted circles show α–Si_3N_4.

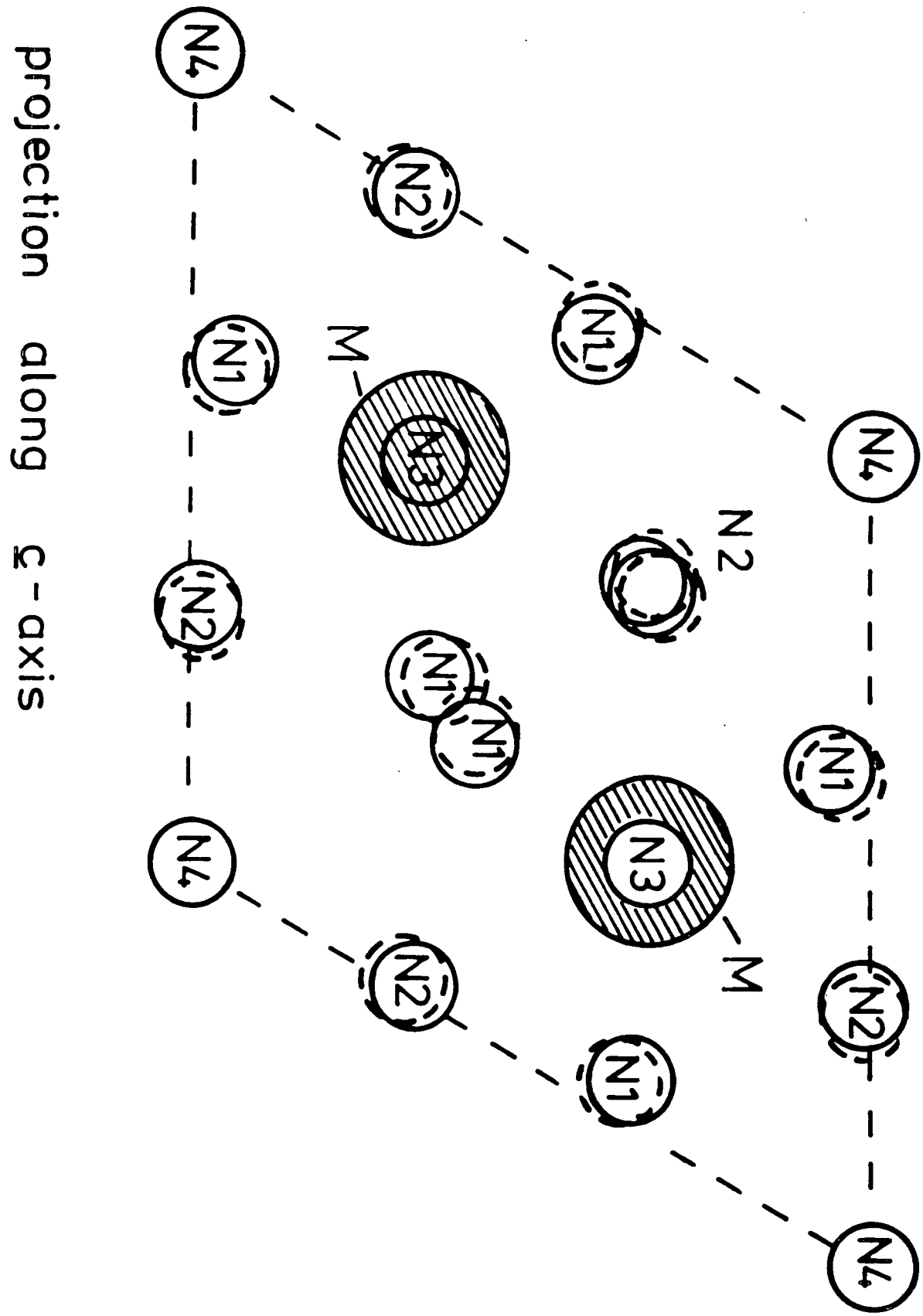

will be described below.

α'–sialons

α'–sialons are not found in the Si–Al–O–N system, but are stabilised by small amounts of large, electropositive metals.[16] Most metals with ionic radii less than 1 Å (e.g. Li, Ca, Y, Ln except La, Ce; but not transition metals) are found to stabilise this structure, which is closely related to that of α–Si_3N_4. The M^{n+} ions occupy the large interstices in the structure (Figure 3.1.5). This phase will be further discussed below in sections corresponding to the specific metals which stabilise it.

3.1.4 M^{III}–Si–Al–O–N Systems

M^{III}–Si–Al–O–N systems (M=Sc, Y, Ln) all show broadly similar behaviour with the exception of the scandium system. The phases encountered in this system have been thoroughly described,[31] and will not be discussed in detail in this Thesis. Of the rest, the yttrium,[32] lanthanum,[33] cerium,[34] and neodymium[35] systems have been the most extensively studied, and the following discussion will concentrate on these four metals unless otherwise stated.

M–Si–O–N Systems

Phase diagrams for the Ce–Si–O–N and Y–Si–O–N systems at 1700^oC are shown in Figures 3.1.6 and 3.1.7. The following silicon-containing phases and phase types can be identified from these diagrams.

(i) M–Si–O phases

Felsche[36] has comprehensively reviewed the structures of the lanthanide silicates, and Liddell and Thompson[37] have described the Y–Si–O system, and the reader is directed to these two articles for detailed references on the following discussion.

All the metals form silicates with the formula M_2SiO_5. There are two modifications: X_1–M_2SiO_5 (M=La, Ce, Nd) and X_2–M_2SiO_5. Yttrium silicate occurs in both forms. The basic structural unit is the isolated Q^0–SiO_4 group,[38] and the structure also contains essentially ionic M^{3+} and O^{2-} moieties.

Figure 3.1.6 The Ce–Si–O–N system at 1700^oC.[34]

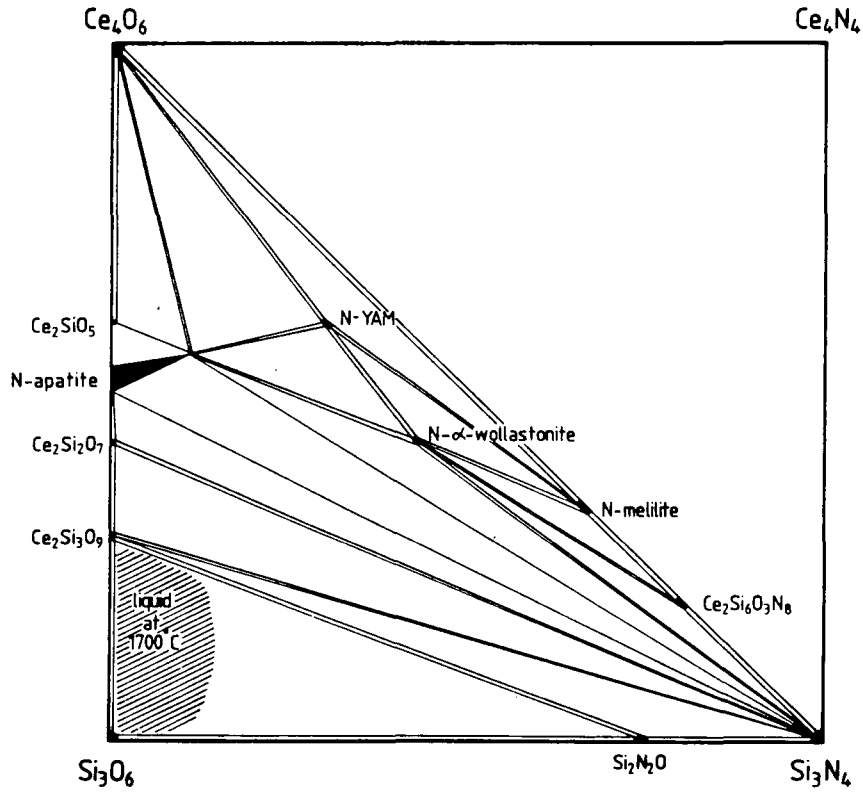

Figure 3.1.7 The Y–Si–O–N system at 1700^oC.[32]

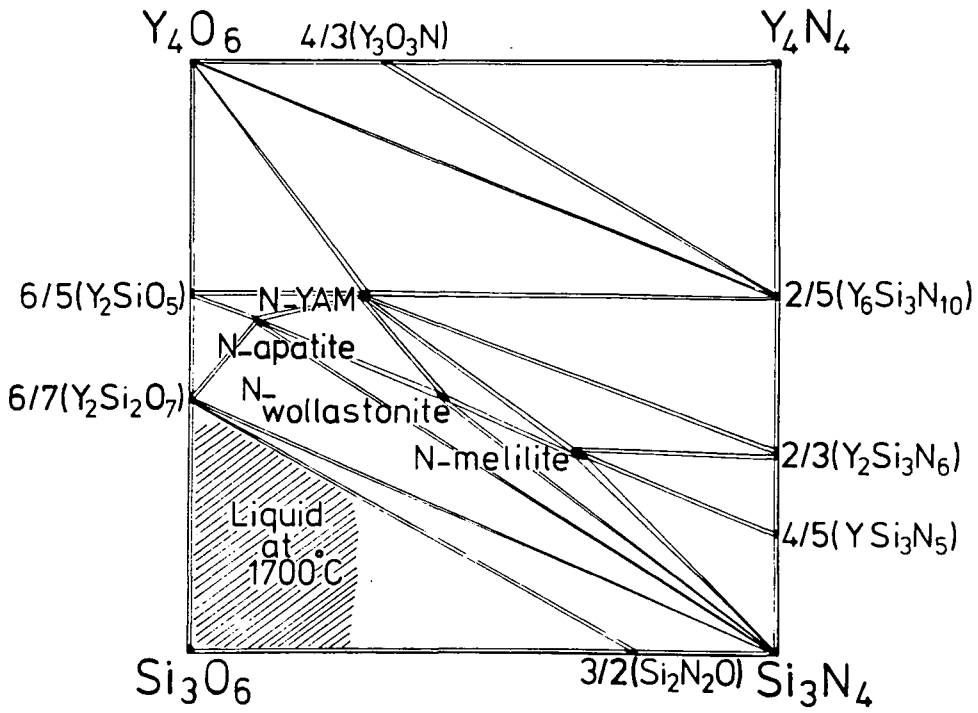

Oxide apatite phases are formed by all of the lanthanides, but the yttrium apatite is only formed when stabilised by nitrogen (*vide infra*). The parent structure, fluorapatite ($Ca_{10}(PO_4)_6F_2$)[39] is made up of $[PO_4]^{3-}$ units, with Ca^{2+} and F^- ions occupying sites between these units, arranged in an hexagonal unit cell. The lanthanide oxide apatites show a range of homogeneity, as determined from variations in unit cell dimensions, with vacancies occurring on both Ca^{2+} and F^- sites, but there has been controversy over the exact compositions and structures of these phases. Felsche postulates that a formula $M_{9.33}\square_{0.67}(SiO_4)_6O_2$ best describes the lanthanide apatites. Hamon *et al.*[40] have determined that for La and Sm, a homogeneity range to $M_8\square_2(SiO_4)_6\square_2$ exists, as determined from compositional and density measurements.

All of the metals form disilicates ($M_2Si_2O_7$). Felsche has identified seven polymorphs in $Ln_2Si_2O_7$ disilicates (A–G), and has shown that an excellent correlation can be made between ionic radius and temperature of formation, and the polymorph which is most stable. Six $Y_2Si_2O_7$ polymorphs have been identified, each of which is isostructural with one of the seven $Ln_2Si_2O_7$ structures. All of the seven $Ln_2Si_2O_7$ structures except the B form are made up of discrete Q^1–$[Si_2O_7]^{6-}$ units and Ln^{3+} ions. The Si–O–Si angle of the bridging unit is found[41] to vary from about 133^o to 180^o.

Doubt has been cast[42] on the existence of $Ce_3Si_2O_9$ (Figure 3.1.6). No other silicate of this formula has been reported.

(ii) M–Si–N phases

The ease with which the precursor metal nitrides (YN and LnN) are hydrolysed by atmospheric moisture has meant that these systems have received little attention. Jameel[43] and Thompson[32] have identified three nitrides in the Y–Si–N system at 1700^oC, but nothing is known about their structures. Inoue *et al.*[44] has reported a compound $LaSi_3N_5$, synthesized by nitridation of La_2O_3–Si_3N_4 mixes at $2000^oC/50$ atm $N_2/2$ h, which they fully characterised by a single crystal x-ray study.[45] Unfortunately, although they published a further paper in which they discuss the crystal structure,[46] no list of atomic coordinates has been issued. The structure of $LaSi_3N_5$ is shown in Figure 3.1.8, taken from Reference 46. From this diagram, and the partial list of coordinates published, La^{3+} would appear to be

Figure 3.1.8 The crystal structure of $LaSi_3N_5$, viewed along (001).[46]

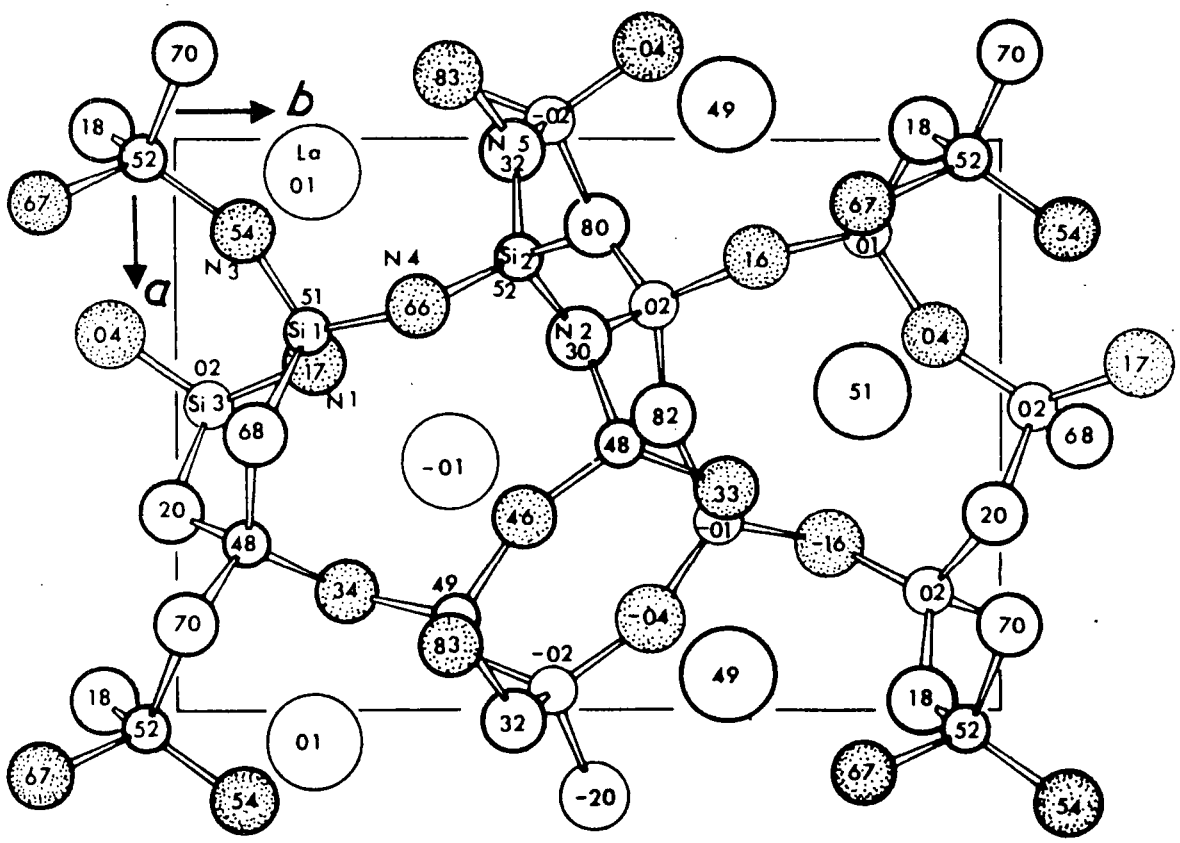

Table 3.1.3 Bond distances in angstroms for $LaSi_3N_5$, calculated from Figure 3.1.8

La - N(1)	2.40
La - N(1)	2.70
La - N(3)	2.60
La - N(3)	2.85
La - N(4)	2.68
La - N(4)	2.81
La - N(2)	2.86
La - N(5)	3.10
N(1) - Si(1)	1.68
N(1) - Si(3)	1.75
N(1) - La	2.40
N(1) - La	2.70
N(2) - Si(2)	1.72
N(2) - Si(2)	1.74
N(2) - Si(3)	1.75
N(2) - La	2.86
N(3) - Si(1)	1.68
N(3) - Si(3)	1.69
N(3) - La	2.60
N(3) - La	2.85
N(4) - Si(1)	1.68
N(4) - Si(2)	1.73
N(4) - La	2.68
N(4) - La	2.81
N(5) - Si(1)	1.81
N(5) - Si(2)	1.78
N(5) - Si(3)	1.77
N(5) - La	3.10

seven-coordinate; and not six, as stated in the paper. Nitrogen atoms N(2) and N(5) are covalently bonded to three silicon atoms, whilst N(1), N(3) and N(4) are covalently bonded to two silicons. Remaining coordination is to lanthanum, and is ionic in nature. All silicon atoms are present in $[SiN_4]$ environments; if La ions are ignored, then Si(1) is in a Q^5 environment, Si(2) is Q^6, and Si(3) is Q^7. Table 3.1.3 lists the bond distances calculated from Figure 3.1.8. Morgan[47] has discussed the structure of $LaSi_3N_5$ in terms of Pauling's Second Crystal Rule (PSCR),[48] and points out that N atoms which are bonded to two silicon atoms are not unique (as claimed by Inoue) but occur in $YSiO_2N$ and other phases.

It is anticipated that other lanthanide silicon nitrides will be discovered, when these systems are more fully investigated.

(iii) New phase, $M_2Si_6O_3N_8$

This phase, of unknown structure, has been reported only for lanthanum[33,49] and cerium.[34,50] It is thus probably stabilised by large cations.

(iv) N–melilite, $M_2Si_3O_3N_4$

This phase, which is isostructural with the mineral melilite, occurs for all of the metals[34,51,52] with the possible exception of lanthanum. Marchand *et al.*[51] report the synthesis of an N–melilite, $La_2Si_3O_3N_4$ at 1500^oC, but later workers[33] failed to prepare this phase. An early report by Wills *et al.*[49] has later been shown[53] to be based on an erroneous indexing of a powder pattern of a mixed phase sample.

The melilite structure consists of layers of composition M_3X_7, with metal ions lying between these sheets. In $Y_2Si_3O_3N_4$, Y^{3+} must occupy the interlamellar sites, whilst the layers have composition $[Si_3O_3N_4]$. The ordering of O and N in these layers will be discussed in Chapter 6.

(v) N–wollastonite, $MSiO_2N$

N–wollastonite phases have been found[33–35,52] in all of the metal systems studied. This phase is isostructural with the mineral α–wollastonite ($CaSiO_3$). The main structural unit is the $[Si_3O_6N_3]$ triangle of tetrahedra (Figure 3.1.9). X–ray[54] studies and PSCR calculations[48] on $YSiO_2N$ both indicate that the N atoms oc-

Figure 3.1.9 The structural unit in N–wollastonite.

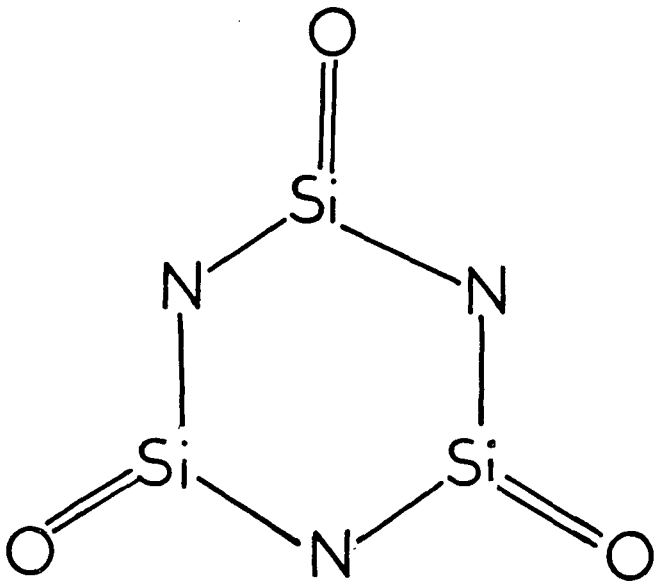

Figure 3.1.10 The basic structural unit in N–YAM.

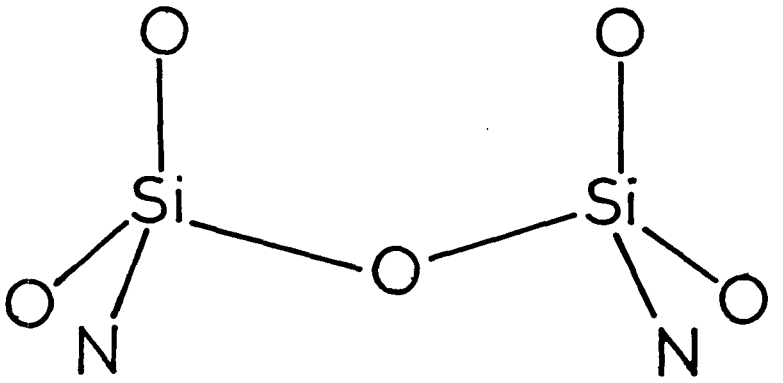

cupy the bridging sites, and this is confirmed by MAS NMR[55] (see Chapter 6). The crystal structures of $LaSiO_2N$ and $CeSiO_2N$ have also been determined.[56]

Various polytypic modifications of the N–α–wollastonite structure occur in which the number of distinct $[Si_3O_6N_3]$ layers varies. XRD and TEM studies show that there are 4×5 Å layers along **c** in $YSiO_2N$, but 6 in $LaSiO_2N$, $CeSiO_2N$ and $NdSiO_2N$.[55,57] Below around 1600^oC, the stacking order in the lanthanide N–wollastonites is disordered, and no systematic repeat units can be discerned from the TEM lattice images.[58]

(vi) N–YAM phase, $M_4Si_2O_7N_2$

Phases of this composition are found in all metal systems.[34,51,52] The phase is isostructural with the mineral cuspidine, $Ca_4Si_2O_7F_2$, and also the aluminates $M_4Al_2O_9$.[59] The monoclinic unit cell can be indexed in two distinct ways, and is pseudo-orthorhombic.[60] The basic structural unit is the $[Si_2O_5N_2]$ group, in which the nitrogen atoms occupy terminal sites[55] (see Figure 3.1.10), in violation of PSCR. Further oxygen atoms occupy essentially ionic sites between these units. No detailed structure determinations have been reported on N–YAM phases.

(vii) N–apatite phases

N–apatite phases have been reported for all of the metals,[34,40,52] but the range of compositions has not yet been mapped out in detail. Yttrium N–apatite, of approximate composition $Y_{10}Si_6O_{24}N_2$, is only stable if it contains significant amounts of nitrogen. PSCR predicts that the N atoms will not occupy the F^- sites, as the formula might suggest, but will be covalently bonded to Si, making a truer representation of $Y_{10}(SiO_4)_4(SiO_3N)_2O_2$. The other apatite phases all seem to show a range of homogeneity from a pure oxide to an approximate composition $M_{10}Si_6O_{24}N_2$. Gaudé *et al.*[61] have determined the crystal structure of samarium N–apatite by single crystal x–ray diffraction.

M–Al–O–N Systems

M–Al–O–N systems have not been studied in as much detail as M–Si–O–N systems. Phase relationships in M–Al–O systems have been described by several workers.[62,63] Yttrium forms three aluminates. $YAlO_3$ occurs in a low-temperature

Figure 3.1.11 The α' plane in the Y–Si–Al–O–N system.[35]

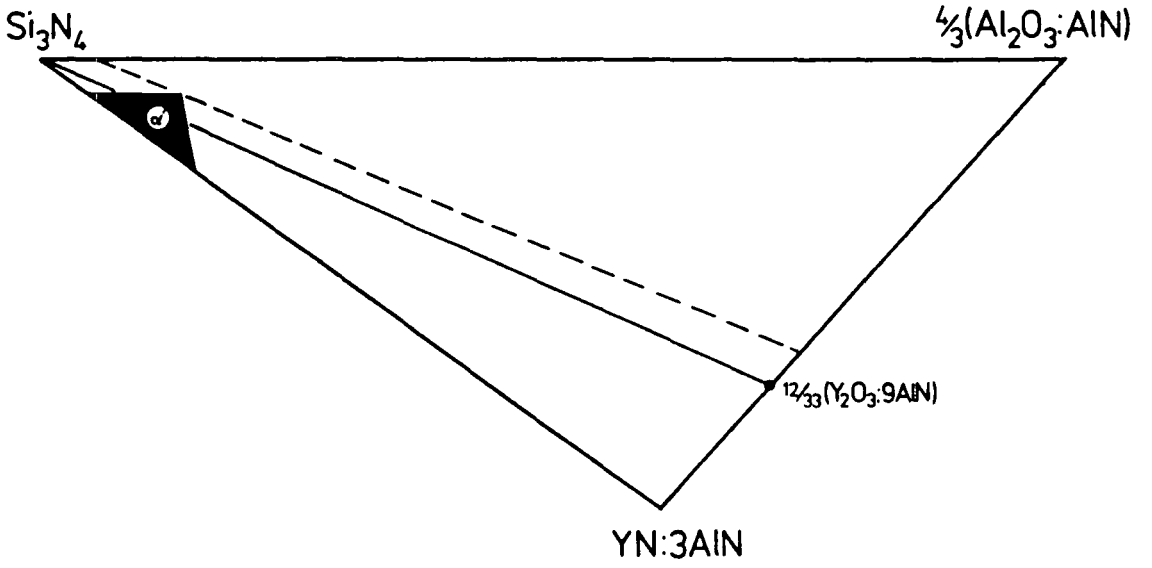

form ($T \leq 1100^oC$) with a wollastonite structure,[64] and a high temperature (1840–1880^oC) form with a perovskite structure.[63] $Y_4Al_2O_9$ is isomorphous with the N–YAM compounds described above. $Y_3Al_5O_{12}$, a garnet, is the third aluminate. La, Ce and Nd form perovskites, $MAlO_3$, of notably high stability, and β'–alumina phases.

A quaternary phase, M_2AlO_3N has been reported[64,65] in the La, Ce and Nd systems. No yttrium analogue has been reported. The phase is isostructural with K_2NiF_4, and is extremely moisture sensitive, hydrolysing on contact with air.

M–Si–Al–O–N Systems

These systems have not been explored in detail. Three types of phase are of interest, and will be discussed.

(i) Isomorphously substituted M–Si–O–N phases

Solid solutions can be extensive, and are accompanied by changes in lattice parameters. The known homogeneity ranges for the Y, Ce and Nd phases (the only ones studied) are listed in Table 3.1.4. Attention is drawn to the existence of a phase, Y_2SiAlO_5N, with a two-layer wollastonite structure; with very little range of homogeneity extending towards $YSiO_2N$. Y_2SiAlO_5N can only be prepared by recrystallisation from a glass at temperatures less than 1100^oC.[52]

Table 3.1.4 Homogeneity ranges in M–Si–Al–O–N phases

	Y[32]	Ce[34]	Nd[35]
N–melilite	NS	$Ce_2Si_2AlO_4N_3$	$Nd_2Si_{1.7}Al_{1.3}O_{4.3}N_{2.7}$
New	—	$Ce_2Si_4Al_2O_5N_6$	—
N–woll.	small*	negligible	negligible
N–YAM	$Y_4Al_2O_9$	Ce_4SiAlO_8N	NS
N–apatite	negligible	negligible	negligible

NS: not studied. *A compound Y_2SiAlO_5N with the wollastonite structure is known.

Figure 3.1.12 The crystal structure of Nd U–phase, viewed along (120).[70]

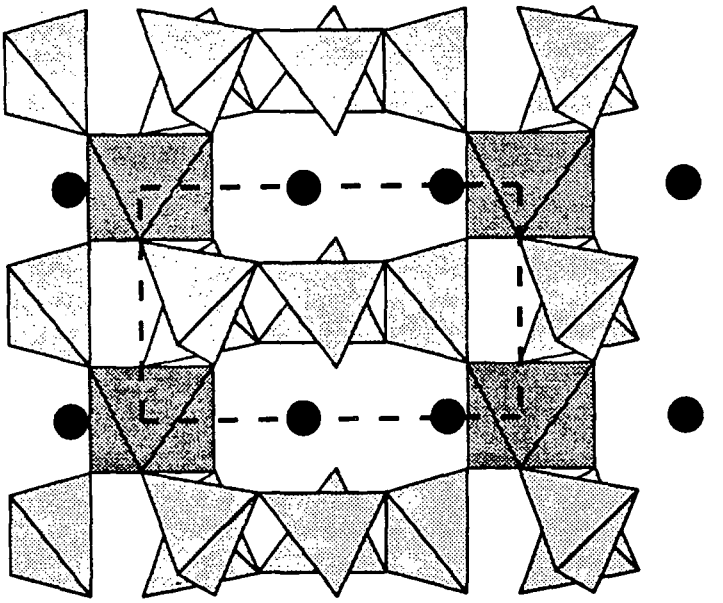

Figure 3.1.13 The structure of $MgSiN_2$, showing the true unit cell, and the hexagonal pseudo-unit cell. Metals are shown as empty shapes, and nitrogens by black shapes.

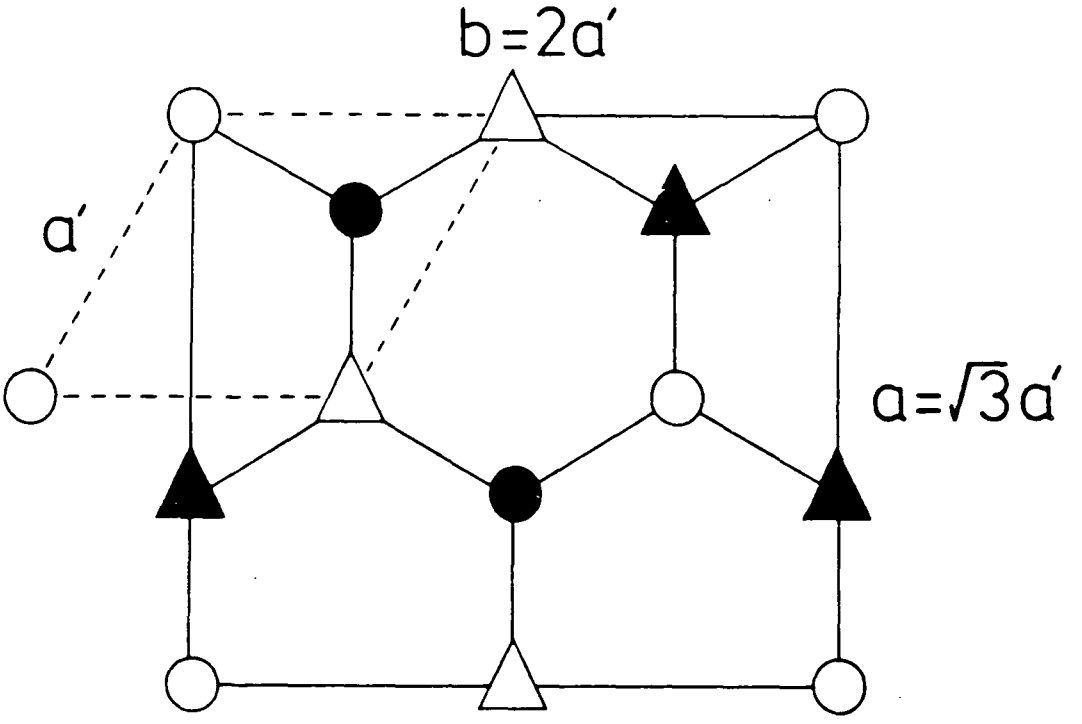

(ii) α'–**sialons, $M_x(Si,Al)_{12}(O,N)_{16}$**

α'–sialons are known for all of the lanthanides with atomic number greater than 59. The range of homogeneity for Nd is, however, small.[22] The α' plane of the Y–Si–Al–O–N system is shown in Figure 3.1.11. It is clear that the α' region does not extend to α–Si_3N_4, and the structure must be stabilised by at least ~ 0.3 Y^{3+} ions per unit cell.

Izumi *et al.*[66,67] have studied the structures of some yttrium α'–sialon phases by powder XRD using Rietveld refinement. They demonstrate that the Y^{3+} ions do indeed occupy some of the large enclosed interstices within the Si–Al–O–N network. Each yttrium ion is found to be coordinated to seven non-metal atoms at distances in the range 2.3–2.69 Å, and has a marked distorting effect on the interstice.

(iii) **U–phase**

U–phase sialons, of approximate composition $M_3Si_3Al_3O_{12}N_2$ have been prepared for M=Y, La, Ce, and Nd by recrystallisation of M–Si–Al–O–N glasses of the above composition.[68–70] The crystal structure of Nd U–phase has recently been determined by Rietveld profile refinement of a powder XRD diffractogram,[71] and is illustrated in Figure 3.1.12. It is found to be isostructural with the gallogermanate $La_3Ga_5GeO_{14}$. Atomic coordinates are listed in Table 3.1.5. It is assumed that aluminium occupies the octahedral sites, at the corners of the unit cell, as well as some of the tetrahedral sites.

In lanthanide U–phases, a range of homogeneity $Ln_3Si_{3-x}Al_{3+x}O_{12+x}N_{2-x}$ $(0 \leq x \leq 0.5)$ is proposed, based on EDAX evidence.[69]

3.1.5 (Li,Mg,Ca)–Si–Al–O–N Phases

Three types of phase encountered in these systems will be discussed: wurtzite type nitrides, α'–sialons and polytypoid phases. Tien *et al.*[21] and Jack [20] have reviewed the detailed phase relationships known for these systems.

(i) **Wurtzite type nitrides and oxynitrides**

Table 3.1.5 Atomic coordinates for $Nd_3Si_3Al_3O_{12}N_2$[71] (Space group P321, a = 7.9 Å,c = 4.9 Å).

Atom	Site	x/a	y/b	z/c
Nd	3(e)	0.4132	0	0
Al	1(a)	0	0	0
(Al,Si)	2(d)	$\frac{1}{3}$	$\frac{2}{3}$	0.5343
(Al,Si)	3(f)	0.7603	0	$\frac{1}{2}$
(O,N)	2(d)	$\frac{1}{3}$	$\frac{2}{3}$	0.2180
(O,N)	6(g)	0.4410	0.2984	0.3252
(O,N)	6(g)	0.2219	0.0923	0.7713

The nitrides $LiSi_2N_3$, $MgSiN_2$ and $MgSiAlN_3$, and the oxynitride LiSiON all crystallise with structures related to that of wurtzite (i.e. AlN). Li forms other silicon nitrides, which have been discussed by Jama.[72] These materials, and the calcium silicon nitrides tend to hydrolyse on contact with air, and have not been studied in this work.

The four phases mentioned above are all ordered variants of the AlN structure. $MgSiN_2$ and LiSiON both crystallise in orthorhombic systems, with $a \approx \sqrt{3}a_{AlN}$, $b \approx 2a_{AlN}$ and $c \approx c_{AlN}$. In the other two phases, the unit cell is also orthorhombic, but with $b \approx 3a_{AlN}$. As an example, the structure of $MgSiN_2$ is shown in Figure 3.1.13. Atomic environments are summarised in Table 3.1.6.

(ii) α'**–sialons**

Li,[72] Ca[16] and Mg[78] all form this phase. The calcium α' phase field is particularly wide: in this system it is found[79] that $0.5 \leq x \leq 2.0$. Izumi *et al.*[66] have determined the structure of a Ca α'–sialon of approximate composition $Ca_{0.67}Si_{10}Al_2O_{0.7}N_{15.3}$, and confirm that the structure is very similar to that of a typical yttrium α'–sialon.

(iii) **Polytypoids**

Buang[34] has studied in detail the polytypoids found in the Mg–Si–Al–O–N

Figure 3.1.14 Structures of the magnesium 6H′ and 12H sialon polytypoids.[28]

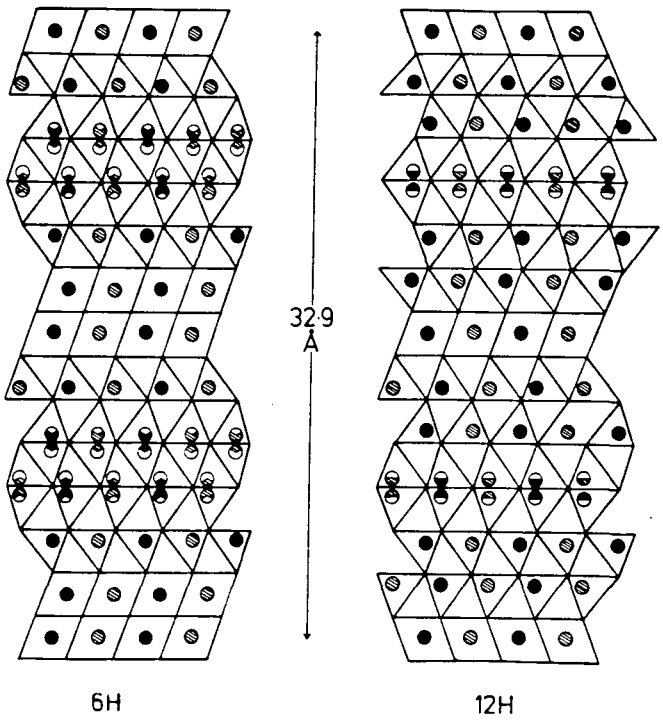

Figure 3.1.15 Phase relationships in the Be–Si–O–N system at 1700°C.[80]

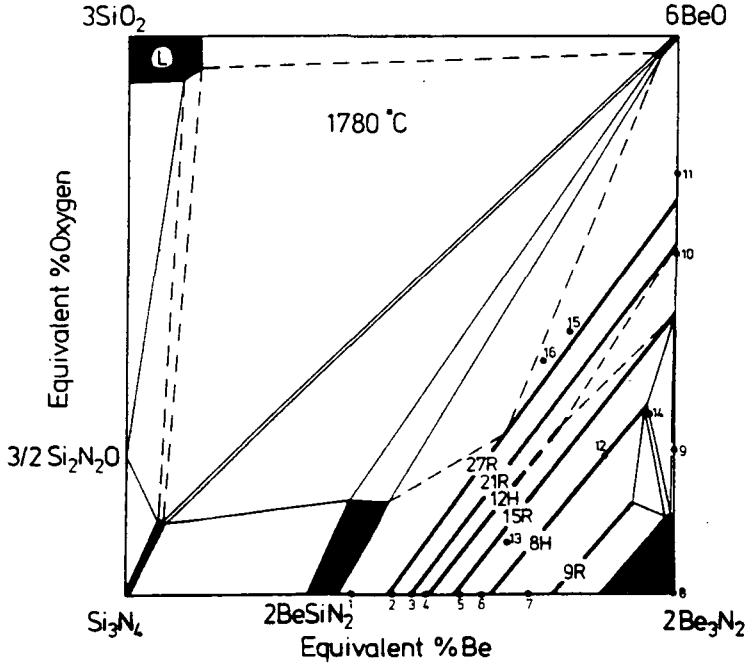

Table 3.1.6 Summary of the structures of wurtzite type nitrides and oxynitrides.

Phase	description	distinct environments	ratio	reference
$MgSiN_2$	Mg and Si ordered	$[MgN_4]$		73,74
	on Al sites	$[SiN_4]$		
		$[NSi_2Mg_2]$	1	
		$[NSi_2Mg_2]$	1	
LiSiON2	Li and Si ordered	$[LiO_3N]$		75
	on Al sites	$[SiN_3O]$		
	O and N ordered	$[OLi_3Si]$		
	on N sites	$[NSi_3Li]$		
$MgSiAlN_3$	Mg and (Si/Al)	$[MgN_4]$		76
	ordered on Al sites	$[(Si,Al)]N_4]$		
	but Si and Al dis-	$[NMg_2(Si,Al)_2]$	1	
	ordered on Si/Al sites	$[NMg(Si,Al)_3]$	2	
$LiSi_2N_3$	Li and Si ordered	$[LiN_4]$		77
	on Al sites	$[SiN_4]$		
		$[NSi_2Li_2]$	1	
		$[NSi_3Li]$	2	

system. These phases are listed in Table 3.1.7. He also performed a structure refinement on the 12H polytypoid, and confirmed that the structure is closely related to that of a Si–Al–O–N polytypoid. Magnesium is assumed to occupy the six–coordinate M environments in preference to Al. Thompson has described the structures of the 6H′ and 12H polytypoids,[28] and the structures of these phases are shown in Figure 3.1.14. The double layers of octahedra in the 6H′ structure, made possible by the higher Mg content of that phase, are noteworthy. The exact order of stacking of layers has not been determined with certainty (compare Si–Al–O–N polytypoids).

Table 3.1.7 Polytypoids in the Mg–Si–Al–O–N system[34]

Ramsdell symbol	M:X	a/Å	c/Å	Interlayer spacing/Å
15R	5:6	3.051	41.87	2.79
12H	6:7	3.072	32.64	2.72
6H′	6:7	3.069	16.33	2.72
21R	7:8	3.076	56.36	2.68
14H	7:8	3.070	37.52	2..68
8H′	8:9	3.083	21.15	2.64

3.1.6 Be–Si–Al–O–N Phases

Huseby *et al.*[80] and Thompson and Gauckler[81,82] have studied the Be–Si–O–N system, and the phase diagram at 1780^oC is shown in Figure 3.1.15. Small β' and $BeSiN_2$ homogeneities are observed ($BeSiN_2$ is isostructural with $MgSiN_2$), but the most interesting feature is the series of polytypoids. All of the Si–Al–O–N polytypoids are formed, plus a 9R and a 4H (β–Be_3N_2). The range of homogeneity of these phases is found to be larger than in the Si–Al–O–N system. Because Be has a low valence, the M:X ratios are all greater than one. The structure of β–Be_3N_2 has ben determined,[83] and no six-coordinate metal atoms are present. The ordering of layers is MX–M_2X–MX–MX_2X. The M_2X layers are of similar structure to the MX_2 layers in the Si–Al–O–N polytypoids, but with metal and non-metal atoms switched.

Thompson[84] has shown that β' Be–Si–Al–O–N phases can be prepared with a limit of solid solution of $Be_{0.2}Si_2Al_{1.4}O_{6.6}N_{1.4}$.

3.1.7 Glasses

It has already been mentioned that the properties of engineering ceramics are profoundly affected by the properties of the grain boundary phases. Often these phases are vitreous in nature. The structures of these glasses are difficult to study by techniques used for crystalline phases (e.g. XRD, TEM). The presence of nitrogen in glasses has the effect of lowering the eutectic temperature,[85] and will

thus profoundly affect the high temperature properties of the glass. Up to $25^a/o$ N can be incorporated into glasses.[85–87]

Devitrification of glasses at temperatures in the region 800–1400^oC often leads to crystallisation of phases, such as Y_2SiAlO_5N and U–phase, which cannot be prepared by direct routes. Shaw and Thomas[88] have studied the crystallisation behaviour of Mg–Si–O–N glasses, including examination of the microstructure during crystallisation.

3.2 NMR Studies of Systems Related to Nitrogen Ceramics

3.2.1 Introduction

The principal nuclei which will be considered in this Thesis are listed in Table 3.2.1. Of these nuclei, ^{29}Si and ^{27}Al have received by far the most attention in so far as inorganic solids are concerned. I shall therefore review NMR studies of these nuclei in silicates, aluminosilicates and related systems, with special reference to the correlation of chemical shift with chemical and crystallographic environment. These correlations will later be seen to have particular applicability when considering the NMR of nitrogen ceramics. I shall then consider the NMR of the other nuclei listed in Table 3.2.1, trying to emphasise aspects which will prove of relevance later in the Thesis.

Most of the published NMR studies on nitrogen ceramics are of direct relevance to the study of systems described in this Thesis, and will be discussed in later chapters. A few studies of silicon carbide ceramics are also of interest, and will be mentioned in a short section at the end of this chapter.

3.2.2 Silicon–29 NMR of Solids

Chemical Shift Values

The main information obtained from ^{29}Si spectra of minerals and ceramics is the isotropic chemical shift, δ_{Si}, and although some shielding anisotropy studies on silicate materials have been undertaken,[90] this section will concentrate on isotropic values.

Figure 3.2.1 Ranges of δ_{Si} for various Q^n units in solid silicates.[94]

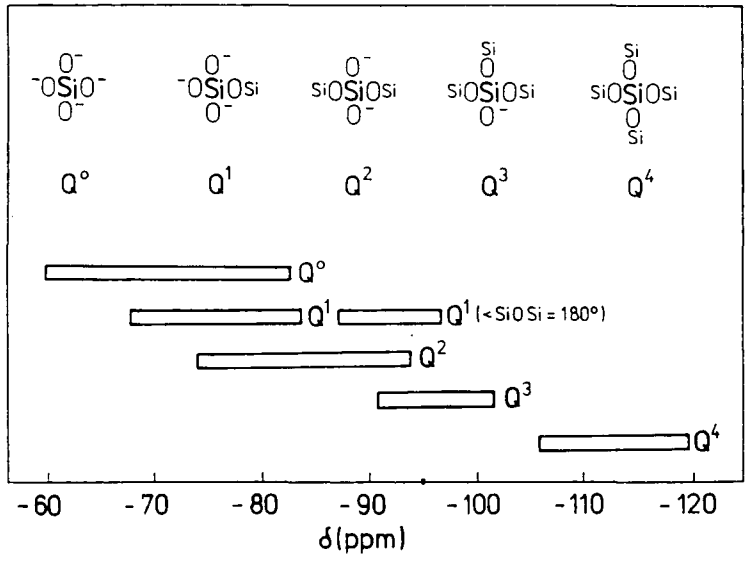

Figure 3.2.2 Ranges of δ_{Si} for $Q^4(n\mathrm{Al})$ units in aluminosilicates.[95]

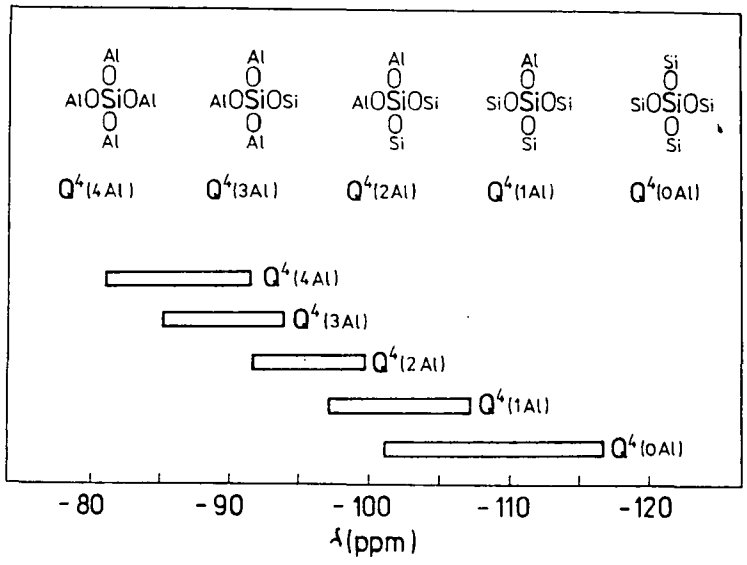

Table 3.2.1 Principal nuclei for NMR of ceramics[89]

Nucleus	I	Abundance/%	$10^{28}Q/m^2$	ν_L/MHz[(a)]	Receptivity[(b)]
^{15}N	$\frac{1}{2}$	0.37	—	30.4	3.85×10^{-6}
^{29}Si	$\frac{1}{2}$	4.70	—	59.6	3.69×10^{-4}
^{89}Y	$\frac{1}{2}$	100.0	—	14.8	1.19×10^{-4}
^{7}Li	$\frac{3}{2}$	92.58	-4×10^{-2}	116.6	0.272
^{9}Be	$\frac{3}{2}$	100.0	$+5 \times 10^{-2}$	42.2	1.39×10^{-2}
^{17}O	$\frac{5}{2}$	0.037	-3×10^{-2}	40.7	1.08×10^{-5}
^{27}Al	$\frac{5}{2}$	100.0	+0.15	78.2	0.207
^{45}Sc	$\frac{7}{2}$	100.0	−0.22	73.0	0.302
^{139}La	$\frac{7}{2}$	99.91	+0.22	42.6	6.02×10^{-2}

(a) At 7.1T; (b) Relative to ^{1}H, at natural abundance.

The ^{29}Si chemical shift range for tetrahedrally coordinated silicon in inorganic solids covers around 100 ppm, from *ca.* −15 ppm in silicon carbides ([SiC_4] coordination) to *ca.* −100 ppm in the various polymorphs of silica ([SiO_4] coordination). Six-coordinate silicon is much rarer. ^{29}Si chemical shifts from [SiO_6] environments occur at much more negative values: −179.6 ppm in thaumanite,[91] −191.6 ppm in stichovite,[92] and −213 ppm in Na-P silicate glass.[93] The last of these values is the most negative δ_{Si} value yet observed in a non-molecular solid.

The first chemical shift correlation to be noted for Si in solid silicates was between δ_{Si} and the Q number of the silicon atom, and with numbers of aluminium next nearest neighbours (n.n.n.) in Q^4 aluminosilicate environments (see Figures 3.2.1 and 3.2.2). It has proved possible to improve significantly upon these rather rough correlations. δ_{Si} can be correlated with electronegativities of nearest and next nearest neighbours, Si–O–M bond angle, Si–O and O–M bond lengths, and lattice parameters.

(i) The electronic environment of the silicon atom.

Janes and Oldfield,[96] and Engelhardt and Michel[95] have reviewed the correlation of chemical shift with nearest neighbour (n.n.) electronegativity. They find

Figure 3.2.3 (a) Calculated paramagnetic shielding constants σ^*, and (b) experimental δ_{Si} of SiX_4 compounds plotted against net atomic charge on the central Si atom, q_{Si}.[95]

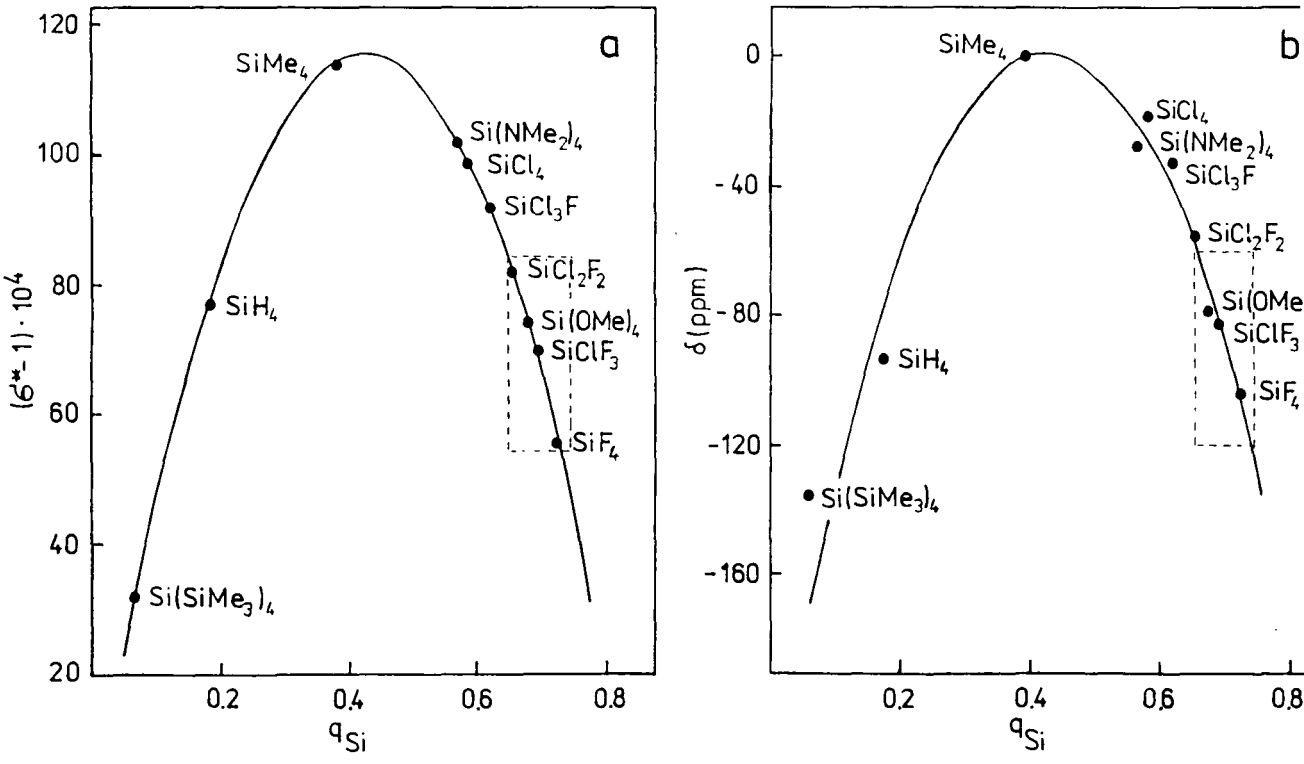

an excellent correlation between calculated and experimental ^{29}Si chemical shifts for a wide range of SiX_4 species, as shown in Figure 3.2.3. Theoretical ^{29}Si shifts were calculated using Slater-type orbitals and Pauling electronegativities (Equation 2.1.13). The curves between $Si(NMe_2)_4$ and $Si(OMe)_4$ are approximately linear, and it is therefore expected that the correlation between n.n. electronegativity and δ_{Si} will be linear in this region. Janes and Oldfield[96] also demonstrate that correlations such as those in Figures 3.2.1 and 3.2.2 can readily be explained by considering the electronegativity of the oxygen atoms attached to the central Si, as modified by the metals coordinated to those oxygens, using a group electronegativity approach. This correlation can be expressed by the formula:

$$\delta_{Si} = -24.336 \sum(EN) + 279.27 \qquad r = 0.991 \tag{3.2.1}$$

The values of the group electronegativities, EN, were calculated by considering minerals in which only one oxygen environment is present.

These models are complicated by coordination to n.n. with significant d-orbitals. Tenhover *et al.*[97] found δ_{Si}=−17 ppm in SiS_2, but δ_{Si}=−93 ppm in $SiSe_2$, despite their similar structures and electronegativities.

(ii) Si–O–M bond angle

Altering the Si–O–M bond angle in a silicate is found to affect the oxygen electronegativity, since s and p electrons themselves have different electronegativities. Changing the bond angle, α, alters the hybridisation of the M—O bond, and hence affects the oxygen electronegativity. Janes and Oldfield[96] suggest the correlation:

$$EN(\mathrm{OSi}) = \alpha/136.7 + 2.9235$$

from δ_{Si} measurements on SiO_2 polymorphs, where EN values are then used in Equation 3.2.1. Various other correlations between $\overline{\alpha}$ and δ_{Si} have been suggested, and these have been reviewed by Engelhardt and Michel.[95] The correlation of δ_{Si} with $\overline{\sec\alpha}$ of Engelhardt and Radeglia[98] of a range of SiO_2 polymorphs and zeolites is particularly successful (r = 0.982, 21 data points).

These correlations have been supported by theoretical treatments (*vide infra*).

Figure 3.2.4 Definitions of angles and distances in Equation 3.2.3.

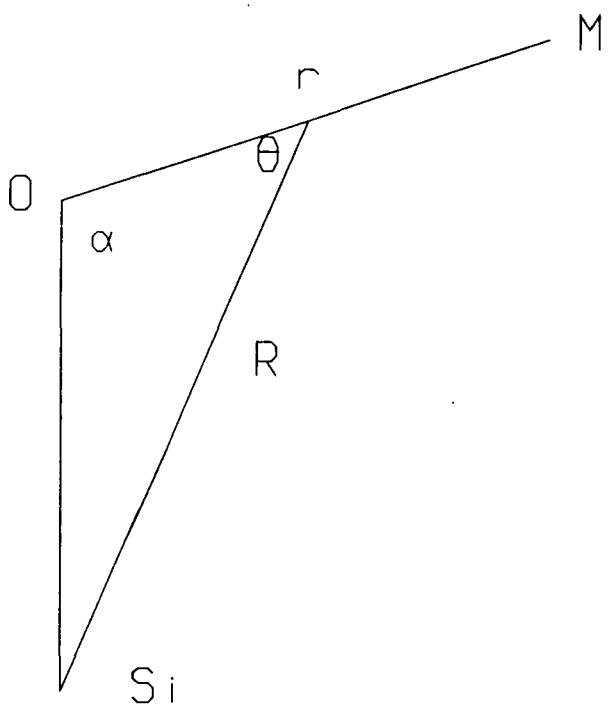

Figure 3.2.5 ^{29}Si MAS NMR spectra of Na_2O–SiO_2 glasses. $^m/_o$ Na_2O is shown.[106]

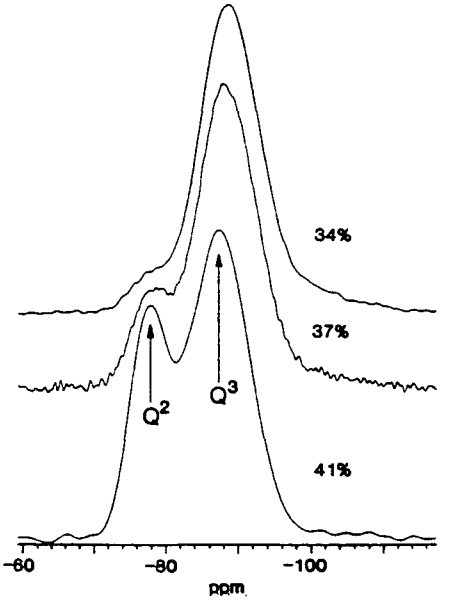

(iii) Si–O and O–M bond lengths

Shallow correlations between δ_{Si} and Si—O bond lengths in silicate minerals have been reported.[99] Mägi *et al.*[94] have also suggested correlation with O—M bond strength, a correlation which they ascribe to changes in the degree of covalency in the O—M bond, changes which would of course affect oxygen electronegativity.

(iv) Lattice parameters

Engelhardt *et al.*[100] have recently demonstrated that in cubic sodalites, δ_{Si} can be accurately correlated with the measured cubic lattice constant:

$$\delta_{Si} = 139.92 - 25.81a_o \qquad r = 0.977, 16\text{points} \tag{3.2.2}$$

The authors explain that such correlations are to be expected because changes in cell constant can be related to variations in Si–O–M bond angles.

(v) More sophisticated correlations

Sherriff and Grundy, and Sternberg have recently attempted to give correlations such as those above a sounder theoretical basis. Sherriff and Grundy[101] have calculated the magnetic anisotropy for the bonds between oxygen and the n.n.n. of the central Si in a wide range of silicates and aluminosilicates. The magnetic anisotropy factor, χ, was calculated for an Si atom by use of the equation:

$$\chi = \sum_i s_i[(1 - 3\cos^2\theta_i)/3R_i^3][\cos\alpha_i/(\cos\alpha_i - 1)] \tag{3.2.3}$$

Angles and distances are defined in Figure 3.2.4, and i refers to all the various O—M bonds. s_i is a small bond valence correction which depends on r.[102] The term in θ and R comes from the magnetic anisotropy equation of McConnell.[103] The term in α is the Gibbs hybridisation correction, to allow for changes in hybridisation at small α. The authors considered 76 silicates and aluminosilicates, and found a correlation between δ_{Si} and χ:

$$\delta_{Si} = 650.08\chi - 56.06 \qquad r = 0.991 \tag{3.2.4}$$

If the Si—O and O—M distances do not vary a great deal in a series of phases, then variations in α and θ can be seen to be geometrically related, and hence small changes in θ can be seen to have a profound effect on δ_{Si}. All of the correlations discussed earlier can thus be seen to be a subset of Equation 3.2.4. This paper is undoubtedly the most important to date on the correlation of δ_{Si} with structural variables. Only the s_i terms cannot be directly measured from the crystal structure.

Sternberg[104] has attempted to correlate δ_{Si} with calculated values of the bond polarisation parameter, as affected by n.n.n. atoms in a series of seven silicates, including the SiO_2 polymorphs. Both n.n.n. electronegativity and Si–O–M bond angles are shown to be important in determining δ_{Si}. This paper is important in that the correlation is given a direct theoretical basis in terms of magnetic shielding.

^{29}Si MAS NMR of Glasses and Disordered Materials

Peaks in ^{29}Si MAS NMR spectra of glasses are much broader than those from crystalline phases. This is readily understood if it is realised that in a glass, atoms occur in a range of environments; in proximity with n.n. and n.n.n. of varying electronegativity, and with a range of bond angles and lengths. NMR spectra of glasses can nevertheless provide useful information on their structures; information which is not easily obtainable by other physical methods.

Kirkpatrick *et al.*[105] have reviewed ^{29}Si MAS NMR studies of silicate glasses. In favourable cases, such as pure SiO_2 glasses, correlations such as Equation 3.2.4 can be used to obtain a mean Si–O–Si bond angle, but in most glasses there are too many variables to extract this kind of information. Stebbins[106] has used ^{29}Si MAS NMR to determine the ratios of Q^2 and Q^3 units in ^{29}Si-enriched sodium silicate glasses (Figure 3.2.5). Static spectra are found to be more sensitive to the amount of Q^4 units, because of the lower shielding anisotropy associated with this environment. Dupree *et al.*[107] have also studied this system, and Schramm *et al.*[106] have used a similar procedure to study Li_2O–SiO_2 glasses. In systems such as B_2O_3–Na_2O–SiO_2, where substantial overlap of peaks occurs, Bunker *et al.*[109] have shown that deconvolution of spectra can still give useful structural information.

MAS NMR is also extremely useful in determining the degree of (Si,Al) ordering on lattice sites in aluminosilicates. The similar x-ray scattering factors of Si and Al mean that such information cannot generally be obtained directly by XRD. Klinowski *et al.*[110] have studied disordered ultramarine by ^{29}Si MAS NMR and have shown by deconvolution of the spectra that Al and Si are randomly distributed across the lattice sites, in apparent contradiction of Lowenstein's rule, which forbids Al–O–Al linkages.[111] Studies of $CaMgSi_2O_6$–$NaAlSi_3O_8$ glasses[112] suggest, however, that truly random distributions of metal atoms do not always occur, even in vitreous phases.

Gerstein and Nichol have shown[113] that differences in T_1 can be used to distinguish glassy and crystalline regions in SiO_2–Al_2O_3 samples by use of differential saturation. Amorphous regions were found to give rise to shorter ^{29}Si T_1 times than crystalline regions. It seems likely that this type of study will be of great benefit in the future in determining the fraction of amorphous material in multiphase samples.

Other Experiments on Silicates

There have been very few reports of spin-lattice relaxation time measurements on silicates, but values can often be very long. Baron *et al.*[114] report a value of 5000 s for nacrite, the longest yet found. Much shorter relaxation times are found in hydrated silicates and zeolites, where some molecular or group motion can occur; and in minerals which contain paramagnetic centres (see Section 3.2.9). It is not however clear what causes relaxation in other systems. Klinowski *et al.*[115] have measured ^{29}Si T_1 times of zeolites under argon and dioxygen, and find that in the latter situation they can be 1–4 orders of magnitude shorter than in the former. The authors postulate that paramagnetic dioxygen is the principal cause of spin-lattice relaxation in zeolites. One would thus expect T_1 times in much less porous silicates to be much longer than in zeolites, and this seems to be true.

Use of many of the modern 2-dimensional techniques which have proved so successful in the elucidation of the structures of organic solids has been virtually impossible on silicate materials because of the long T_1 times and relatively low natural abundance of ^{29}Si. Fyfe *et al.*[116–118] have used ^{29}Si CP/MAS NMR 2D-COSY on $80^{\alpha}/o$ isotopically enriched zeolites to establish Si–O–Si connectivities,

Figure 3.2.6 Frequency shift of ^{27}Al $(\frac{1}{2}, -\frac{1}{2})$ transition in a 7.1 T magnet (ν_L = 78.2 MHz).

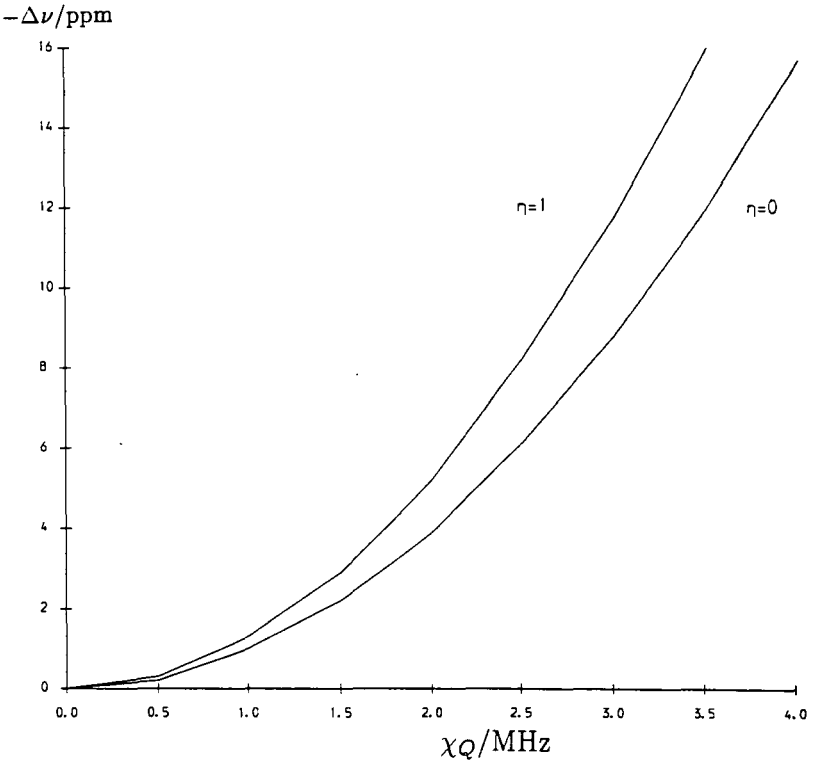

Figure 3.2.7 Ranges of δ_{Al} for various environments in aluminosilicates.[95]

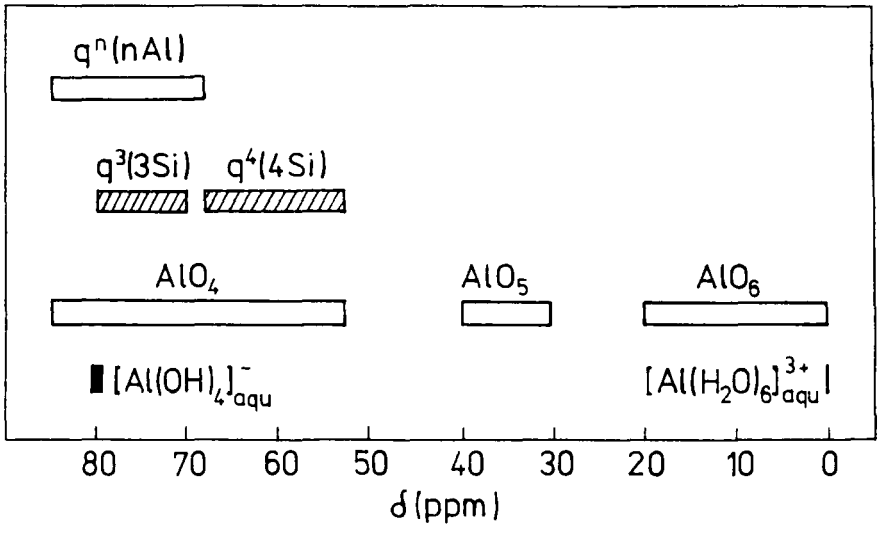

and it seems likely that similar experiments will, in the future provide valuable structural information on related systems.

3.2.3 Aluminium–27 NMR of Solids

Correlations of δ_{Al} values with structure of a similar nature to those discussed above for δ_{Si} should occur, but because of the quadrupolar broadening, it is much more difficult to determine resonance positions accurately, and to resolve overlapping peaks. Complications also arise from second order quadrupolar coupling, which must be corrected for by determination of χ_Q and η_Q. Extensive ssb manifolds also tend to complicate the appearance of spectra. Nevertheless, a considerable amount of useful information on aluminosilicate structure has been obtained from ^{27}Al NMR.

Approximate correlations of δ_{Al}

Many workers have used ^{27}Al chemical shifts without attempting to correct the values for quadrupolar coupling. At 300 MHz (^{1}H resonance) the field-dependent shift is only around 10 ppm for χ_Q=3 MHz (Figure 3.2.6), and so this is not unreasonable for coarse correlations.

The main structural information available from ^{27}Al MAS NMR spectra of aluminosilicates is the aluminium coordination environment. It is found that [AlO_4] coordination gives δ_{Al} values in the range +45–+80 ppm, and [AlO_6] in the range −10–+15 ppm;[119] both environments are commonly encountered in minerals (contrast the rarity of [SiO_6]). Caution needs to be taken in the quantitative interpretation of peak areas because of the loss in intensity caused if only the central transition is being observed (Equation 2.1.16).

Five-coordinate aluminium in andalusite has recently been found[120] to resonate at a corrected shift of +35 ppm, intermediate between [AlO_4] and [AlO_6]. Sanz *et al.*[121] have postulated the existence of [AlO_5] in dehydroxylated kaolinite, from uncorrected shifts in the region of +30 ppm (at a ^{27}Al frequency of 104.26 MHz).

Stebbins *et al.*[122] have used ^{27}Al MAS NMR to look at very low levels of Al dissolved in TiO_2, demonstrating that the high natural abundance and short

relaxation times of ^{27}Al make feasible the study of much lower levels than possible by ^{29}Si NMR.

^{27}Al MAS NMR can be used[105] to study amorphous materials, although resonances tend to be very broad because Al is normally present in asymmetric environments with high χ_Q values. Indeed, it is often found that the majority of Al atoms cannot be seen at all because of the broadness of their resonances. In some systems nevertheless, useful information can still be obtained. Turner *et al.*[119] have used ^{27}Al MAS NMR on aluminosilicate glasses to determine the amount of [AlO_6] present, and find that only glasses with $>50^m/_o$ Al_2O_3 contain significant amounts of this structural unit.

Accurate determinations of δ_{Al} and χ_Q

Accurate determinations of δ_{Al} and χ_Q in aluminosilicates have used all of the methods listed in Section 2.1.5 to determine the field-dependent shift. Lippmaa *et al.*[123] have examined a series of 17 framework aluminosilicates, and find an excellent correlation between δ_{Al} and Al–O–Si angle for tetrahedrally coordinated Al. The sensitivity of δ_{Al} to changes in bond angle ($\sim$0.5 ppm deg^{-1}) is similar to that of δ_{Si} ($\sim$0.62 ppm deg^{-1}). Müller *et al.*[124] have found, however, that δ_{Al} is much less sensitive than δ_{Si} to Q^n index. They conclude that δ_{Al} is instead more sensitive to n.n.n. electronegativity. They also find that in general, Q^1, Q^2 and Q^3 [AlO_4] units have larger values of χ_Q than Q^0 and Q^4, although there is a great deal of overlap in the ranges. Typical values of χ_Q were found to lie in the range 1–10 MHz. The effect of environment on δ_{Al} is summarised in Figure 3.2.7.

3.2.4 Nitrogen–15 NMR

Referencing of ^{15}N shifts is discussed in Appendix B. All shifts quoted in this section are converted to $\delta_N(\mathrm{NH_4NO_3}(s)) = 0$.

There have been few reported studies of ^{15}N NMR in inorganic solids, principally because of the need for isotopic enrichment in the majority of systems. Natural abundance studies have generally been acquired with the aid of CP from protons. This has allowed the study of a few inorganic,[125,126] and organic and polymeric[127,128] systems. Recently, Bunker *et al.*[129] have studied a series of ^{15}N-

Figure 3.2.8 Ranges of δ_N in solution.

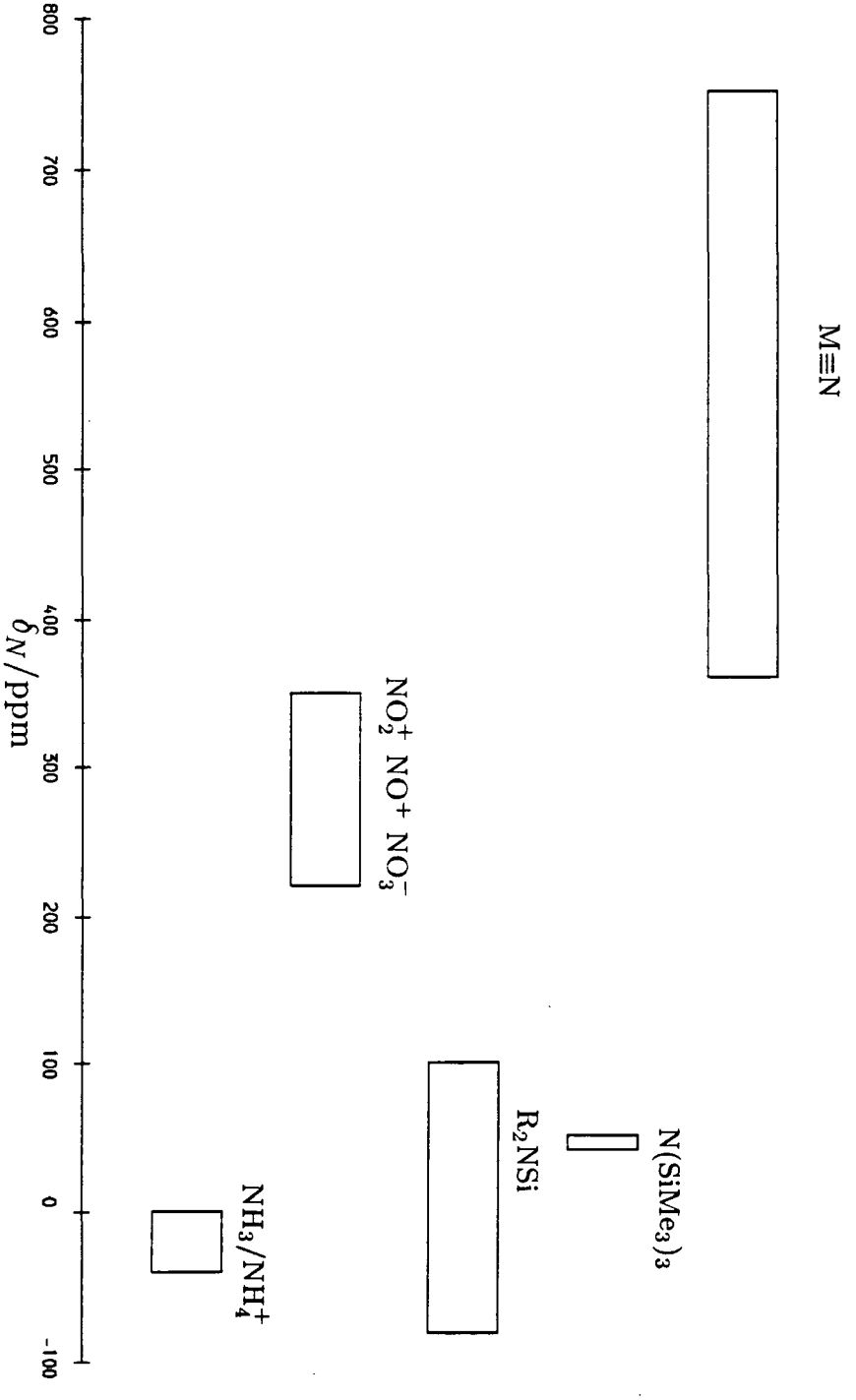

enriched sodium phosphate glasses. Nitrogen in [NP_3] and [NP_2] environments can readily be distinguished, the former environment gives δ_N in the range 88–93 ppm, and the latter in the range 55–63 ppm.

There is a considerable body of literature on solution-state ^{15}N (and^{14}N) NMR.[130–132] Shift ranges are summarised in Figure 3.2.8. Of particular interest to the ^{15}N NMR results discussed later are the δ_N values for nitrogen bonded directly to Si or other metals.[133] As in other systems, it is found that more electron withdrawing groups lead to more positive δ_N values, whilst electron donating groups, such as metal atoms, lead to more negative shifts. In $N(SiMe_3)_3$, for example, δ_N=+18 ppm, but for $[(Me_3Si)_2N]_3Al$, δ_N=+52 ppm.

3.2.5 Oxygen–17 NMR

Because of the low natural abundance and high cost of the ^{17}O isotope, few ^{17}O NMR studies of inorganic solids have been reported. ^{17}O is a relatively favourable NMR nucleus, with $I = \frac{5}{2}$ and a small quadrupole moment: about 1/6 that of ^{27}Al. Samples enriched in ^{17}O should thus give spectra with acceptably narrow lines. In most cases, only the $(\frac{1}{2}, -\frac{1}{2})$ transition is observed, broadened principally by second order quadrupolar coupling. Studies of non-molecular inorganic systems fall into two related areas: metal oxides (basically ionic), and silicates and zeolites (basically covalent).

(i) Metal oxides

The group IIa metal oxides, MO, all have regular crystal structures in which the oxygen atom environment is symmetric. ^{17}O linewidths are found to be narrow, and values of χ_Q, small.[134,135] Values of δ_O, χ_Q and metal ion radii for the group IIa and IIb oxides are listed in Table 3.2.2. δ_O can be correlated[135] with r^3_{2+}, although no explanation has been proposed for this observation. It has also been shown that χ_Q can be correlated with the ionicity of the M–O bond, presumably because a degree of covalency implies a deviation from the regular sites of the idealised crystal structure. Mercuric oxide is an extreme case: it is a fully covalent solid, with oxygen in a highly asymmetric environment.

Walter and Oldfield[136] have studied a series of aluminium oxides and hydrox-

Table 3.2.2 ^{17}O NMR data and ionic radii of group IIa and IIb oxides.[135]

	δ_O/ppm	χ_Q/kHz	r_{2+}/Å
BeO	26	20	0.31
MgO	47	14	0.65
CaO	294	<5	0.99
SrO	390	<5	1.13
BaO	629	<5	1.35
ZnO	-18	130	0.74
CdO	60	NM	0.97
HgO	121	7100	1.10

NM: not measured.

ides, and their results are summarised in Table 3.2.3. The different oxygen environments can clearly be differentiated both from δ_O and χ_Q values.

Yang *et al.*[137] have obtained the ^{17}O spectra of other group III oxides, and some other phases, and their data is summarised in Table 3.2.4. It seems likely that correlations of δ_O with r_{3+} exist.

Walter *et al.*[138] have also studied several inorganic hydroxides using ^{17}O CP MAS NMR. They use this experiment to examine selectively oxygen on the surface of amorphous SiO_2 present in an [Si–O–H] environment.

(ii) Silicate systems

Oxygen-17 resonances from silicates and related systems tend to be much broader than those from metal oxide systems: oxygen environments tend to be much more asymmetric and covalent.Typical values for χ_Q in silicate systems are in the region 1–5 MHz.[139] VAS NMR has been used successfully to minimise broadening due to second order quadrupolar coupling,[140] but more recent work has concentrated on measuring χ_Q and η_Q as well as δ_O, and then attempting to correlate all of these parameters with the structural and electronic characteristics of the system under investigation.

Table 3.2.3 ^{17}O NMR data for aluminas[136]

	O environment	δ_O/ppm	χ_Q/MHz	η_Q
α–Al_2O_3	$[OAl_4]$	75	2.17	0.55
AlOOH	$[OAl_4]$	70	1.20	0.1
	$[Al_2OH]$	40	5.0	0.5
$Al(OH)_3$	$[Al_2OH]$	40	6.0	0.3
γ–Al_2O_3	$[OAl_4]$	73	1.8	
η–Al_2O_3	$[OAl_4]$	73	1.6	
δ–Al_2O_3	$[OAl_4]$	72	1.6	
θ–Al_2O_3	$[OAl_4]$	72	1.2	
	$[OAl_3]$	79	4.0	0.6

Table 3.2.4 ^{17}O NMR data of Yang *et al.*[137]

	δ_O/ppm	χ_Q/MHz
Tl_2O_3	364	
$Tl_2Ba_2CaCuO_{8+x}$	315–345	
Bi_2O_3	195	
$Bi_2Sr_2CaCu_2O_{8+x}$	~200	
Y_2O_3	355	
BaO_2	334	17.2

Figure 3.2.9 Summary of δ_O in silicates and zeolites.
1=$BaSiO_3$, 2=$SrSiO_3$, 3=$CaSiO_3$, 4=$CaMgSi_2O_6$, 5=Mg_2SiO_4, 6=$MgSiO_3$, 7=glass, 8=SiO_2, 9=zeolites

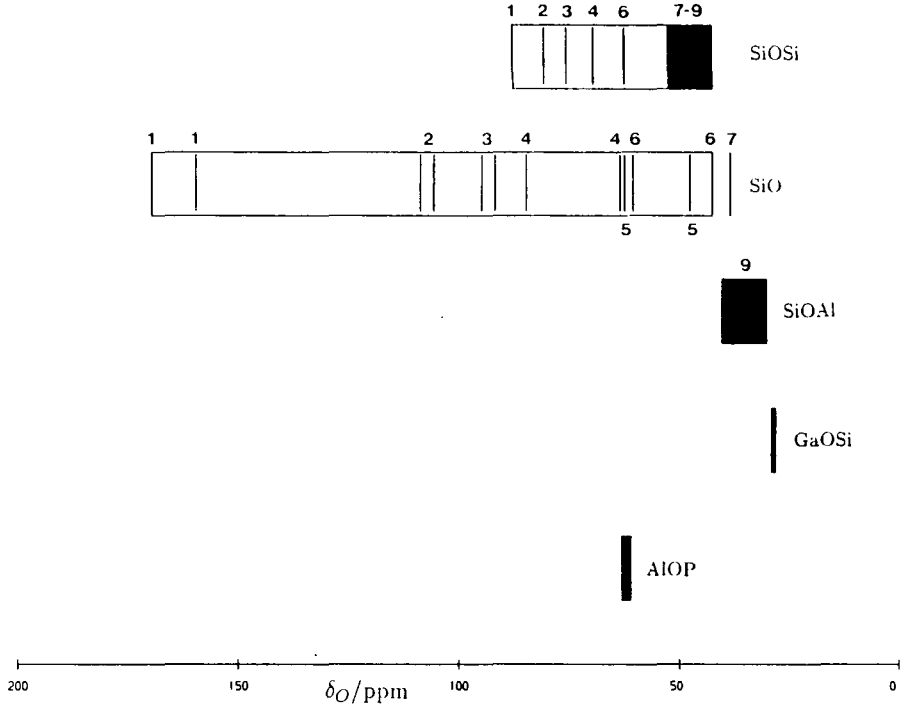

Figure 3.2.10 Summary of χ_Q in silicates and zeolites.
1=$BaSiO_3$, 2=$SrSiO_3$, 3=$CaSiO_3$, 4=$CaMgSi_2O_6$, 5=Mg_2SiO_4, 6=$MgSiO_3$, 7=glass, 8=SiO_2, 9=zeolites, 10=Al_2O_3/AlOOH

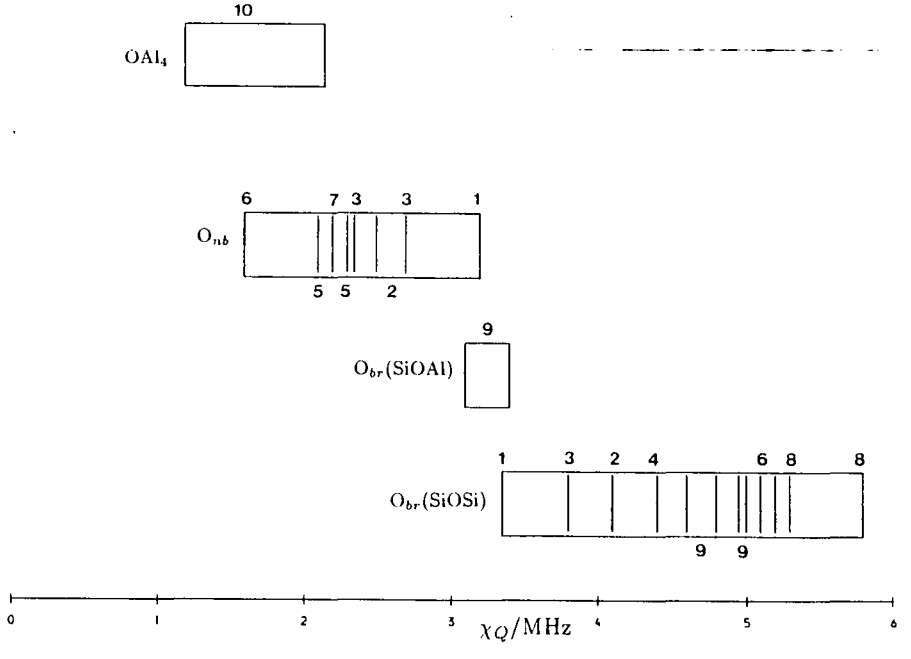

The chemical shift range for ^{17}O in silicates is around 100 ppm, but often substantial band overlap still occurs. Spectral simulation has thus proved necessary in many cases, as a method of deconvoluting complex spectra. The data thus obtained is summarised in Table 3.2.5.

(a) Chemical shifts

Chemical shift data from Table 3.2.5 is summarised in Figure 3.2.9. Within these ranges, correlations with other variables have been suggested. Timken *et al.*[141] have shown that δ_O can be correlated with the counter-ion radius in the $MSiO_3$ phases, in an analogous manner to the metal oxides. The effect of cation radius is greater (r_{2+}^2) for non-bridging oxygens, which are in a more ionic environment, than for bridging oxygens ($r_{2+}^{0.5}$). It is clear from these results that a great deal could be learnt about oxygen environment from studies of isostructural series. For small cations, it is clear that δ_O values alone are not sufficient to distinguish bridging and non-bridging sites.

Kirkpatrick *et al.*[105] and Bunker *et al.*[142] have shown that despite the much broader resonances obtained from glasses, it is possible to differentiate up to four types of oxygen environment in these systems; both groups have used deconvolution to get accurate quantitative data on the distribution of environments which correlates well with calculated and Raman[142] data.

(b) Quadrupole coupling constants

Rough correlations of χ_Q with oxygen coordination (Figure 3.2.10) shows that the value of χ_Q can provide a valuable indication of oxygen environment. It is also possible to make more accurate correlations. Timken *et al.*[141] found a good correlation between χ_Q and cation electronegativity for the O_{br} and O_{nb} sites in the series of metasilicates. Interestingly, the gradients of the correlations were roughly equal for the two sites.

Janes and Oldfield[145] have attempted to calculate values of χ_Q and η_Q from considerations of the oxygen valence bond orbital asymmetry, using a Townes-Dailey approach. The agreement between calculated and experimental results was good ($\pm 20\%$) for the systems studied: SiO_2 and diaposide, considering the fact

Table 3.2.5 ^{17}O data from silicate systems

	O enviromnent	δ_Q/ppm	χ_Q/MHz	η_Q	technique	reference
SiO_2(low-cryst)	O_{br}[a]	46	5.6	0.1	static	137
SiO_2(low-cryst)	O_{br}	44	5.3	0.0	MAS	141
$MgSiO_3$	O_{nb}[b]	60	3.2	0.0	static	141
(clinoenstatite)	O_{nb}	42	3.2	0.0		
	O_{br}	62	5.1	0.3		
$CaMgSi_2O_6$	O_{nb}	84	2.7	0.0	MAS	141
(diaposide)	O_{nb}	63	2.7	0.1		
	O_{br}	69	4.4	0.3		
$CaSiO_3$	O_{nb}	94	2.1	0.1	MAS	141
(α-wollast.)	O_{nb}	91	2.3	0.1		
	O_{br}	75	3.8	0.2		
$SrSiO_3$	O_{nb}	108	2.1	0.1	MAS	141
(α-wollast.)	O_{nb}	105	2.2	0.1		
	O_{br}	80	4.1	0.4		
$BaSiO_3$	O_{nb}	169	2.1	0.1	MAS	141
(α-wollast.)	O_{nb}	159	1.6	0.1		
	O_{br}	87	3.7	0.4		
Mg_2SiO_4	O_{nb}	61	2.35	0.2	MAS	140
(forsterite)	O_{nb}	62	2.35	1.0		
	O_{nb}	47	2.70	0.3		
Na_2O-B_2O_3-SiO_2[c]	B-O-B	72	5.2	1.0	MAS/static	142
(glasses)	Si-O-Si	48	5.0	0.0		
	Si-O-B	20	2.5	0.2		
	Si-O-Na	38	2.5	0.0		
Aluminosilicate	Si-O-Si	43–51	4.6–5.6	0.1–0.2	MAS	137/143
zeolites[d]	Si-O-Al	31–40	3.1–3.4	0.2–0.4		
Gallosilicate	Si-O-Ga	28–29	4.0	0.3	MAS	144
zeolites[e]	Si-O-Si	49–51	5.0–5.1	0.0		
$AlPo_4$-5[f]	Al-O-P	61–63	5.6–5.7	0.0	MAS	144

(a) O_{br}: bridging O (Si-O-Si); (b) O_{nb}: non-bridging O ($Si\text{-}O^-$); (c) typical of data from several samples; (d) summary of data from 8 samples; (e) summary of data from 3 samples; (f) 3 environments.

that the effect of the electropositve counter-ions were ignored. Timken *et al.*[144] have performed similar calculations on zeolites.

3.2.6 Beryllium–9 NMR

Lindman and Forsén,[146] and Akitt[147] have reviewed ^{9}Be solution-state NMR studies. The chemical shift range is small because variations are due primarily to changes in σ_d, but it is nevertheless possible to differentiate tetrahedral and other environments relatively easily. $[Be(NH_3)_4]^{2+}$ resonates at δ_{Be}~2 ppm, whilst $[Be(OH_2)_4]^{2+}$ resonates at δ_{Be}~0 ppm. Solvent and concentration effects are often important.

There has been only one report of a ^{9}Be MAS NMR study.[148] Results are summarised in Table 3.2.6. No substantive trends are evident. The linewidths of the spectra shown in Reference 148 suggest a rather lower accuracy in the δ_{Be} values than indicated in the Table.

Table 3.2.6 ^{9}Be MAS NMR data of Romannikov *et al.*[148]

material	δ_{Be}/ppm[(a)]
$[Be(H_2O)_4]^{2+}_{aq}$	-1.73
BeO_s	-2.3
Unspecified Non-zeolitic silicate	-3.47
Be-ZSM-5	-5.8

(a) relative to $\delta_{Be}(Na_2BeO_4)$= 0. All solutions 0.05 M

3.2.7 Group IIIa Metals (^{45}Sc, ^{89}Y, ^{139}La)

All three of the group IIIa metals have suitable NMR nuclei present in > 99% abundance. ^{89}Y has $I = \frac{1}{2}$, and, although it resonates at a very low frequency, it is otherwise ideal for MAS study. There have been several ^{89}Y solid-state MAS studies reported recently, mainly on relatively simple systems, such as salts,[149] Y_2O_3[148,149] and yttrium silicates and aluminates.[151] The shift range in these phases is found to be large (>200 ppm), but no satisfactory explanation of these data has been proposed. There have also been some recent studies on superconducting

ceramics,[152,153] which have proved useful in understanding the band structure of these materials.

^{45}Sc and ^{139}La both have $I = \frac{7}{2}$ and possess large quadrupole moments. It has nonetheless been shown[149] that under favourable conditions, reasonable spectra can be obtained. Values of χ_Q tend to be large, partly because environments are generally irregular. An exception is LaB_6, in which the La occupies a regular octahedral site, giving rise to a relatively narrow ^{139}La resonance.[154] The ^{45}Sc nutation spectrum of $Sc_2(SO_4)_3$ has recently been reported.[155]

3.2.8 Other Nuclei

Other nuclei of potential or actual interest in NMR of ceramics are listed in Table 3.2.7. Only ^{7}Li was examined in work described in this Thesis. ^{13}C MAS NMR studies of carbide ceramics will be mentioned in Section 3.2.10.

Table 3.2.7 Other possible nuclei for NMR of ceramics

Nucleus	I	Shift range/ppm	Use	Ref.
^{1}H	$\frac{1}{2}$	10	Characterisation of surface materials on AlN	156
			NMR imaging of injection moulding	157
^{13}C	$\frac{1}{2}$	400	NMR of silicon carbides	Sect. 3.2.10
^{19}F	$\frac{1}{2}$	1200	F in e.g. apatites	158,159
^{7}Li	$\frac{3}{2}$	10	Li environment characteristaion	
^{25}Mg	$\frac{5}{2}$	60	Mg in simple phases	160

3.2.9 Effect of Paramagnetic Centres on NMR Spectra of Solids

The effect of paramagnetic centres on spectra has already been referred to in Section 2.1.6. There are four principal effects.

(i) Linewidth. Grimmer *et al.*[161] have found an increase in ^{29}Si MAS NMR linewidth of a factor of ten in the series Mg_2SiO_4–$Mg_{1.9}Fe_{0.1}SiO_4$. No signal could be observed from $Mg_{1.8}Fe_{0.2}SiO_4$.

(ii) Spinning side-band manifold. Oldfield *et al.*[162] have shown that minerals containing paramagnetic centres give rise to much broader ssb manifolds. A similar effect was noted by Grey *et al.*[163] in a recent comprehensive study of lanthanide–tin pyrochlores by ^{119}Sn MAS NMR.

(iii) Resonance position. Recent studies[163,164] of a series of nine isostructural pyrochlores, $Ln_2Sn_2O_7$ by ^{119}Sn MAS NMR show that a shift in resonance position akin to the lanthanide shift of solution-state NMR of up to ±4000 ppm can occur, attributed to a through-space dipolar "pseudo-contact" mechanism.

(iv) Relaxation times. In the same studies, it was found that T_1 varies significantly with distance of paramagnetic ions from the observed nucleus.

3.2.10 Silicon Carbide Ceramics

^{29}Si and ^{13}C MAS NMR have proved of value in understanding the structures of the silicon carbide polytypes. The number and intensity of peaks observed in ^{13}C and ^{29}Si spectra have been found to agree well with that predicted from consideration of the stacking of the layers (Table 3.2.8). In the ^{29}Si spectra, peaks are found to be separated by up to 10 ppm, large splits for crystallographic inequivalence. Apperley[170] has also shown that ^{29}Si T_1 times can be extremely long in silicon carbides: 2000 s in β–SiC.

Recent work[167] has shown that ^{27}Al MAS NMR can also be used with success to characterise Al environments in aluminium silicon carbides. δ_{Si} values in these phases were also often found to be very different (~ -35 ppm) to those found in the silicon carbide polytypes.

Table 3.2.8 ^{29}Si and ^{13}C MAS NMR of SiC polytypes

Polytype	predicted peak ratio	δ_{Si}/ppm	Intensity	δ_C/ppm	Intensity	Reference
β–SiC	1	−17.2		23.7		165,166
4H	1:1	−19.7	1	14.7	1	167
		−22.5	1	21.5	1	
6H	1:1:1	−14.3	1	15.2	1	168,169
		−20.4	1	20.2	1	
		−24.9	1	22.7	1	
15R	1:2:2	−14.6	1	16.0	1	165,168,169
		−20.5	2	20.7	2	
		−24.1	2	22.7	2	

REFERENCES

1. Parr, N. L.; Martin, G. F.; May, E. R. W. *Admiralty Materials Laboratory Report No. A/75(S)*; 1959.
2. Kingery, W. D. *J. Appl. Phys.* **30**, 301–306 (1959).
3. Jack, K. H. *Science of Ceramics* **11**, 125–142 (1981).
4. Jack, K. H. *Non-oxide Technical and Engineering Ceramics*; Hampshire, S. Ed.; Elseveir: London, 1986. pp 1–30.
5. Lang, J. *Nitrogen Ceramics*; Riley, F. L. Ed.; NATO ASI Ser. E; Martinus Nijhoff: The Hague. **23**, 89–108 (1977).
6. Lang, J.; Laurent, Y.; Maunaye, M. *Prog. Cryst. Growth Char.* **2**, 207–235 (1979).
7. Deville, H.; Wohler, F. *Liebigs Ann.* **104**, 256 (1857).
8. Turkdogan, F. T.; Bills, P. M.; Tippett, V. A. *J. Appl. Chem.* **8**, 296–302 (1958).
9. Hardie, D.; Jack, K. H. *Nature* **180**, 332–333 (1957).
10. Thompson, D. S; Pratt, P. S. *Science of Ceramics* **3**, 33–51 (1967).
11. Wild, S.; Grievson, P.; Jack, K. H. *Special Ceramics* **5**, 385–395 (1972).
12. Borgen, O.; Seip, H. M. *Acta Chem. Scand.* **15**, 1789 (1961).
13. Grün, R. *Acta Crystallogr.* **B35**, 800–804 (1979).
14. Marchand, R.; Laurent, Y.; Lang, J.; Le Bihan, M. Th. *Acta Crystallogr.* **B25**, 2157–2160 (1969).
15. Kato, K.; Inoue, Z.; Kijima, K.; Yamane, T.; Kawada, J. *J. Am. Ceram. Soc.* **58**, 90–94 (1975).
16. Jack, K. H. *Progress in Nitrogen Ceramics*; Riley, F. L. Ed.; NATO ASI Ser. E; Martinus Nijhoff: The Hague. **65**, 45–60 (1983).
17. Idrestedt, I.; Brosset, C. *Acta Chem. Scand.* **18**, 1879–1886 (1964).
18. McCauley, J. W.; Corbin, N. D. *J. Am. Ceram. Soc.* **62**, 476–479 (1979).
19. Gauckler, L. J.; Lukas, H. L.; Petzow, J. *J. Am. Ceram. Soc.* **58**, 346–347 (1975).
20. Jack, K. H. Reference 5, pp 109–128.
21. Tien, T. Y.; Petzow, G.; Gauckler, L. J.; Weiss, J. Reference 16, pp 89–99.
22. Slasor, S. Ph.D. Thesis, University of Newcastle upon Tyne, 1987.

23. Gillott, L.; Cowlam, N.; Bacon, G. E. *J. Mater. Sci.* **16**, 2263–2268 (1981).

24. van Dijen, F. K.; Metselaar, R.; Helmholdt, R. B. *J. Mater. Sci.* **6**, 1101–1102 (1987).

25. Trigg, M. B.; Jack, K. H. *Ceramic Components for Engines: Proceedings of the First International Symposium, Japan*; Shigeyuki Somiya *et al.* Ed.; Elsevier: London, 1983. pp 199–207.

26. Thompson, D. P.; Korgul, P. Reference 16, pp 375–380.

27. Jack, K. H. *Trans. Brit. Ceram. Soc.* **72**, 376–384 (1973).

28. Thompson, D. P.; Korgul, P.; Hendry, A. Reference 15, pp 61–74.

29. Bando, Y.; Mitomo, M.; Kitami, Y.; Izumi, F. *J. Microsc. (Oxford)* **142**, 235–246 (1986).

30. Thompson, D. P. Reference 5, pp 129–135.

31. Liddell, K. Ph.D. Thesis, University of Newcastle upon Tyne, 1984; and Dodsworth, J. Ph.D. Thesis, University of Newcastle upon Tyne, 1980.

32. Thompson, D. P. *Tailoring Multiphase and Composite Ceramics*; Tressler, R. E. *et al.* Ed.; Plenum: New York, 1986. pp 79–91.

33. Mitomo, M.; Izumi, F.; Horiuchi, S.; Matsui, Y. *J. Mater. Sci.* **17**, 2359–2364 (1982).

34. Buang, K. Ph.D. Thesis, University of Newcastle upon Tyne, 1979.

35. Slasor, S.; Liddell, K.; Thompson, D. P. *Special Ceramics* **8**, 51–64 (1986).

36. Felsche, J. *Struct. Bond.* **13**, 100–197 (1973).

37. Liddell, K.; Thompson, D. P. *Br. Ceram. Trans. J.* **85**, 17–22 (1986).

38. The Q number defines the number of $[SiO_xN_{4-x}]$ tetrahedra directly bonded to the central tetrahedron.

39. see Deer, W. A.; Howie, R. A.; Zussman, J. *An Introduction to the Rock Forming Minerals*; Longman: London, 1966. pp 504–509.

40. Hamon, C.; Marchand, R.; Maunaye, M.; Gaudé, J.; Guyader, J. *Revue de Chim. Mineral.* **12**, 259–267 (1975).

41. Greenwood, N. N.; Earnshaw, A. *Chemistry of the Elements*; Pergamom: Oxford, 1984. p 401.

42. Liddell, K.; Thompson, D. P. Unpublished results.

43. Jameel, N. S. Ph.D. Thesis, University of Newcastle uopn Tyne, 1984.

44. Inoue, Z.; Mitomo, M.; Ii, N. *J. Mater. Sci.* **15**, 2915–2920 (1980).

45. Inoue, Z.; Sawada, T.; Ohsumi, K.; Sadanaga, R. *Acta Crystallogr.* **A37**, C154 (1981).

46. Inoue, Z. *J. Mater. Sci. Lett.* **4**, 656–658 (1985).

47. Morgan, P. E. D. *J. Mater. Sci. Lett.* **5**, 372 (1986).

48. Morgan, P. E. D. *J. Mater. Sci.* **21**, 4305–4309 (1986).

49. Wills, R. R.; Stewart, R. W.; Cunningham, J. A.; Wimmer, J. M. *J. Mater. Sci.* **11**, 749–759 (1976).

50. Mah, T. -I.; Mazdiyasni, K. S.; Ruh, R. *J. Am. Ceram. Soc.* **62**, 12–16 (1979).

51. Marchand, R.; Jayaweera, A.; Verdier, P.; Lang, J. *C. R. Acad. Sci. Paris* **283**, C675–C677 (1983).

52. Rae, A. W. J. M. Ph.D. Thesis, University of Newcastle upon Tyne, 1976.

53. Thompson, D. P. Unpublished work.

54. Morgan, P. E. D.; Carroll, P. J.; Lange, F. F. *Mater. Res. Bull.* **12**, 251–260 (1977).

55. Dupree, R.; Lewis, M. H.; Smith, M. E. *J. Am. Chem. Soc.* **110**, 1083–1087 (1988).

56. Morgan, P. E. D.; Carroll, P. J. *J. Mater. Sci. Lett.* **12**, 2243–2244 (1977).

57. Jameel, N. S.; England, P. J. *Inst. Phys. Conf. Ser. No. 8*; Chapter 10, pp 393–396 (1983).

58. Korgul, P.; Thompson, D. P. *Brit. Ceram. Proc.* **42**, 69–80 (1989).

59. Brandle, C. D.; Steinfink, H. *Inorg. Chem.* **8**, 1320–1324 (1969).

60. Liddell, K.; Slasor, S.; Thompson, D. P. Manuscript in preparation.

61. Gaudé, J.; l'Haridon, P.; Hamon, C.; Marchand, R.; Laurent, Y. *Bull. Soc. Fr. Min. Crist.* **98**, 214–217 (1975).

62. Godina, N. A.; Keler, É. K. *Izv. Akad. Nauk. SSR Ser. Khim.* **1**, 18–23 (1966).

63. *Phase Diagrams for Cermicists, 1975 Supplement*; Am. Ceram. Soc.: Ohio. p 132.

64. Bertaut, E. F.; Mareschal, J. *C. R. Acad. Sci. Paris* **C257**, 8617 (1963).

65. Marchand, R. *C. R. Acad. Sci. Paris* **C282**, 329–331 (1976).

66. Izumi, F.; Mitomo, M.; Bando, Y. *J. Mater. Sci.* **19**, 3115–3120 (1984).

67. Izumi, F.; Mitomo, M.; Suzuki, J. *J. Mater. Sci. Lett.* **1**, 533–535 (1982).

68. Spacie, C. J.; Liddell, K.; Thompson, D. P. *J. Mater. Sci. Lett.* **7**, 95–96 (1988).

69. Grins, J.; Käll, P. -O.; Liddell, K.; Korgul, P.; Thompson, D. P. In press.

70. Fernie, J. A.; Lewis, M. H.; Leng-Ward, G. *Mat. Sci. Eng. Lett.* **9**, 29 (1989).

71. Käll, P. -O.; Grins, J.; Liddell, K.; Korgul, P.; Thompson, D. P. In preparation.

72. Jama, S. A. B. Ph.D. Thesis, University of Newcastle upon Tyne, 1975.

73. Wild, S.; Grievson, P.; Jack, K. H. *Special Ceramics* **5**, 289–297 (1972).

74. David, J.; Laurent, Y.; Lang, J. *Bull. Soc. Fr. Min. Crist.* **93**, 153–159 (1970).

75. Laurent, Y.; Guyader, J.; Roult, G. *Acta Crystallogr.* **B37**, 911–913 (1981).

76. Perera, D. S. Ph.D. Thesis, University of Newcastle upon Tyne, 1976.

77. David, J.; Laurent, Y.; Charlot, J. P.; Lang, J. *Bull. Soc. Fr. Min. Crist.* **96**, 21–24 (1973).

78. Kuang, S. F.; Huang, Z. K.; Sun, W. Y.; Yen, T. S. *J. Mater. Sci. Lett.* **9**, 69–71 (1990).

79. Patience, M. M. Ph.D. Thesis, University of Newcastle upon Tyne, 1983.

80. Huseby, I. C.; Lukas, H. L.; Petzow, G. *J. Am. Ceram. Soc.* **58**, 377–380 (1975).

81. Thompson, D. P. *J. Mater. Sci.* **11**, 1377–1380 (1976).

82. Thompson, D. P.; Gauckler, L. J. *J. Am. Ceram. Soc.* **60**, 470–471 (1977).

83. Hall, D.; Gurr, G. E.; Jeffrey, G. A. *Z. Anorg. Allg. Chem.* **304**, 218 (1960).

84. Thompson, D. P. Progress Report, Crystallography Laboratory, University of Newcastle upon Tyne, January 1978.

85. Hampshire, S.; Drew, R. A. L.; Jack, K. H. *Phys. Chem. Glasses* **26**, 182–186 (1985).

86. Drew, R. A. L.; Hampshire, S.; Jack, K. H. Reference 16, pp 323–330.

87. Makishima, A.; Mitomo, M.; Tanaka, H.; Ii, N.; Tsutsumi, M.; *Yogyo–Kyokai–Si* **88**, 701–702 (1980).

88. Shaw, T. M.; Thomas, G. Reference 16, pp 331–336.

89. Harris, R. K. *Nuclear Magnetic Resonance Spectroscopy*; Longman: Harlow, U.K. 1983. Adapted from Appendices 1 and 2.

90. Smith, K. A.; Kirkpatrick, R. J.; Oldfield, E.; Henderson, D. M. *Am. Mineral.* **68**, 1206–1215 (1983).

91. Grimmer, A.-R.; Wieker, W.; v. Lampe, F.; Fechner, E.; Peter, R.; Molgedey, G. *Z. Chem.* **20**, 453 (1980).

92. Thomas, J. M.; Gonzales-Calbert, J. M.; Fyfe, C. A.; Gobbi, G. C.; Nichol, M. *Geophys. Res. Lett.* **10**, 91–92 (1983).

93. Dupree, R.; Holland, D.; Mortuza, M. G. *Nature* **328**, 416–417 (1987).

94. Mägi, M.; Lippmaa, E.; Samoson, A.; Engelhardt, G.; Grimmer, A. -R. *J. Phys. Chem.* **88**, 1518–1522 (1984).

95. Engelhardt, G.; Michel, D. *High Resolution Solid-State NMR of Silicates and Zeolites*; Wiley: Chichester, U.K. 1987. Chapter 4.

96. Janes, N.; Oldfield, E. *J. Am. Chem. Soc.* **107**, 6769–6775 (1985).

97. Tenhover, M.; Boyer, R. D.; Henderson, R. S.; Hammond, T. E.; Shreve, G. A. *Solid State Commun.* **65**, 1517–1521 (1988).

98. Engelhardt, G.; Radeglia, R. *Chem. Phys. Lett.* **108**, 271–274 (1984).

99. Grimmer, A. -R.; Radeglia, R. *Chem. Phys. Lett.* **106**, 262–265 (1984).

100. Engelhardt, G.; Luger, S.; Buhl, J. Ch.; Felsche, J. *Zeolites* **9**, 182–185 (1989).

101. Sherriff, B. L.; Grundy, H. D. *Nature* **332**, 819–822 (1988).

102. Brown, I. D.; Altermatt, D. *Acta. Crystallogr.* **B41**, 244–247 (1985).

103. McConnell, H. M. *J. Chem. Phys.* **27**, 226–229 (1957).

104. Sternberg, U. *Mol. Phys.* **63**, 249–267 (1988).

105. Kirkpatrick, R. J.; Dunn, T.; Schramm, S.; Smith, K. A.; Oestrike, R.; Turner, G. *Structure and Bonding in Non-Crystalline Solids*; Walrafer and Reeves (1986); pp 303–327.

106. Stebbins, J. F. *Nature* **330**, 465–467 (1987).

107. Dupree, R.; Holland, D.; McMillan, P. W.; Pettifer, R. F. *J. Non-Cryst. Sol.* **68**, 398–410 (1984).

108. Schramm, C. M.; de Jong, B. H. W. S.; Parziale, V. E. *J. Am. Chem. Soc.* **106**, 4396–4402 (1984).

109. Bunker, B. C.; Tallant, D. R.; Kirkpatrick, R. J.; Turner, G. L. *Phys. Chem. Glasses* **31**, 30–41 (1990).

110. Klinowski, J.; Carr, S. W.; Tarling, S. E.; Barnes, P. *Nature* **330**, 56–58 (1987).

111. Lowenstein, W. *Am. Mineral.* **39**, 92–96 (1953).

112. Fraser, D. G.; Clayden, N. J. *Chem. Geol.* **62**, 43–47 (1987).

113. Gerstein, B. C.; Nichol, A. T. *J. Non-Cryst. Sol.* **75**, 423–428 (1985).

114. Barron, P. F.; Frost, R. L.; Skjemstad, J. O. *J. Chem. Soc. Chem. Commun.*, 581–583 (1983).

115. Klinowski, J.; Carpenter, T. A.; Thomas, J. M.; *J. Chem. Soc. Chem. Commun.*, 956–958 (1986).

116. Fyfe, C. A.; Gies, H.; Feng, Y. *J. Chem. Soc. Chem. Commun.*, 1240–1242 (1989).

117. Fyfe, C. A.; Gies, H.; Feng, Y.; Kokotailo, G. T. *Nature* **341**, 223–225 (1989).

118. Fyfe, C. A.; Gies, H.; Feng, Y. *J. Am. Chem. Soc.* **111**, 7702–7707 (1989).

119. Turner, G. L.; Kirkpatrick, R. J.; Risbud, S. H.; Oldfield, E. *Am. Ceram. Soc. Bull.* **66**, 656–663 (1987).

120. Alemany, L.; Kirker, G. W. *J. Am. Chem. Soc.* **108**, 6158–6162 (1986).

121. Sanz, J.; Madani, A.; Serratosa, J. M.; Moya, J. S.; Aza, S. *J. Am. Ceram. Soc.* **71**, C418–C421 (1988).

122. Stebbins, J. F.; Farnan, I.; Klabunde, U. *J. Am. Ceram. Soc.* **72**, 2198–2200 (1989).

123. Lippmaa, E.; Samoson, A.; Mägi, M. *J. Am. Chem. Soc.* **108**, 1730–1735 (1986).

124. Müller, D.; Gessner, W.; Samoson, A.; Lippmaa, E.; Scheler, G. *J. Chem. Soc. Dalton*, 1277–1281 (1986).

125. Mason, J.; Mingos, D. M. P.; Schaefer, J.; Sherman, D.; Stejskal, E. O. *J. Chem. Soc. Chem. Commun.*, 444–446 (1985).

126. Harris, R. K.; Merwin, L. H.; Hägele, G. *Magn. Reson. Chem.* **27**, 470–475 (1989).

127. Merwin, L. H. Ph.D. Thesis, University of Durham, 1987.

128. Chuang, I. D.; Hawkins, B. L.; Maciel, G. E.; Meyers, G. E. *Macromolecules* **18**, 1482–1485 (1985).

129. Bunker, B. C.; Tallant, D. R.; Balfe, C. A.; Kirkpatrick, R. J.; Turner, G. L.; Reidmeyer, M. R. *J. Am. Ceram. Soc.* **70**, 675–681 (1987).

130. Mason, J. *Chem. Rev.* **81**, 205–227 (1981).

131. Mason, J. *Multinuclear NMR*; Mason, J. Ed.; Plenum, New York, 1987; pp 335–367.

132. Levy, G. C.; Lichter, R. L. *Nitrogen-15 Nuclear Magnetic Resonance Spectroscopy*; Wiley: New York, 1979.

133. Barlos, K.; Hübler, G.; Nöth, H.; Wanninger, P.; Wiberg, N.; Wrackmeyer, B. *J. Magn. Reson.* **31**, 363–376 (1978).

134. Schramm, S.; Kirkpatrick, R. J.; Oldfield, E. *J. Am. Chem. Soc.* **105**, 2483–2485 (1983).

135. Turner, G. L.; Chung, S. E.; Oldfield, E. *J. Magn. Reson.* **64**, 316–324 (1985).

136. Walter, T. H.; Oldfield, E. *J. Phys. Chem.* **93**, 6744–6751 (1989).

137. Yang, S.; Park, K. D.; Oldfield, E. *J. Am. Chem. Soc.* **111**, 7278–7279 (1989).

138. Walter, T. H.; Turner, G. L.; Oldfield, E. *J. Magn. Reson.* **76**, 106–120 (1988).

139. Oldfield, E.; Kirkpatrick, R. J. *Science* **227**, 1537–1544 (1985).

140. Schramm, S.; Oldfield, E. *J. Am. Chem. Soc.* **106**, 2502–2506 (1984).

141. Timken, H. K. C.; Schramm, S. E.; Kirkpatrick, R. J.; Oldfield, E. *J. Phys. Chem.* **91**, 1054–1058 (1987).

142. Bunker, B. C.; Tallant, D. R.; Kirkpatrick, R. J.; Turner, G. L. *Phys. Chem. Glasses* **31**, 30–41 (1990).

143. Timken, H. K. C.; Turner, G. L.; Gilson, J. P.; Welsh, L. B.; Oldfield, E. *J. Am. Chem. Soc.* **108**, 7231–7235 (1986).

144. Timken, H. K. C.; Janes, N.; Turner, G. L.; Lambert, S. L.; Walsh, L. B.; Oldfield, E. *J. Am. Chem. Soc.* **108**, 7236–7241 (1986).

145. Janes, N.; Oldfield, E. *J. Am. Chem. Soc.* **108**, 5743–5753 (1986).

146. Lindman, B.; Forsén, S. *NMR and the Periodic Table*; Harris, R. K.; Mann, B. E. Ed.; Academic Press: London, U.K. 1978. pp 183–194.

147. Akitt, J. W. Reference 132, pp 189–220.

148. Romannikov, V. N.; Churnachenko, L. S.; Mastikhin, V. M.; Ione, K. G. *J. Catal.* **94**, 508–513 (1985).

149. Thompson, A. R.; Oldfield, E. *J. Chem. Soc. Chem. Commun.* 27–29 (1987).

150. Battle, P. D.; Montez, B.; Oldfield, E. *J. Chem. Soc. Chem. Commun.* 584–585 (1988).

151. Dupree, R.; Smith, M. E. *Chem. Phys. Lett.* **148**, 41–44 (1988).

152. Markert, J. T.; Noh, T. W.; Russek, S. E.; Cotts, R. M. *Sol. State Commun.* **63**, 847–851 (1987).

153. Balakrishnan, G.; Dupree, R.; Farnan, I.; Paul, D. McK.; Smith, M. E. *J. Phys. C: Sol. State Phys.* **21**, L847–L852 (1988).

154. Lutz, O.; Oehler, H. *J. Magn. Reson.* **37**, 261–267 (1980).

155. Kentgens, A. P. M.; Lemmens, J. J. M.; Geurts, F. M. M.; Veeman, W. S. *J. Magn. Reson.* **71**, 62–74 (1987).

156. Hayashi, S.; Hayamizu, K.; Yamamoto, O. *Bull. Chem. Soc. Jpn.* **60**, 761–762 (1987).

157. Wong, P. D.; Ellingson, W. A.; Botto, R. E.; Yeh, H. C.; Pollinger, J. P. *Proc. Third Int. Symp. on Ceramic Materials and Components for Engines, Las Vegas, N. V.*; Tennery, V. J. Ed.; Am. Ceram. Soc. 1989. pp 1147–1158.

158. Clark, J. H.; Goodman, E. M.; Smith, D. K.; Brown, S. J.; Miller, J. M. *J. Chem. Soc. Chem. Commun.* 657–658 (1986).

159. Yesinowski, J. P.; Mobley, M. J. *J. Am. Chem. Soc.* **105**, 6191–6193 (1983).

160. Dupree, R.; Smith, M. E. *J. Chem. Soc. Chem. Commun.* 1483–1485 (1988).

161. Grimmer, A. -R.; v. Lampe, F.; Mägi, M.; Lippmaa, E. *Z. Chem.* **23**, 343–344 (1983).

162. Oldfield, E.; Kinsey, R. A.; Smith, K. A.; Nichols, J. A.; Kirkpatrick, R. J.; *J. Magn. Reson.* **51**, 325–329 (1983).

163. Grey, C. P.; Dobson, C. M.; Cheetham, A. K.; Jakeman, R. J. B. *J. Am. Chem. Soc.* **111**, 505–511 (1989).

164. Cheetham, A. K.; Dobson, C. M.; Grey, C. P.; Jakeman, R. J. B. *Nature* **328**, 706–707 (1987).

165. Finlay, G. R.; Hartman, J. S.; Richardson, M. F.; Williams, B. L. *J. Chem. Soc. Chem. Commun.* 159–161 (1985).

166. Wagner, G. W.; Na, B. -K.; Vannice, M. A. *J. Phys. Chem.* **93**, 5061–5064 (1989).

167. Apperley, D. C.; Harris, R. K.; Marshall, G. L.; Thompson, D. P. In preparation.

168. Guth, J. R.; Petuskey, W. T. *J. Phys. Chem.* **91**, 5361–5364 (1987).

169. Hartman, J. S.; Richardson, M. F.; Sherriff, B. L.; Winsborrow, B. G. *J. Am. Chem. Soc.* **109**, 6059–6067 (1987).

170. Apperley, D. C. Unpublished results.

Chapter IV

Experimental Details

4.1 Solid–state NMR

4.1.1 Pulse Sequences

The majority of spectra were obtained using a standard single pulse excitation pulse sequence. Saturation of resonances was difficult to avoid because of the long but generally undetermined T_1 relaxation times of spin–1/2 nuclei in ceramics; it was nevertheless considered important to choose experimental conditions to maximise signal-to-noise (see discussion in Reference 1). This was achieved by the combination of short pulse angles ($\ll \pi/2$) and long recycle delays. If T_1 is known or can be estimated, then the optimum pulse angle, α_E, for a given recycle delay, RD, can be calculated from the formula:[2]

$$\cos \alpha_E = \exp(\frac{\mathrm{RD}}{\mathrm{T_1}}) \tag{4.1.1}$$

Determinations of T_1 on ^{29}Si and ^{15}N in ceramic samples (Chapter 5) give typical values of $\sim$ 3000 s. A recycle delay of 300 s would thus require the use of a 25^o pulse angle. Many early ^{29}Si spectra were obtained under non-optimised conditions (typically 90^o pulse angle and 120 s recycle delay). The spectra of quadrupolar nuclei were acquired using very short ($< 30^o$) pulse angles, where the pulse angle is always measured with respect to a 90^o pulse on a solution. Only under such conditions is signal intensity independent of the value of χ_Q.[3]

The spectra of a few reference materials were obtained using cross-polarisation (CP) from protons.[4]

Static ^{139}La spectra were obtained using a spin–echo pulse sequence to overcome the problems of probe–ringing.[5] The sequence used was

Figure 4.1.1 ^{27}Al background of 5 mm DOTY probe.
SF=78.2 MHz; PA=15^{o}; NT=700; RD=1 s; SR=9.90 kHz; AF=0.01 s.

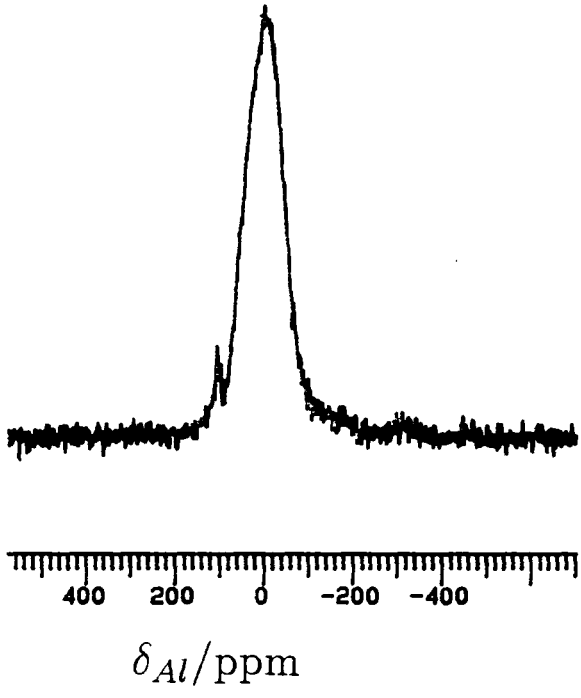

$$(\theta_1)\phi_1 - \tau_1 - (\theta_2)\phi_2 - \tau_2 - (AQ)\phi_3$$

A sixteen-step phase cycling routine was used to eliminate the effects of pulse imperfections, as given in Reference 5. The durations of the two pulses and delays were varied to give maximum signal, subject to the condition $\theta_2 = 2\theta_1$.

Spin-lattice relaxation times were measured using an inversion recovery pulse sequence,[6] with a relaxation delay estimated as at least $5T_1$. Spin-spin relaxation times were measured using a rotation-synchronised Carr-Purcell-Meiboom-Gill (CPMG) sequence.[6]

4.1.2 Instrumentation Used

The majority of spectra were acquired using the Varian VXR 300 spectrometer equipped with a 7.1 T narrow-bore magnet, at the University of Durham Industrial Research Laboratory.[7] Three probe systems were used:

7 mm Doty probe: this system was used for the acquisition of ^{29}Si, ^{15}N and most ^{17}O spectra, using fixed value tuning capacitors where necessary. Samples were contained in zirconia or alumina rotors, fitted with nordel or Kel-f end-caps, and were spun at 3–4 kHz during acquisition.

5 mm Doty probe: ^{27}Al and some ^{17}O spectra were acquired using this system, with fixed value tuning capacitors where necessary. Samples were packed in silicon nitride rotors, and were spun at rates of up to 10 kHz during acquisition. A background spectrum acquired under identical conditions was subtracted in the case of ^{27}Al spectra (Figure 4.1.1).

Wideline probe: Static ^{139}La spectra were acquired using a broadband wideline probe.

^{9}Be, ^{7}Li and some other spectra were acquired using the Bruker CXP 200 spectrometer in the Chemistry Department, University of Durham,[8] equipped with one of two double-bearing probes. Samples were packed in boron nitride rotors, and were spun at rates up to 4 kHz during acquisition.

4.1.3 Preparation of Samples for MAS

The spinning systems used, notably on the CXP spectrometer, were found to be extremely sensitive to the distribution and size of powder grains. Ceramic materials had therefore to be prepared with some care for MAS work. Samples were first ground coarsely using a tungsten carbide percussion mortar. Powders were then finely ground using an agate pestle and mortar, and sieved to 150 μm. Rotors were packed slowly, with each layer of material being carefully compacted before further material was introduced. The rotor caps for the CXP probes were packed with finely powdered boron nitride. Few problems with spinning of samples are encountered if this method is used.

Beryllium-containing samples had to be treated with extreme care because of the well-known acute toxicity[9] of beryllium. Samples of beryllium-containing materials were ground using the method outlined above, but all operations were conducted in a glove bag, with further protection against leaks being provided by a fume hood. Samples were packed into rotor inserts of the type described by Merwin *et al.*,[10] which could easily be inserted into the rotors used on the CXP spectrometer. Reference solutions containing beryllium were sealed into glass phials.

4.1.4 Details of Specific Nuclei

The approximate spectrometer frequencies and reference materials for all nuclei studied in this Thesis are listed in Table 4.1.1.

Nitrogen–15: A ^{15}N–enriched sample of $NH_4NO_3(s)$ was used as a reference material. A linewidth of 9 Hz form the $[NH_4]^+$ resonance meant that referencing errors of $< \pm 0.1$ ppm were introduced. The peak shape of the $[NO_3]^-$ resonance is very sensitive to the precise value of the spinning angle; only when set at exactly 54.74^o is a symmetric lineshape obtained. The material was thus used for accurately setting the magic angle.

Silicon–29: Different referencing materials were used on the two spectrometers. Linewidths of < 15Hz meant that referencing errors of $< \pm 0.1$ppm were introduced. The long T_1 time of ^{29}Si meant that some ^{29}Si spectra of ^{15}N-enriched materials

Table 4.1.1 Spectrometer frequencies and reference materials used.

Nucleus	Approximate SF/MHz		Primary reference	Secondary reference
	VXR 300	CXP 200		
^{15}N	30.4	N.U.	$NH_4NO_3(s)$[a]	—
^{29}Si	59.6	39.8	$Si(CH_3)_4(l)$	$Me3SiCH_2SO_3^-Na^+$ δ_{Si}=1.8 ppm[b] silica gum δ_{Si}=−22.74 ppm[c]
^{7}Li	N.U.	77.7	$Li^+(aq)$ (∞ dil.)	$LiCl(aq)$ (1 M)[d]
^{9}Be	N.U.	28.1	$Be^{2+}(aq)$ (∞ dil.)	$BeSO_4$ (0.05 M)[d]
^{17}O	40.7	27.1	$H_2O(l)$	—
^{27}Al	78.2	52.1	$Al^{3+}(aq)$ (∞ dil.)	$AlBr_3(aq)$ (1 M)[d]
^{139}La	42.4	N.U.	$La^{3+}(aq)$ (∞ dil.)	$La(OAc)_3(aq)$ (1 M)[d]

N.U. not used. (a) See Appendix B. (b) Used on VXR 300. An early sample has δ_{Si}=1.18 ppm. (c) Used on CXP 200. (d) No significant solvent effect found.

could advantageously be acquired using a single 90^o pulse after acquisition of the ^{15}N spectrum. No significant cross-relaxation was observed.

Quadrupolar Nuclei: Typical linewidths of resonances from solutions of 50–200 Hz were observed, the large values being partially due to magnetic field homogeneities, which were not averaged because sample spinning was not applied. This led to typical referencing errors of up to ±0.5 ppm. Typically, dead times of 50 μs and SW of 100000 Hz were used.

Beryllium–9: Acquisition of ^{9}Be spectra was hampered by the presence of electronic noise which invariably gave rise to a sharp peak at 70 ppm in the spectrum. This could be cosmetically removed using processing routines on the CXP spectrometer.

4.1.5 Treatment of Data

Gaussian broadening (LB) or apodisation functions (AF) were generally applied to FIDs prior to Fourier Transformation. FIDs were also checked for pulse breakthrough, and if necessary, the first 2 or 4 points were excluded from the transformation. Zero-filling[11] was used in transformation to further improve signal-to-noise. For typical ^{29}Si and ^{15}N acquisitions, chemical shifts are accurate to ± 0.2 ppm unless significant broadening of spectra occurs (e.g. for disordered materials). Values of observed chemical shifts for ^{7}Li, ^{9}Be, ^{17}O and ^{27}Al are only accurate to ± 0.5–2 ppm depending on the width of the observed resonance. Full width at half height (FWHH) was routinely measured to an accuracy of $\pm 5\%$, with major errors being difficulty in definition of baseline, and deviation from Gaussian lineshape. FWHH measurements were always made on spectra to which no linebroadening had been applied. Intensities were measured using digital integration routines, and are accurate to $\pm 10\%$ in favourable cases; the main error is due to baseline imperfections and is greatest for broad peaks. Intensities are only strictly quantitative if no saturation occurred during acquisition. In general, it was impossible to tell whether this was so, since it would require measurement of T_1. Conclusions based solely on intensity measurements must therefore be somewhat tentative.

Spectral deconvolution was carried out using a non-linear least squares iterative fitting program.

4.2 Preparation of Materials

4.2.1 General Considerations

Samples were generally prepared by sintering of small pellets at temperatures in the range 1400–1800^oC, in a range of furnaces.

The starting materials used in the synthesis of ceramic samples are listed in Table 4.2.1. La_2O_3 and MgO were calcined at 750^oC for 2 h prior to use to remove volatile impurities including H_2O, and were then stored in a desiccator. YN was stored under N_2. Starting compounds for preparations of isotopically enriched materials are also listed in Table 4.2.1. Samples donated by other workers are listed in Table 4.2.2.

Table 4.2.1 Starting materials used in synthesis.

	Supplier	Impurities
α–Si_3N_4 (LC12)	Herman-Starck, Berlin	$\sim 5\%$ β–Si_3N_4 $\sim 4^w/o$ SiO_2 $\sim 0.05^w/o$ Fe
AlN	Herman-Starck, Berlin	$\sim 6^w/o$ Al_2O_3 $\sim 0.05^w/o$ Fe
Al_2O_3	BDH	—
SiO_2 (precip.)	BDH	—
La_2O_3	BDH/Aldrich	—
Li_2CO_3	BDH	—
MgO	BDH	
Y_2O_3	Rare Earth Products	—
$CaCO_3$	BDH	—
Mg	BDH	—
YN	Alfa	—
C	Cabot Carbon Black	$0.08^w/o$ S
$SiCl_4$	Aldrich	—
1.15 M $MgEt_2$ in Et_2O	Alfa	—
$^{15}N_2$	Isotec/Isogas $99.8^a/o$ ^{15}N	—
$H_2^{17}O$	Amersham $22^a/o$ ^{17}O	—

Table 4.2.2 Donated samples

Si_2N_2O	M. L. H. Chan
$YMgSi_2O_5N$	P. Korgul
Y_2SiAlO_5N	P. Korgul
β'–sialons	D. P. Thompson
Be samples	D. P. Thompson/L. J. Gauckler[(a)]
$YSiO_2N$	P. Korgul
$LaSiO_2N$ (6–layer)	P. Korgul

(a) Synthesis described in Reference 12.

4.2.2 Powder Processing

Starting materials in the correct proportions (including, in general, corrections for SiO_2 on α–Si_3N_4, and Al_2O_3 on AlN) were mixed by one of the following methods:

(i) Ball milling: 20–50 g of premix was sealed in a cylindrical rubber container with 1 cm ZrO_2 balls and IPA (1:6:1 by weight) and placed on rotating rollers for 3 days. The ZrO_2 balls were then removed by sieving, and the IPA was evaporated off under a heat lamp.

(ii) Smaller quantities of powder were mixed in an agate pestle and mortar in IPA for 5–30 min, depending on the particle size reduction required. In a few cases, e.g. when Mg was present, hydrocarbon liquids were used in place of IPA.

(iii) Mixes involving La_2O_3 were dry-mixed in an alumina Glen-Creston mill.

Cylindrical 'green' pellets were pressed by one of two methods:

(i) For light compaction, it was sufficient to use a uniaxial pressure of 1000 p.s.i. on material contained in 1.0 or 1.5 cm diameter steel dies, to give 3–5 mm thick pellets.

(ii) In some cases, it was further necessary to isostatically press uniaxially pressed

pellets contained in sealed, evacuated balloons, to a pressure of 25,000 p.s.i. This was achieved using a Stansted hydraulic isostatic press containing a 1:20 water:oil mix.

4.2.3 Furnace Systems Used

The majority of samples were sintered in a carbon resistance furnace.[13] The furnace was equipped with a low-voltage, high-current transformer, and a Variac transformer to control the power supply. Temperature was monitored by means of a PtRh(6%)/PtRh(30%) alumina sheathed thermocouple resting below the hot-zone. The temperature difference between the hot-zone and the monitoring thermocouple was determined from calibration runs, in which a thermocouple was temporarily placed in the hot-zone, and was found to vary linearly with temperature in the range 1200–1800^oC.

Pellets were packed in BN in a graphite crucible, and this was placed in the hot-zone. For reactions involving N_2, the pellet was placed on a bed of BN in an open crucible to facilitate gas flow. The furnace was evacuated, and back-filled with N_2. Pellets were sintered for 15–120 min under a flowing N_2 atmosphere.

A few samples were sintered in a tungsten element furnace[13] to avoid the reducing atmosphere of the carbon furnace.

The La U–phase glass was melted in an inductively heated graphite furnace.[14] The sample was quenched by rapidly removing it from the hot-zone, and pouring the liquid onto a cold metal plate. The glass was recrystallised in a vertical molybdenum element tube furnace.

Calcining of oxides and preparations of some silicate materials was undertaken using a standard Isoheat silicon carbide element muffle furnace.

Hot pressing was carried out using the arrangement described by Cheng.[14] A uniaxial pressure of 25 bar was applied to samples packed in BN. Temperatures of 1700–1800^oC were attained by use of a copper induction coil, and monitored with an optical pyrometer.

Figure 4.2.1 The SiC furnace used for nitridations (but unadapted).

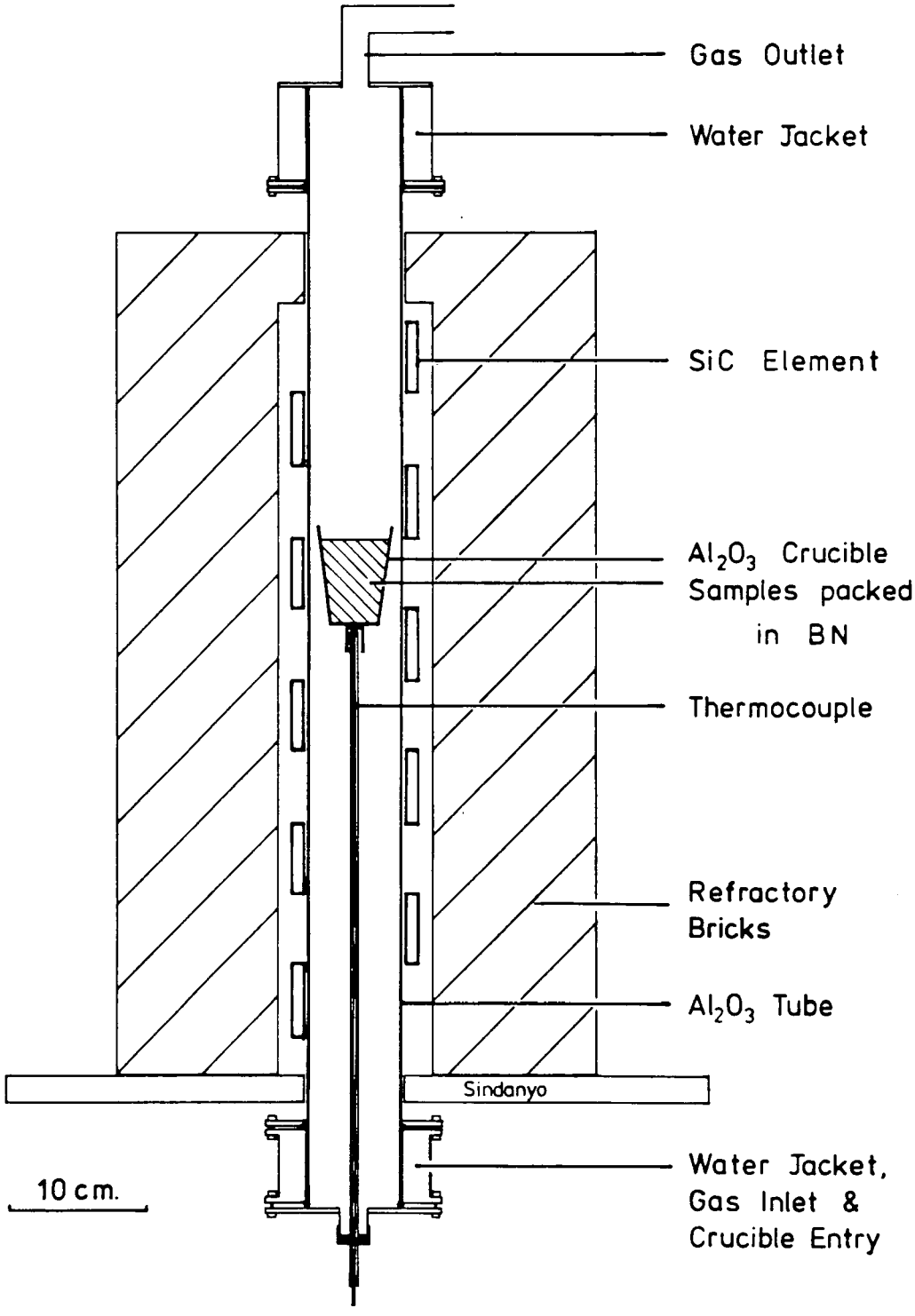

4.2.4 Nitridation

Nitridation was carried out in an adapted vertical mullite tube furnace fitted with a silicon carbide element, and flat brass endplates (see Figure 4.2.1). The power supply was varied by use of a Variac variable transformer and a thermostatic temperature control unit (Clearspan P130L). An external Pt/PtRh(6%) thermocouple was used to feed back into the thermostat unit. Experimental procedure is described in Section 5.1.3.

4.3 X–Ray Diffraction

The purity of samples was routinely checked by powder XRD from photographs taken with an XDC–700 Hägg–Guinier focussing camera and CuKα_1 radiation (λ = 1.54056 Å). KCl was used as an internal standard. Typically, an exposure time of 1.5 h at 50 kV and 20 mA was found to give satisfactory peak to background ratio. It is difficult to determine the relative amounts of phases present in mixed systems using powder XRD. Estimates of the relative intensities of the patterns can nevertheless be used as a measure of amounts of phases present. Relative pattern intensity in this Thesis is indicated qualitatively on a scale varying from very strong to very weak (vs, s, ms, m, mw, w, vw).

Unit cell dimensions were determined from measurements of line positions. Positions of the KCl lines were used to determine the camera constant, and $\sin^2\theta$ and camera constant values were refined using a least squares program.[15] Cell dimensions were refined on indexed $\sin^2\theta$ values using a least squares program. Accuracy of $\pm$0.001Å is possible using this procedure.

Accurate intensity data was obtained on Station 8.3 at SRS Daresbury with the aid of Dr. K. J. O'Reilly. A wavelength of 1.52904$\pm$0.0008 Åwas used, and data was collected in the 2θ range 6–100^o over 8 h on a two–circle diffractometer. Patterson synthesis was performed using the SHEL–X program.[17] Rietveld profile refinement was performed using the MPREP (X2.0.0) and MPROF (X15.0) programs[18] on the convex mainframe computer at Daresbury.

REFERENCES

1. Dupree, R.; Smith, M. E. *J. Magn. Reson.* **75**, 153–157 (1987).

2. Ernst, R. R.; Anderson, W. A. *Rev. Sci. Inst.* **37**, 93–102 (1966).

3. Samoson, A.; Lippmaa, E. *Phys. Rev. B* **28**, 6567–6570 (1982).

4. Pines, A.; Gibby, M. G.; Waugh, J. S. *Chem. Phys. Lett.* **15**, 373–376 (1972).

5. Kunwar, A. C.; Turner, G. L.; Oldfield, E. *J. Magn. Reson.* **69**, 124–127 (1986).

6. Fukushima, E.; Roeder, S. B. W. *Experimental Pulse NMR- a Nuts and Bolts Approach*; Addison-Wesley: Reading, MA. 1981.

7. *Systems Operation Manual for VXR Series NMR Spectrometer Systems*; Varian.

8. *Pulse NMR Spectrometer CXP Users Manual*; Bruker Spectrospin Ltd.

9. Tepper, L. B.; Hardy, H. L.; Chamberlain, R. I. *Toxicity of Beryllium Compounds*; Elsevier: London, U.K. 1961.

10. Merwin, L. H.; Sebald, A.; Espidel, J. E.; Harris, R. K. *J. Magn. Reson.* **84**, 367–371 (1989).

11. Freeman, R. *A Handbook of Nuclear Magnetic Resonance*; Longman: Harlow, U.K. 1988.

12. Gauckler, L. J. Ph.D. Thesis, University of Stuttgart, 1976.

13. Jameel, N. S. Ph.D. Thesis, University of Newcastle upon Tyne, 1984.

14. Cheng, Y. Ph.D. Thesis, University of Newcastle upon Tyne, 1988.

15. Carr, A. J. Ph.D. Thesis, University of Newcastle upon Tyne, 1986.

16. Thompson, D. P. *Least Squares Refinement Program*; University of Newcastle upon Tyne, 1974.

17. Sheldrick, G. *SHEL-X: A Program for Crystal Structure Determination*; unpublished, 1975.

18. Fitch, A. N.; Murray, A. D. *Manual for Multipattern Rietveld Profile Refinement Program*; PDPL, Daresbury Laboratory, 1989.

Chapter V

Synthesis and Magic-angle Spinning NMR of Isotopically Enriched Precursor Materials

5.1 Preparation of α–$Si_3^{15}N_4$

5.1.1 Introduction

The aim of a major part of the work described in this Thesis was to use ^{15}N NMR to characterise the nitrogen environments in various ceramic phases. To realise this aim, it was necessary to synthesize samples enriched in nitrogen-15. The usual sources of nitrogen for nitrogen ceramics are α–Si_3N_4 and AlN. Many of the phases of interest, however, do not contain aluminium, and therefore α–Si_3N_4 was chosen at an early stage as the material through which to introduce nitrogen-15 into samples. It was thus necessary to prepare α–Si_3N_4 enriched in ^{15}N to a level of *ca.* $50^a/o$, to achieve a sensitivity similar to that of ^{29}Si.

There exists a considerable body of literature on the preparation of α–Si_3N_4.[1,2] Four main methods have been used:[3]

(i) Nitridation of silicon:

$$3Si + 2N_2 \longrightarrow Si_3N_4 \qquad (5.1.1)$$

(ii) Carbothermal reduction of silica under a nitrogen atmosphere:

$$3SiO_2 + 6C + 2N_2 \longrightarrow Si_3N_4 + 6CO$$

(iii) Vapour phase reactions:

$$3SiCl_4 + 4NH_3 \longrightarrow Si_3N_4 + 12HCl$$

$$3SiH_4 + 4NH_3 \longrightarrow Si_3N_4 + 6H_2$$

(iv) Decomposition of silicon imide:

$$SiCl_4 + 6NH_3 \longrightarrow Si(NH)_2 + 4NH_4Cl$$

$$3Si(NH)_2 \xrightarrow{\Delta} Si_3N_4 + 2NH_3$$

The potential advantages and disadvantages of each of these methods for the preparation of α–$Si_3^{15}N_4$ are summarised in Table 5.1.1.

Carbothermal reduction was ruled out because of the very severe problems of carbon contamination which would result from nitridation at the low nitrogen pressures necessary from consideration of the cost of $^{15}N_2$. Vapour phase routes were ruled out because of the specialised gas handling and recycling equipment required, and the lack of detailed literature on the processes. Nitridation of silicon was thus selected as the most promising route. Contamination of samples with small amounts of iron had not caused great problems in the recording of good quality ^{29}Si spectra, and was thus not considered too serious a drawback.

Nitridation of silicon has been the most widely used method of preparing silicon nitride, but always using a huge excess of nitrogen, normally in a flowing atmosphere. The expense of $^{15}N_2$ meant that the method normally used would have to be modified so that losses of unreacted $^{15}N_2$ were minimised.

5.1.2 The nitridation of silicon

The reaction of silicon with nitrogen is a complex process, the mechanism of which is not fully understood.[6] It is most commonly performed on fine-grained silicon compacts under a flowing, mixed nitrogen/hydrogen (90–95$^v/o$ N_2) atmosphere, at temperatures in the region 1200–1450^oC. Under these conditions, both α–Si_3N_4 and β–Si_3N_4 are formed. Rossetti *et al.*,[7] in a recent analysis of kinetic data from previous studies, confirm the accepted notion that the α–polymorph is formed by reaction of N_2 with a gaseous silicon species (SiO or Si), whilst the β–polymorph is formed by the gas–liquid (or gas–solid) reaction between N_2 and silicon. A high α/β ratio is desirable in the product in this study because the α–polymorph is the more reactive of the two forms.

Table 5.1.1 Potential methods for preparation of α-$Si_3^{15}N_4$.

Method	Advantages	Disadvantages	Ref.
Nitridation of silicon	•Raw materials readily available •Large literature means most synthetic problems more easily solvable •Net reduction in gas volume during reaction means reaction easy to contain and follow	•Silicon generally contains ~0.1% Fe to aid nitridation •Product not normally a powder, thus reqiures grinding or milling	1
Carbothermal reduction of SiO_2	•Raw materials readily available •Powder product •No Fe contamination	•Product likely to be contaminated with C, SiO_2, SiC and Si_2N_2O. Could cause problems in later synthesis of samples •Product likely to have high oxygen content •Net increase in gas volume during reaction could make containment of reaction difficult	4
Vapour phase reactions and imide decomposition	•No carbon or Fe contamination, product is very pure	•corrosive and toxic gases involved and type of reaction means specialised equipment required •Net increase in gas volume during reaction •Imide route requires recycling of $^{15}NH_3$ •Little detailed literature	5

Two other factors were considered important in the design of the final synthesis: rapid overall reaction to minimise the chance of system leaks, and production of as fine a grain size as possible to maximise product reactivity. The complexity of the nitridation reaction mechanism is demonstrated by the number of experimental parameters which affect these considerations. The most important of these are summarised below:

(i) Nitriding temperature

The rate of silicon nitridation is extremely sensitive to temperature. The reaction is extremely exothermic[1] ($\Delta H = -733$ kJ mol^{-1}), and entropically unfavourable ($\Delta S = -320$ Jmol^{-1}K^{-1}). The rate of nitridation is invariably found to be negligible below 1100^oC. In the range 1100–1400^oC, the initial reaction rate increases with temperature,[8] but increasing the reaction temperature also has the effect of producing a coarse-grained product, with a lower α/β ratio.[6] These observations can be complicated by 'hot-spot' formation if thermal transfer is inefficient.[1] The fraction of β–Si_3N_4 is highest at temperatures above 1410^oC, the melting point of silicon.

It was therefore considered important to nitride at the lowest temperature at which the overall reaction rate was acceptable.

(ii) Initiation and catalysis

Silicon powder is covered by a protective coating of SiO_2 which must be removed before nitridation can occur. Many methods have been used, but the most common methods are addition of hydrogen to the nitriding mix:

$$SiO_2 + H_2 \longrightarrow SiO_{(g)} + H_2O_{(g)}$$

and the addition of iron to the silicon. The iron is thought to aid nitridation by devitrification of the SiO_2, allowing rupture of the protective film.

Both hydrogen and iron are also found to have longer-lasting catalytic effects. The mechanisms of these catalytic effects are not well understood, but the effects themselves are large. Boyer and Moulson[9] have shown that at 1350^oC, the α/β ratio and the extent of nitridation after 10 hours are markedly dependent on iron

Figure 5.1.1 Schematic diagram of the apparatus used for the preparation of α-$Si_3^{15}N_4$.

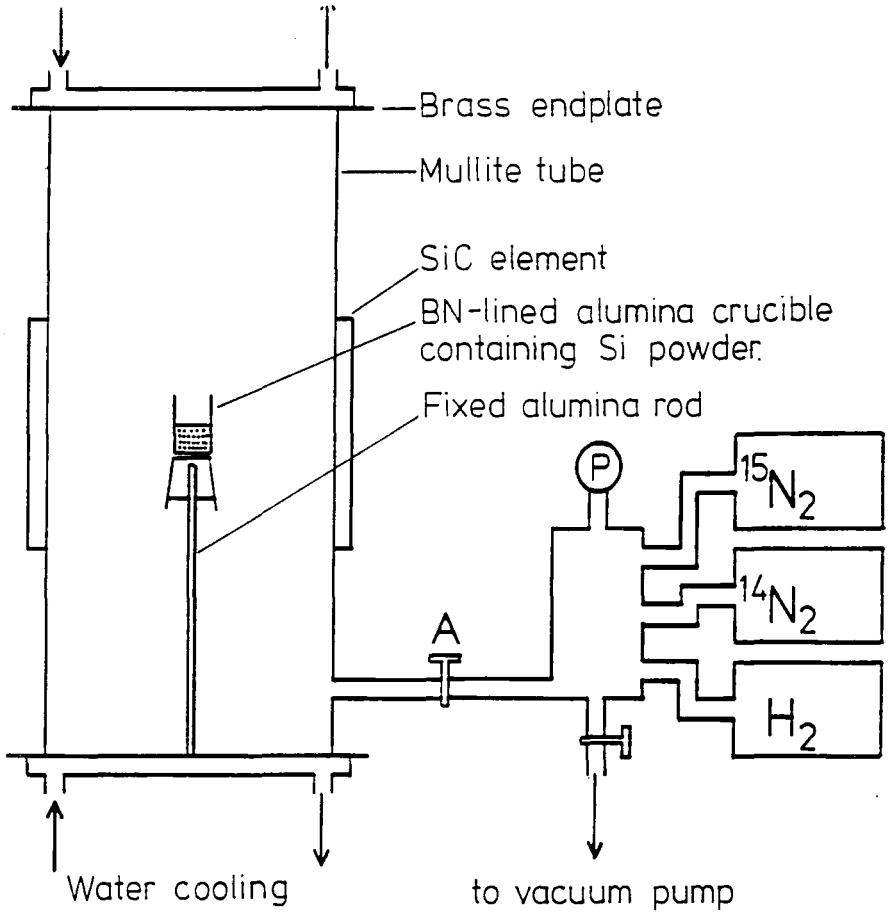

Figure 5.1.2 Calibration curve for the SiC furnace.

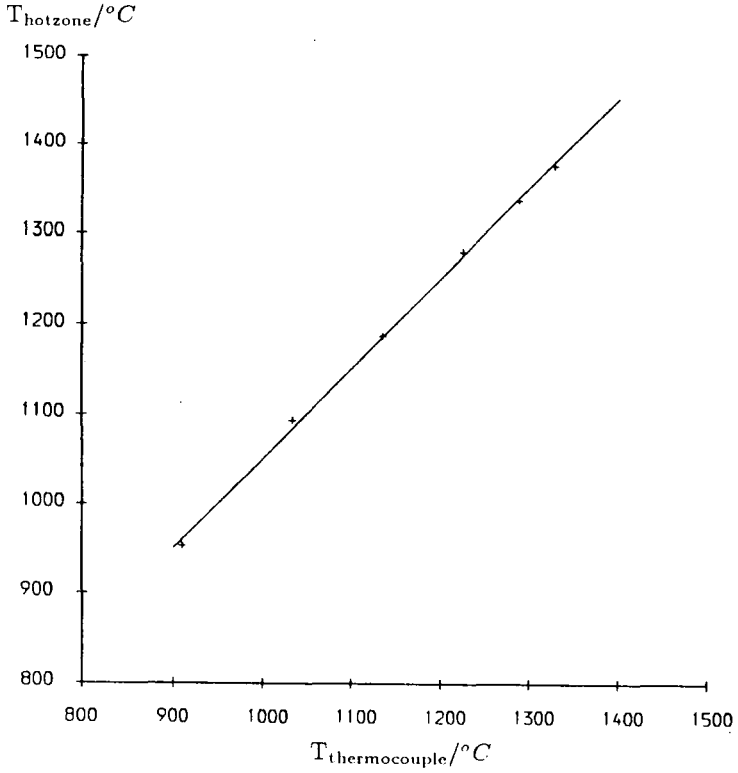

concentration. The yield of β–Si_3N_4 was found to depend only very slightly on [Fe], but the total percentage reaction ranged from 11.4% at zero iron concentration, to 47.2% at a concentration of 5000 ppm. It was found that it is particularly critical that the iron concentration is greater than 1000 ppm in the precursor silicon powder.

(iii)**Total gas pressure**

Atkinson *et al.*[8] have shown that at 1375^oC under pure N_2, the initial nitridation rate increases as the pressure of nitrogen is increased; but that higher nitrogen pressures also have the effect of leading to formation of a protective nitride barrier, leading to incomplete nitridation. They attribute this effect to the large number of nucleation sites at higher nitrogen pressure. The effect is less marked if catalysts are present, but it is clear that a slow initial nitridation rate has the effect of facilitating nitridation in the later stages of the reaction.

5.1.3 The Preparation of α–$Si_3^{15}N_4$

The apparatus for the nitridation is shown in Figure 5.1.1. Technical details were described in Section 4.2. A fixed-volume system was chosen so that as little $^{15}N_2$ was discarded as possible, but it also had the advantage that after admittance of $^{15}N_2$, pressure changes in the system could be used to calculate the extent of the nitridation reaction. Before the system could be used, it had to be fully callibrated so that the precise conditions during the reaction would be known.

(i) **Temperature ca librations**

In normal furnace operation, the sample is mounted on a movable thermocouple. This thermocouple allows a direct reading of the hot-zone temperature to be made. A positive pressure of nitrogen is used to minimise the effect of leaks at the base of the thermocouple. During the silicon nitridation reaction, however, it was expected that the total pressure of nitriding gas would fall well below 1 atm for considerable lengths of time, and thus it was decided that the movable thermocouple should be replaced with a fixed mounting rod to minimise the number of potential leaks. It was thus necessary to determine the temperature difference between the hot-zone of the furnace and the external furnace thermocouple used in

Figure 5.1.3 Plot of average gas temperature against hot-zone temperature for nitrogen in the nitriding furnace, assuming perfect gas behaviour.

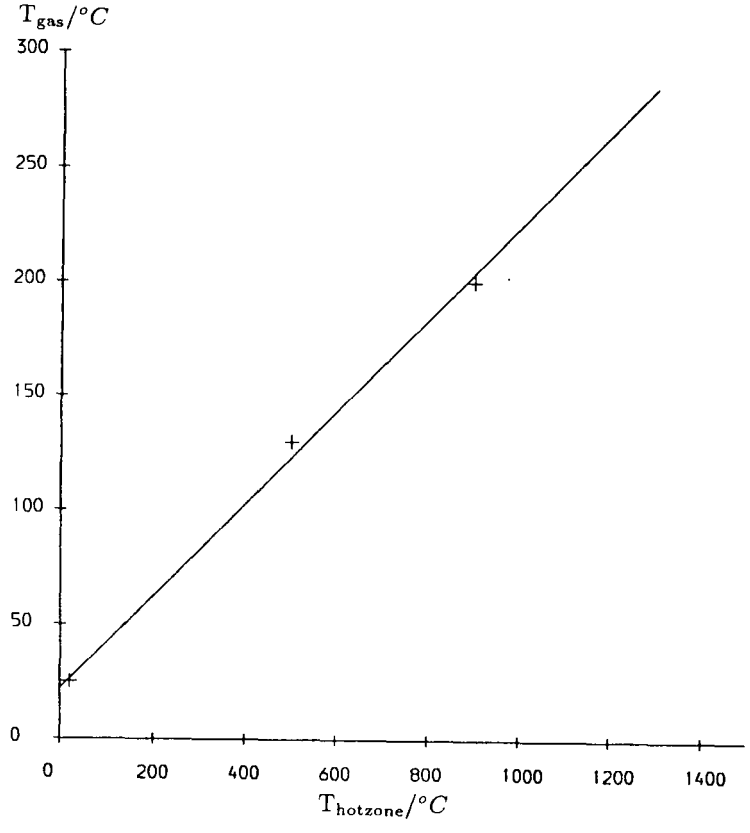

the furnace thermostat system. This was measured at a series of temperatures by temporarily replacing the fixed rod with a standard thermocouple. The callibration curve is given in Figure 5.1.2.

(ii) **Furnace volume measurement**

The volume of the furnace and gas-line were needed to determine the amounts of gases present during the reaction. These volumes were measured by expanding a known volume of air at 1 atm into the evacuated system, and measuring the observed pressure changes. Perfect gas behaviour was assumed. The furnace (to Tap A) was found to have a volume of 1060 ml, and the gas-line, 150 ml.

(iii) **Average temperature ca.libration**

To determine the amount of gas present in the system at temperatures above room temperature, it was necessary to estimate the average temperature throughout the furnace system. This was achieved by measuring the changes in pressure of a fixed amount of nitrogen as the furnace temperature was increased. The average temperature of the furnace atmosphere could then be calculated using the perfect gas law. The results are shown in Figure 5.1.3.

Initial investigations

Several methods of performing the nitridation were tried before a successful process was found. The results of these early experiments are briefly summarised below. Effects are difficult to quantify because studies were not comprehensive.

(i) **Carbon** Initially it was reasoned that use of a carbon crucible would aid in the removal of the protective silica layer on the silicon powder. Unfortunately, carbon in the system also leads to significant silicon carbide formation (as determined by XRD), even if not in direct contact with the silicon powder. In one experiment, the silicon powder was placed in an alumina crucible on a carbon plinth. Silicon carbide was still seen in the nitrided product. Small amounts of oxygen are thought to facilitate carbon transfer in the form of carbon monoxide. Only by rigorously eliminating carbon from the system could a silicon carbide-free material be prepared.

(ii) **Hydrogen and seeding** When hydrogen was not present in the furnace atmosphere, nitridation did not commence at temperatures below 1300^oC at the nitrogen pressures used (i.e. $\sim$0.7 atm). At hydrogen partial pressures of around 0.05 atm, nitridation could be achieved at the temperatures used in the successful process if the silicon was seeded with $5^w/_o$ α–Si_3N_4.

A successful method for the synthesis of α–$Si_3^{15}N_4$

The following method was developed for the synthesis of α–$Si_3^{15}N_4$:

(i) Preparation

Silicon powder containing approximately 0.1% iron was thoroughly mixed with $5^w/_o$ α–Si_3N_4 in IPA in an agate pestle and mortar. After removing the IPA, 1.05 g of this powder (0.0356 mol Si) was placed in a 2 cm diameter alumina crucible lined with a layer of boron nitride, and placed in the furnace on a second, upturned alumina crucible. This was attached to the alumina mounting rod using kaolin wool.

(ii) Nitridation

The furnace chamber was evacuated, and the furnace was heated to 1240^oC under vacuum over approximately 4 h. $^{15}N_2$ and H_2 were then admitted to the furnace to partial pressures of 0.053 atm of H_2, and 0.520 atm of $^{15}N_2$. The latter volume corresponds to approximately 0.014 mols of $^{15}N_2$. Nitridation was allowed to proceed for 23 h, during which time pressure changes in the system were monitored. Tap A (Figure 5.1.1) was kept closed except when pressure readings were being taken as a precaution against a leak developing in the gas line. These pressure readings were then converted into amounts of $^{15}N_2$ remaining in the furnace chamber using the average gas temperature determined from Figure 5.1.3. After about 23 h, it was estimated that around 85% of the $^{15}N_2$ initially admitted had reacted. At this point, $^{14}N_2$ was admitted to the furnace chamber to a total pressure of around 1 atm (without removing the H_2 or remaining $^{15}N_2$), and the reaction was allowed to proceed for a further 5 h. Over the next 3 h, the temperature was slowly raised to 1400^oC to increase the rate of nitridation, which is slowest when there is little silicon present. Further $^{14}N_2$ was admitted to the furnace chamber

Figure 5.1.4 Extent of reaction with time for a typical nitridation run.

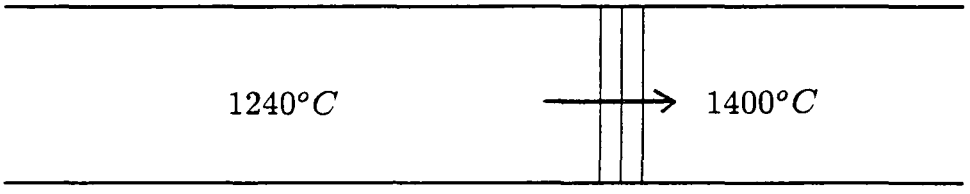

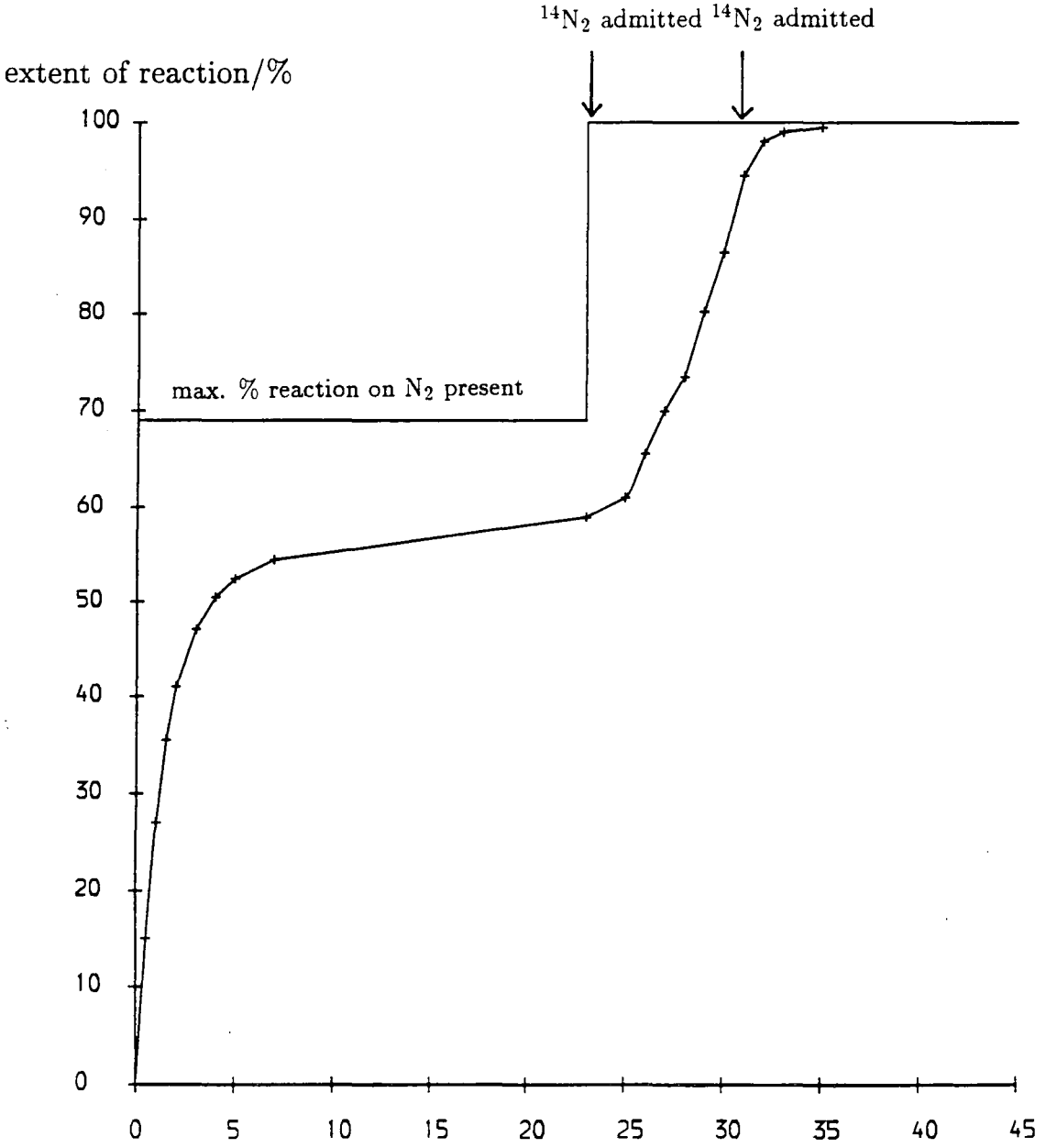

to bring the gas pressure back up to 1 atm, and nitridation was allowed to proceed for a further 16 h. The furnace was then slowly cooled and the crucible containing the nitrided silicon could be retrieved. The process is summarised in the reaction profile in Figure 5.1.4.

(iii) **Post-nitridation**

The silicon nitride produced in the reaction as weighed to determine the total weight gain during the reaction. This is predicted to be +69% according to Equation 5.1.1 (assuming an enrichment level of $60^a/o$ ^{15}N), but typical observed weight gains were +60 to +63%. The difference is accounted for by volatilisation of silicon either as $Si_{(v)}$ or $SiO_{(g)}$. Thus, the enrichment level of ^{15}N is calculated as approximately $60^a/o$ ^{15}N, and the incorporation of ^{15}N as 85–90% of initial $^{15}N_2$ admitted.

The silicon nitride produced in the reaction was always partially fused. It was ground to 150 μm using a tungsten carbide percussion mill and then an agate pestle and mortar. The powder XRD photograph (Figure 5.1.5) shows that the only crystalline phases present are α– and β–$Si_3^{15}N_4$, in the estimated ratio 90–95:5–10%. Unreacted silicon was never detected.

5.2 Preparation of β–$Si_3^{15}N_4$and $Si_2^{15}N_2O$

5.2.1 Preparation of β–$Si_3^{15}N_4$

β–Si_3N_4 is considered the more stable of the two silicon nitride polymorphs. No observation of a $\beta \rightarrow \alpha$ transition has ever been made.[10] α–Si_3N_4 may be stabilised by small amounts of oxygen,[11] and when this oxygen is lost, β–Si_3N_4 is formed.

β–Si_3N_4 is most easily prepared from α–Si_3N_4 by sintering, using a small amount of metal oxide as a sintering agent. Hampshire[10] has studied this reaction in detail. If no sintering agent is used, incomplete transformation and large weight losses invariably result. The metal oxide is thought to react with surface silica on the α–Si_3N_4 to form a silicate liquid, in which α–Si_3N_4 can dissolve. β–Si_3N_4 recrystallises from this liquid, which itself forms a grain boundary glass on cooling.

Figure 5.1.5 Hägg–Guinier photographs of (a) unreacted silicon and (b) α–$Si_3^{15}N_4$.

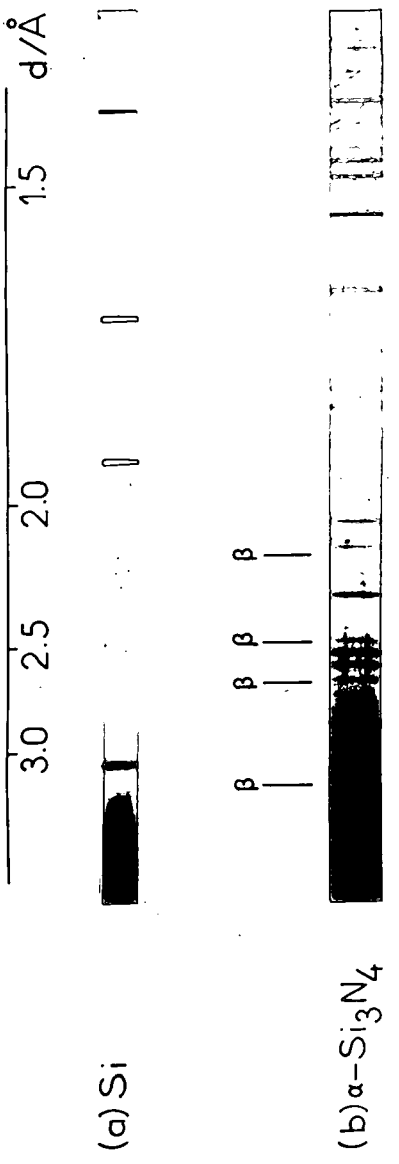

β–$Si_3^{15}N_4$ was prepared by sintering an isostatically pressed pellet of α–$Si_3^{15}N_4$ containing $1^w/o$ MgO, at 1750^oC for 2 h in a carbon resistance furnace. The observed weight loss for this reaction was $\sim 4\%$. Powder XRD photographs of the product showed that the only crystalline phase present was β–Si_3N_4.

The main source of weight loss in most reactions involving α–Si_3N_4 is considered to be the following:

$$3[O]_{g/s} + \alpha - Si_3N_4 \longrightarrow 3SiO_g + 2N_2 \qquad (5.2.1)$$

where [O] can be provided by oxygen present in the α–Si_3N_4 itself, other metal oxides, or from impurities in the nitrogen atmosphere.

If more than $1^w/o$ MgO is used, then weight losses were found to increase, and the $\alpha \rightarrow \beta$ conversion to be less efficient. This suggests that MgO is acting as an additional source of oxygen:

$$3MgO + Si_3N_4 \longrightarrow 3SiO_{(g)} + 2N_2 + 3Mg_{(v)}$$

5.2.2 Preparation of $Si_2^{15}N_2O$

Si_2N_2O is a difficult compound to prepare. It can be made in reasonably pure form by hot-pressing the stoichiometric quantities of α–Si_3N_4 and SiO_2.[13] No liquid phase is thought to be present, explaining the difficulty in effecting the reaction without pressure. Hot-pressing is not the preferred method for preparing materials on the sub-gram scale, and an alternative method was sought. Only one nitrogen environment is present in Si_2N_2O,[14] and thus only one peak was expected in the ^{15}N NMR spectrum of this material. it was thus considered satisfactory to prepare $Si_2^{15}N_2O$ in an impure form by sintering in the presence of a liquid. The $Si_2^{15}N_2O$ synthesised was to be used in the preparation of $LaSiO_2^{15}N$ and $La_4Si_2O_7^{15}N_2$ (Section 6.1), and thus the La-Si-O-N system was chosen. A section of the La-Si-O-N phase diagram at 1550^oC is shown in Figure 5.2.1. An overall composition corresponding to point A ($La_{0.32}Si_{2.76}O_{1.86}N_{2.76}$) should therefore give a mix $(La_2Si_2O_7)(\beta\text{–}Si_3N_4)_2(Si_2N_2O)_{4.72}$ at equilibrium.

Figure 5.2.1 Part of the La–Si–O–N phase diagram at 1550^oC. Only phases and tie lines of relevance to the synthesis of Si_2N_2O are shown. Only full lines are tie lines.

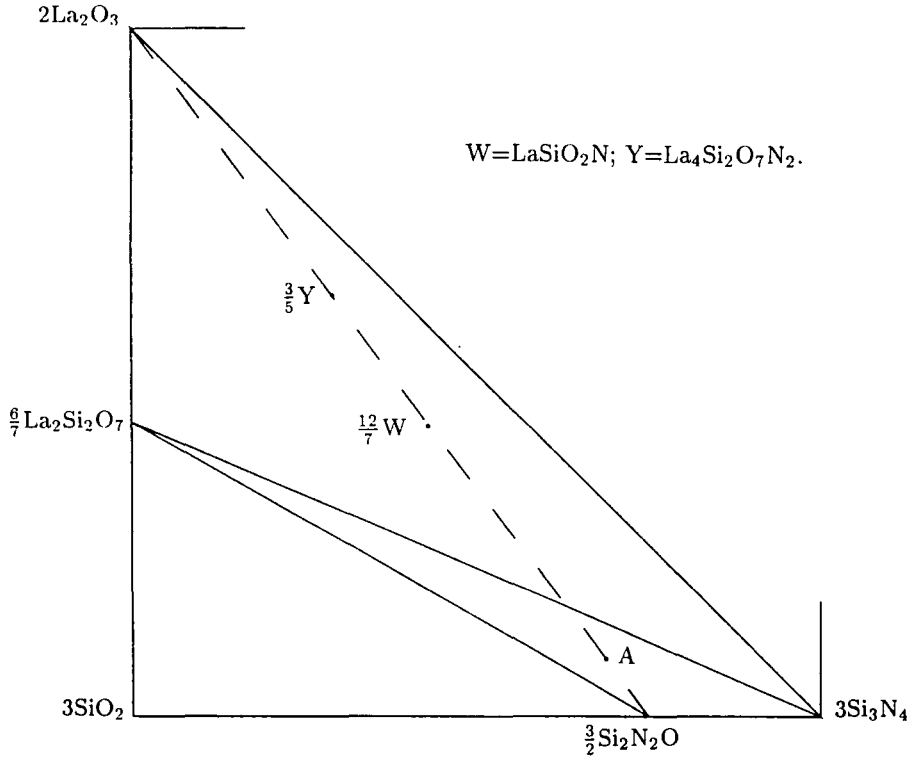

Figure 5.2.2 ^{29}Si MAS spectrum of impure $Si_2^{15}N_2O$, showing the presence of β–Si_3N_4 and $La_2Si_2O_7$.

SF=59.6 MHz; PA=23^o; NT=130; RD=300 s; SR=3.10 kHz; AF=0.05 s.

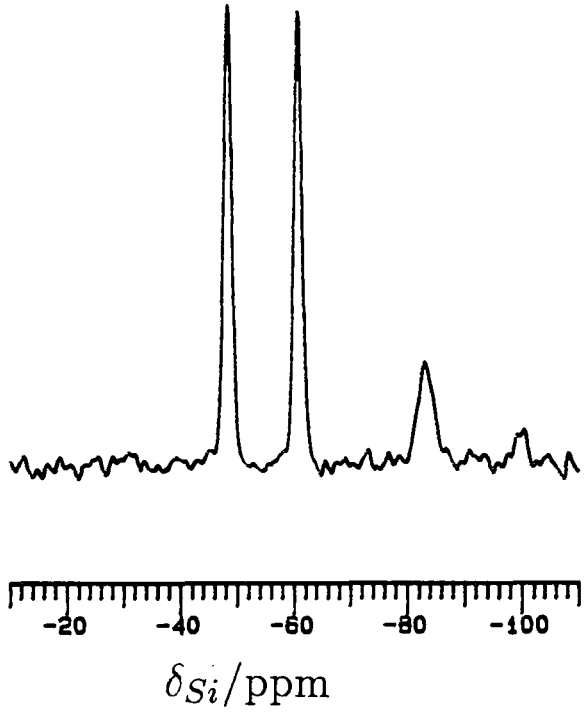

Material corresponding to this composition was prepared by sintering for 2 hours at 1550^oC in a carbon resistance furnace. A weight loss of ~8% was observed. The powder XRD photograph of the product shows the presence of $La_2Si_2O_7$, Si_2N_2O and β–Si_3N_4 as the only crystalline phases. The ^{29}Si MAS NMR spectrum of the sample (Figure 5.2.2) confirms that only these three phases are present. If the peak areas are assumed quantitative, then an overall composition $(La_2Si_2O_7)(\beta\text{–}Si_3N_4)_{1.7}(Si_2N_2O)_{2.6}$ is calculated. If the observed weight loss is assumed to occur via Equation 5.2.1, then a composition of $(La_2Si_2O_7)(\beta\text{–}Si_3N_4)_{2.6}(Si_2N_2O)_{2.6}$ would be predicted if all of the oxygen comes from added oxides. Some of the weight loss is, however, due to oxygen in the α–$Si_3^{15}N_4$, leading to less β–$Si_3^{15}N_4$ in the product than predicted by the calculation. The ^{29}Si NMR will be further discussed in Section 5.3.1.

5.3 NMR of Silicon Nitrides and Oxynitride

5.3.1 ^{29}Si Studies

The ^{29}Si MAS NMR spectra of α– and β–Si_3N_4, and Si_2N_2O were first described by Dupree *et al.*[15] The authors demonstrate that β–Si_3N_4 gives rise to one peak (−48.5 ppm), and α–Si_3N_4 to two peaks (−47.0,−49.7 ppm), as would be predicted from the numbers of unique silicon atoms in the unit cells (Table 3.1.1). The chemical shift values are consistent with a less shielded Si environment than in silicates. Later workers have confirmed these results.

Several groups have successfully used ^{29}Si MAS NMR to characterise small amounts of impurities in commercial silicon nitride samples. Apperley[16] and Marshall *et al.*[17] have shown that differential saturation of ^{29}Si spectra could lead to enhancement of low-intensity peaks arising from the presence of amorphous SiO_2, oxynitride and carbide species. A similar technique was used by Carduner *et al.*[18] to determine the silicon content of commercial α– and β–Si_3N_4. Apperley has also shown[16] that a high iron content leads to a much broader ssb manifold. In a more recent study, Carduner *et al.*[19] have obtained MAS spectra of carefully machined bulk β–Si_3N_4 samples, and characterised minor phase components in such samples. The same group have also shown[18,19] that spectral deconvolution can be used to

Figure 5.3.1 ^{29}Si MAS NMR spectra of
(a) α-Si_3N_4 SF=59.6 MHz: PA=23^o; NT=472; RD=120 s: SR=6.40 kHz.
(b) α-$Si_3^{15}N_4$ SF=59.6 MHz: PA=23^o; NT=500; RD=120 s: SR=6.40 kHz.
(c) β-Si_3N_4 SF=59.6 MHz: PA=13^o; NT=606; RD=120 s; SR=2.64 kHz.
(d) β-$Si_3^{15}N_4$ SF=59.6 MHz: PA=13^o; NT=500; RD=120 s: SR=2.65 kHz.

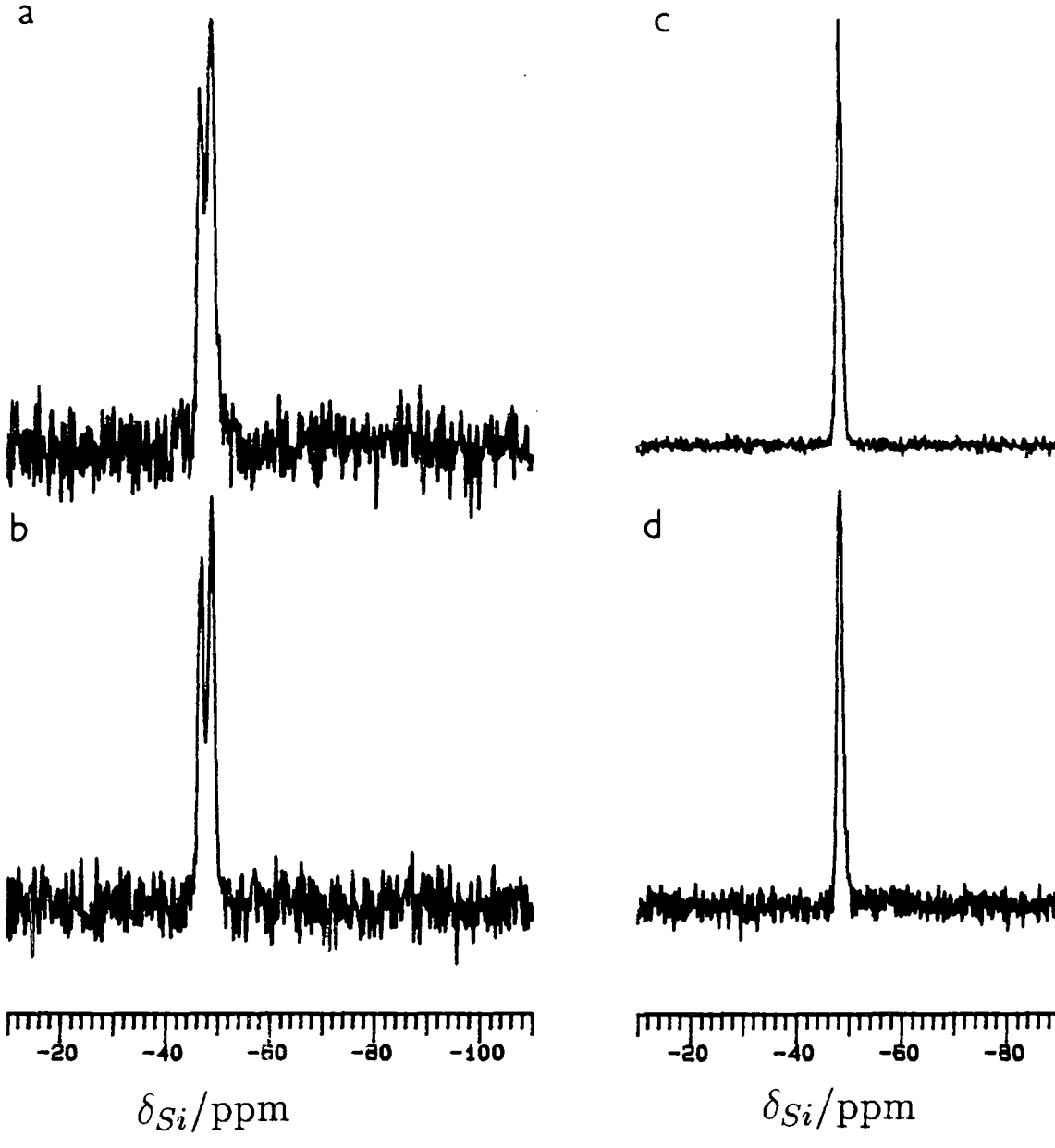

determine the quantities of α, β and amporphous silicon nitrides in commercial samples.

The spectrum of Si_2N_2O gives a single resonance at -63.0 ppm,[15] consistent with the crystal structure of this phase (Figure 3.1.2). Silicon in this phase is present in an $[SiON_3]$ environment, and the chemical shift is consistent with a more oxygen-rich environment than in Si_3N_4. A recent study of a high surface area, probably amorphous Si_2N_2O sample[20] failed to observe a ^{29}Si signal.

The ^{29}Si spectra of α– and β–$Si_3^{15}N_4$, and unenriched samples prepared by an identical route are shown in Figure 5.3.1. The ^{29}Si spectrum of the sample of $Si_2^{15}N_2O$ was given in Figure 5.2.2. Chemical shift and linewidth data are summarised in Table 5.3.1, including data for a pure sample of Si_2N_2O. A spin-lattice relaxation time of 3000±300 s was measured for a low-iron sample of α–Si_3N_4, which compares with a literature value of 2600±100 s for a sample of commercial silicon nitride.[18]

The ^{29}Si spectra of the silicon nitride samples are in excellent agreement with previous studies, and confirm that no silicon metal or other major silicon-containing impurities are present; except that the linewidths of the β–Si_3N_4 samples (75 Hz) were significantly narrower than previously reported (120–150 Hz[21,22]). The explanation of this last observation is probably connected with the experimental conditions.

The measurement of the spin-lattice relaxation time of high purity silicon nitride indicates that the small amount of iron normally present in silicon nitride is not the principal cause of longitudinal relaxation for the majority of silicon atoms in such samples; the effect of the paramagnetic centres on relaxation is very short-range, as found in stannates.[23] Therefore, it is to be expected that saturation of spectra containing paramagnetic centres will lead to increases in overall linewidth, because the silicon atoms close to such centres relax more quickly, and also give rise to broader resonances (see Section 2.1.6). The increase in linewidth will depend on the degree of saturation. It seems likely that variations in linewidth reported in the literature and in this Thesis are due, in part, to this effect.

The samples of Si_2N_2O all gave ^{29}Si resonances at rather less negative chemical

Table 5.3.1 NMR data for silicon nitrides and oxynitride

phase	Silicon–29		Nitrogen–15		
	δ_{Si}/ppm	FWHH/Hz	δ_N/ppm	FWHH/Hz	Intensity
α–Si_3N_4	−49.0				
	−47.1				
α–$Si_3^{15}N_4$	−49.0		51.2	50	7
	−47.1		52.9	50	7
			63.7	50	1
			75.6	55	1
β–Si_3N_4	−48.5	75			
β–$Si_3^{15}N_4$	−48.5	75	51.5	30	4
			68.7	35	1
$Si_2N_2O^{(a)}$	−61.6	140			
$Si_2N_2O^{(b)}$	$-48.5^{(c)}$	85			
	−60.9	85			
	$-83.6^{(d)}$	150			
$Si_2^{15}N_2O$	$-48.5^{(c)}$	100	40.3	30	
	−61.0	100	$51.2^{(c)}$	30	
	$-83.3^{(d)}$	200	$68.6^{(c)}$	40	

(a) pure sample. (b) Mixed sample (see text). (c) assigned to β–Si_3N_4. (d) assigned to $La_2Si_2O_7$.

shifts (1.4–2.0 ppm) than the literature value, and with narrower lines (100 Hz against 120–200 Hz[24,21]).

Most authors[21,25] have believed that broadening of ^{29}Si resonances in nitrogen ceramics is due, in part, to unaveraged (^{29}Si,^{14}N) dipole-quadrupole coupling, as discussed in Section 2.1.3. It was thus expected that ^{29}Si lines from the ^{15}N–enriched samples would be significantly narrower than from the unenriched samples

Figure 5.3.2 ^{15}N MAS NMR spectra of
(a) α-$Si_3^{15}N_4$ SF=30.4 MHz; PA=90^o; NT=11; RD=3600 s; SR=4.40 kHz.
(b) β-$Si_3^{15}N_4$ SF=30.4 MHz; PA=10^o; NT=192; RD=300 s; SR=4.40 kHz.

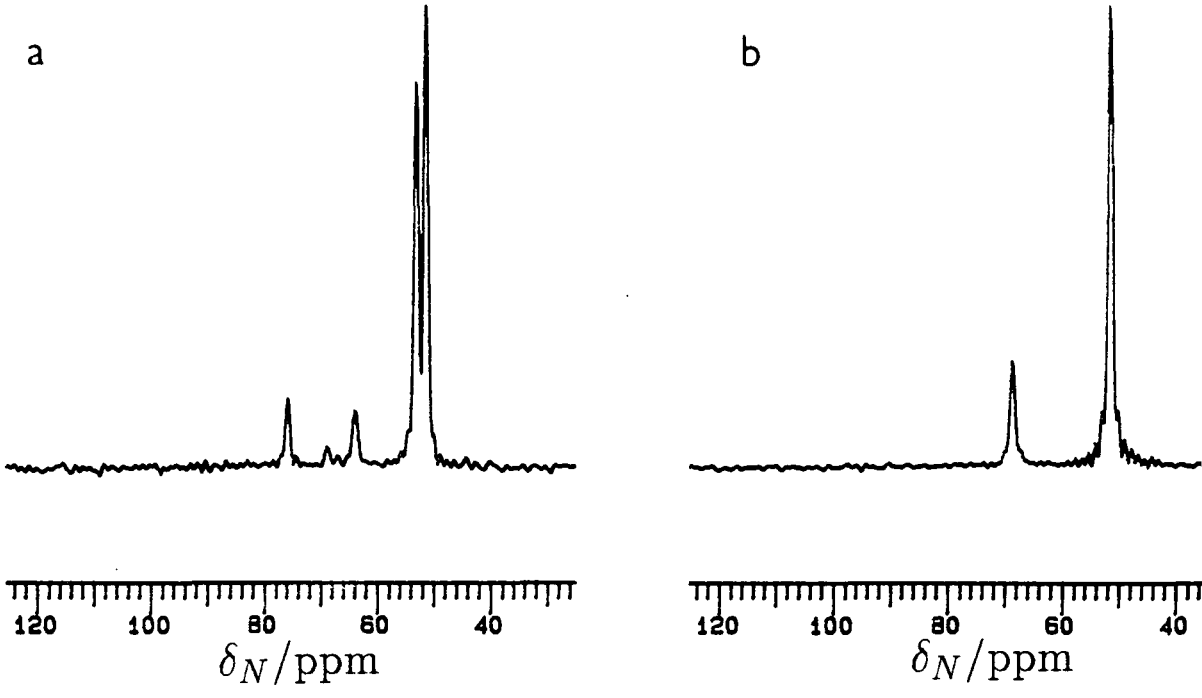

Figure 5.3.3 ^{15}N MAS spectrum of $Si_2^{15}N_2O$
SF=30.4 MHz; PA=11^o; NT=184; RD=120 s; SR=3.03 kHz; AF=0.05 s.

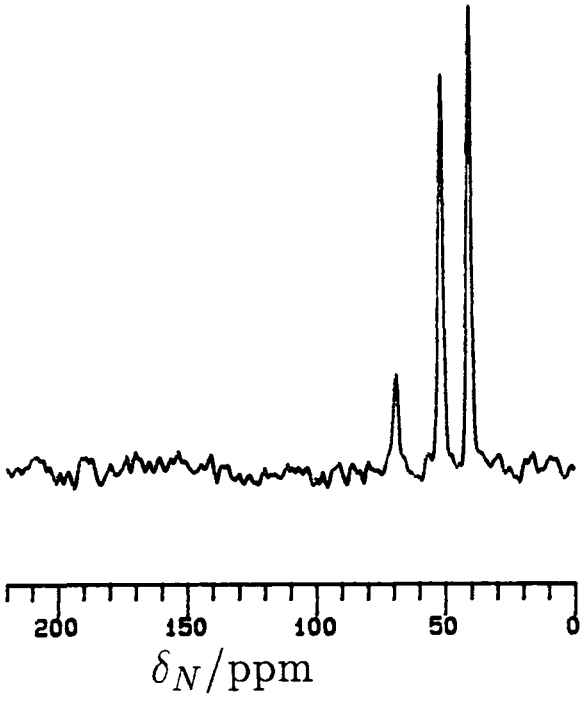

under identical acquisition conditions. This was found not to be the case. There was a marginal narrowing in the case of α–Si_3N_4, but it seems likely that line-broadening is due to other sources. The origins of relaxation and linewidth effects will be further discussed in Section 10.4.

5.3.2 ^{15}N NMR Studies

The ^{15}N spectra of α– and β–$Si_3^{15}N_4$ are shown in Figure 5.3.2, and that of $Si_2^{15}N_2O$ in Figure 5.3.3. Chemical shift data was summarised in Table 5.3.1. Turner *et al.*[26] report the spectrum of a mixed $Si_2^{15}N_2O/Si_3^{15}N_4$ sample, with peaks at 40.4, 51.6 and 68.9 ppm. The peaks at 40.6 and 51.6 ppm were correctly assigned to $Si_2^{15}N_2O$ and β–$Si_3^{15}N_4$. The peak at 68.9 ppm was wrongly assigned to a MoN species, and is clearly also due to β–$Si_3^{15}N_4$.

Spin-lattice times in β–$Si_3^{15}N_4$ were measured as 2700±400 s for the 51.7 ppm resonance, and 3000±600 s for the 68.7 ppm resonance, and indicate that similar, but as yet uncharacterised relaxation processes are occurring as for ^{29}Si in α–Si_3N_4.

Comparison of the intensity data in Table 5.3.1 and the crystallographic data in Table 3.3.1 for β–Si_3N_4 demonstrates unequivocably that the peak at 68.7 ppm is due to nitrogen in on the 2(b) sites, on the threefold axis, and the peak at 51.6 ppm to nitrogen on the 6(c) sites. The intensity ratio of the two peaks is rather more than the predicted 3:1. The measured T_1 values for β–Si_3N_4 demonstrate, however, that both resonances are saturated during acquisition, and as the 2(b) site probably has a somewhat longer T_1 relaxation time, it is differentially saturated.

The two resonances from β–$Si_3^{15}N_4$ are separated by 17.4 ppm. Both nitrogen environments are planar, [NSi_3] coordinated, although the Si–N–Si bond angles are unequal at the 6(c) site ($113.5^o, 121.3^o, 125.1^o$), whereas they are all equal at the 2(b) site (120.0^o). There is a similar variation in N—Si bond lengths at the two sites. It is apparent that ^{15}N chemical shifts are very sensitive to local coordination geometry, in an, as yet unapparent manner.

In α–$Si_3^{15}N_4$, little change is seen in the chemical shifts of the 6(c) nitrogen atoms, which are clearly in very similar environments to the 6(c) environment in β–Si_3N_4. The 2(a) and 2(b) sites, which are still on threefold axes, however,

are clearly in rather different environments, both to each other, and to the 2(b) environment in β–Si_3N_4. The 2(b) site, N(2), is no longer a planar coordination environment, with an Si–N–Si angle[27] of 116.0°, whereas the 2(a) site, N(1), is still planar. In addition, the N(2)–N(2) distance is roughly twice both the N(1)–N(1) distance, and the corresponding N(1)–N(1) distance in β–Si_3N_4. It is thus unsurprising that the chemical shifts of nitrogen in the two environments are very different, but the crystallography of the two phases might lead one to predict that only one of the two peaks would be significantly shifted from the 68.7 ppm resonance in β–Si_3N_4, whereas in fact, both are so shifted. As with β–$Si_3^{15}N_4$, predicted and observed intensity ratios for the four peaks do not agree. Although no T_1 measurements have been made for α–$Si_3^{15}N_4$, it is to be expected that similar influences are at work.

The ^{15}N chemical shift from $Si_2^{15}N_2O$ is the least positive observed from the Si–N–O phases. The nitrogen environment is [NSi_3] coordinated, and approximately planar. It seems likely that the oxygen n.n.n. is affecting the value of δ_N, but it is not clear exactly how.

To conclude, δ_N values of 40–76 ppm have been observed in the three Si–N–O phases for nitrogen in [NSi_3] environments. It has proved impossible to identify explanations for the observed variations within this range.

5.4 Synthesis and ^{17}O NMR of $Mg^{17}O$ and $Si^{17}O_2$

Oxygen, unlike nitrogen, can be provided by a vast range of source materials in nitrogen ceramics. Most metal oxides can be used, depending on the phase being prepared. The systems of interest for this study were the sialon and Mg–sialon polytypoids, and the M–Si–O–N systems, and thus SiO_2 and MgO were selected as suitable materials through which to introduce oxygen-17. $Mg^{17}O$ has the added benefit of giving a very narrow ^{17}O resonance by virtue of its high-symmetry oxygen environment,[28] making it a useful secondary reference material.

Three methods have been used in the literature to prepare ^{17}O–enriched materials:

(i) Hydrolysis of metal-containing compounds with $H_2^{17}O$.

Figure 5.4.1 ^{29}Si MAS NMR spectrum of amorphous $Si^{17}O_2$, showing the presence of SiOH groups as a shoulder to the main peak.
SF=59.6 MHz; PA=90^o; NT=488; RD=120 s; SR=4.40 kHz; AF=0.005 s.

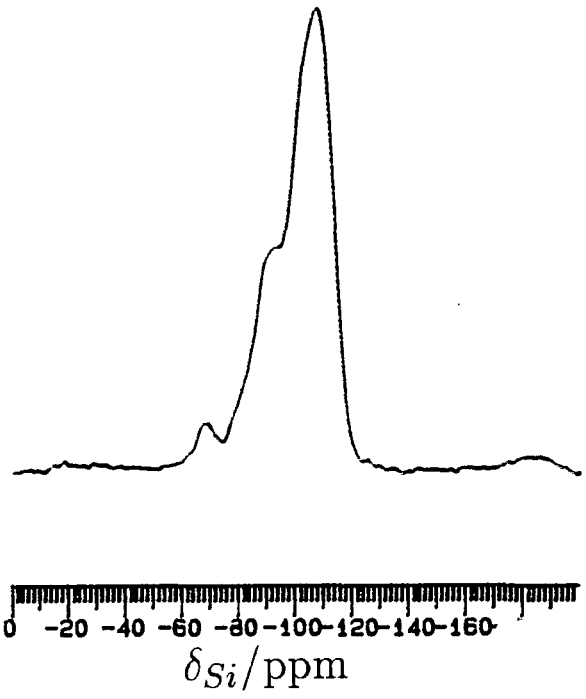

(ii) Exchange or precipitation in $H_2^{17}O$.

(iii) Exchange of ^{17}O using $^{17}O_2$ over oxides.

Oxidation of metals using $^{17}O_2$ could also be considered. A comparison of these methods is given in Table 5.4.1.

5.4.1 Synthesis of $Si^{17}O_2$

The literature method,[29] hydrolysis of $SiCl_4$ in $H_2^{17}O$ was used to prepare $Si^{17}O_2$, and is described in this Section.

4.70 g $SiCl_4$ (0.0277 mol) and 50 ml dried diethyl ether were placed in a dried, round-bottomed flask in a glove box. The flask was then attached to a dry-nitrogen line, and placed in an ice bath. $H_2^{17}O$ (0.97 g, 0.0532 mol) was slowly added from a syringe fitted with a plastic needle (to avoid corrosion from HCl) over 1 h with vigorous stirring. The mixture was stirred for a further 1 h at room temperature. The diethyl ether was then removed on a rotary evaporator. The resulting powder was heated at 250^oC for 4 h under vacuum to remove unreacted $SiCl_4$ and HCl. At this stage, the yield of solid was 1.66 g (0.0267 mol SiO_2). The solid was x-ray amorphous, but the ^{29}Si MAS NMR spectrum (Figure 5.4.1) indicated the presence of residual Si–O–H groups. Sintering the powder at 1500^oC for 15 min gave 1.48 g (0.0246 mol, 89% yield) of x-ray pure low cristobalite.

5.4.2 Synthesis of $Mg^{17}O$

The literature method for the preparation of $Mg^{17}O$ involves precipitation of $Mg(^{17}OH)_2$ by the addition of base to a solution of $Mg(NO_3)_2$ in $H_2^{17}O$.[28] This method was not considered suitable for the preparation of small amounts of $Mg^{17}O$ because of the excess of $H_2^{17}O$ required. It was therefore decided to prepare $Mg^{17}O$ by the hydrolysis of a reactive magnesium organometallic. Diethyl magnesium was chosen because the hydrolysis product is a non-corrosive gas which can easily be purged from the system. The reaction is as follows:[33]

$$Mg(C_2H_5)_2 + H_2^{17}O \xrightarrow{Et_2O} Mg^{17}O_{(s)} + 2C_2H_{6(g)}$$

Small amounts of $Mg(OH)_2$ were also expected to form.

Table 5.4.1 Methods of preparing ^{17}O-enriched oxides

Method	Examples	Reference	Advantages	Disadvantages
Hydrolysis of metal-containing species	$SiCl_4+2H_2^{17}O \rightarrow Si^{17}O_2+4HCl$	29	•$H_2^{17}O$ readily available and easy to handle	•Hydroxides nearly always formed. Drying leads to loss of ^{17}O
	$BCl_3+3H_2^{17}O \rightarrow B(^{17}OH)_3+3HCl$	29	•Reactions easily containable using standard equipment	•HCl corrosive product
	$Al(OPr)_3+2H_2^{17}O \rightarrow Al^{17}OOH+3PrOH$	30		
Exchange or precipitation in $H_2^{17}O$	$[^{16}O]Na\text{-}Y+H_2^{17}O \rightarrow [^{17}O]Na\text{-}Y+H_2O$	31	•Very mild conditions	•Vast excess of $H_2^{17}O$ needed
	$Mg^{2+}+2[^{17}OH]^- \rightarrow Mg(^{17}OH)_2$	28	•$H_2^{17}O$ readily available	•Not successful for all oxides •Hydroxide always formed
Exchange of ^{17}O in $^{17}O_2$	$Y_2O_3+^{17}O_2 \rightarrow Y_2^{17}O_3+O_2$	32	•No hydroxide intermediate •Some oxides cannot be prepared hydrothermally	•Vast excess of $^{17}O_2$ needed •Recovery of $^{17}O_2$ difficult (c.f. $H_2^{17}O$)
Oxidation of metal in $^{17}O_2$	None		•Could be stoichiometric	•Conditions may have to be 'violent'

Figure 5.4.2 ^{17}O NMR spectra of
(a) $Mg^{17}O$ SF=40.7 MHz; PA=90^o; NT=12; RD=30 s; SR=3.85 kHz.
(b) $MgAl_2O_4$ SF=40.7 MHz; PA=15^o; NT=1200; RD=1 s; SR=7.95 kHz; AF=0.01 s.
(c) $Si^{17}O_2$ SF=40.7 MHz; PA=23^o; NT=1000; RD=1 s; SR=8.95 kHz; AF=0.001 s.
(d) $Si^{17}O_2$ SF=40.7 MHz; PA=23^o; NT=132; RD=10 s; SR=0; AF=0.0021 s.

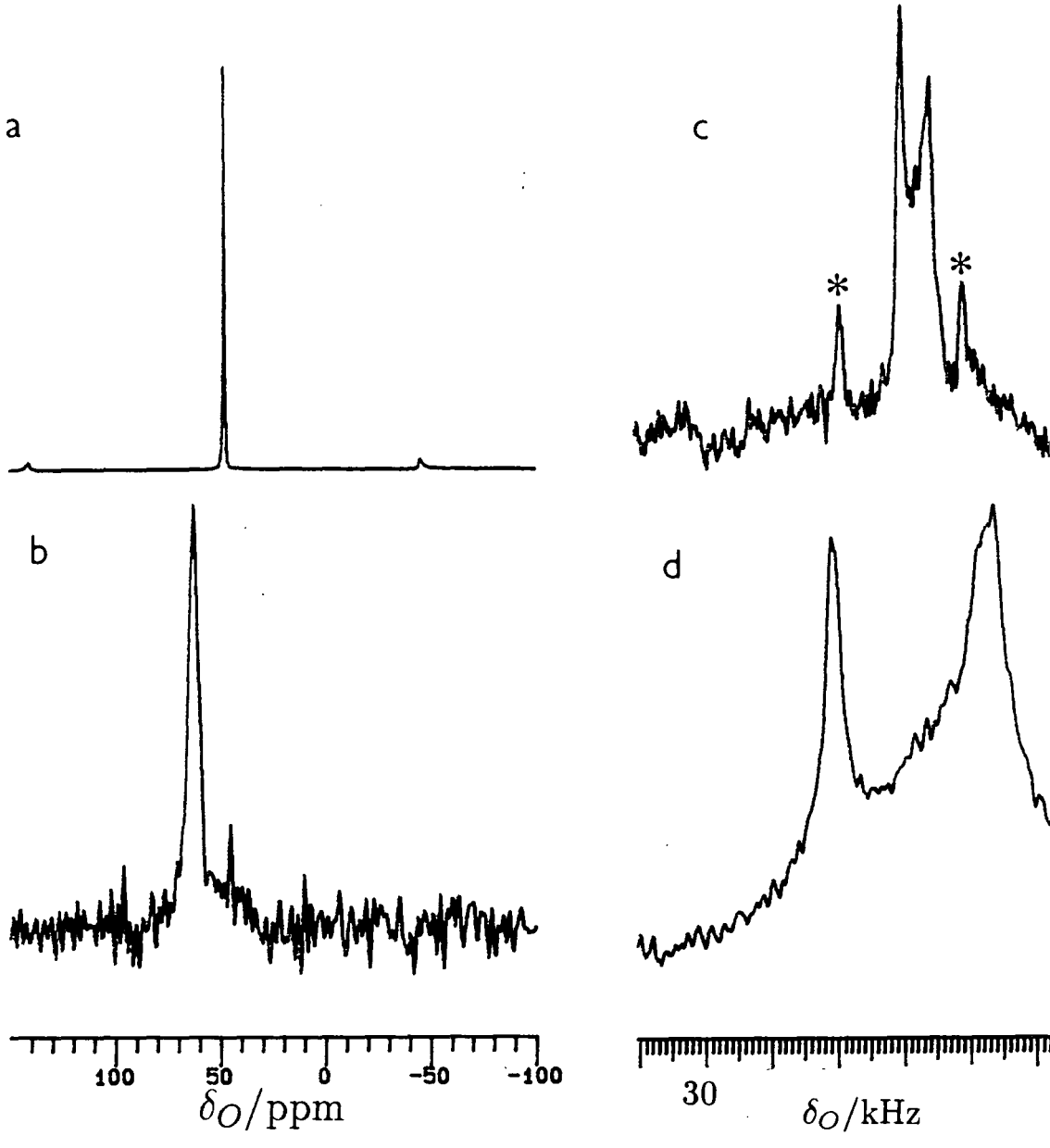

The following method was used: 33 ml (0.0495 mol) of 1.5 M $Mg(C_2H_5)_2$ in Et_2O was syringed into a dried round-bottomed flask in a glove box. The flask was then attached to a dry-nitrogen line and placed in an ice bath. $H_2^{17}O$ (0.97 g, 0.0532 mol) was slowly added over 90 min from a syringe with stirring. The mixture was stirred for a further 16 h at room temperature. The diethyl ether was removed by gently heating the flask in a water bath under flowing nitrogen. The resulting solid (2.48 g) was then heated to 1150^oC for 4 h under flowing nitrogen to remove volatile impurities including magnesium metal, giving 1.84 g of x-ray pure magnesium oxide (0.0457 mol, 92% yield).

A sample of $MgAl_2^{17}O_4$ was also prepared, by sintering $Mg^{17}O$ and Al_2O_3 in stoichiometric proportions at 1400^oC for 3 h in a tungsten element furnace.

5.4.3 ^{17}O NMR of Precursor Oxides

The ^{17}O MAS NMR spectra of $Mg^{17}O$ and $Si^{17}O_2$ have both been reported, and were discussed in Section 3.2.5. The ^{17}O MAS NMR spectrum of $Mg^{17}O$ (Figure 5.4.1) gives a chemical shift of 47.4 ppm, in exact agreement with the result of Turner *et al.*[28] The quadrupole coupling constant in $Mg^{17}O$ can be seen from the linewidth (30 Hz) to be negligible. The linewidth is also a great deal less than that of $H_2^{17}O$ (100 Hz), and thus MgO would make a more suitable reference material for ^{17}O MAS NMR.

The ^{17}O MAS and static NMR spectra of $Si^{17}O_2$ are shown in Figure 5.4.1 together with a simulated spectrum for δ_O=46 ppm, χ_Q=5.6 MHz, η_Q=0.08 in Figure 5.4.3, the literature values for low-cristobalite. The agreement is excellent.

$MgAl_2^{17}O_4$ gives δ_O=62.4 ppm (FWHH=260 Hz), indicating an oxygen environment similar to that in MgO or Al_2O_3. The low FWHH indicates a high degree of site symmetry, as expected from the known spinel structure.

REFERENCES

1. Riley, F. L. *Progress in Nitrogen Ceramics*; Riley, F. L. Ed.; NATO ASI Ser. E; Martinus Nijhoff: The Hague. **65**, 121–133 (1983).
2. Schweir, G. Reference 1; pp 157–166.

Figure 5.4.3 Simulated ^{17}O MAS NMR spectrum of $Si^{17}O_2$

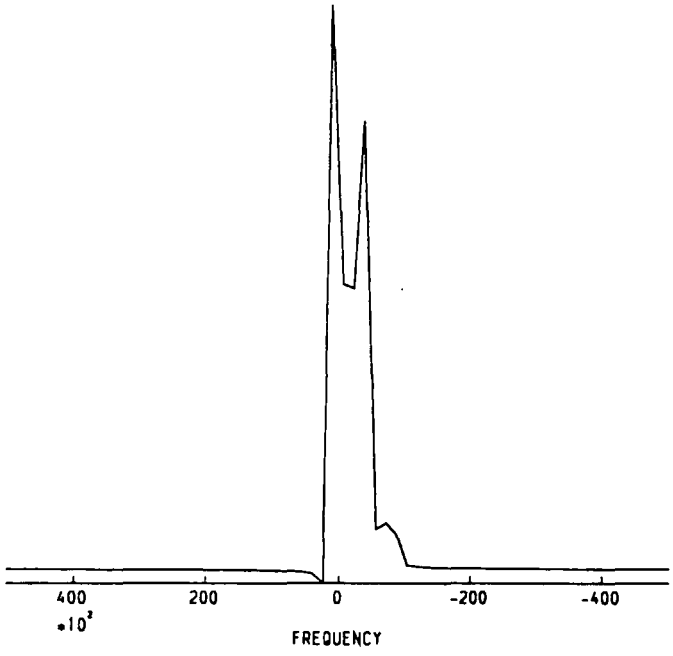

3. Vandeneede, V.; Leriche, A.; Cambier, F.; Pickup, H.; Brook, R. J. *Non-oxide Technical and Engineering Ceramics*; Hampshire, S. Ed.; Elsevier: London, 1986; pp 53–68.

4. Siddiqi, S. A. Ph.D. Thesis, University of Newcastle upon Tyne, 1984.

5. See for example Mazdiyasni, K. S.; Coke, C. M. *J. Am. Ceram. Soc.* **56**, 628–633 (1973).

6. Jennings, H. M. *J. Mater. Sci.* **18**, 951–967 (1983).

7. Rossetti, G. A., Jnr.; Denkewicz, R. P., Jnr. *J. Mater. Sci.* **24**, 3081–3086 (1989).

8. Atkinson, A.; Moulson, A. J.; Roberts, E. W. *J. Am. Ceram. Soc.* **59**, 285–289 (1976).

9. Boyer, S. M.; Moulson, A. J. *J. Mater. Sci.* **13**, 1637–1646 (1978).

10. Hampshire, S. Ph.D. Thesis, University of Newcastle upon Tyne, 1980.

11. Jack, K. H. Reference 1; pp 45–60.

12. Buang, K. Ph.D. Thesis, University of Newcastle upon Tyne, 1979.

13. Schumb, W. C.; Lefevre, R. A. *J. Am. Ceram. Soc.* **76**, 5882 (1954).

14. Idrestedt, I.; Brosset, C. *Acta Chem. Scand.* **18**, 1879–1886 (1964).

15. Dupree, R.; Lewis, M. H.; Leng-Ward, G.; Williams, D. S. *J. Mater. Sci. Lett.* **4**, 393–395 (1985).

16. Apperley, D. Internal Report, University of Durham, October 1987.

17. Marshall, G. L.; Harris, R. K.; Apperley, D.; Yeung, R. *Science of Ceramics* **14**, 347–352 (1987).

18. Carduner, K. R.; Carter, R. O. III; Milberg, M. E.; Crosbie, G. M. *Anal. Chem.* **59**, 2794–2797 (1987).

19. Carduner, K. R.; Carter III, R. O.; Rokosz, M. J.; Peters, C.; Crosbie, G. M.; Stiles, E. D. *Chem. Mater.* **1**, 302–307 (1989).

20. Lednor, P. W.; de Ruiter, R. *Chem. Commun.*, 320–321 (1989).

21. Dupree, R.; Lewis, M. H.; Smith, M. E. *J. Am. Chem. Soc.* **110**, 1083–1087 (1988).

22. Hatfield, G. R.; Carduner, K. R. *J. Mater. Sci.* **24**, 4209–4219 (1989).

23. Grey, C. P.; Dobson, C. M.; Cheetham, A. K.; Jakeman, R. J. B. *J. Am. Chem. Soc.* **111**, 505–511 (1989).

24. Dupree, R.; Lewis, M. H.; Smith, M. E. *J. Am. Chem. Soc.* **111**, 5125–5132 (1989).

25. Harris, R. K.; Leach, M. J.; Thompson, D. P. *Chem. Mater.* **1**, 336–338 (1989).

26. Turner, G. L.; Kirkpatrick, R. J.; Risbud, S. H.; Oldfield, E. *Am. Ceram. Soc. Bull.* **66**, 656–663 (1987).

27. Kato, K.; Inone, Z.; Kijima, K.; Yamane, T.; Kawada, J. *J. Am. Ceram. Soc.* **58**, 90–94 (1975).

28. Turner, G. L.; Chung, S. E.; Oldfield, E. *J. Magn. Reson.* **64**, 316–324 (1985).

29. Abys, J. A.; Barnes, D. M.; Feller, S.; Rouse, G. B.; Risen Jnr, W. M., *Mat. Res. Bull.* **15**, 1581–1587 (1980).

30. Kim, H. -E.; Zinkle, S. J.; Allen, W. R. *J. Am. Ceram. Soc.* **73**, 425–429 (1990).

31. Timken, H. K. C.; Turner, G. L.; Gilson, J. -P.; Welsh, L. B.; Oldfield, E. *J. Am. Chem. Soc.* **108**, 7231–7235 (1986).

32. Yang, S.; Park, K. D.; Oldfield, E. *J. Am. Chem. Soc.* **111**, 7278–7279 (1989).

33. *Comprehensive Organometallic Chemistry*; Wilkinson, G. Ed.; Pergamon: Oxford, UK, 1982. Vol. 1.

Chapter VI

NMR and Crystallographic Studies of Lanthanum and Yttrium Sialons

The Y–Si–Al–O–N and La–Si–Al–O–N systems are notable for the wide range of phases found, and the variety displayed in their structures. This made them ideal for a comprehensive multinuclear magnetic resonance study, which proved successful both in settling points of issue in the structures of many of the phases, and in identifying structural factors which affect NMR spectra of solids.

6.1 Synthesis of Samples

Phase relationships in the Y–Si–O–N and La–Si–O–N systems were discussed in Section 3.1.4. Sample synthesis was by standard methods.[1,2] Samples prepared of high enough purity for NMR study are listed in Table 6.1.1. Weight losses during reaction in these systems were generally found to be negligible (< 5%), except in the case of sample 6.11 (*vide infra*).

Several attempts were made to prepare the lanthanum N–melilite, $La_2Si_3O_3N_4$, reported by Marchand *et al.*,[3] but no evidence for the existence of this phase was found in any of the work described in this Thesis, confirming the findings of Mitomo *et al.*[2] and Smith.[4]

$LaSi_3N_5$ (sample 6.8) was prepared by carbothermal reduction of a 3:2:1 mix of C + α–Si_3N_4 + La_2O_3 at 1600^oC. Small amounts of a second phase, which is probably another lanthanum silicon nitride or a carbonitride were also formed during this reaction, as detected by XRD. $LaSi_3^{15}N_5$ (6.17, 6.18) was prepared by a similar carbothermal reduction of $La_2Si_6O_3^{15}N_8$, although the problem of incomplete reaction was encountered, leading to the presence of unreacted new phase in the product. $LaSi_3N_5$ can also be prepared by direct nitridation of a 2:1 mix of Si_3N_4 + La_2O_3,[5] but the reaction was found to be much slower than the carbothermal reduction. Early attempts to prepare $La_2Si_6O_3N_8$ at 1800^oC were, however always accompanied by $LaSi_3N_5$ formation at the surface of the pellet.

Table 6.1.1a Lanthanum sample preparation

Sample no.	phase	target comp.	mix	furnace	temp/°C	time/h	notes	XRD analysis
6.1	New phase	$La_2Si_6O_3N_8$	D	C	1700	0.5		N(vs); A(tr); β-Si_3N_4(tr)
6.2	N-wollastonite	$LaSiO_2N$	D	C	1550	2.0		W(vs); A(tr)
6.3	N-YAM	$La_4Si_2O_7N_2$	A	C	1550	2.0		Y(vs); W(tr)
6.4	N-apatite	$La_{10}Si_6O_{24}N_2$	D	C	1550	2.0		A
6.5	$La_2Si_2O_7$	$La_2Si_2O_7$	A	M	1500	24.0	1	G-$La_2Si_2O_7$(s); A(m)
6.6	oxide apatite	$La_{9.33}Si_6O_{26}$	A	C	1700	1.5		A
6.7	La_2SiO_5	La_2SiO_5	A	M	1500	24.0	1	X_1-La_2SiO_5(s); A(m)
6.8	$LaSi_3N_5$	La_2O_3+2Si_3N_4+3C	A	C	1600	1.0	2	$LaSi_3N_5$(s); ?(w)
6.9	Al-new phase	$La_2Si_{4.5}Al_{1.5}O_{4.5}N_{6.5}$	D	C	1700	0.5		N
6.10	Al-N-YAM	La_4SiAlO_8N	D	C	1550	2.0		Y(vs); $LaAlO_3$(w)
6.11	La U glass	$La_8Si_{6.7}Al_{9.4}O_{33.5}N_4$	B	G	1650	1.0	1,3	No lines
6.12	La U-phase	$La_3Si_3Al_3O_{12}N_2$	-	V	1200	24.0	4	U(vs); $LaAlO_3$(w)
6.13	La perovskite	$LaAlO_3$	A	W	1450	3.0		$LaAlO_3$
6.14	^{15}N-New phase	$La_2Si_6O_3N_8$	A	C	1550	2.0		N(vs); A(tr); β-Si_3N_4(tr)
6.15	^{15}N-wollastonite	$LaSiO_2N$	A	C	1550	2.0	5	W(s); A(w); Y(tr)
6.16	^{15}N-YAM	$La_4Si_2O_7N_2$	A	C	1550	2.0	5	Y(s); La_2O_3(w); A(w)
6.17	$LaSi_3^{15}N_5$ I	(6.14 + 3C)	A	C	1600	1.0	2	$LaSi_3N_5$(s); N(m)
6.18	$LaSi_3^{15}N_5$ II	(6.17 + C)	A	C	1600	1.3	2	$LaSi_3N_5$(vs); N(vw)
6.19	Al-^{15}N-New	$La_2Si_{4.5}Al_{1.5}O_{4.5}N_{6.5}$	A	C	1700	0.5		N(vs); β-Si_3N_4(w)
6.20	^{17}O-N-wollastonite	$LaSiO_2N$	A	C	1550	2.0		W(s); A(w); N(vw)
6.21	^{17}O-N-YAM	$La_4Si_2O_7N_2$	A	C	1550	2.0		Y(s); W(w); A(vw)
6.22	^{17}O-N-Apatite	$La_{10}Si_6O_{24}N_2$	A	C	1700	1.5		A
6.23	^{17}O-Al-N-YAM	La_4SiAlO_8N	A	C	1550	2.0		Y

Notes. 1: under air; 2: carbothermal reduction; 3:quenched; 4: recrystallised from 6.11; 5: from mixed $Si_2^{15}N_2O$ sample.
N=new, W=Woll., A=apatite, Y=YAM

Table 6.1.1b Yttrium sample preparation

Sample no.	phase	target comp	mix	furnace	Temp/°C	time/h	notes	XRD analysis
6.24	N-apatite	$Y_{10}Si_6O_{24}N_2$	A	C	1700	0.75		A(s); Y(w)
6.25	N-YAM	$Y_4Si_2O_7N_2$	A	C	1750	0.33		Y
6.26	$Y_6Si_3N_{10}$	$Y_2O_3+2Si_3N_4+3C$	A	C	1800	1.0	1	$Y_6Si_3N_{10}$(s); M(m); SiC(m)
6.27	N-YAM	$Y_2La_2Si_2O_7N_2$	A	C	1750	0.5		Y(s); A(w)
6.28	Al-N-YAM	Y_4SiAlO_8N	A	C	1700	0.5		Y(vs); $Y_4Al_2O_9$(w); AlN(tr)
6.29	^{15}N-YAM	$Y_4Si_2O_7^{15}N_2$	A	C	1700	0.5		Y(vs); ?(w)
6.30	^{17}O-N-YAM	$Y_4Si_2^{17}O_7N_2$	A	C	1550	2.0		Y

Note. 1: Carbothermal reduction. Y=YAM, A=Apatite, M=melilite.

Table 6.1.1c Other samples for Chapter 6 (all XRD pure).

6.31	6-layer La N-Wollastonite	$LaSiO_2N$
6.32	Y N-wollastonite	$YSiO_2N$
6.33	Y Al-N-Wollastonite	Y_2SiAlO_5N
6.34	Pyroxene	$YMgSi_2O_5N$

Figure 6.1.1 The La–Si–O–N system at $1550^{o}C$.

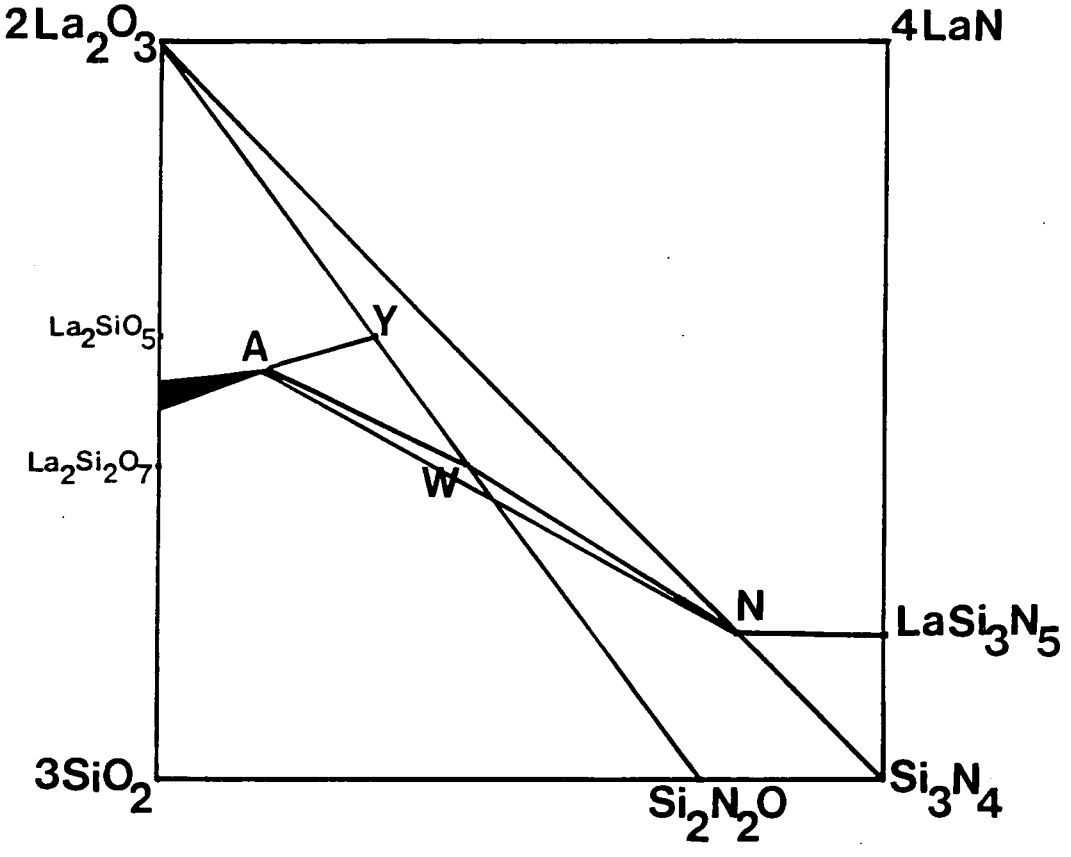

Attempts were made to prepare the yttrium silicon nitrides by carbothermal reduction of Y_2O_3/α–Si_3N_4 mixes. $Y_6Si_3N_{10}$ (sample 6.25) was successfully prepared at 1800^oC, but the other nitrides could not be prepared by this method. Samples containing all three yttrium silicon nitrides were prepared by sintering YN + α–Si_3N_4 mixes, but the sluggishness of the reaction between these two materials, caused by the lack of a liquid phase, meant that acceptably pure samples could not be prepared.

The $LaSiO_2N$ phase prepared (sample 6.2) was of the disordered type. A 6–layer sample prepared by Dr. P. Korgul at Newcastle (sample 6.31) was included for comparison.

The range of compositions of lanthanum apatite was found to be large from measurements of unit cell dimensions of samples prepared in this and other studies (Table 6.1.2). The apatite phase is extremely stable. Attempts to prepare the other lanthanum silicates were only successful in a non-reducing atmosphere, such as air. In a reducing atmosphere, only the apatite was formed. Even in air, significant quantities of apatite were always formed.

The phase diagram of the La–Si–O–N system, including results obtained in this study, is shown in Figure 6.1.1. Cell dimensions for many of these phases are given in Tables 6.1.2 and 6.1.3.

Attempts were made to prepare aluminium substituted lanthanum N–melilite, new phase, N–wollastonite, N–YAM and N–apatite, but only in the case of new phase (sample 6.9) and N–YAM (6.10) could significant amounts of Al be incorporated. A sample of yttrium N–YAM (6.28) containing aluminium was also prepared, and a sample of Y_2SiAlO_5N (6.33) was supplied by Dr. D. P. Thompson.

Preparation of lanthanum U–phase glass (sample 6.11) was accompanied by a substantial weight loss (20%), and this will be discussed further in Section 6.2.2. No further weight loss accompanied recrystallisation of the glass.

Figure 6.2.1 ^{29}Si MAS NMR spectra of

(a) Mixed Y-Si-N sample SF=59.6 MHz; PA=13^{o}; NT=940; RD=120 s; SR=2.55 kHz; AF=0.01 s

(b) $Y_6Si_3N_{10}$ (sample 6.26) SF=59.6 MHz; PA=90^{o}; NT=128; RD=120 s; SR=3.45 kHz; AF=0.01 s

(c) $Y_4Si_2O_7N_2$ (sample 6.25) SF=59.6 MHz; PA=23^{o}; NT=170; RD=120 s; SR=3.05 kHz; AF=0.01 s

(d) $YSiO_2N$ (sample 6.32) SF=59.6 MHz; PA=90^{o}; NT=459; RD=120 s; SR=3.30 kHz; AF=0.01 s

(e) Y_2SiAlO_5N (sample 6.33) SF=59.6 MHz; PA=23^{o}; NT=514; RD=120 s; SR=3.38 kHz; AF=0.01 s

(f) $Y_{10}Si_6O_{24}N_2$ (sample 6.24) SF=59.6 MHz; PA=18^{o}; NT=90; RD=120 s; SR=3.08 kHz; AF=0.01 s

n=$Y_6Si_3N_{10}$, o=YSi_3N_5, p=β-Si_3N_4, q=$Y_2Si_3N_6$, r=SiC, s=$Y_2Si_3O_3N_4$.

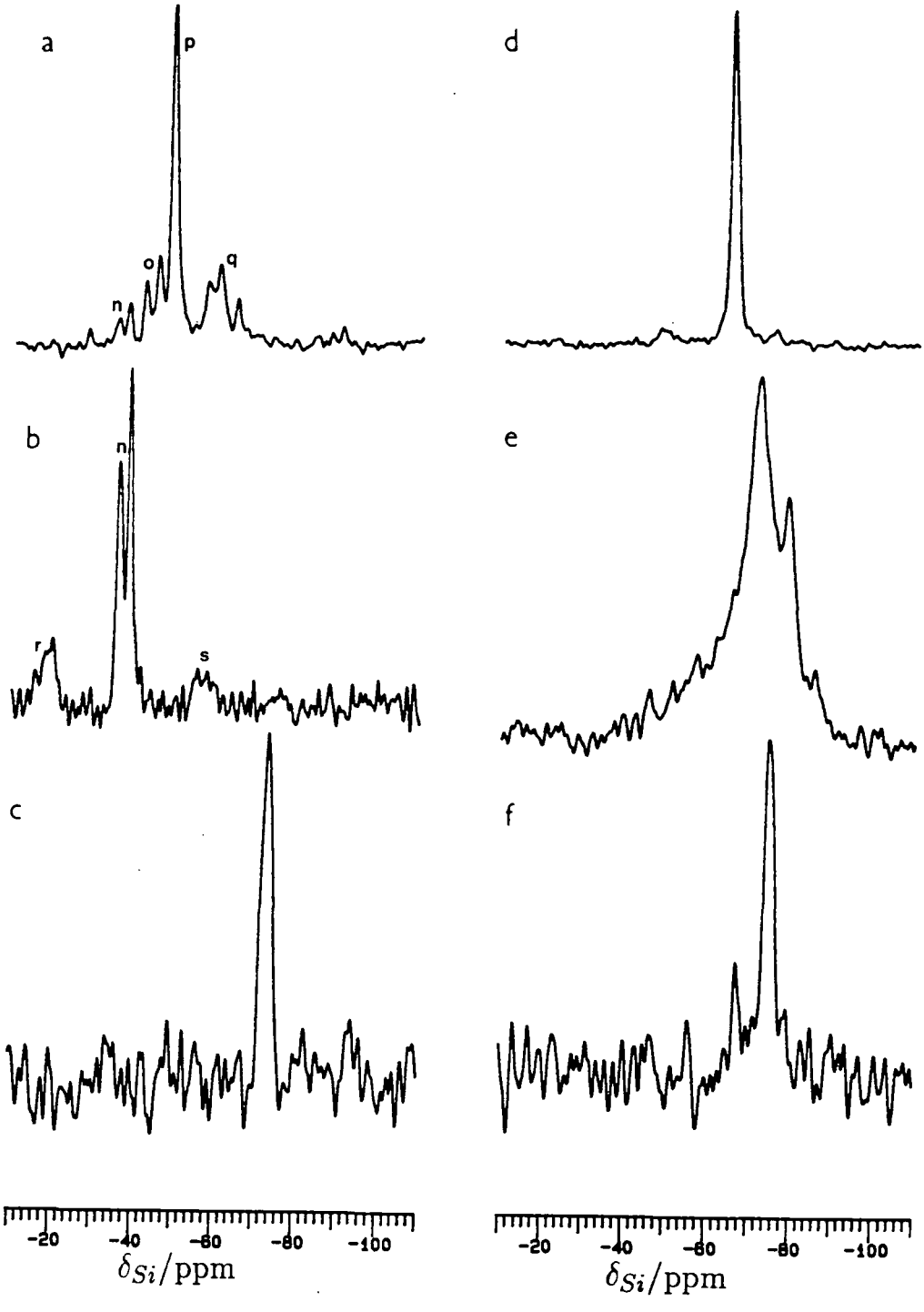

Table 6.1.2 Unit cell dimensions of lanthanum apatites (hexagonal cells).

Phase	a/Å	c/Å
N–apatite (6.4)	9.701	7.255
Oxide apatite (6.6)	9.711	7.211
N–apatite (Ref. 2)	9.721	7.258
Oxide apatite (Ref. 6)	9.713	7.194

Table 6.1.3 Unit cell dimensions of La–Si–Al–O–N phases

Sample	phase	Cell symmetry	dimensions
6.2	New	Monoclinic	$a = 18.37$ Å; $b = 4.865$ Å; $c = 7.890$ Å; $\beta = 117.0^o$
			$a = 17.97$ Å; $b = 4.865$ Å; $c = 7.889$ Å; $\beta = 114.4^o$
6.3	N–YAM	Monoclinic	$a = 8.035$ Å; $b = 10.999$ Å; $c = 11.14$ Å; $\beta = 111.4^o$
6.8	$LaSi_3N_5$	Orthorhombic	$a = 7.813$ Å; $b = 11.162$ Å; $c = 4.797$ Å
6.12	U–phase	Hexagonal	$a = 8.073$ Å; $c = 4.897$ Å

6.2 Silicon–29 Studies

6.2.1 Yttrium Sialons

The silicon n.n. coordination environment in these phases varies from $[SiN_4]$ to $[SiO_4]$, and thus Dupree *et al.*[7] considered the Y–Si–O–N system an excellent choice for a ^{29}Si NMR study, with the aim of establishing approximate shift ranges for the various environments. Their results are summarised in Table 6.2.1, together with the ^{29}Si NMR data on the phases prepared for this study. Carduner *et al.*[8] have recently confirmed many of the findings summarised in this Table; their results are not given.

Nitrides

NMR data on YSi_3N_5 and $Y_2Si_3N_6$ were collected from an impure sample prepared by sintering a pellet of $1YN + 1\alpha$–Si_3N_4 at 1750^oC for 1 hour, and the spectrum was assigned by comparison with the work of the Warwick group,[4,7] see Figure 6.2.1. The structures of all three Y–Si–N phases are unknown, but the

Table 6.2.1 ^{29}Si data on yttrium sialons

Phase	This work				other studies			
	sample	δ_{Si}/ppm	FWHH/Hz	intensity	δ_{Si}/ppm	FWHH/Hz	intensity	referenc
N–melilite	(a)	−56.6	330		−56.7	430		7
N–woll.	6.32	−65.0	130		−65.3	400		7
N–YAM	6.25	−73.6	200		−74.4	320		7
N–apatite	6.24	−67.3	200	1	−67.5	250	(b)	7
		−75.0	160	3	−74.8	210		
YSi_3N_5	(a)	−41.9			−42.3	140	(b)	7
		−45.1			−45.5	140	(b)	
$Y_2Si_3N_6$	(a)	−57.3			−58.3	150	2	4
		−60.2			−60.6	150	2	
		−64.8			−65.3	150	1	
$Y_6Si_3N_{10}$	6.26	−36.0	105	1	−35.3	200	1	4
		−38.5	90	1	−37.7	200	1	
$Y_2La_2Si_2O_7N_2$	6.27	−78.6	480					
Al–N–YAM	6.28	−73.4	250					
Al–N–woll.	6.33	−72.3	560		−72.2	430		
		−79.0						
$YMgSi_2O_5N$	6.34	−71.0	400	3				
		−84.0	300	1				

(a) data taken from impure samples. (b) Not reported.

Figure 6.2.2 Possible atomic arrangements in Y_2SiAlO_5N.

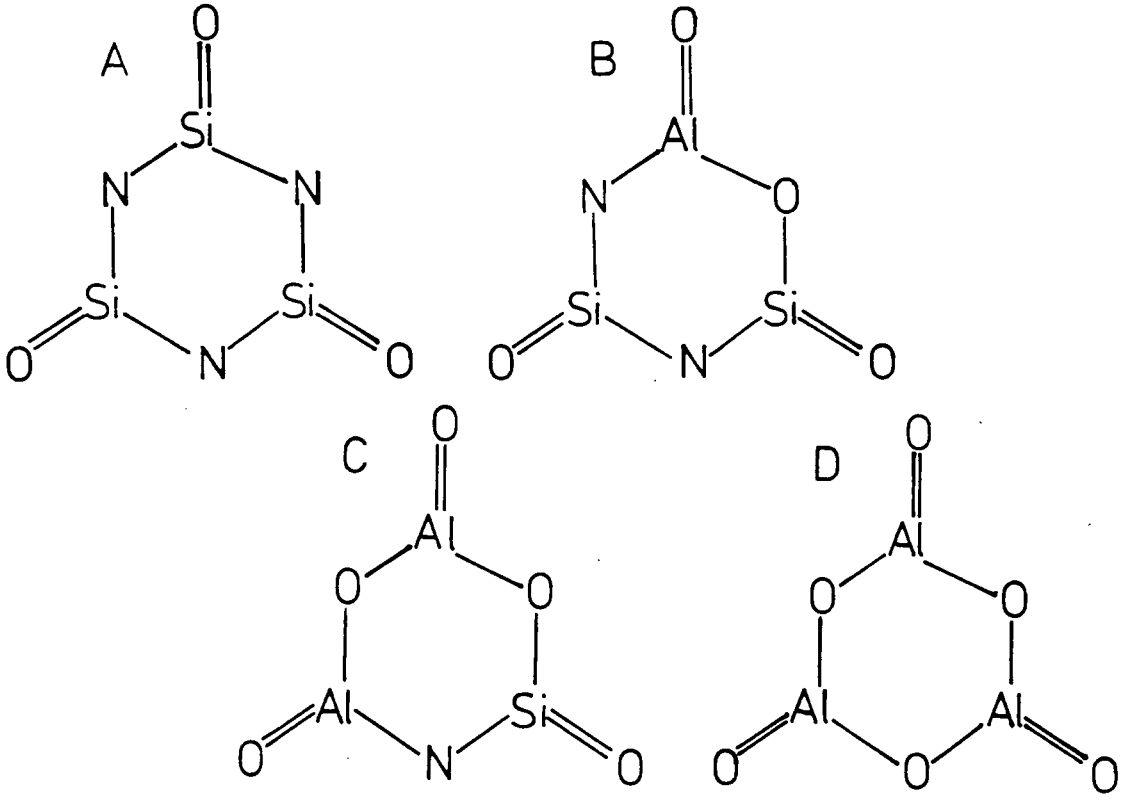

Figure 6.2.3 ^{29}Si MAS NMR spectrum of $YMgSi_2O_5N$ (sample 6.34)
SF=59.6 MHz; PA=90^o; NT=1700; RD=30 s; SR=3.30 kHz; AF=0.01 s

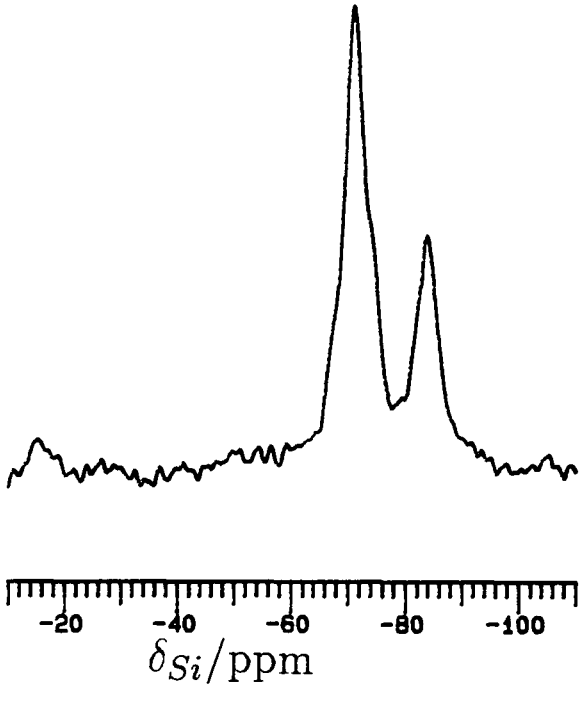

silicon environments can be assumed to be [SiN_4] throughout. With the exception of $Y_2Si_3N_6$, all of the δ_{Si} values lie within ± 10 ppm of those observed from [SiN_4] environments in silicon nitrides. The spectra of YSi_3N_5 and $Y_6Si_3N_{10}$ closely resemble that of α–Si_3N_4 in that two narrow resonances of approximately equal intensity and similar but not identical chemical shift are observed, and it seems probable that this is caused by a similar crystallographic inequivalence in each case. The spectrum of $Y_2Si_3N_6$ in many ways resembles that of $LaSi_3N_5$, which will be discussed below.

Oxynitrides

The NMR results obtained on the Y–Si–O–N phases (Table 6.2.1 and Figure 6.2.1) agree well with those of Dupree *et al.*,[7] although in most cases, observed linewidths were smaller in this study. This could be because of more homogeneous samples and/or improved NMR acquisition conditions. The difference is particularly noticable in the case of N–wollastonite.

The structure of N–melilite was discussed in Section 3.1.4. The NMR spectrum is consistent with only one O/N ordering scheme if n.n. coordination environment is considered the most important factor in determining δ_{Si}.[7] In this scheme, all silicon is present in [SiO_2N_2] environments, with Q^3 and Q^4 n.n.n. arrangements, which cannot be resolved in the NMR. The chemical shift (-56.7 ppm) is slightly more positive than from $YSiO_2N$, which contains a single [SiO_2N_2]–Q^2 environment.

The atomic arrangement in the [$Si_2O_5N_2$] unit in N–YAM cannot be determined by XRD, but PSCR predicts that N should occupy the bridging site. This arrangement would give rise to two distinct silicon environments: [SiO_3N] and [SiO_2N_2], which would be expected to give rise to two peaks in the ^{29}Si NMR. The fact that only one peak is observed implies that nitrogen occupies only the terminal sites (see Figure 3.1.10).[7]

Peaks from both [SiO_3N] and [SiO_4] environments can be resolved in the ^{29}Si NMR spectrum of N–apatite. The approximately 1:3 ratio in peak areas corresponds to a composition $Y_{10}Si_6O_{24.75}N_{1.5}$ if peak areas are assumed quantitative, close to the accepted composition $Y_{10}Si_6O_{24}N_2$.

Figure 6.2.4 (a) and (b) Possible arrangements of the atoms in the chains of $YMgSi_2O_5N$.

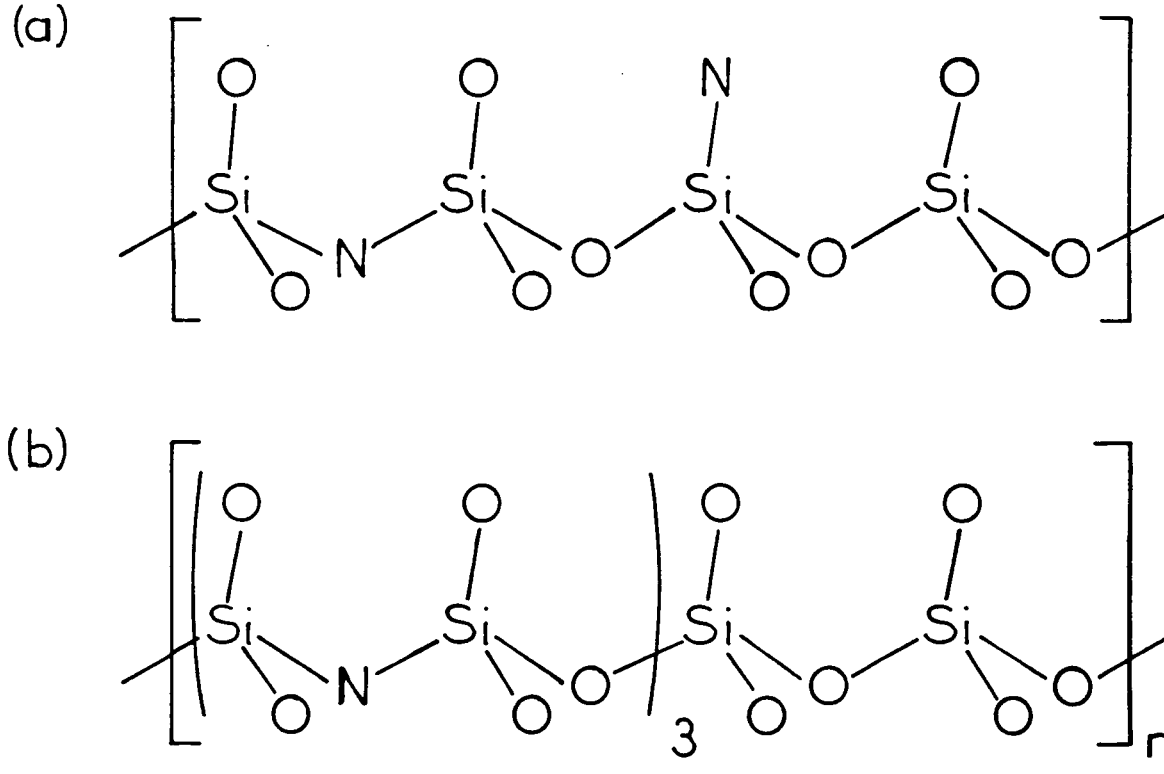

The spectra of $YSiO_2N$ and Y_2SiAlO_5N (Figure 6.2.1) show surprising differences. The single Si environment in $YSiO_2N$ ($[SiO_2N_2]$-Q^2) can be replaced with four different silicon environments in Y_2SiAlO_5N, if random Si/Al substitution occurs, and nitrogen is assumed to occupy bridging sites, and remain bonded to silicon (Figure 6.2.2). The spectrum of Y_2SiAlO_5N seems to be made up of two peaks, with shifts of -72.3 and -79.0 ppm, plus a broad underlying peak, assigned to unrecrystallised glass. From peak area data alone, it would seem likely that the peak at -72.3 ppm is due to $[SiO_2N_2]$ environments (A + B), and that at -79.0 ppm to $[SiO_3N]$ environments (B + C), but what causes the change in δ_{Si} between $[SiO_2N_2]$ environments in $YSiO_2N$ and Y_2SiAlO_5N is not clear.

In contrast, the spectra of N-YAM and Al-N-YAM are very similar. It seems unlikely that the formula of the latter phase is the target (Y_4SiAlO_8N) because $Y_4Al_2O_9$ and AlN were detected in the sample by powder XRD, indicating that the N-YAM phase had a Si/Al ratio of greater than one. The increase in linewidth on incorporation of Al is much less than in the corresponding lanthanum phase (Section 6.2.2), in agreement with this conclusion.

The phase $YMgSi_2O_5N$ is isostructural with the mineral pyroxene, and consists of chains of approximate composition $[Si_2O_5N]$, plus discrete Y^{3+} and Mg^{2+} ions. The ^{29}Si NMR spectrum (Figure 6.2.3) demonstrates the existence of two silicon environments, presumably $[SiO_3N]$-Q^2 and $[SiO_4]$-Q^2, in the approximate ratio 3:1 (note that the spectrum was acquired using a short RD). The chemical shifts compare with δ_{Si}=-82.0 ppm for a non-nitrogen containing pyroxene phase[9] ($MgSiO_3$), in which Si is in an $[SiO_4]$-Q^2 environment, close to the -84 ppm in $YMgSi_2O_5N$.

The observed peak ratio is consistent with two arrangements of Si, O and N in the pyroxene chain if assumed quantitative. In the first, N occupies both bridging and terminal sites (Figure 6.2.4a) alternately, to give a composition of exactly $YMgSi_2O_5N$. In the second, N is assumed to occupy only bridging sites (Figure 6.2.4b) to give a composition $Y_3Mg_5Si_8O_{21}N_3$, very close to the accepted composition.

Figure 6.2.5 ^{29}Si MAS NMR spectra of

(a) $La_2Si_6O_3N_8$ (sample 6.1) SF=59.6 MHz: PA=23^o; NT=54; RD=900 s; SR=3.34 kHz; AF=0.01 s

(b) $LaSi_3N_5$ (sample 6.2) SF=59.6 MHz: PA=23^o; NT=70: RD=900 s; SR=3.31 kHz; AF=0.01 s

(c) $LaSiO_2N$ (sample 6.3) SF=59.6 MHz: PA=90^o; NT=508: RD=120 s; SR=3.22 kHz; AF=0.01 s

(d) $LaSiO_2N$ (sample 6.31) SF=59.6 MHz: PA=90^o; NT=28: RD=120 s; SR=3.18 kHz; AF=0.01 s

(e) $La_4Si_2O_7N_2$ (sample 6.3) SF=59.6 MHz: PA=90^o; NT=200; RD=120 s; SR=2.70 kHz; AF=0.01 s

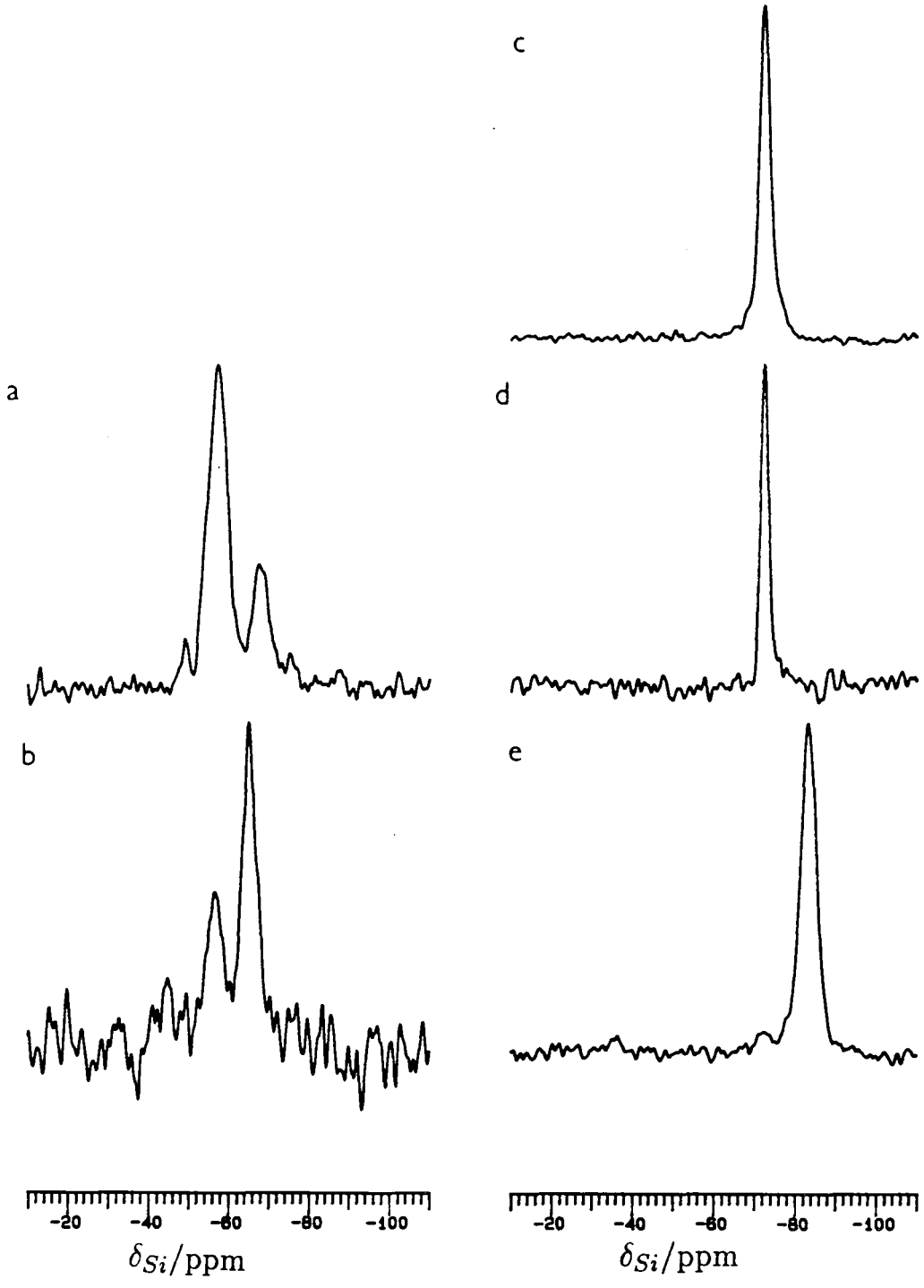

6.2.2 Lanthanum Sialons

La–Si–O–N Phases

Silicon–29 NMR data obtained from samples prepared in this study are listed in Table 6.2.2, together with the results of other recent studies. The results presented in this Section on the La–Si–O–N system were published simultaneously[10] with those of Dupree *et al.*[11]

There has been debate over whether the less intense peaks in the spectra of $LaSi_3N_5$ and new phase (Figure 6.2.5) are due to cross-contamination: $LaSi_3N_5$ in new phase and *vice versa*. Cross-contamination would not be unexpected because the two phases have identical La/Si ratios. Dupree *et al.*[11] proposed that both phases give rise to a single peak, but XRD data obtained in the course of this work (Table 6.1.1) demonstrate almost conclusively that the sample of new phase (6.1) contains no $LaSi_3N_5$, and only traces of other impurities; and that the sample of $LaSi_3N_5$ (6.8), whilst containing significant amounts of an unidentified impurity, contains no new phase. Both phases contain significant quantities of lanthanum, and would therefore be expected to give very intense diffraction patterns. It is possible from the spectrum of $LaSi_3N_5$ in Figure 6.2.5 alone that the peak at -56.7 ppm is due to the impurity phase, but ^{29}Si spectra of other, less pure samples of $LaSi_3N_5$ discount this possibility. The peaks in the spectrum of sample 6.8 at -46 and -72 ppm are assigned to impurities. A recent report[12] of the spectrum of $LaSi_3N_5$ also shows two peaks, in a similar ratio to that observed in this study (Figure 6.2.6).

The structure of $LaSi_3N_5$ was discussed in Section 3.1.4. Three silicon environments: $[SiN_4]$-Q^5, Q^6 and Q^7 were identified from incomplete crystallographic data. Clearly, two environments give rise to the more intense peak, and the third to the less intense peak. The explanation for this distribution, and the fact that the observed chemical shifts are so much more negative than normally observed for $[SiN_4]$ coordination is not obvious. In the structure, however, many of the nitrogen atoms are coordinated to only two silicon atoms as well as lanthanum, and this must have a significant effect on δ_{Si}. The effect is not a simple one: if it were, three approximately evenly spaced peaks from the three environments might be expected. Hatfield and Carduner[12] have proposed that the lanthanum atoms

Figure 6.2.6 ^{29}Si MAS NMR spectrum of $LaSi_3N_5$ (from Reference 12)

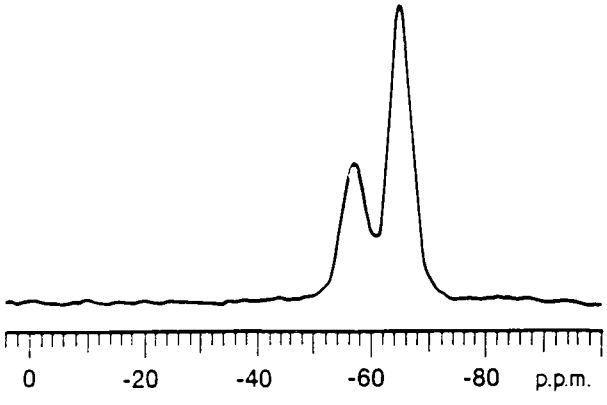

Table 6.2.2 ^{29}Si NMR data on lanthanum sialons

Phase	this work				other studies			
	Sample	δ_{Si}/ppm	FWHH/Hz	intensity	δ_{Si}/ppm	FWHH/Hz	intensity	referen
New	6.1	−57.3	330	3	−56.5	350		11
		−68.2	260	1				
N-woll.	6.2	−72.7	160		−72.4	160		11
	6.31	−72.5	135					
N-YAM	6.3	−83.8	250		−84.2	220		11
N-apatite	6.4	−77.9	290		−77.7	200		11
$La_2Si_2O_7$	6.5	−83.8	200		−82.6	230		11 (a)
					−84,7	280		11 (b)
Oxide apatite	6.6	−78.4	300		−77.7	200		11
La_2SiO_5	6.7	−83.5	200					
$LaSi_3N_5$	6.8	−56.7	330	1	−64.6	120		11
		−65.0	250	2	−56.5		1	12
					−64.5		2	
Al-new	6.9	−56.1	600	2.5				
		−67.1	530	1				
Al-N-YAM (c)	6.10	−80.8	345	1				
		−85.6	230	1				
U-phase glass	6.11	−70						
		−81						
U-phase	6.12	−68.1	170	2.5	−65.9			13
		−75.6	150	1				

(a) h form. (b) l form. (c) data obtained by spectral deconvolution

Figure 6.2.7 ^{29}Si MAS NMR spectra of

(a) $La_2Si_2O_7$ (sample 6.5) SF=59.6 MHz; PA=90^o; NT=156; RD=120 s; SR=3.70 kHz; AF=0.01 s

(b) La_2SiO_5 (sample 6.7) SF=59.6 MHz; PA=90^o; NT=484; RD=120 s; SR=2.90 kHz; AF=0.01 s

(c) $La_{10}Si_6O_{24}N_2$ (sample 6.4) SF=59.6 MHz; PA=90^o; NT=250; RD=120 s; SR=2.75 kHz; AF=0.01 s

(d) $La_{9.33}Si_6O_{26}$ (sample 6.6) SF=59.6 MHz; PA=90^o; NT=424; RD=120 s; SR=2.80 kHz; AF=0.01 s

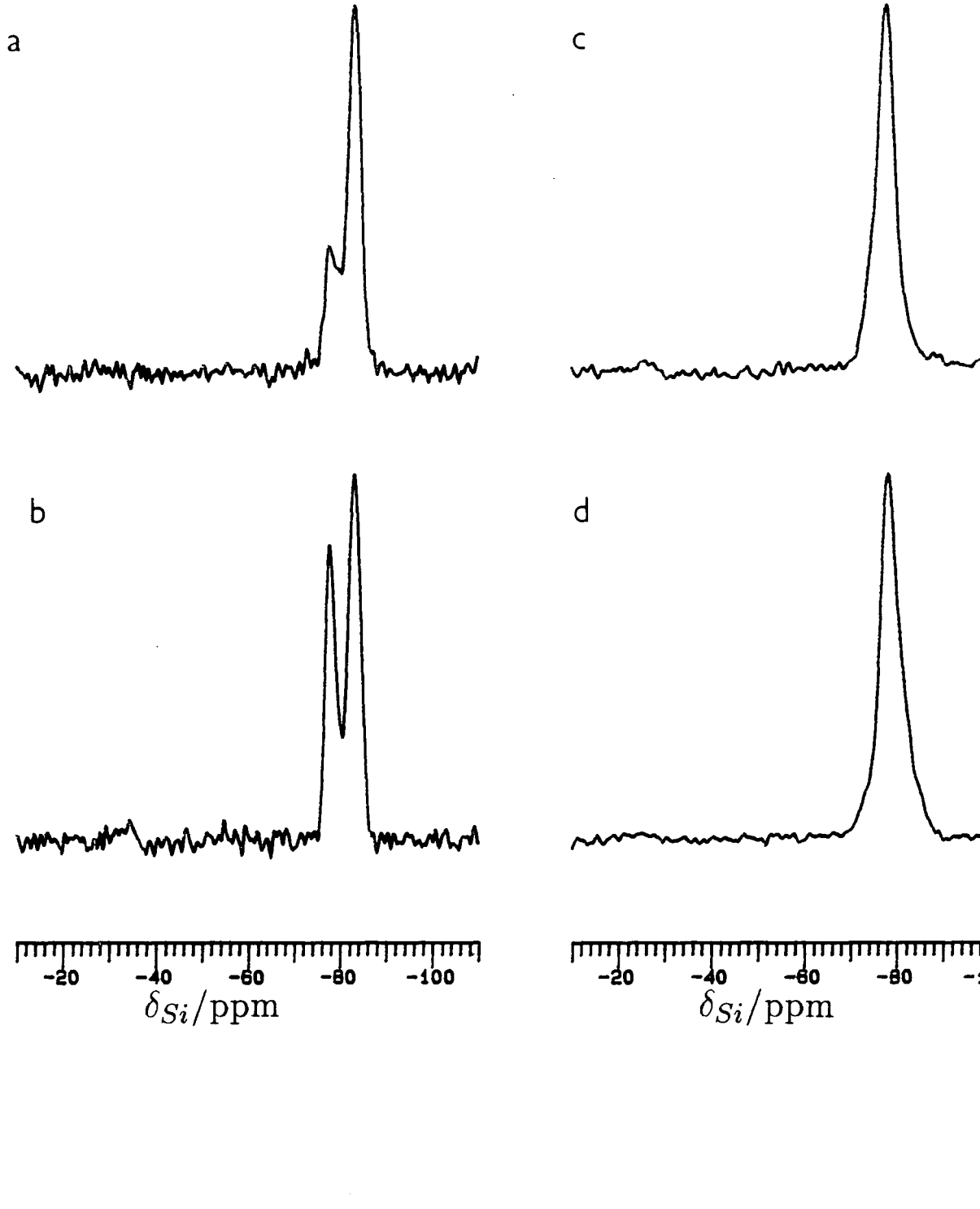

themselves affect δ_{Si}. It is indeed clear from Figure 3.1.8 that Si(2) and Si(3) are coordinated to four La, and Si(1) to only three La. No such cation effect has been noted in minerals.

In the light of the spectrum of $LaSi_3N_5$, it is of interest to reconsider the spectra of the three Y–Si–N phases. The spectrum of $Y_2Si_3N_6$ is similar to that of $LaSi_3N_5$, and the presence of $[NSi_2]$ links can be postulated; whereas the other two phases give spectra similar to α–Si_3N_4, and it seems likely that in these phases, only $[NSi_3]$ coordination occurs. It is possible that the cation effects in ^{29}Si spectra are large only in cases where nitrogen is coordinated directly to the cation.

The spectrum of new phase indicates that the phase contain two distinct silicon environments, present in a 3:1 ratio, or four environments, three of which give coincident peaks.

The two N–wollastonite phases (sample 6.2 and 6.31) give essentially identical ^{29}Si spectra (Figure 6.2.5), with δ_{Si}=−72.6 ppm, corresponding to an $[SiO_2N_2]$-Q^2 environment. The effect of differences in the stacking of layers in the structure is thus found to be slight, with a small increase in FWHH in going from the 6–layer (6.31) to the disordered (6.2) sample.

The N–YAM phase (6.3) gives a single peak (Figure 6.2.5) with δ_{Si}=−83.8ppm, indicating that, as in the yttrium N–YAM, nitrogen occupies terminal sites in the disilicate unit, in violation of PSCR. The chemical shift is identical to that observed from $La_2Si_2O_7$, in which the structural unit is also a disilicate group, in which, of course, no nitrogen is present. This implies that the Si–O–Si bond angle bridging the disilicate group is significantly greater in the N–YAM than in $La_2Si_2O_7$ (neither bond angle has been determined crystallographically), to compensate for the expected positive shift due to coordination to nitrogen.

The apatite phases (6.4 and 6.6) give indistinguishable spectra (Figure 6.2.7), despite their different compositions. No evidence was seen in the spectrum of N–apatite for a second peak due to $[SiO_3N]$ coordination, in contrast to the yttrium N–apatite. Dupree *et al.*[11] report a shoulder on the main peak from La N–apatite, which is indeed visible in their published spectrum, but no such shoulder was observed in this study. This must be because of variations in the precise composition

Figure 6.2.8 ^{29}Si MAS NMR spectra of

(a) $La_2Si_{4.5}Al_{1.5}O_{4.5}N_{6.5}$ (sample 6.9) SF=59.6 MHz; PA=18^o; NT=410; RD=120 s; SR=3.09 kHz; AF=0.01 s

(b) La_4SiAlO_8N (sample 6.10) SF=59.6 MHz; PA=18^o; NT=528; RD=120 s; SR=3.60 kHz; AF=0.01 s

(c) La U-phase (sample 6.12) SF=59.6 MHz; PA=27^o; NT=222; RD=300 s; SR=3.24 kHz; AF=0.01 s

(d) La U glass (sample 6.11) SF=59.6 MHz; PA=27^o; NT=140; RD=300 s; SR=2.73 kHz; AF=0.01 s

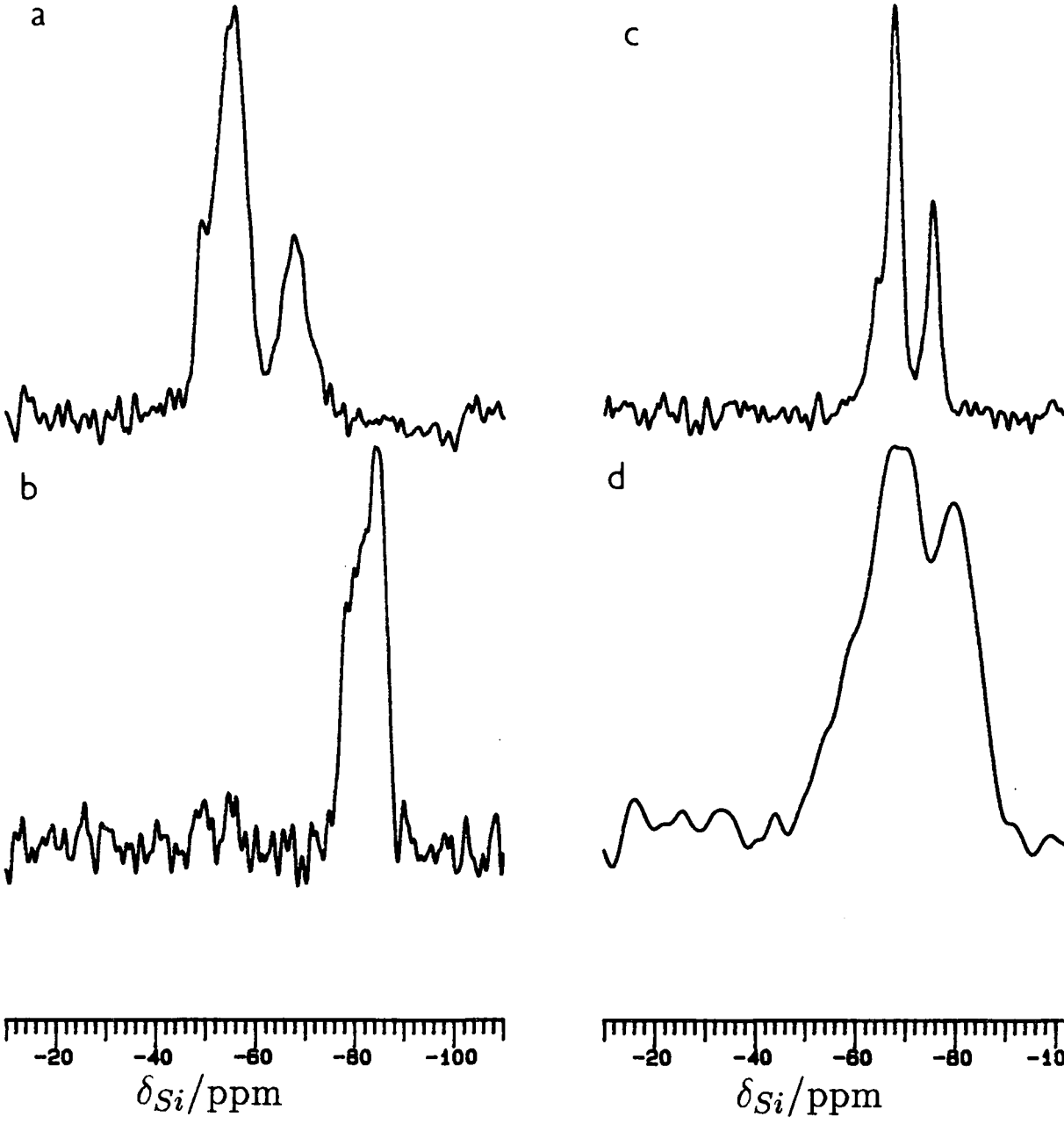

of the phase, as indicated from measurements of the unit cell dimensions.

The spectra of La_2SiO_5 and $La_2Si_2O_7$ (Figure 6.2.7) show peaks in positions typical[14] of $[SiO_4]$–Q^0 and $[SiO_4]$–Q^1 coordination respectively.

Aluminium containing phases

The ^{29}Si spectra of the aluminium containing phases are shown in Figure 6.2.8. The spectrum of Al–new phase is complex and difficult to interpret. Both peaks are now clearly composite: splitting is caused by isomorphous substitution of Al for Si. The intensity ratio of the peaks is approximately the same as for the non-aluminium new phase, implying that substitution of Al is occurring on all of the possible sites in a random or pseudo-random manner. Surprisingly, there is no shift in peak positions to negative δ_{Si}, as expected from the increased oxygen content of the phase. The same lack of shift will be seen in β'–sialons, and will be discussed further in Chapter 8. The high frequency shoulder on the -56.1 ppm peak is due to a small quantity of β–Si_3N_4 in the sample. The spectrum will be further discussed in Section 6.7.

The spectrum of Al–N–YAM, in contrast to that of the yttrium analogue, clearly shows the effect of Al substitution. The peak in the ^{29}Si spectrum of the phase is composite, and can be deconvoluted to give two peaks of approximately equal intensity. The two peaks correspond to Si in $[Si_2O_5N_2]$ and $[SiAlO_6N]$ disilicate units.

The spectrum of La U–phase reported in this Thesis shows the presence of two distinct silicon environments. Fernie *et al.*[13] report only one peak for this phase, but no experimental or other details were given. The structure of U–phase was discussed in Section 3.1.4. Two distinct Si environments were identified in the crystal structure determination, but the picture is complicated by the fact that O/N and Si/Al orderings have not been determined. Two explanations of the ^{29}Si spectrum are possible:

(i) The two peaks result from the two crystallographic environments. The 2(d) sites are in a more La/O rich environment, and it would thus be predicted that they would give rise to a more negative chemical shift, and it would also be expected that these sites would be preferentially occupied by Al. The observed 2.5:1 ratio

Figure 6.2.9 Simulated ^{29}Si MAS NMR spectrum of a glass of composition $La_8Si_{6.7}Al_{9.4}O_{33.5}N_4$.

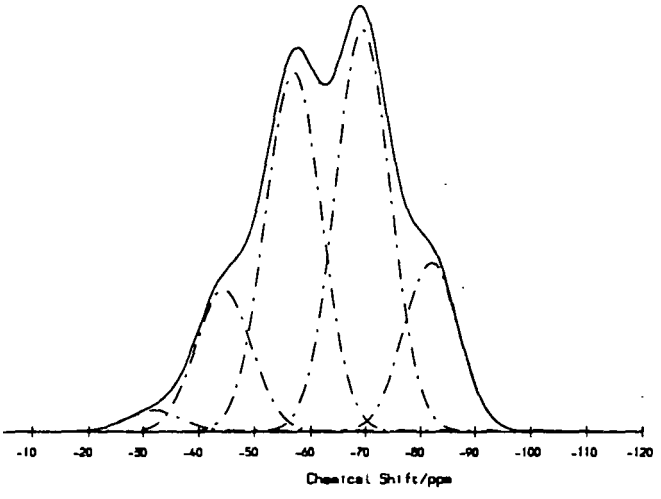

would then imply that the 2(d) sites are occupied 45% by Si and 55% by Al, and the 3(f) sites 30% by Al and 70% by Si, assuming an overall composition $La_3Si_3Al_3O_{12}N_2$. This explanation ignores the specific effect of O/N atoms in the Si n.n. coordination environment, by analogy to new phase (Section 6.7).

(ii) The two peaks result from $[SiO_3N]$ and $[SiO_4]$ n.n. coordination environments, with the effect of crystallographic environment being neglected. If the N atoms are assumed to occupy only the (O,N)2 sites, the tetrahedral bridging sites, then a peak ratio of at least 2:1 would be expected, depending on the distribution of (Si/Al) atoms on the lattice sites. If exclusively Al is assumed to occupy the 2(d) sites, then a peak ratio of 2:1 would be observed under quantitative conditions.

The two explanations can be combined: if all of the Si atoms are present in $[SiO_3N]$ environments, then half of the N atoms must bridge 2(d) and 3(f) centred tetrahedra, both of which are occupied by Si atoms. The third Si atom would then occupy a second 3(f) site, coordinated to a N atom which is also bonded to an Al atom. This would lead to a predicted 2:1 peak ratio. If, however, the Si content of the phase is decreased to $x = 0.5$, then the peak ratio should drop to 3:2.

It is difficult to determine which of these explanations is correct: the chemical shift difference between the two peaks (7 ppm) is characteristic both of changes in crystallographic environment (e.g. new phase) and n.n. environment (e.g. Y N–apatite), but the structure is clearly related to that of new phase, so similar factors might be expected to influence δ_{Si} in the two phases. The position is complicated by the fact that the exact composition of the phase is not known.

The spectrum of the glass from which the U–phase was crystallised is similar to those obtained from Y–Si–Al–O–N and Mg–Si–Al–O–N glasses.[15–17] The results of these studies suggest that Si in $[SiO_4]$ environments resonates at -82 ppm, in $[SiO_3N]$ at -69.5 ppm and in $[SiO_2N_2]$ at -57 ppm, and it is clear from this spectrum that all three environments are present in the glass. The large weight loss found in preparing this glass ($\sim$ 20%) is consistent with the apparent low nitrogen content of the glass. The simulated spectrum of a glass of the starting composition using the binomial model of Aujla *et al.*,[16] and a similar distribution of N to that found in Mg and Y glasses[17] is shown in Figure 6.2.9. Comparison

Figure 6.2.10 δ_{Si} against environment in (Y/La)–Si–Al–O–N ceramics
1=$Y_6Si_3N_{10}$, 2=YSi_3N_5, 3=Si_3N_4, 4=$Y_2Si_3N_6$, 5=$LaSi_3N_5$, 6=$La_2Si_6O_3N_8$, 7=Si_2N_2O, 8=$Y_2Si_3O_3N_4$, 9=$YSiO_2N$, 10=$LaSiO_2N$, 11=$Y_{10}Si_6O_{24}N_2$, 12=U-phase, 13=U glass, 14= $YMgSi_2O_5N$, 15=$Y_4Si_2O_7N_2$, 16=$La_4Si_2O_7N_2$, 17=$La_{10}Si_6O_{24}N_2$, 18=SiO_2

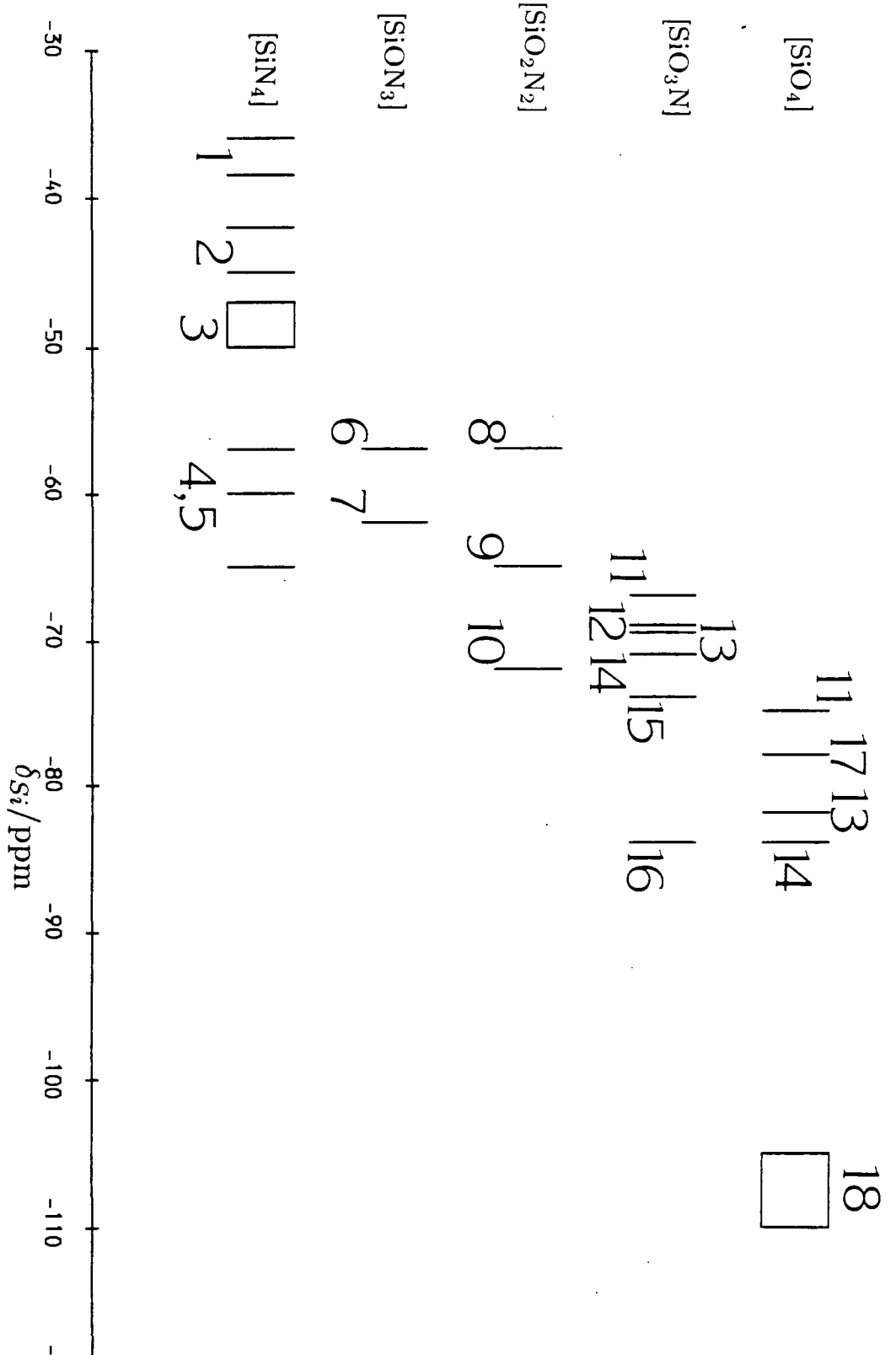

with Figure 6.2.8 indicates that significant quantities of Si_3N_4 have been lost on preparation of the glass.

6.2.3 Discussion

Effects of coordination on chemical shift

Silicon–29 chemical shifts of Y and La sialons are found to depend on n.n. coordination environment to a significant degree, particularly in open structures, in which bonding of O/N atoms is partially or basically ionic. This was particularly noticable in Y N–apatite and $YMgSi_2O_5N$, where two peaks in the ^{29}Si NMR spectra could be assigned to two different coordination environments. In closed structures, such as U–phase and $LaSi_3N_5$, in which O/N bonding is mainly covalent, the effect of long-range structure is found to become more important, and it is less easy to rationalise δ_{Si} values in terms of n.n. coordination.

Silicon–29 chemical shift values of Y and La sialons are plotted against known or predicted Si n.n. environment in Figure 6.2.10. Each additional oxygen atom in the $[SiO_xN_{4-x}]$ tetrahedron is found to decrease δ_{Si} by an average of about 10 ppm. This is of a similar order of magnitude to the shift observed in the silicates in increasing the Q index by one (Figure 3.2.1). This is perhaps surprising because in the former case the effect is at the n.n. level, whereas in the latter case it is at n.n.n. level, but the important factor is really the electronegativities of each of the coordinating groups of the central Si atom. Correlations between group electronegativity and δ_{Si} were reviewed in Section 3.2.2. It is extremely difficult to apply a group electronegativity approach to most of the phases discussed in this Chapter because of the complexities of their structures and the lack of accurate crystal structure data, but it is instructive to compare the group electronegativities of more ionic oxygen (as in ONa) and more covalent oxygen (as in OSi), which in this case differ by 0.6;[18] and atomic oxygen and atomic nitrogen, which differ by 0.5.[19] It is therefore to be expected that substitutional effects at n.n. and n.n.n. levels should be of similar orders of magnitude.

In closed, basically covalent, structures, such as $LaSi_3N_5$, new phase (see Section 6.7), and U–phase, it is found that the precise identity of n.n. coordinating

atoms is not critical in determining δ_{Si}. It is thought that δ_{Si} is determined principally by other factors such as Si–X–Si bond angles and coordination to cations, though the precise nature of such effects is not known. This finding must also cast some doubt on the conclusions on O/N ordering in yttrium N–melilite based on ^{29}Si NMR,[11] another basically covalent structure. Another O/N ordering scheme might be possible, as suggested by neutron diffraction.[20]

The correlation in Figure 6.2.10 makes no attempt to include the effect of n.n.n. coordination. It must however be apparent from the above discussion that such effects will be important in many cases. Even more data points on a wide range of phases of known structure will be needed before such effects can be explored.

Effects of counter-ion

Little attention has previously been paid to the effect of counter-ion on δ_{Si} in silicate minerals or nitrogen ceramics, but it is clear from the data presented in this Chapter that the counter-ion does profoundly affect ^{29}Si NMR spectra. In the four isostructural yttrium and lanthanum phases: M_2SiO_5, N–wollastonite, N–apatite and N–YAM, there are changes of −4, −7.5, −10.5 and −10 ppm in δ_{Si} on replacing Y by La. There are three possible explanations of these changes to examine:

(i) Incorporation of La leads to changes in Si–X–Si bond angles (probably an increase) which would have a proven effect on δ_{Si}. It is extremely difficult to measure bond angles accurately in these phases because of the dominance of the heavy atom on the diffraction pattern.

(ii) Electronegativity differences between Y and La could lead to deshielding of Si because of changes in partial ionic charge in coordinating O/N. The Pauling electronegativities of the two metals are, however, almost identical (Y 1.2, La 1.1).

(iii) Counter-ion identity was found to affect ^{17}O chemical shift very profoundly (Section 3.2.5). Large sized ions were found to give rise to more positive δ_O values. No explanation of this effect has been proposed in the literature, but it must be true that the positive shift is caused by increased shielding of the oxygen atoms. This would be expected to be partially at the expense of deshielding of silicon, leading to a more negative ^{29}Si chemical shift. The most straightforward explanation of the

increased shielding of the oxygen atoms is that the atoms are becoming more ionic in their bonding, and are thus carrying a larger negative charge. Larger cations are known to be less polarising, and more polarisable,[21] because the valence orbitals are more diffuse. This means that coordinating oxygen atoms can accommodate a larger negative charge than when coordinated to smaller counter-ions. This will partially be achieved by polarisation of electrons from round the Si atom(s) to which the oxygen is bonded. Polarisability, the ability to donate electrons to an ion, must be distinguished from electronegativity, which is concerned with the electronic properties of atoms.

The possible effect of lanthanum ions on δ_{Si} in closed structures such as $LaSi_3N_5$ was discussed above. Increased numbers of neighbouring La^{3+} ions leads to deshielding, because, according to the above model, the coordinating N (or O) can accommodate a greater negative charge, leading to increased polarisation of electrons round the Si atoms. A similar effect is presumably occurring in $Y_2Si_3N_6$. In $Y_6Si_3N_{10}$ and YSi_3N_5, the yttrium ions have no deshielding effect on δ_{Si}, probably because the N atoms are in fully covalent [NSi_3] environments, as in Si_3N_4, and the sole effect of incorporating metal ions is to supply extra electrons to the SiN framework, leading to shielding of Si.

The spectrum of $La_2Y_2Si_2O_7N_2$ (sample 6.27, see Table 6.2.1) shows that the effect of mixing Y and La in a single phase is partially additive. The overall δ_{Si} is, as expected, intermediate between that of pure Y and La N–YAMs. There is significant broadening of the resonance, suggesting that varying La/Y coordination is at least partially responsible for differences in δ_{Si} in these phases: changes in bond angle might be expected to give a resonance for the mixed phase of similar width to the pure La or Y phases. This argument assumes that the sample is homogeneous, and this is supported by the sharpness of the diffraction pattern of the phase.

Linewidth

The ^{29}Si linewidths measured from M–Si–O–N phases fall in the range 130–330 Hz. The lanthanum silicates give rather broad lines (200–300 Hz) in comparison to the yttrium silicates (50–100 Hz).[11]

Figure 6.3.1 ^{29}Si MAS NMR spectra of nitrogen–15 enriched
(a) $LaSiO_2N$ (sample 6.15) SF=59.6 MHz; PA=90^O; ST; SR=3.75 kHz; AF=0.01 s
(b) $La_4Si_2O_7N_2$ (sample 6.16) SF=59.6 MHz; PA=90^O; ST; SR=3.64 kHz; AF=0.007 s
(c) $La_2Si_6O_3N_8$ (sample 6.14) SF=59.6 MHz; PA=90^O; ST; SR=3.80 kHz; AF=0.005 s
(d) $LaSi_3N_5$ II (sample 6.18) SF=59.6 MHz; PA=27^O; NT=56; RD=300 s; SR=3.17 kHz; AF=0.01 s
(e) $La_2Si_{4.5}Al_{1.5}O_{4.5}N_{6.5}$ (sample 6.19) SF=59.6 MHz; PA=90^O; ST; SR=3.07 kHz; AF=0.005 s

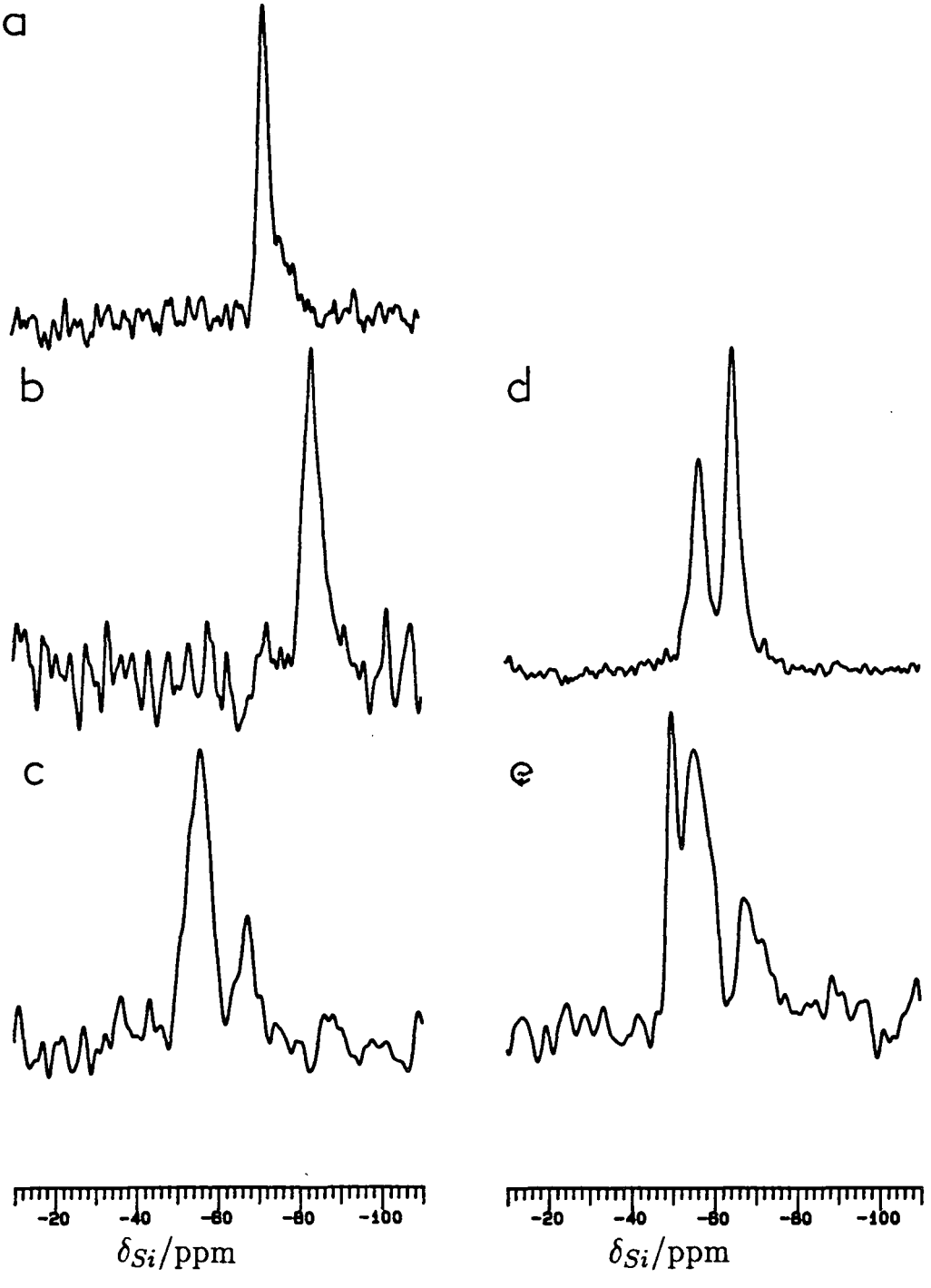

The effect of dipole-quadrupole coupling as a broadening mechanism in MAS NMR spectra has already been discussed (Sections 2.1.6 and 5.3.1). It was shown that in α– and β–Si_3N_4, unaveraged (^{29}Si,^{14}N) coupling is not a major source of broadening. The data on Y–Si–O and La–Si–O phases would seem to suggest, however, that unaveraged (^{29}Si,^{139}La) coupling is a significant broadening influence in lanthanum silicates, and indeed, the quadrupole moment of ^{139}La is 13 times that of ^{14}N. In the oxynitride phases, a broadening is also observed between Y and La phases, although the magnitude is less (0–100 Hz). It is extremely difficult to demonstrate conclusively that (^{29}Si,^{139}La) coupling is significant because many other factors such as sample inhomogeneity, and faulting and disorder within the structure also affect linewidth, but the extent of these effects in different samples cannot easily be determined. There is, for example, a noticable broadening of resonances in moving from Y–Si–O to Y–Si–O–N phases, but it is unlikely given the findings of Sections 5.3.1 and 6.3.1 that unaveraged (^{29}Si,^{14}N) coupling is important. It is more likely that broadening in nitrogen ceramics is caused by chemical shift dispersion due to sample inhomogeneity and disorder, possibly compounded by the presence of paramagnetic materials such as iron, which is incorporated into the phase in varying amounts (unlike in Si_3N_4, where it is present principally in grain boundary material, and does not significantly affect linewidth). In La sialons, (^{29}Si,^{139}La) coupling seems also to be important.

6.3 NMR of Nitrogen–15 Enriched Materials

6.3.1 ^{29}Si MAS NMR of Enriched Samples

NMR data on ^{15}N-enriched samples are summarised in Table 6.3.1, and ^{29}Si spectra are presented in Figure 6.3.1. Most are indistinguishable from the spectra of the unenriched materials (Figures 6.2.5, 6.2.7, 6.2.8). The spectra obtained with a single transient after ^{15}N acquisition were in some cases of poor signal to noise, leading to larger than average errors in δ_{Si} and FWHH.

The spectrum of La N–wollastonite (sample 6.15) is very similar to that of sample 6.2. Peaks from minor impurities (N–YAM and N–apatite) can be seen to low frequency of the main peak. The linewidth is slightly larger than from sample 6.2, indicating that (^{29}Si,^{14}N) coupling is negligible as a line-broadening

Table 6.3.1 ^{29}Si and ^{15}N MAS NMR data on ^{15}N-enriched La and Y sialons

Phase	sample	Silicon-29			Nitrogen-15		
		δ_{Si}/ppm	FWHH/Hz	intensity	δ_N/ppm	FWHH/Hz	intensity
La new	6.14	$-56.0^{(a)}$	350	3	~ 64	500	4
		-67.5	280	1	~ 126	1400	7
La N-woll.	6.15	$-72.2^{(a)}$	200		154.9	330	
La N-YAM	6.16	$-83.8^{(a)}$	250		—(b)		
$LaSi_3N_5$ I	6.17				$51.4^{(c)}$	75	
					69.7	170	
					120	500	
					140	500	
$LaSi_3N_5$ II	6.18	-57.1	260	1	$51.4^{(c)}$	60	0.2
		-65.2	220	1.7	71.3	175	3
					160-110	1500	4
La Al-new	6.19	$-48.7^{(c)}$			$50.1^{(c)}$	100	
		-54.2	500	4	66.9	500	2
		-67.8	420	1	130	1400	3
Y N-YAM	6.29	$-75.2^{(a)}$	180		—(b)		

(a) ST aquisition. (b) No signal observable. (c) Signal from β-Si_3N_4

Figure 6.3.2 ^{15}N MAS NMR spectra of

(a) $LaSiO_2N$ (sample 6.15) SF=30.4 MHz: PA=90^o; NT=10: RD=3600 s; SR=3.75 kHz: AF=0.01 s

(b) $La_4Si_2O_7N_2$ (sample 6.16) SF=30.4 MHz: PA=70^o; NT=31; RD=3600 s; SR=4.02 kHz; AF=0.01 s

NEW PHASE → (c) $La_2Si_6O_3N_8$ (sample 6.14) SF=30.4 MHz: PA=23^o; NT=300; RD=300 s; SR=3.75 kHz; AF=0.01 s

(d) $La_2Si_{4.5}Al_{1.5}O_{4.5}N_{6.5}$ (sample 6.19) SF=30.4 MHz; PA=17^o; NT=141; RD=300 s; SR=3.15 kHz; AF=0.01 s

(e) $LaSi_3N_5$ I (sample 6.17) SF=30.4 MHz: PA=30^o; NT=214; RD=300 s; SR=3.00 kHz; AF=0.01 s

(f) $LaSi_3N_5$ II (sample 6.18) SF=30.4 MHz: PA=17^o; NT=219; RD=300 s; SR=3.28 kHz; AF=0.01 s

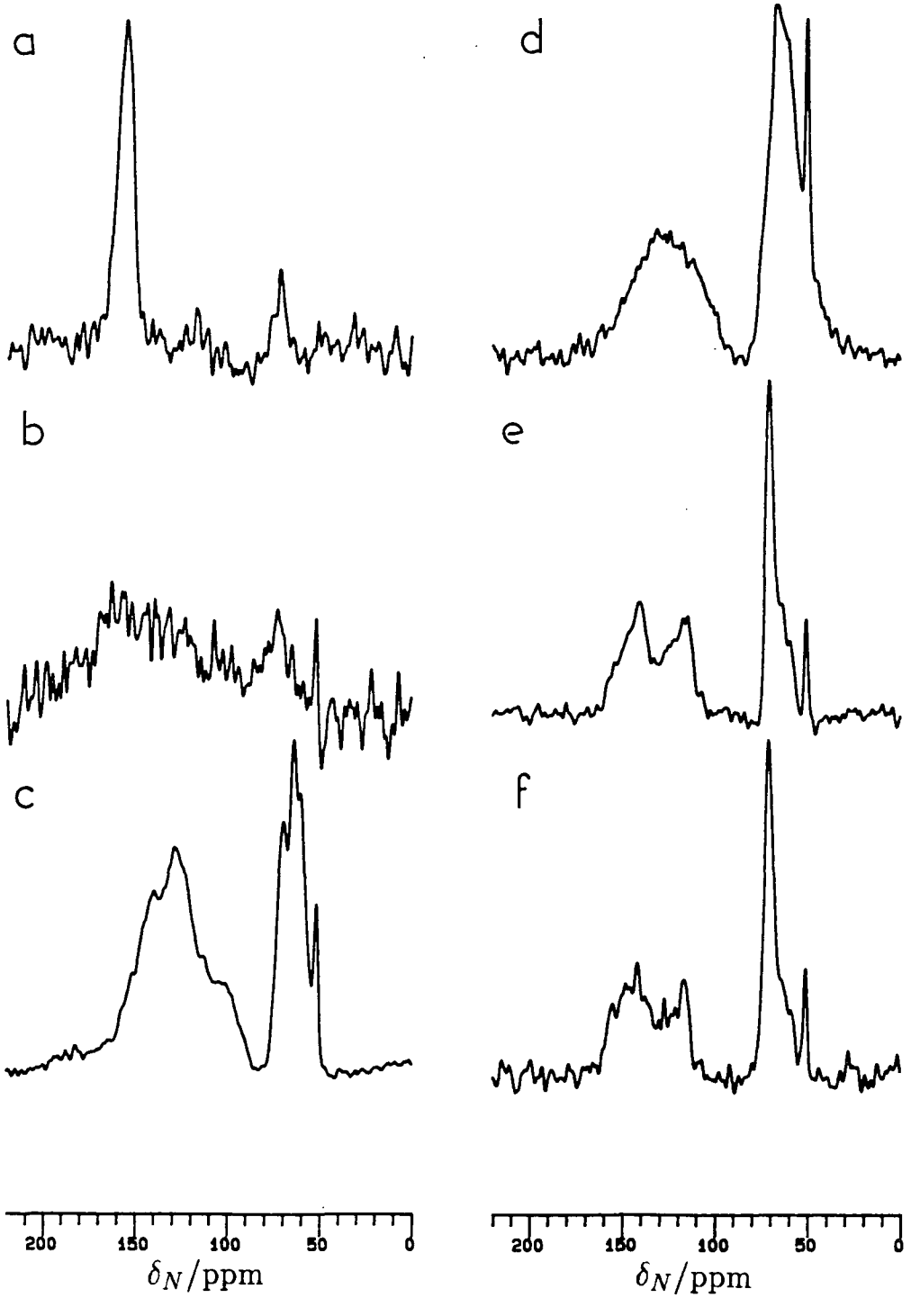

mechanism. Similar results were found from the Y and La N–YAM phases, the spectra of which are otherwise unremarkable.

The spectra of both La new and La Al–new phases (Figure 6.3.1) are of interest because the higher frequency peak is shifted by 1–2 ppm to high frequency in each case. It is inconceivable that this is due directly to the presence of nitrogen–15, and can be attributed most simply to the existence of small ranges of homogeneity. The spectrum of Al–new phase shows that sample 6.19 is contaminated with a significant quantity of β–Si_3N_4, but peaks from this material are easy to identify in ^{15}N MAS NMR spectra.

The spectrum of $LaSi_3N_5$ (sample 6.18) shows, as does the XRD, that the sample is contaminated with a small amount of new phase. The peak area ratio from the spectrum is 1.7:1, compared with 2:1 for pure $LaSi_3N_5$. This corresponds to a phase composition $95^m/_o$ $LaSi_3N_5$:$5^m/_o$ $La_2Si_6O_3N_8$, and implies that 90–95% of the ^{15}N isotope is present in the nitride phase.

In none of the nitride or new phase samples were any anomalous linewidths observed. In no case therefore, is (^{29}Si,^{14}N) coupling significant as a broadening mechanism.

6.3.2 ^{15}N MAS NMR of La and Y Sialons

NMR data on the ^{15}N-enriched materials prepared for this study are listed in Table 6.3.1. Only the La–Si–O–N system was studied in detail, although a sample of $Y_4Si_2O_7^{15}N_2$ was prepared after no signal could be obtained from $La_4Si_2O_7^{15}N_2$.

The ^{15}N spectrum of $LaSiO_2N$ (Figure 6.3.2) shows a resonance at significantly higher frequency than those of Si_3N_4 or Si_2N_2O. The nitrogen environment in $LaSiO_2N$ bridges two silicon atoms, and the atom is also coordinated to two lanthanum ions. It is more ionic than the nitrogen environments in Si_3N_4 or Si_2N_2O. This leads to shielding of the ^{15}N nucleus, and a positive shift in δ_N.

It was hoped that La N–YAM, in which N is bonded covalently to only one Si atom, would also give rise to a characteristic chemical shift, probably at an even more positive value of δ_N. It proved impossible, however, to observe a ^{15}N signal from either the Y or La phases (Figure 6.3.2). This must be either because

of extremely long T_1 times in these phases, coupled to the low N concentration, or exchange of ^{15}N with the $^{14}N_2$ atmosphere during synthesis. No evidence for exchange was found in the synthesis of any other phase in this study, so the latter explanation is less likely to be correct.

The spectrum of new phase (Figure 6.3.2) shows that the structure of the phase is complex. The low frequency composite peak is made up of at least 3 components in addition to the peak at 51.6 ppm, which is assigned to β–Si_3N_4. It is possible that the peak at 63.6 ppm is caused by a superposition of the minor peak in the β–$Si_3^{15}N_4$ spectrum plus the resonance from new phase. It is impossible to determine the number of peaks superimposed on the higher frequency resonance.

A full discussion of this spectrum is delayed until Section 6.7, but by comparison of the spectrum with those of $LaSiO_2N$, Si_3N_4 and Si_2N_2O, the lower frequency peak has been assigned to N covalently bonded to three Si, [NSi_3] as in Si_3N_4, and the higher frequency peak to N bonded to two Si, as in $LaSiO_2N$.

The spectrum of Al–new phase (Figure 6.3.2) shows clearly that the intensity of the high frequency peak has decreased markedly with respect to the low frequency peak. This is consistent with oxygen preferentially occupying [NSi_2] rather than [NSi_3] sites on isomorphous substitution.

The spectra of $LaSi_3N_5$ are surprising. On the basis of the crystal structure analysis and the above discussion, it would be expected that a 3:2 ratio in peak areas would be observed for [NSi_2]:[NSi_3] resonances. The observed ratio (4:3) is very close to this (areas under very broad peaks are difficult to measure accurately), but the shape of the [NSi_2] peak is very complex for a peak resulting from only three environments. These nitrogen atoms are, however, coordinated directly to La^{3+} ions, and it is possible that (^{15}N,^{139}La) coupling is a significant cause of broadening in this phase. It is certainly noticable that the ^{15}N resonance from $LaSiO_2N$ is much broader than from Si_3N_4 and Si_2N_2O, in which N is not coordinated to quadrupolar nuclei. It has already been demonstrated by ^{29}Si MAS NMR that there are many other possible causes of linebroadening in La–Si–O–N phases. The peak in the spectrum of $LaSi_3N_5$ due to [NSi_3] environments is, by contrast, very narrow, as found in other phases containing the environment.

Figure 6.3.3 δ_N against coordination environment for La–Si–O–N phases

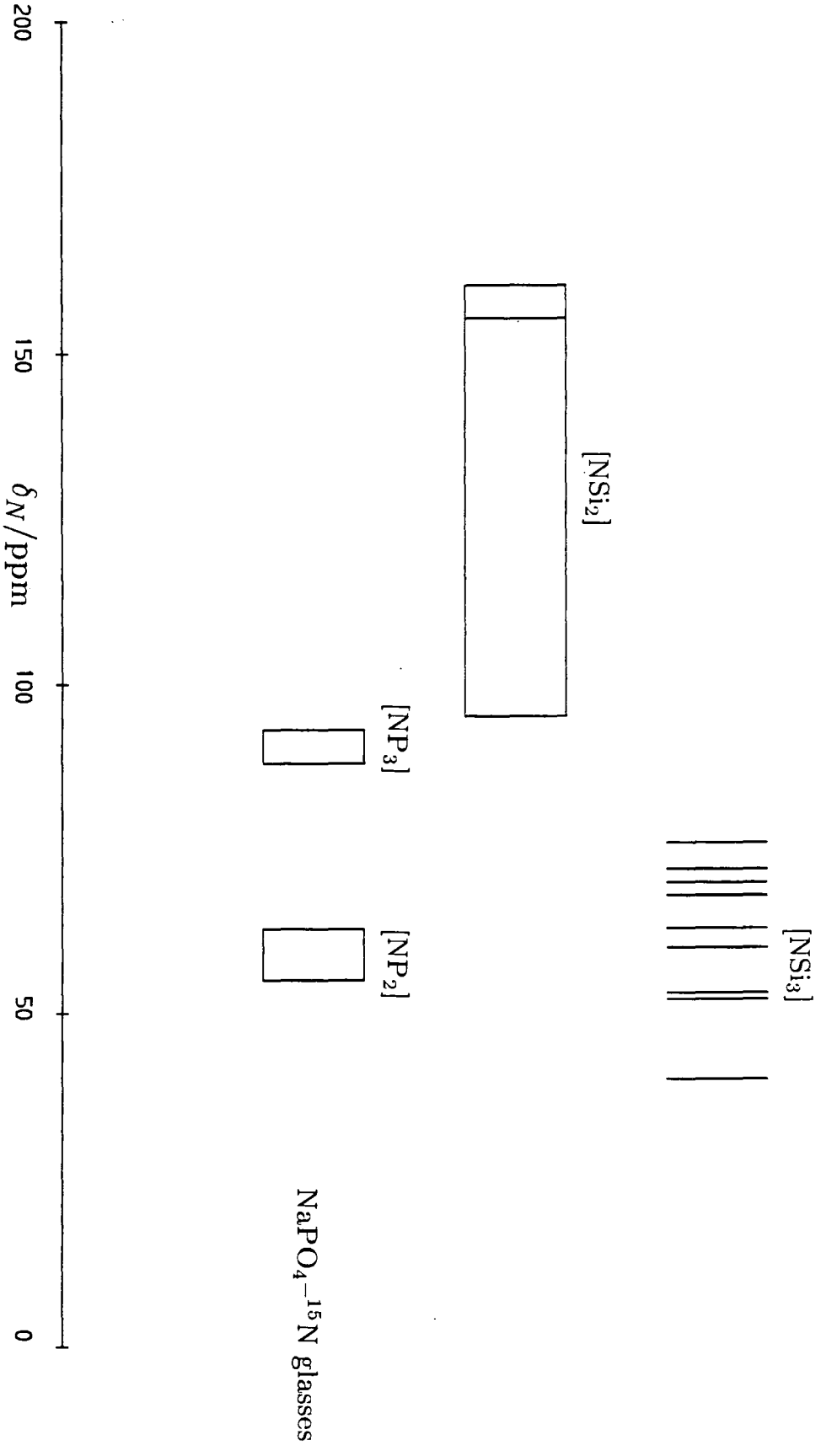

The δ_N values obtained from phases studied in Chapters 5 and 6 are summarised in Figure 6.3.3. The two possible nitrogen environments give distinctly different chemical shift values. The separation in shifts is found to be much greater than in ^{29}Si NMR for changes in environment, as would be expected from consideration of the effect of p–electron density on σ_p. The spread of shifts within each range is also found to be greater than in ^{29}Si NMR. No explanation for the value of δ_N within each range has been proposed.

The results summarised in Figure 6.3.3 contrast with those of Bunker *et al.*[22] on ^{15}N–doped sodium phosphate glasses, where two-coordinate nitrogen gives rise to lower shifts than three-coordinate nitrogen. In these glasses, however, nitrogen is bonded to phosphorous, which is much more electronegative than silicon. In these glasses, therefore, phosphorous has a shielding effect on nitrogen, in contrast to the effect of silicon, which is deshielding.

6.4 Oxygen–17 NMR of La and Y Sialons

Oxygen–17 spectra of lanthanum N–apatite, N–wollastonite, N–YAM and Al–N–YAM were obtained at Larmor frequencies of 40.7 and 27.1 MHz, and the spectrum of yttrium N–YAM at 40.7 MHz only (Figures 6.4.1 and 6.4.2). The shifts in positions of the centres of gravity of peaks were used to calculate the true chemical shifts and quadrupole coupling constants of the various resonances using Equation 2.1.18 and assuming $\eta = 0$. Accurate determinations on silicates discussed in Chapter 3 indicate $\eta \leq 0.4$ in all phases studied: the error in χ_Q would then be $< 5\%$ in letting $\eta = 0$, substantially less than errors from other sources.

If the observed chemical shifts of the centres of gravity of resonances at 4.7 and 7.1 T are δ_O^{200} and δ_O^{300} respectively, then Equation 2.1.18 can be used to demonstrate that

$$\chi_Q = 0.47(\delta_O^{300} - \delta_O^{200})^{\frac{1}{2}}$$

$$\delta_O = \delta_O^{300} + 0.8(\delta_O^{300} - \delta_O^{200})$$

Corrected shifts and quadrupole coupling constants are listed in Table 6.4.1. The error in determination of δ_O^{200} and δ_O^{300} is large; in particular, it is very difficult to identify the centre of gravity of a non-symmetric resonance such as one broadened by second order quadrupolar coupling. For the systems studied in this Chapter,

Figure 6.4.1 ^{17}O MAS NMR spectra of

(a) $LaSiO_2N$ (sample 6.20) SF=40.7 MHz; PA=10^o; NT=1200; RD=2 s; SR=4.10 kHz; AF=0.001 s

(b) $La_4Si_2O_7N_2$ (sample 6.21) SF=40.7 MHz; PA=10^o; NT=1200; RD=2 s; SR=4.15 kHz; AF=0.001 s

(c) $La_{10}Si_6O_{24}N_2$ (sample 6.22) SF=40.7 MHz; PA=23^o; NT=6000; RD=1 s; SR=8.00 kHz; AF=0.005 s

(d) $LaSiO_2N$ (sample 6.20) SF=27.1 MHz; PA=23^o; NT=600; RD=5 s; SR=3.01 kHz; LB=0.001s

(e) $La_4Si_2O_7N_2$ (sample 6.21) SF=27.1 MHz; PA=23^o; NT=800; RD=5 s; SR=3.00 kHz; LB=0.001s

(f) $La_{10}Si_6O_{24}N_2$ (sample 6.22) SF=27.1 MHz; PA=23^o; NT=6700; RD=1 s; SR=3.00 kHz; LB=0.001s

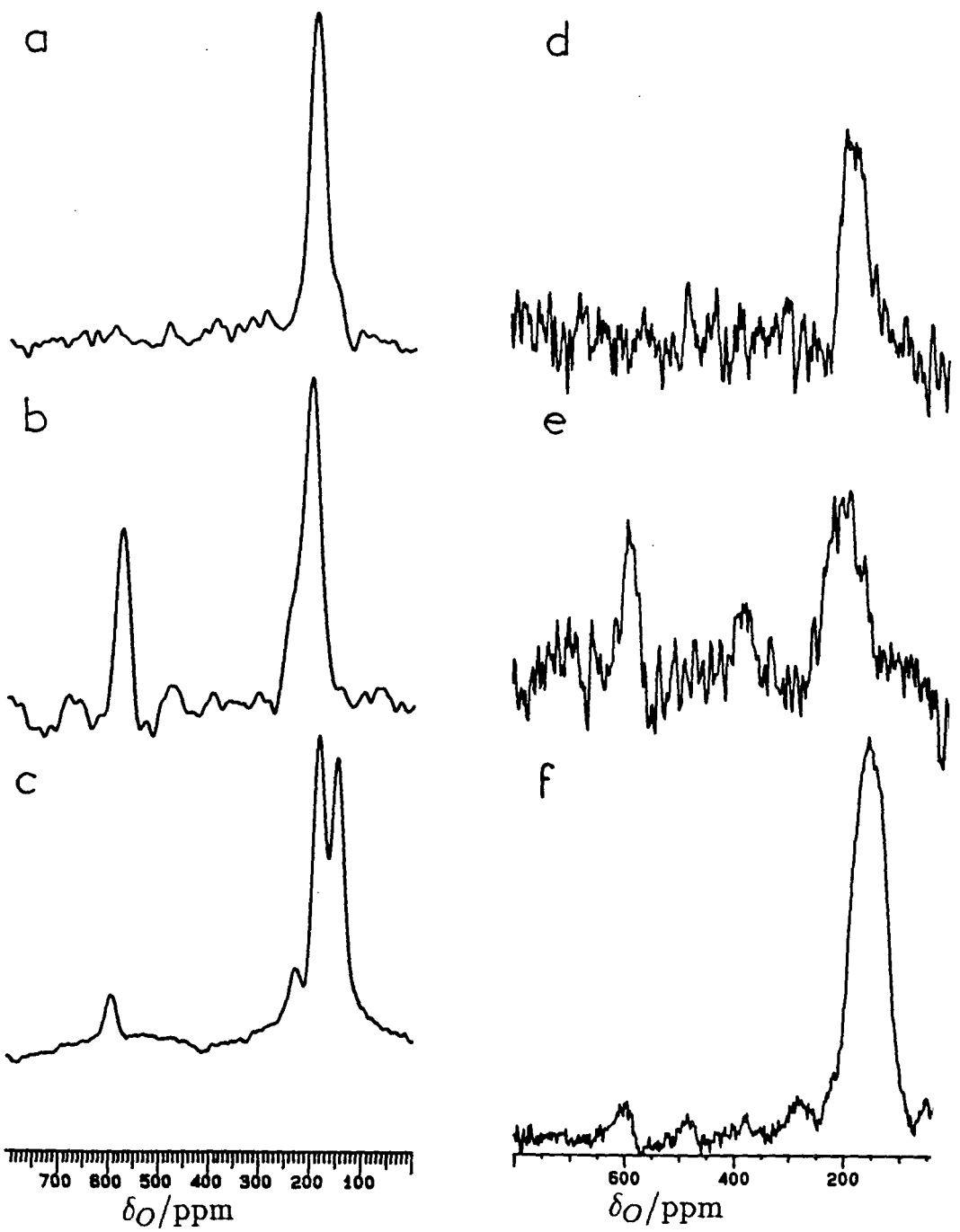

an error in δ_O^{200} or δ_O^{300} of ±5 ppm is estimated, although since peak shapes at the two frequencies are similar, errors in δ_O^{200} and δ_O^{300} are not cumulative, and the total error in $(\delta_O^{300} - \delta_O^{200})$ is much less than ±10 ppm. An estimate of ±5 ppm leads to an error of ±0.3 MHz in χ_Q, and ±5 ppm in the value of δ_O.

Table 6.4.1 ^{17}O MAS NMR data on La–Si–Al–O–N phases.

Sample	phase	27.1 MHz		40.7 MHz		corrected	
		δ_O^{200}/ppm	FWHH/Hz	δ_O^{300}/ppm	FWHH/Hz	δ_O/ppm	χ_Q/MHz
6.20	N–woll.	170	1700	195	1600	215	2.4
6.21	N–YAM	575	950	575	1100	575	0.0
		175	2000	200	1700	220	2.4
6.23	Al–N–YAM	573	1000	570	1000	575	0.0
		286	1500	300	2000	311	1.8
		169	1600	212	2000	246	3.1
6.22	N–apatite	(a)		596	1000	(596)	(b)
		153	1600	170	—	184	1.9

(a) No peak observed at 27.1 MHz, so error in δ_O large. (b) < 1 MHz, as estimated from linewidth.

The spectra of La N–wollastonite show a single peak, with δ_O=215 ppm and χ_Q = 2.4 MHz. This can be compared with the data listed in Table 3.2.5 for oxide wollastonite phases. Only O_{nb} sites are present in $LaSiO_2N$, because the bridging sites are occupied by nitrogen. $LaSiO_2N$ is isoelectronic and isostructural with $BaSiO_3$, and the chemical shifts and coupling constants of the O_{nb} sites are similar in the two phases, although δ_O is rather more positive in N–wollastonite phase. This could be caused by an increase in the ionicity in the Si—O bonds in $LaSiO_2N$, caused by increased covalency in the Si—N bonds.

The spectra of La N–YAM unambiguously show the presence of two distinct resonances: δ_O=575 ppm, χ_Q = 0, and δ_O=220 ppm, χ_Q = 2.4 MHz. The spectrum obtained at 27.1 MHz also seems to indicate the presence of a third resonance

Figure 6.4.2 ^{17}O MAS NMR spectra of

(a) $Y_4Si_2O_7N_2$ (sample 6.30) SF=40.7 MHz; PA=15^o; NT=55000; RD=1 s; SR=8.00 kHz; AF=0.001 s

(b) La_4SiAlO_8N (sample 6.23) SF=40.7 MHz; PA=15^o; NT=2000; RD=1 s; SR=8.90 kHz; AF=0.003 s

(c) La_4SiAlO_8N (sample 6.23) SF=27.1 MHz; PA=23^o; NT=600; RD=5 s; SR=3.03 kHz; LB=0.001 s

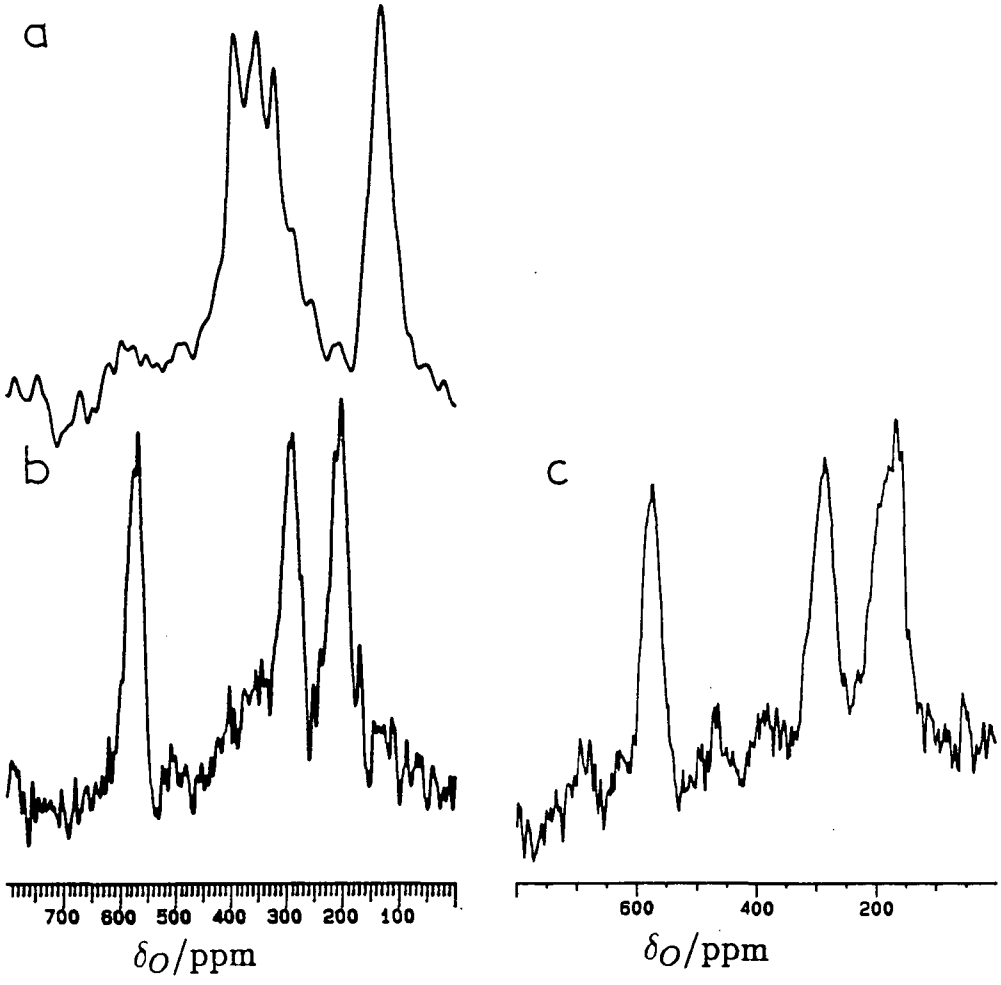

Figure 6.4.3 Simulated ^{17}O MAS NMR spectrum of $La_{10}Si_6O_{24}N_2$ (see text for details)

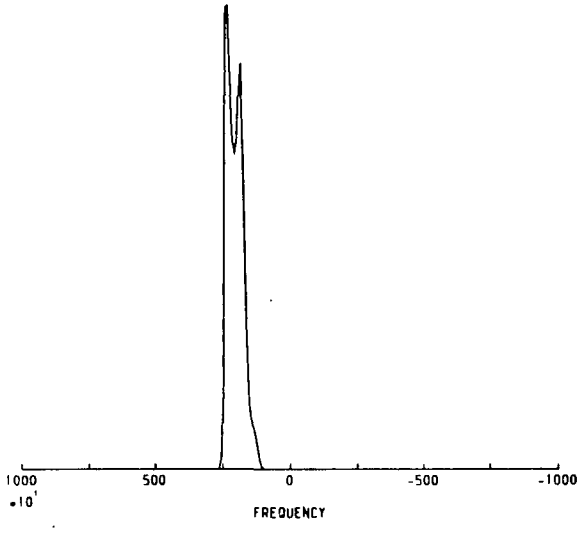

with δ_O^{200}=380 ppm, but no corresponding peak was seen in the higher quality spectrum at 40.7 MHz.

The structure of La N–YAM indicates that peaks from three distinct oxygen environment types should be observable in the NMR spectrum: one due to terminal (O_{nb}) oxygens and one from a single bridging (O_{br}) oxygen, both in the [$Si_2O_5N_2$] unit; plus one from two ionic oxygens (O^{2-}), which are coordinated to four lanthanum ions in an approximately tetrahedral arrangement. The peak at 220 ppm can be assigned to O_{nb}: δ_O and χ_Q are very similar to those observed for O_{nb} environments in other phases. The high frequency peak must be due to O^{2-} environments, both because of the high chemical shift, indicative of oxygen in the vicinity of high ionic radius atoms, and the low value of χ_Q. The O_{br} oxygen would be expected to give rise to a resonance with $\delta_O \sim 85$ ppm and $\chi_Q \sim 4$ MHz by consideration of the data in Table 3.2.5. This resonance is clearly not observed: it would be expected at $\delta_O \sim 20$ ppm. It must be broadened by second order quadrupolar coupling and other interactions to such an extent that it cannot be distinguished from background.

A satisfactory explanation for the appearance of a peak at 380 ppm at 27.1 MHz is not apparent. It is not in a region of the spectrum in which a peak is to be expected. It is possible that it is a sum of several ssb's from other transitions, but the limitations of the probe used at 27.1 MHz meant that higher rotation rates could not be attained to test fully this hypothesis.

The related phase, Al–N–YAM, gives three peaks in the ^{17}O NMR spectra at both frequencies. In the structure, up to half of (SiO_2N) groups are replaced by (AlO_3) in the [$Si_2O_5N_2$] units. The two peaks, with similar values of χ_Q, can be assigned to O—Si and O—Al non-bridging environments. The lower value of χ_Q for the O—Al resonance (δ_O=311 ppm, χ_Q = 1.8 MHz) is consistent with the fact that this bond is more ionic than O—Si, and therefore the O valence orbitals are less perturbed by Al than by Si. The peak at 575 ppm is of course due to ionic oxygen. No peaks due to O_{br} are again observed.

Lanthanum N-apatite is the only phase in these systems to give an ^{17}O MAS NMR spectrum in which the quadrupole splitting can be resolved. The phase contains oxygen in both O_{nb} environments (SiO_4 and SiO_3N units) and an ionic

environment, in which oxygen is located on a C_3 axis, and is coordinated to three identical lanthanums.

In the ^{17}O spectrum obtained at 40.7 MHz, two regions can be identified; the peak at 596 ppm is not, however, observed at 27.1 MHz. This peak, with an undetermined value of χ_Q, can be assigned to the ionic site. It is assumed that at 27.1 MHz, and a spin rate of only 3 kHz, this peak is lost in the background of unresolvable ssb's from other transitions.

The main peak in both spectra can be assigned to the O_{nb} environments. A simulation of the peak shape (Figure 6.4.3) based on δ_O and χ_Q determined from the field-dependent shift confirms these values, and demonstrates that the shoulder at 219 ppm seen in Figure 6.4.1c is due to a second O_{nb} environment. Two types of silicate unit are present in the phase: $[SiO_4]$ and $[SiO_3N]$, and it is likely that the 219 ppm shoulder is due to oxygen in the latter unit, which is the less abundant.

The spectrum of yttrium N–YAM (Figure 6.4.2) is surprisingly complex in comparison to that of the lanthanum analogue. There is a clear peak at δ_O^{300}=125 ppm, assigned to O_{nb} environments. The FWHH of this peak indicates that the value of χ_Q is similar to that in the La N–YAM for the same environment, giving a corrected shift of $\sim$ 150 ppm, around 70 ppm lower than δ_O for O_{nb} in $La_4Si_2O_7N_2$. This change in shift is of a similar order of magnitude to that observed for O_{nb} between $SrSiO_3$ and $BaSiO_3$ (60 ppm), see Table 3.2.5.

The complex series of peaks in the region 350–400 ppm is clearly due to oxygen bonded to four yttrium ions. The reason for the complex splitting of the peak is not apparent: it is likely that quadrupolar splitting is important. Co-addition of ssb's from various transitions probably adds to the complexity. The value of 2 MHz for χ_Q is estimated from the splitting of the two most intense peaks; this is much greater than that for the similar environment in the La analogue ($<$ 0.3 MHz). This has important implications in considering the bonding in the two phases (see Discussion). Oxygen in O_{br} environments is not observed.

The signal to noise ratio in the spectrum of yttrium N–YAM is much lower than for any of the lanthanum phases studied, indicating that the ^{17}O T_1 time is much longer in this phase, and that saturation is occurring.

Lippmaa *et al.*[23] have shown that the predicted linewidth of a resonance for a $I = \frac{5}{2}$ nucleus is given by $(\ln 4)^{\frac{1}{2}}\Delta\nu$, in the absence of other broadening influences, where $\Delta\nu$ is defined as for Equation 2.1.18. Use of this relationship indicates that at 40.7 MHz, a χ_Q of 2 MHz would give rise to a resonance of width 700 Hz, rising to 1550 Hz for χ_Q = 3 MHz. Table 6.4.1 therefore indicates that all resonances are broadened significantly by other interactions apart from quadrupolar coupling. This extra broadening is particularly noticable in the high frequency resonances due to O^{2-} sites, which give rise to FWHH of 1–2 kHz in the La phases, despite a χ_Q of < 0.3 MHz. The reason for this broadening are not clear, but it may be due in part to unaveraged (^{17}O,^{139}La) dipolar coupling.

Discussion

Chemical shifts in the M–Si–O–N systems are found to follow similar trends to those observed in the metal silicates. In general, increasing coordination to large ions leads to a high frequency shift. This allows ready distinction of O_{nb} and O^{2-} sites.

No explanation for the increase in δ_O with coordination to large ions has been proposed in the literature. It has been pointed out[24] that the trend is not directly related to cation electronegativity. In Section 6.2.3 it was proposed that δ_O can be related to ion polarisability rather than electronegativity. An oxygen atom in the vicinity of more polarisable (i.e. larger) cations can accommodate a larger negative charge, leading to shielding of the nucleus. This hypothesis is supported by the literature evidence that δ_O increases much more slowly with r_{2+}^3 in the group IIb metal oxides in comparison with the corresponding group IIa oxides: the valence d–electrons in group IIb metals are much poorer at shielding the nucleus than the s–electrons in the main group metals.

This effect will, of course, be most noticable in the cases where oxygen is bonded principally to large ions (e.g. O^{2-} sites), in comparison to cases where coordination is partially to Si (e.g. O_{nb} sites). O_{br} sites would be expected to give the smallest cation-dependent shifts, and this was found to be so in the metal silicates listed in Table 3.2.5.

The trend in δ_O would also be expected to be seen in δ_N values, and the

observations described in Section 6.3 can be rationalised in terms of this model. Nitrogen in phases such as $LaSiO_2N$, where coordination is to two Si atoms plus La gives much more positive δ_N values than in Si_3N_4 or Si_2N_2O, where coordination is only to silicon. In new phase, where both types of environment are found, two peak regions are observed, in which δ_N is very different. A small high frequency shift ($\sim$ 10 ppm) is also found in the [NSi_3] environments in comparison with Si_3N_4, indicating that the La^{3+} ions have some effect on δ_N in this case. No ^{15}N measurements have been made on yttrium phases, but measurements on Mg and Li wurtzite phases (Section 7.3) will show that in these compounds, δ_N is similar to that from Si_3N_4, despite coordination to metals of similar electronegativity to lanthanum. The much smaller Mg^{2+} and Li^+ are much less polarisable than La^{3+}, and therefore nitrogen can accommodate a much smaller negative charge than when coordinated to lanthanum.

Values of χ_Q for O_{nb} sites are of a similar order of magnitude to those found in silicates (Figure 3.2.10). It proved impossible to observe O_{br} oxygens in N–YAM phases, probably because resonances are further broadened by chemical shift dispersion and (^{17}O,^{139}La) coupling. Values of χ_Q for O^{2-} sites in La–Si–Al–O–N phases are surprisingly low. In La N–YAM, for example, χ_Q is under 0.3 MHz, yet the symmetry of the site is not cubic. This suggests that bonding is basically ionic in these phases, and that the oxide ion orbitals are barely perturbed by La^{3+}. Only in $Y_4Si_2O_7N_2$ does the value of χ_Q become measurably large for the O^{2-} site, indicating that bonding is more covalent in this compound, consistent with the lower ionic radius of Y^{3+}.

6.5 Aluminium–27 NMR

Aluminium–27 MAS NMR spectra were obtained at 78.2 MHz on most of the aluminium containing phases prepared for this Chapter, and are illustrated in Figure 6.5.1. Data are listed in Table 6.5.1. No corrections for quadrupolar coupling have been made. The spectrum of $LaAlO_3$ is in agreement with the work of Dupree *et al.*[11] who report δ_{Al}=11.7 ppm at a Larmor frequency of 93.83 MHz, and estimate $\chi_Q = 0.12 \pm 0.02$ MHz.

Aluminium–27 chemical shifts in aluminosilicate minerals were discussed in Section 3.2.3. A shift range of +45–+80 ppm for [AlO_4] environments is to be

Figure 6.5.1 ^{27}Al MAS NMR spectra of

(a)* $La_2Si_{4.5}Al_{1.5}O_{4.5}N_{6.5}$ (sample 6.9) SF=78.2 MHz; PA=15^o; NT=120; RD=1 s; SR=10.10 kHz; AF=0.005 s

(b)* La_4SiAlO_8N (sample 6.10) SF=78.2 MHz; PA=15^o; NT=120; RD=1 s; SR=10.40 kHz; AF=0.005 s

(c) $LaAlO_3$ (sample 6.13) SF=78.2 MHz; PA=15^o; NT=120; RD=1 s; SR=9.01 kHz

(d)* La U-phase (sample 6.12) SF=78.2 MHz; PA=30^o; NT=500; RD=2 s; SR=12.00 kHz

(e)* La U glass (sample 6.11) SF=78.2 MHz; PA=30^o; NT=1500; RD=2 s; SR=9.44 kHz; AF=0.002 s

*background subtracted

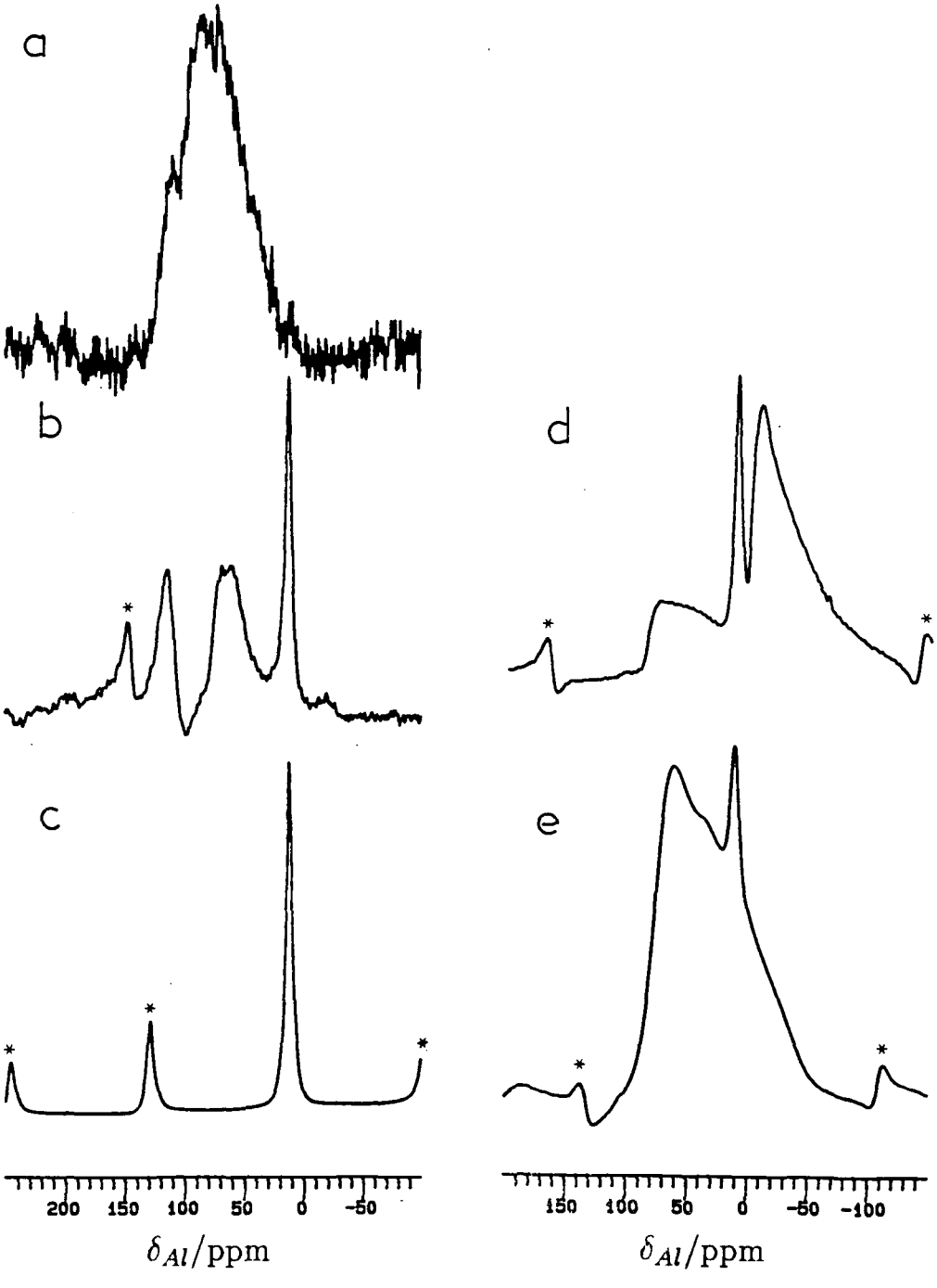

Table 6.5.1 ^{27}Al MAS NMR data on La-Si-Al-O-N phases

Sample	phase	δ_{Al}^{300}/ppm	FWHH/Hz	assignment
6.9	Al-new	72	4500	Al-new
6.10	Al-N-YAM	111	900	AlN
		57	2000	Al-N-YAM
		11.9	600	$LaAlO_3$
6.13	$LaAlO_3$	11.9	400	$LaAlO_3$
6.12	U-phase	67	5000	U-phase (CN=4)
		11.6	600	$LaAlO_3$
		−6.3	2000	U-phase (CN=6)
6.11	U-phase glass	50	5600	glass
		11.4		$LaAlO_3$

compared with a shift of 115 ppm for AlN, in which aluminium is present in an $[AlN_4]$ environment.[25] Aluminium in mixed four coordinate environments would be expected to give chemical shifts intermediate between these two values, although the asymmetry of such sites would be expected to lead to significant extra broadening of resonances.

The spectrum of La Al-new phase shows a single, very broad peak, with an observed chemical shift characteristic of an oxygen rich environment. This is consistent with the general observation that in sialon materials, N tends to bond predominantly to Si, and O to Al. The very high FWHH is indicative of a large value of χ_Q, with further broadening by chemical shift dispersion and other influences. This spectrum will be discussed further in Section 6.7.

The spectrum of La Al-N-YAM shows three peaks, two of which can be assigned to impurities: $LaAlO_3$ and AlN. The observed chemical shift of the peak assigned to Al-N-YAM: 57 ppm, is wholly consistent with $[AlO_4]$ coordination. The relative intensity of the three peaks is surprising in relation to the XRD of the sample (Table 6.1.1). No AlN and only a little $LaAlO_3$ were detected on the photograph. Two factors are important:

Figure 6.6.1 Static ^{139}La NMR spectrum of $La_{10}Si_6O_{24}N_2$ (sample 6.4)
SF=42.4 MHz; PA=23^o; NT=4000; RD=1 s; AF=0.00005 s

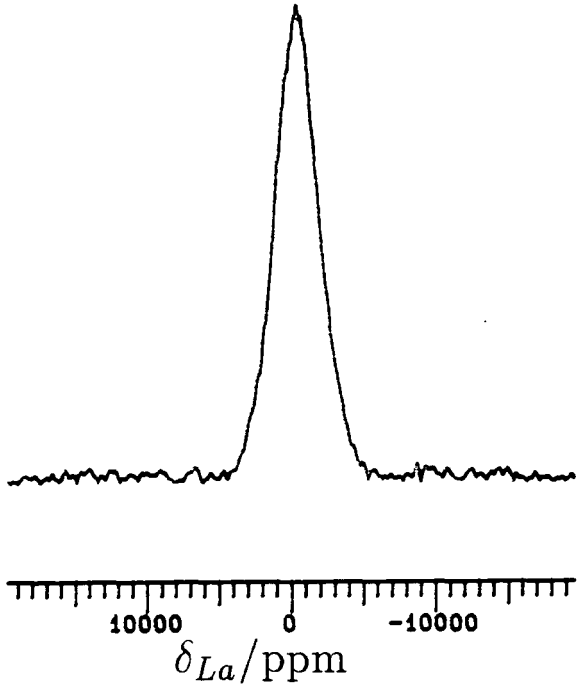

(i) La_4SiAlO_8N contains by far the greatest amount of La of the three phases, and thus gives the strongest scattering pattern.

(ii) In both $LaAlO_3$ and AlN, the Al environment is much more symmetric than in La_4SiAlO_8N, and thus less intensity is lost in the other transitions (Equation 2.1.16).

The spectrum of $LaAlO_3$ is consistent with the known, symmetric $[AlO_6]$ environment in this phase.

The sample of U–phase glass shows two peaks, one of which (δ_{Al}=11.4 ppm) can be assigned to $LaAlO_3$. This phase was not detected by XRD, but is clearly present in the sample in small amounts, probably in a microcrystalline form. The very broad resonance is indicative of the large degree of disorder present in glasses, and the chemical shift implies an oxygen rich four coordinate aluminium environment, as found in other metal sialon glasses.[15]

Lanthanum U–phase gives three peaks in the ^{27}Al NMR, one of which is clearly due to $LaAlO_3$, which is also detected by XRD. The structure of U–phase was discussed in Section 3.1.4. The phase contains aluminium in both six and four coordinate environments, in approximately a 1:2 ratio. Both environments can be readily detected by ^{27}Al NMR. The peak areas in such complex spectra are difficult to measure accurately, but it is clear from Figure 6.5.1 that the ratio of the peaks from the two environments is much greater than 1:2. This implies that χ_Q is much greater at the four coordinate sites, leading to greater loss in intensity. If the O/N ordering scheme means that Al is present in a range of four coordinate environments, then it is to be expected that the environments will have different values of χ_Q, and some may thus be broadened to a greater degree than others. The observed chemical shift is consistent with the expected oxygen rich environment.

The ^{27}Al MAS NMR spectra presented in this Section demonstrate that ^{27}Al NMR is of some use in identifying Al environments, although it is never easy to determine whether all of the Al is being observed or not. It is particularly convenient for determining whether 6– or 4–coordinate environments are present in samples. It is also very sensitive to impurities in which the Al environment is symmetric, and could thus be used as a valuable analytical tool.

Figure 6.7.1 Powder XRD diffractograms of (a) $La_2Si_6O_3N_8$ (sample 6.1) and (b) $La_2Si_{4.5}Al_{1.5}O_{4.5}N_{6.5}$ (sample 6.9)

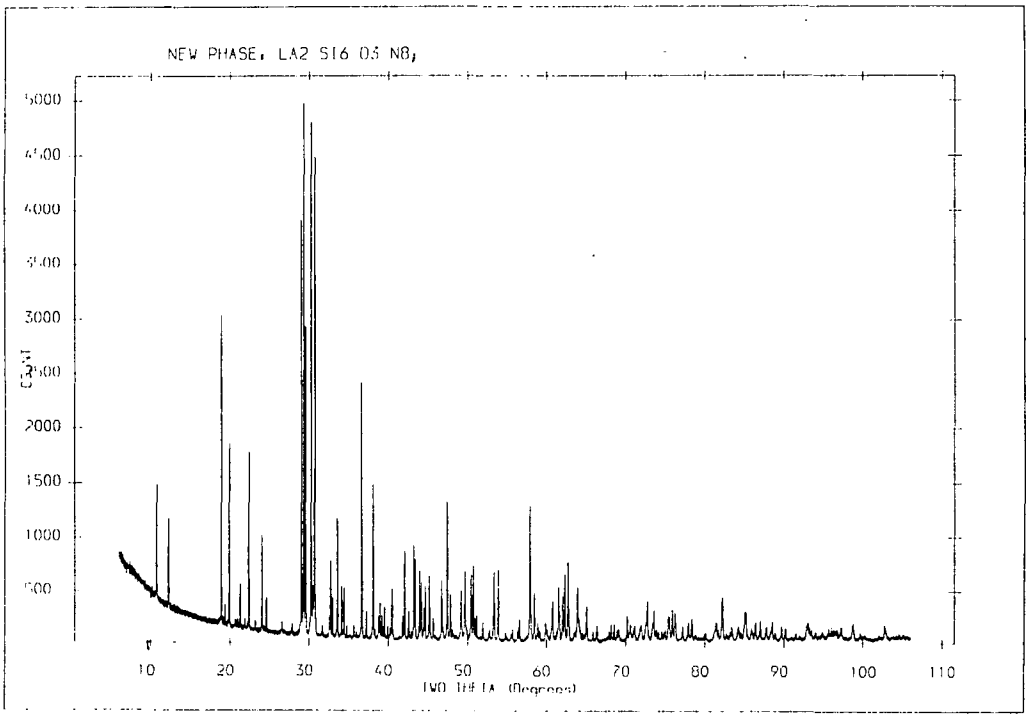

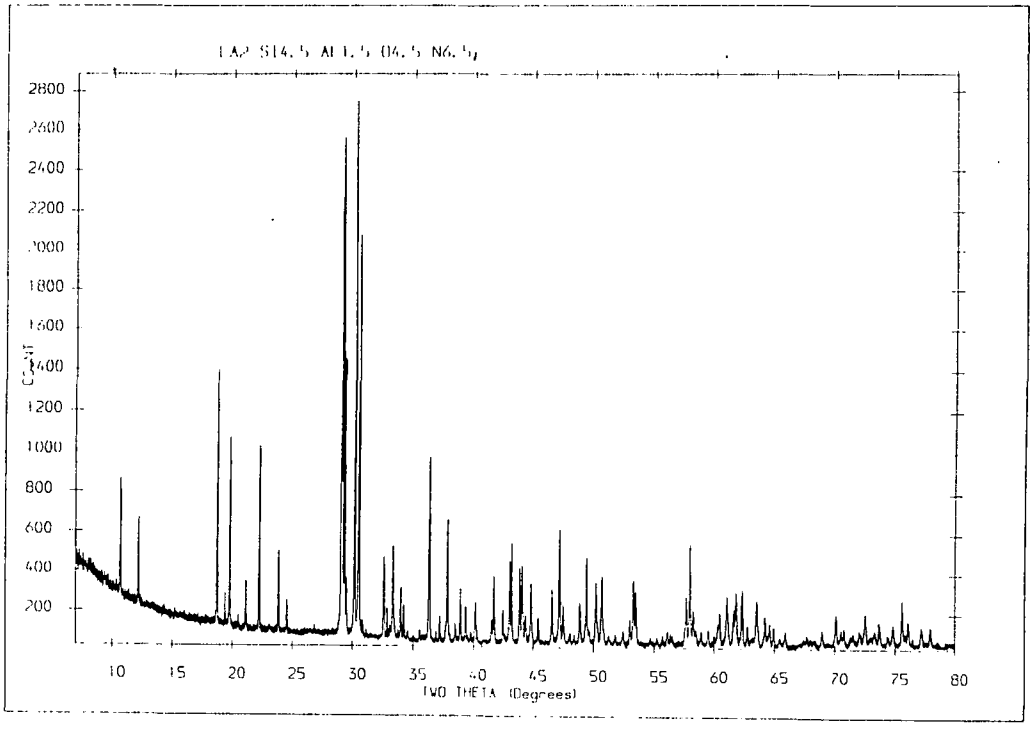

6.6 Group IIIa Metals

6.6.1 Lanthanum–139 NMR

Several attempts were made to obtain static and MAS ^{139}La NMR spectra of the La–Si–O–N phases. Initial attempts were thwarted by problems of probe-ringing, and a spin–echo sequence had to be used, as discussed in Section 4.1.1.

Static spectra were obtained from N–apatite (sample 6.4), N–YAM (sample 6.3), N–wollastonite (sample 6.2), new phase (sample 6.1) and oxide apatite (sample 6.6). The spectra were all very broad (FWHH>150 kHz) and featureless. A typical spectrum is shown in Figure 6.6.1. If it is assumed that only the central transition is being observed in this spectrum, then a FWHH of 150 kHz corresponds to a quadrupole coupling constant of 20–25 MHz.

Attempts to obtain MAS spectra using a rotation synchronised spin–echo sequence were unsuccessful.

Dupree *et al.*[11] have recently examined a series of La sialons by ^{139}La NMR, with similar results. They did, however, obtain a significantly narrower resonance from $LaAlO_3$, in which the La environment is of approximately cubic symmetry, and successfully narrowed the resonance using MAS. They calculate a value of 6 MHz for χ_Q in this phase.

6.6.2 Yttrium–89 NMR

Attempts were made to obtain ^{89}Y NMR spectra, but the very low Larmor frequency of the ^{89}Y nucleus proved an insurmountable obstacle on the spectrometers available. Dupree and Smith[26] have obtained ^{89}Y MAS NMR spectra on Y–Si–O and Y–Al–O phases, but have not yet reported any spectra on nitrogen containing phases, which could yield interesting structural information.

6.7 A Crystallographic Study of Lanthanum New Phase

The crystal structure of lanthanum new phase (and of the aluminium substituted analogue) was not known when this study commenced, and it was hoped that the ^{29}Si and ^{15}N NMR spectra of the phase would aid in the determination

Figure 6.7.2 Symmetry in the C2 space group

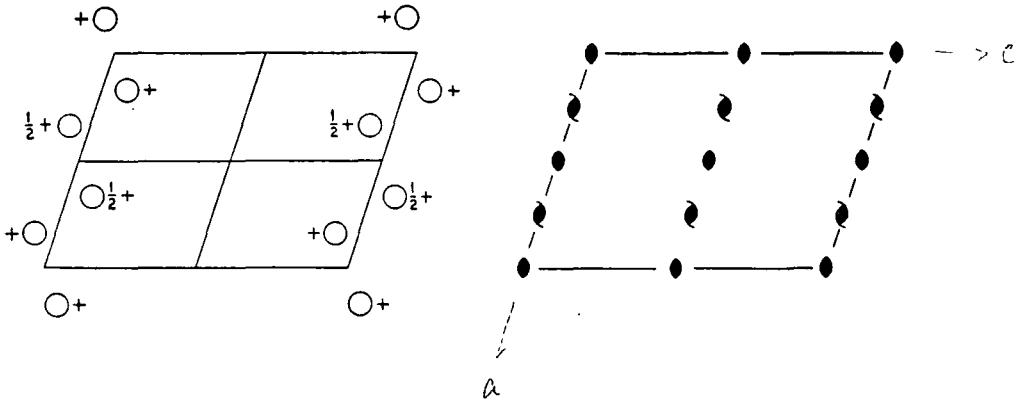

of the structure. Single crystals of the material were not available, so high quality synchrotron powder XRD data were obtained on the two samples (6.1 and 6.9) at SRS Daresbury (see Figure 6.7.1).

6.7.1 Lanthanum New Phase

The XRD pattern of new phase can be indexed on two equivalent monoclinic unit cells, with $\beta = 114^o$,[27] and $\beta = 117^o$.[2] The cell with $\beta = 117^o$ was arbitrarily chosen for further analysis. Line indices and intensities are listed in Table 6.7.1. The unit cell is clearly C face centred, because reflections with h+k odd are systematically absent. No other systematic absences are observed, and a space group of C2 (No. 5) was assumed (Figure 6.7.2).

In an attempt to obtain La and Si positions, a Patterson synthesis was undertaken on the intensity data listed in Table 6.7.1. The major density was found to lie in the $y = 0.0$ and $y = 0.5$ planes. Part of the map for $y = 0.0$ is shown in Figure 6.7.3. Only half of the unit cell is shown in the Figure: the other half, with $0.5 < x < 1.0$ is related to that with $0.0 < x < 0.5$ by the C_2 axis which passes through ($\frac{1}{2}$,0,$\frac{1}{2}$) parallel to y. Furthermore, as a consequence of the C centering, the map for $y = 0.5$ is related to that for $y = 0.0$ by the 2–fold screw axis which operates parallel to the y–axis, and passes through ($\frac{1}{4}$,0,$\frac{1}{2}$). Peaks in the map at the corners of the cell are always neglected.

The most intense peak in the map occurs at the point (0.12,0,0.66) and symmetry related points. The intensity of a peak is roughly proportional to the product of the scattering factors of the atoms which define the interatomic vector, and so is assigned to a La—La vector in this phase. If a La atom (La(1)) is assumed to occupy a point at the origin of the unit cell, then a further La (La(2)) at (0.12,0,0.66) would give rise to this peak in the Patterson map due to La(1)—La(2) interatomic vectors. The peak at (0.24,0,0.32) in the Patterson map can then be assigned to La(2)–La(2) vectors between adjacent atoms linked by the C_2 axis. Similar considerations lead to explanations of the peaks related by symmetry to these two peaks in the $y = 0$ plane. La positions in the half unit cell are shown in Figure 6.7.4.

There is a total of 6 La in the full unit cell, and three in the half cell. The ^{29}Si NMR suggested that it was most likely that there are four distinct Si environments,

Figure 6.7.3 Patterson map from XRD data from new phase through $y = 0$. Only $\frac{1}{2}$ of the unit cell is shown.

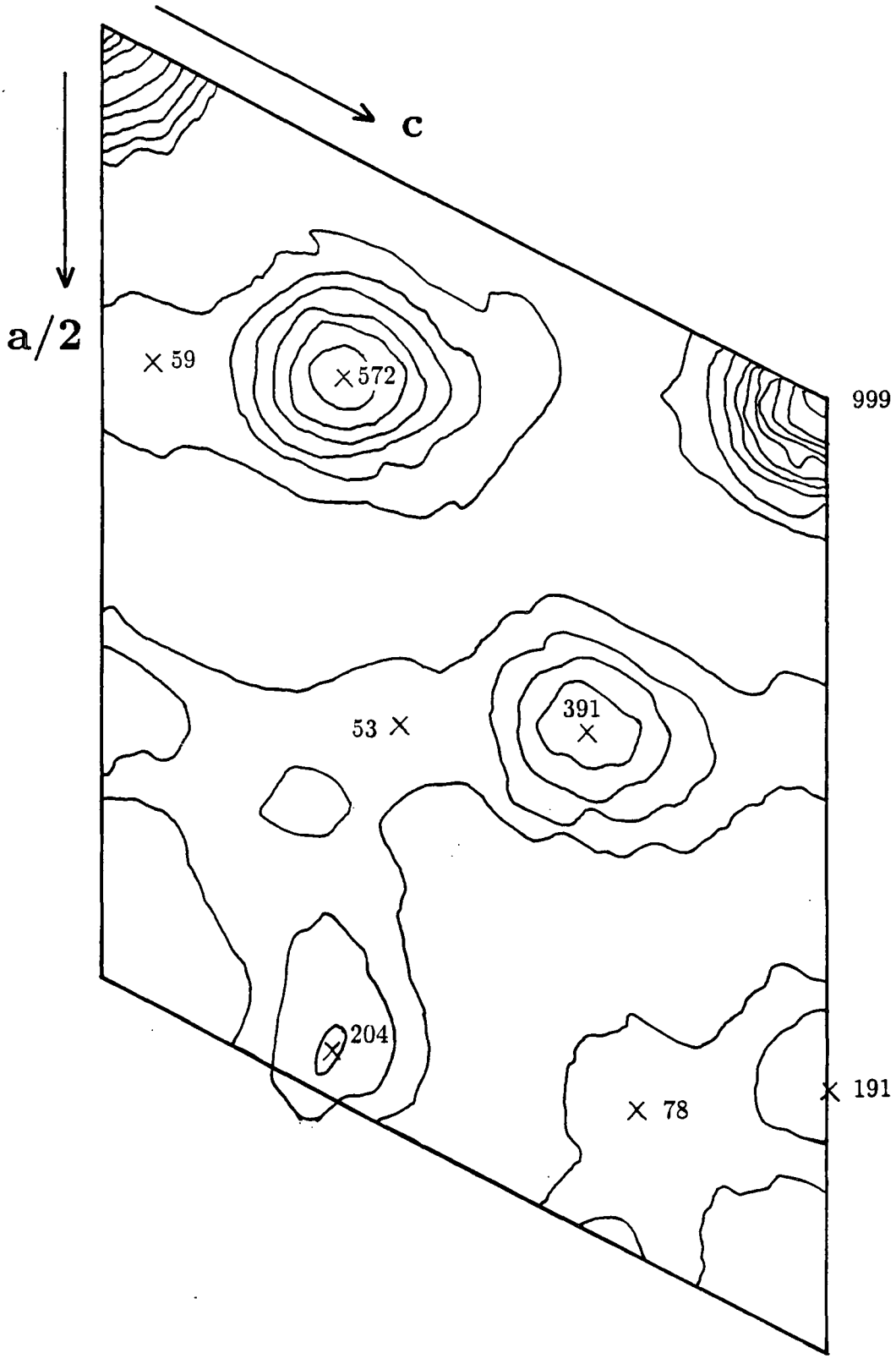

Table 6.7.1 h, k, l, and intensity (Io) data from powder XRD diffractogram of lanthanum new phase.

h	k	l	Io	h	k	l	Io	h	k	l	Io	h	k	l	Io	h	k	l	Io
0	0		6136	2	0	-1	4896	0	0	1	95	1	1	0	16805	4	0	-1	1253
0	1		11875	1	1	-1	2643	4	0	0	167	2	0	-2	10363	3	1	-1	0
1	1		5980	3	1	0	550	4	0	-2	2183	0	0	2	20	6	0	-1	27147
1	-2		34684	1	1	-2	18884	4	0	1	5208	5	1	-1	35192	3	1	1	34684
0	-2		1355	2	0	2	1148	6	0	0	1688	5	1	0	5924	5	1	-2	2787
1	2		9384	4	0	-3	3870	2	0	-3	3713	0	2	0	19015	6	0	-3	2126
0	3		12763	2	2	0	928	3	1	-3	133	2	2	-1	1695	0	2	1	750
1	-1		2459	8	0	-2	1606	5	1	1	2319	7	1	-2	224	8	0	-1	243
1	-3		983	6	0	1	1183	4	0	2	564	3	1	2	2071	1	1	-3	2452
2	-1		1806	2	2	1	6847	7	1	0	2573	4	2	0	626	8	0	-3	7500
2	-2		6803	8	0	0	5996	7	1	-3	5136	2	0	3	2968	4	2	-2	4190
2	2		161	1	1	3	6137	4	0	-4	1802	6	0	-4	6030	2	0	-4	601
2	-1		12537	4	2	1	4443	9	1	-2	1273	6	2	-2	491	9	1	-1	331
1	2		4310	10	0	-2	1524	2	2	2	883	7	1	1	1572	5	1	-4	6461
2	0		1120	3	1	-4	793	8	0	-4	1442	6	0	2	6705	9	1	-3	6685
0	-1		418	4	2	-3	1910	10	0	-3	542	2	2	-3	1360	8	0	1	3
0	4		138	7	1	-4	1539	3	1	3	55	4	0	3	607	1	1	-4	1246
2	-3		2445	9	1	0	7176	0	2	3	7168	8	2	-2	901	8	2	-1	177
2	1		575	4	2	2	364	10	0	0	770	10	0	-4	811	9	1	-4	878
3	0		1462	1	3	-1	776	8	2	-3	4626	11	1	-2	10939	1	1	4	1354
0	4		1287	6	0	-5	743	4	0	-5	660	8	2	0	4290	3	3	-1	74
3	1		420	2	2	3	1618	3	3	0	207	11	1	-3	50	7	1	2	1116
2	-4		1697	11	1	-1	547	8	0	-5	113	12	0	-2	1075	12	0	-3	41
1	1		852	5	1	3	1173	6	2	-4	3630	2	0	-5	48	5	1	-5	114
2	-4		446	8	0	2	410	3	3	-2	5638	1	3	-2	2155	5	3	-1	4649
1	-5		460	3	3	1	7409	6	0	3	417	12	0	-1	783	3	1	-5	7845
2	-2		1426	11	1	-4	0	10	0	1	43	5	3	0	833	5	3	-2	1082
2	-4		790	6	2	2	6126	1	3	2	1374	12	0	-4	1882	10	2	-1	879
0	-5		445	10	2	-3	922	8	2	1	308	0	2	4	234	11	1	0	29
1	4		3266	9	1	-5	1369	4	2	3	690	0	0	5	250	4	0	4	186
1	-5		1566	3	3	-3	5	7	3	-1	33	5	3	1	456	7	3	-2	259
3	-3		919	12	0	0	443	3	3	2	390	10	2	0	797	1	3	-3	374
1	-3		690	13	1	-2	68	10	2	-4	1759	7	3	0	0	11	1	-5	1693
1	2		25	12	0	-5	404	2	2	4	1257	6	2	-5	97	7	1	3	152
2	-5		851	6	0	-6	868	7	3	-3	748	14	0	-3	5	13	1	-4	409
0	-6		1312	1	3	3	1628	13	1	-1	957	14	0	-2	230				

Figure 6.7.4 La positions in new phase deduced from Figure 6.7.3.

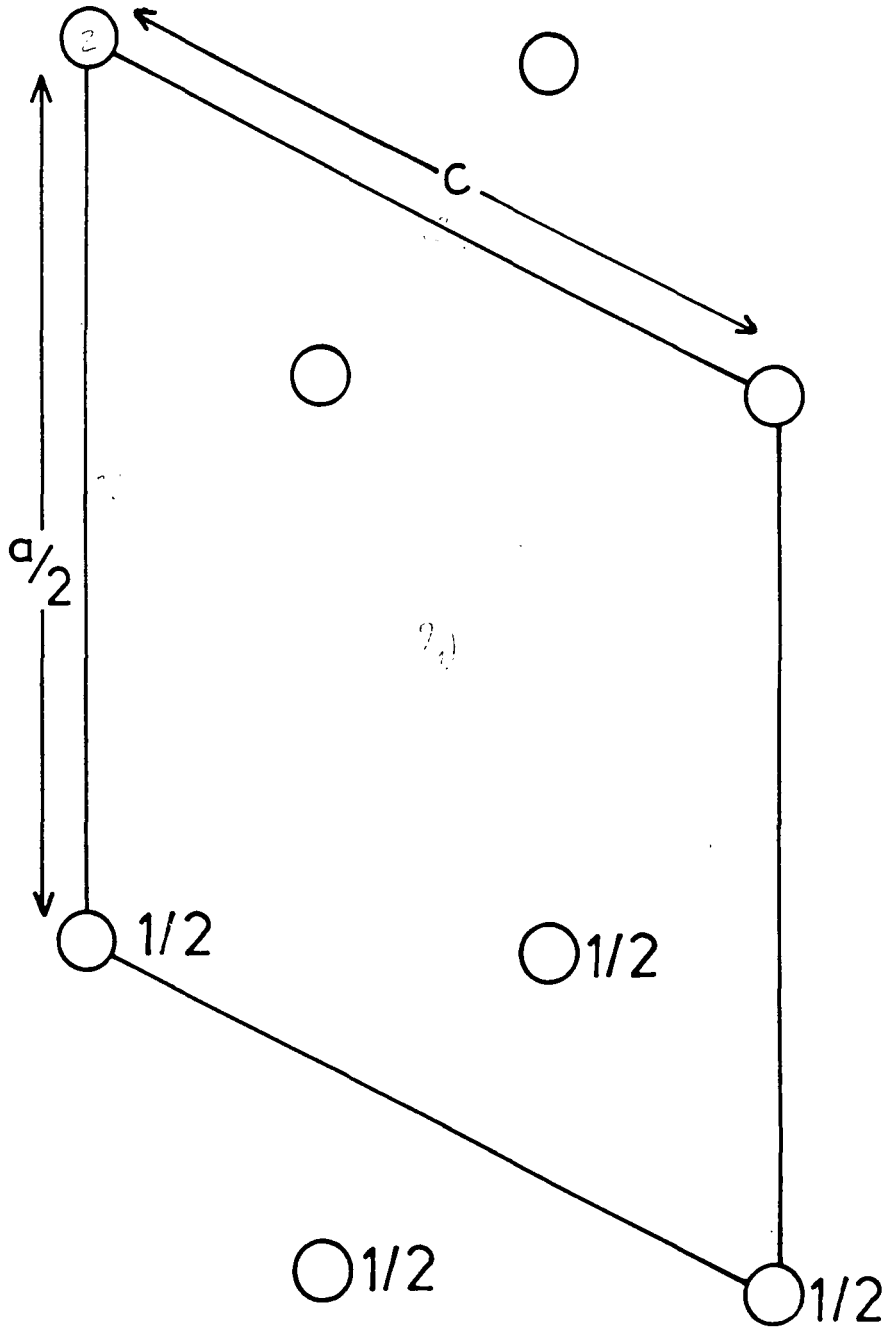

giving 2 peaks in a 3:1 ratio (the symmetry of the C2 space group rules out the possibility of only 2 distinct Si environments in a 3:1 ratio). In the half unit cell, assuming Si atoms do not occupy special sites, there will thus be 8 Si atoms. This implies that the correct composition of the phase is $La_3Si_8O_4N_{11}$: the composition with an M:X ratio closest to that of the originally proposed formula ($La_2Si_6O_3N_8$).

The Patterson map was used again, in an attempt to identify Si positions. There are peaks at (0.48,0,0.68) and (0.36,0,0.00) which are of lower intensity than the peaks assigned to La—La vectors, and these were assigned to La—Si vectors. These peaks were found not to be due to single La—Si vectors, but to superpositions of many such vectors. By examining graphically the effect of varying Si positions, a set of four Si positions was finally devised. O/N positions were then slotted into the La/Si framework to give sensible Si coordination numbers and Si–(O/N) distances, and by analogy with the structures of $LaSi_3N_5$ and U–phase. Nitrogen coordination was determined by reference to the ^{15}N MAS NMR spectrum, which suggested a 7:4 ratio in $[NSi_2]$:$[NSi_3]$ environments, and the trial structure predicted exactly this ratio. In the half unit cell, two nitrogen sites (N(7) and N(8)) are $[NSi_3]$, and five (including one, N(1) on a special site) $[NSi_2]$, of which 22% are occupied by oxygen. One site is coordinated to only one Si, and is assumed occupied by oxygen.

This structure was refined using Rietveld profile refinement in the range $10^o < 2\theta < 72^o$ on 179 reflections. All O and N atoms were assumed to have identical scattering factors. Final coordinates are listed in Table 6.7.2 together with other refined parameters. It is difficult to estimate errors in atom positions and other parameters, but in general, La coordinates are refined to a much higher degree of accuracy than say O or N. The final R indices indicate that the fit is good. The value of χ^2, 1.400, is to be compared with a value of 1.0, which would indicate that the fit is as good as could be expected for the data. The value of R_I is greater than found for typical single crystal refinements, but values of R_I from powder refinements can be larger for a number of reasons:

(i) Many parameters, such as anisotropic temperature factors, preferred orientation effects, site occupation factors and depolarisation were not included in the final refinement. When each of these factors was allowed to vary, it was found that their

Table 6.7.2 Final atomic coordinates for new phase determination

	x	y	z	B_{iso}	Occupancy
La(1)	0	-0.0546	0	1.46	0.5
La(2)	0.117	-0.0426	0.6598	1.06	1.0
Si(1)	0.0186	0.4300	0.3263	0.15	1.0
Si(2)	0.1507	0.4416	0.9902	0.15	1.0
Si(3)	0.2713	0.4300	0.8102	0.15	1.0
Si(4)	0.3030	0.0001	0.6125	0.15	1.0
N(1)	0	0.601	$\frac{1}{2}$	-0.02	0.5
N(2)	0.024	0.139	0.333	-0.02	1.0
N(3)	0.050	0.545	0.890	-0.02	1.0
N(4)	0.145	0.835	0.013	-0.02	1.0
N(5)	0.100	0.628	0.361	-0.02	1.0
N(6)	0.182	0.492	0.830	-0.02	1.0
N(7)	0.244	0.330	0.583	-0.02	1.0
N(8)	0.207	0.310	0.214	-0.02	1.0

S= 0.637×10^{-2} $a = 18.372$ Å $R_I = 7.48\%$

Z= 0.567 $b = 4.8645$ Å $R_{wp} = 15.86\%$

U= 203.6 $c = 7.8911$ Å $R_E = 13.40\%$

V= 3.449 $\beta = 117.03^o$ $\chi^2 = 1.400$

W= 15.135

$n = 0.621$

Figure 6.7.5 The crystal structure of La new phase projected along y

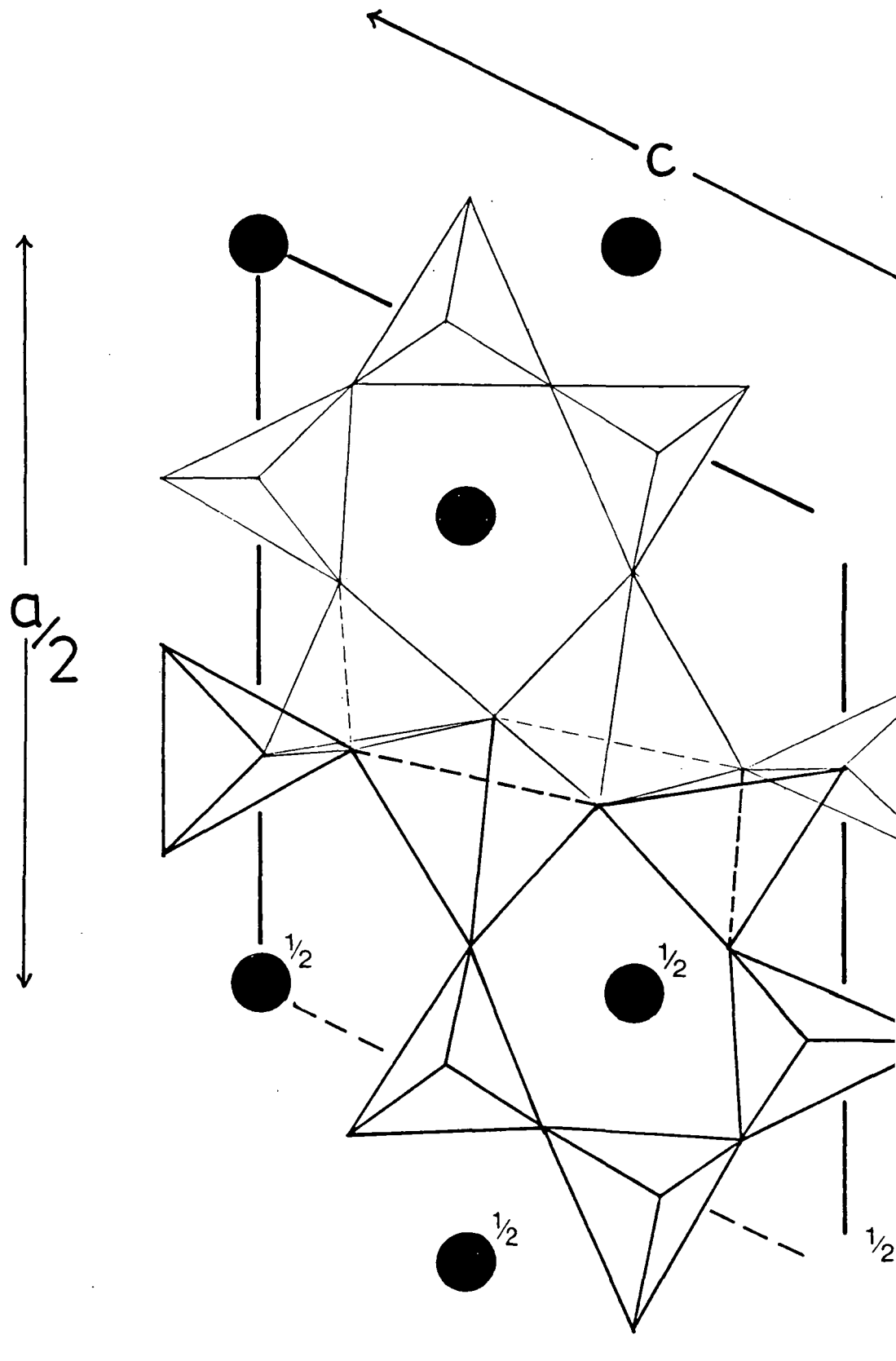

values fluctuated wildly whilst having little effect on χ^2. The overall effect of a large number (> 100) of individually negligible variations could be very significant.

(ii) No allowance was made for O/N ordering. Disorder could lead to variations in atom positions and other factors.

(iii) The linewidth and background functions used clearly did not fully describe the pattern.

(iv) No correction was made for the small amounts of crystalline impurities present (principally N–apatite and β–Si_3N_4, at estimated levels of 1–2% each), or any amorphous material.

Discussion

The structure of new phase, shown in Figure 6.7.5, is unique to the La and Ce sialon systems. No mineral analogues have been found. Main bond distances are listed in Table 6.7.3. Most distances are reasonable, but there is a rather large variation in some of the Si—N lengths. It is of course very difficult to obtain accurate O/N positions from XRD because of the low scattering factors of these atoms, and it is clear that there is some error in the O/N positions listed in Table 6.7.2. An attempt was made to refine the structure whilst keeping Si—N distances fixed at sensible values. This gave R_I=9.03%, indicating the lack of sensitivity in the refinement. Neutron diffraction is the ideal technique to obtain more accurate O/N positions.

The Si—N(2) bond length is particularly short. The N(2) site is coordinated to only one Si atom, and PSCR predicts that it will be occupied by oxygen, but the bond length is still 0.2 Å shorter than typical Si—O distances. Interestingly, in the refinement of Nd U–phase by Rietveld methods[28] a shortening of a structurally similar Si—O bond was noted. In the latter case, it was also found that R_I was very insensitive to Si—O distance.

There are also several long Si—N(7,8) bonds (> 1.85 Å). Nitrogen in these sites is three coordinate to silicon, so it would be expected that distances of around 1.7–1.8 Å would be found, by comparison with the structures of α– and β–Si_3N_4.[29–31]

Table 6.7.3 Bond distances in lanthanum new phase

oxygen →	La(1)–N(2)	2.631 Å	Si(1)–N(1) 1.764 Å
	La(1)–N(3)	2.469 Å	Si(1)–N(2) 1.416 Å
	La(1)–N(4)	2.671 Å	Si(1)–N(5) 1.686 Å
	La(1)–N(5)	3.020 Å	Si(1)–N(3) 1.691 Å
	La(2)–N(1)	2.603 Å	Si(2)–N(3) 1.730 Å
oxygen →	La(2)–N(2)	2.524 Å	Si(2)–N(4) 1.931 Å
	La(2)–N(3)	3.310 Å	Si(2)–N(6) 1.630 Å
	La(2)–N(4)	2.664 Å	Si(2)–N(8) 1.716 Å
	La(2)–N(5)	2.741 Å	Si(3)–N(4) 1.605 Å
	La(2)–N(6)	2.625 Å	Si(3)–N(6) 1.739 Å
	La(2)–N(7)	3.218 Å	Si(3)–N(7) 1.698 Å
	La(2)–N(8)	2.771 Å	Si(3)–N(8) 1.920 Å
			Si(4)–N(5) 1.818 Å
			Si(4)–N(7) 1.614 Å
			Si(4)–N(7) 1.888 Å
			Si(4)–N(8) 1.724 Å

The structure can be thought of as a composite structure. A single silicon, Si(1) occupies a site in a region rich in La and O. Coordination is to at least one oxygen (on the N(2) site), but possibly to more. The ^{29}Si chemical shift for this site would thus be expected to be more negative than for the other sites. The other three silicon atoms occupy a region of the structure which is rich in N, and relatively deficient in La; it is structurally rather similar to $LaSi_3N_5$. Si in these environments would be expected to resonate at a less negative chemical shift. This is in agreement with the ^{29}Si MAS NMR spectrum reported in Section 6.2.2.

The effect of counter-ion on δ_{Si} was discussed in Section 6.2.3; it was proposed that in the case of $LaSi_3N_5$, coordination to La is a crucial factor in determining δ_{Si}, and a similar effect can be seen in the spectrum of new phase. In this phase, $\frac{1}{4}$ of Si atoms are in a La rich environment, whereas in $LaSi_3N_5$, $\frac{2}{3}$ of Si atoms are in such an environment. The effect of oxygen in new phase at the N(2) site is to reduce the shortest La—La distance in the oxygen rich region to around 3.8 Å. The shortest La—La distance in $LaSi_3N_5$ is 4.4 Å; the phase has a much more uniform distribution of La. The effect of O/N coordination seems to be small in comparison with the effect of La coordination: probably a general observation in closed, partially covalent structures.

The ^{15}N MAS NMR is in total agreement with the structure, as mentioned above. [NSi_2] sites (N(1), N(3–6)) give rise to the broad peak at around 130 ppm, and the [NSi_3] sites (N(7), N(8)) to those peaks in the region of 64 ppm not due to β–Si_3N_4. New phase should give two peaks in the latter region if the effect of n.n.n. identity is neglected, and if the peak at 63.6 ppm is indeed due to β–Si_3N_4, then two other peaks can clearly be discerned. As with $LaSi_3N_5$, the higher frequency peak, is found to be significantly broader than the lower frequency peak, although in the case of new phase many more environments give rise to the composite peak. It seems likely, nevertheless, that the individual resonances in the higher frequency peak are broader, and this may be due to unaveraged (^{15}N,^{139}La) coupling.

6.7.2 Lanthanum Aluminium–New Phase

A Rietveld refinement was undertaken on XRD data from sample 6.9 in the range $10^o < 2\theta < 73^o$, 180 reflections, using the coordinates of Table 6.7.2 as a trial structure. No account was taken of Si/Al identity: all atoms on sites Si(1–4)

were assumed to have identical scattering factors. Details of refined parameters are listed in Table 6.7.4. Shifts in La and Si positions were generally $< \pm 0.2$ Å, although some larger shifts in N positions were noted. These were not considered significant in the light of the probable errors in atomic coordinates of these atoms.

If the interpretation of the ^{29}Si NMR spectrum is assumed to be the same as for the non-Al new phase, then Si and Al are effectively randomly distributed across the two types of Si environments (Si(1) and Si(2–4)). Aluminium might be expected preferentially to occupy the more oxygen rich sites, notably Si(1), but this is clearly not happening. The ^{29}Si spectrum is broad in comparison with that of the non-Al new phase, because of Si/Al disorder at the n.n.n. level.

No significant overall change is observed in δ_{Si} on incorporation of Al, despite the increase in oxygen content of the phase, and hence the effect of the identity of the n.n. silicon coordination on δ_{Si} in this structure is shown to be negligible.

The ^{15}N NMR spectrum shows that the ratio of $[NSi_2]$:$[NSi_3]$ environments is lower (1.5:1) than in the non-Al new phase (1.75:1). This is consistent with the increasing oxygen content of the phase. Oxygen would be expected to occupy solely the $[NSi_2]$ sites. If a formula $La_3Si_6Al_2O_6N_9$ is assumed for sample 6.9 (based on synthetic considerations) then a ratio of 1.25:1 would be expected for the two environments. It is possible that O could occupy a few $[NSi_3]$ sites, as for example in β'–sialons, but in that system, there are no 2–coordinate sites to occupy. It is more likely that the composition stated above is not quite correct.

The ^{27}Al MAS NMR spectrum of the phase (Section 6.5) is wholly consistent with the structure. Aluminium is present only in four coordinate environments, and the value of δ_{Al}^{300} implies that the environments are quite oxygen rich: in agreement with PSCR. The width of the resonance and the uncertainty as to whether all of the aluminium is being seen makes further interpretation of the spectrum difficult.

6.7.3 Concluding Remarks

This study illustrates nicely the strengths and weaknesses of XRD and MAS NMR in the study of materials of unknown structure. The XRD allowed La and Si positions to be determined to a considerable degree of accuracy, but O/N posi-

Table 6.7.4 Final atomic coordinates in aluminium new phase determination

	x	y	z	B_{iso}	Occupancy
La(1)	0	0.0000	0	1.75	0.5
La(2)	0.1175	0.0102	0.6550	0.83	1.0
Si(1)	0.0187	0.4748	0.3239	0.64	1.0
Si(2)	0.1503	0.4717	0.9960	0.64	1.0
Si(3)	0.2724	0.4960	0.8106	0.64	1.0
Si(4)	0.2978	0.0431	0.6074	0.64	1.0
N(1)	0	0.662	$\frac{1}{2}$	−1.80	0.5
N(2)	0.026	0.211	0.328	−1.80	1.0
N(3)	0.048	0.587	0.885	−1.80	1.0
N(4)	0.142	0.888	0.003	−1.80	1.0
N(5)	0.110	0.677	0.364	−1.80	1.0
N(6)	0.180	0.585	0.830	−1.80	1.0
N(7)	0.246	0.387	0.598	−1.80	1.0
N(8)	0.208	0.356	0.226	−1.80	1.0

S= 0.379×10^{-2} $a = 18.3448$ Å $R_I = 7.62\%$

Z= 0.501 $b = 4.9024$ Å $R_{wp} = 18.04\%$

U= 397.4 $c = 7.9240$ Å $R_E = 18.05\%$

V= −28.856 $\beta = 116.80^o$ $\chi^2 = 0.999$

W= 17.772

$n = 0.762$

tions could not be deduced to nearly the same degree. ^{29}Si and ^{15}N MAS NMR spectra gave important clues about the trial structure: number and type of crystallographically distinct environments, and the ^{15}N NMR also confirms that all three coordinate sites are occupied by nitrogen, and one coordinate sites by oxygen, with mixed occupation of two coordinate sites. Neither technique allows the distribution of O/N on the two coordinate sites and accurate anion coordinates to be determined. Neutron diffraction is the method of choice for these problems.

The ^{29}Si NMR spectra of the two samples confirm strongly that in closed, covalent structures, n.n. identity is not the most important factor in determining δ_{Si}. For example, introduction of extra oxygen in the aluminium containing phase does not lead to the expected negative shift in δ_{Si}. This question will be reexamined in Chapter 8.

Despite the expense, ^{15}N NMR of enriched sample is shown to be of considerable value in the study of the structures of nitrogen ceramics. The spectra provide powerful evidence for the correctness of the structure.

REFERENCES

1. Rae, A. W. J. M. Ph.D. Thesis, University of Newcastle upon Tyne, 1976.
2. Mitomo, M.; Izumi, F.; Horiuchi, S.; Matsui, Y. *J. Mater. Sci.* **17**, 2359–2364 (1982).
3. Marchand, R.; Jayaweera, A.; Verdier, P.; Lang, J. *C. R. Acad. Sci. Paris* **283**, C675–C677 (1983).
4. Smith, M. E. Ph.D. Thesis, University of Warwick, 1987.
5. Inoue, Z.; Mitomo, M.; Ii, N. *J. Mater. Sci.* **15**, 2915-2920 (1980).
6. Dupree, R.; Lewis, M. H.; Smith, M. E. *J. Am. Chem. Soc* **110**, 1083–1087 (1988).
7. Carduner, K. R.; Carter III, R. O.; Rokosz, M. J.; Peters, C.; Crosbie, G. M.; Stiles, E. D. *Chem. Mater.* **1**, 302–307 (1989).
8. Felsche, J. *Str. Bond.* **13**, 100–197 (1973).
9. Mägi, M.; Lippmaa, E.; Samoson, A.; Engelhardt, G.; Grimmer, A. -R. *J. Phys. Chem.* **88**, 1518–1522 (1984).
10. Harris, R. K.; Leach, M. J.; Thompson, D. P. *Chem. Mater.* **1**, 336–338 (1989).
11. Dupree, R.; Lewis, M. H.; Smith, M. E. *J. Am. Chem. Soc.* **111**, 5125–5132 (1989).
12. Hatfield, G. R.; Carduner, K. R. *J. Mater. Sci.* **24**, 4209–4219 (1989).
13. Fernie, J. A.; Lewis, M. H.; Leng-Ward, G. *Mater. Sci. Eng. Lett.* **9**, 29 (1989).
14. Engelhardt, G.; Michel, D. *High Resolution Solid-State NMR of Silicates and Zeolites*; Wiley: Chichester, U.K. 1987. Chapter 5.
15. Apperley, D. C. Internal Report, University of Newcastle upon Tyne, 1987.
16. Aujla, R. S.; Leng-Ward, G.; Lewis, M. H.; Seymour, E. F. W.; Styles, G. A.; West, G. W. *Phil. Mag. B* **54**, L51–L56 (1986).
17. Leach, M. J. Internal Report, University of Durham, 1988.
18. Janes, N.; Oldfield, E. *J. Am. Chem. Soc.* **107**, 6769–6775 (1985).
19. Gordy, W.; Thomas, W. J. O. *J. Chem. Phys.* **24**, 439–444 (1956).
20. Roult, R.; Backer, P.; Liebant, G.; Marchand, R.; Goursat, P.; Laurent, Y. *Acta Crystallogr. A* **40**, C226 (1984).

21. See for example the discussion in Douglas, B.; McDaniel, D. H.; Alexander, J. J. *Concepts and Models in Inorganic Chemistry*; Second Edition; John Wiley: New York, 1983. pp 197–198.

22. Bunker, B. C.; Tallant, D. R.; Balfe, C. A.; Kirkpatrick, R. J.; Turner, G. L.; Reidmeyer, M. R. *J. Am. Ceram. Soc.* **70**, 675–681 (1987).

23. Lippmaa, E.; Samoson, A.; Mägi, M. *J. Am. Chem. Soc.* **108**, 1730–1735 (1986).

24. Turner, G. L.; Chung, S. E.; Oldfield, E. *J. Magn. Reson.* **64**, 316–324 (1985).

25. Han, O. H.: Timken, H. K. C.; Oldfield, E. *J. Chem. Phys.* **89**, 6046–6052 (1988).

26. Dupree, R.; Smith, M. E. *Chem. Phys. Lett.* **148**, 41–44 (1988).

27. Mah, T. -I.; Mazdiyasni, K. S.; Ruh, R. *J. Am. Ceram. Soc.* **62**, 12–16 (1979).

28. Grins, J.; Käll, P. -O.; Liddell, K.; Korgul, P.; Thompson, D. P. In Preparation.

29. Grün, R. *Acta Crystallogr.* **B35**, 800–804 (1979),

30. Kato, K.; Inoue, Z.; Kijima, K.; Kawada, I, Tanaka, H.; Yamane, T. *J. Am. Ceram. Soc.* **58**, 90–91 (1975).

31. Marchand, M.; Laurent, Y.; Lang, J.; Le Bihan, M. Th. *Acta Crystallogr.* **B25**, 2157–2160 (1969).

Chapter VII

NMR Studies of Wurtzite Phases

There are series of Li– and Mg–containing nitrogen ceramic phases with structures which are based on the wurtzite (and AlN) structure. The ordering of Si and other metals on the metal sites leads to orthorhombic unit cells, as discussed in Section 3.1.5. The structures of all of the phases have been fully characterised, and the main aim of studying them was therefore to provide data on systems in which the atom environments are known, for comparison with phases studied in the other chapters in this Thesis, in the hope of further defining characteristic chemical shift ranges.

7.1 Synthesis

Preparation and purity of samples for this Chapter are summarised in Table 7.1.1. Wurtzite phases were found to be straightforward to prepare at low temperatures.

Non-enriched $MgSiN_2$ (sample 7.2) was prepared by nitridation of a mix of 2Mg + Si at a low temperature. The reaction is thought to proceed via formation of magnesium silicide (Mg_2Si) at $\sim 600^oC$.[1,2] It was therefore important to increase the temperature very slowly below 650^oC, the temperature at which Mg metal melts. Reaction was completed by nitriding Mg_2Si by slowly raising the temperature to 1400^oC. At this temperature, free Mg metal formed by nitridation of Mg_2Si is lost as $Mg(v)$, leaving essentially pure $MgSiN_2$.

$MgSi^{15}N_2$ had to be prepared from α–$Si_3^{15}N_4$. This was effected by preparing Mg_3N_2 *in situ* by nitridation of a mix of Mg + α–$Si_3^{15}N_4$. An excess of Mg was found to be necessary, as significant amounts are lost by decomposition of Mg_3N_2 to give $Mg(v) + N_2$ during the subsequent reaction between Mg_3N_2 and α–$Si_3^{15}N_4$. Any excess Mg_3N_2 decomposes at 1400^oC to leave essentially pure $MgSi^{15}N_2$.

Table 7.1.1 Synthesis of wurtzite materials

Sample no.	phase	Preparation					XRD analysis
		Mix	Furnace	T/°C	Time/h	Notes	
7.1	LiSiON	A	C	1400	0.25		LiSiON(s); α-Si_3N_4(w);Li_2SiO_3(w)
7.2	$MgSiN_2$	AH	C	1420	2.0	1,2,	$MgSiN_2$
7.3	$MgSiAlN_3$	AH	C	1400	0.50	1,2	$MgSiAlN_3$(s); AlN(w); Si_3N_4(w) $MgSiN_2$(tr)
				1700	0.50		
7.4	$LiSiO^{15}N$	A	C	1400	0.25		LiSiON(s); Li_2SiO_3(w);α-Si_3N_4(vw)
7.5	$MgSi^{15}N_2$	AH	C	1400	2.00	2,3	$MgSiN_2$(vs); MgO(w)
7.6	$MgSiAl^{15}N_3$	AH	C	1750	1.00		$MgSiAlN_3$(vs); ?(w); AlN(vw)
7.7	$LiSi_2N_3$						$LiSi_2N_3$

1. Nitridation of 2Mg + Si; 2. Very slow heat-up; 3. Nitridation of Mg + Si_3N_4.

$MgSiAlN_3$ was prepared either by reaction of $MgSiN_2$ and AlN, or by nitridation of a 2Mg + Si + AlN mix.[3]

LiSiON was prepared by the reaction of $2Li_2CO_3$ + α–Si_3N_4 + SiO_2 at temperatures below 1400^oC. Above this temperature, melting occurs, and recrystallisation leads to formation of other phases (e.g. Li_2SiO_3) in preference to the oxynitride.

7.2 Silicon–29 NMR

Silicon n.n. coordination in all of the phases except LiSiON is $[SiN_4]$. In LiSiON, the environment is $[SiON_3]$. Silicon–29 data is summarised in Table 7.2.1, and spectra are shown in Figure 7.2.1.

Table 7.2.1 NMR data on wurtzite phases.

Phase	Sample	Silicon–29		Nitrogen–15		
		δ_{Si}/ppm	FWHH/Hz	δ_N/ppm	FWHH/Hz	Intensity
LiSiON	7.1	-51.0	70	—	—	—
LiSiON	7.2	-50.0	80	54.4	25	—
$LiSi_2N_3$	7.7	-49.0	150	—	—	—
$MgSiN_2$	7.2	-44.5	60	—	—	—
$MgSiN_2$	7.5	-44.1	50(1)	65.5	25	1
				76.7	25	1
$MgSiAlN_3$	7.3	-47.8	570	—	—	—
$MgSiAlN_3$	7.6	-47.2	350	45.0	500	3
				70.2	500	4

1. Single transient.

The chemical shift range observed in the four phases is very narrow, suggesting that the environments are geometrically and electronically similar. The shift observed from LiSiON is the most negative of the four, as might be expected from consideration of n.n. environments, but the difference between the shifts of

Figure 7.2.1. Silicon–29 MAS NMR spectra of

(a) $LiSi_2N_3$ (Sample 7.7) SF=59.6 MHz: PA=90^O; NT=100; RD=120 s; SR=3.90 kHz: AF=0.01 s.

(b) LiSiON (Sample 7.1) SF=59.6 MHz: PA=90^O; NT=232; RD=120 s; SR=3.28 kHz; AF=0.02 s.

(c) $MgSiN_2$ (Sample 7.2) SF=59.6 MHz: PA=18^O; NT=204; RD=120 s; SR=3.38 kHz; AF=0.05 s.

(d) $MgSiAlN_3$ (Sample 7.3) SF=59.6 MHz: PA=18^O; NT=532; RD=120 s; SR=3.20 kHz: AF=0.007 s.

(e) $MgSiAlN_3$ (Sample 7.6) SF=59.6 MHz: PA=27^O; NT=61; RD=300 s; SR=3.23 kHz; AF=0.007 s.

The shoulder on spectrum (a) is thought to be due to small amounts of impurity LiSiON.

n Li_2SiO_3

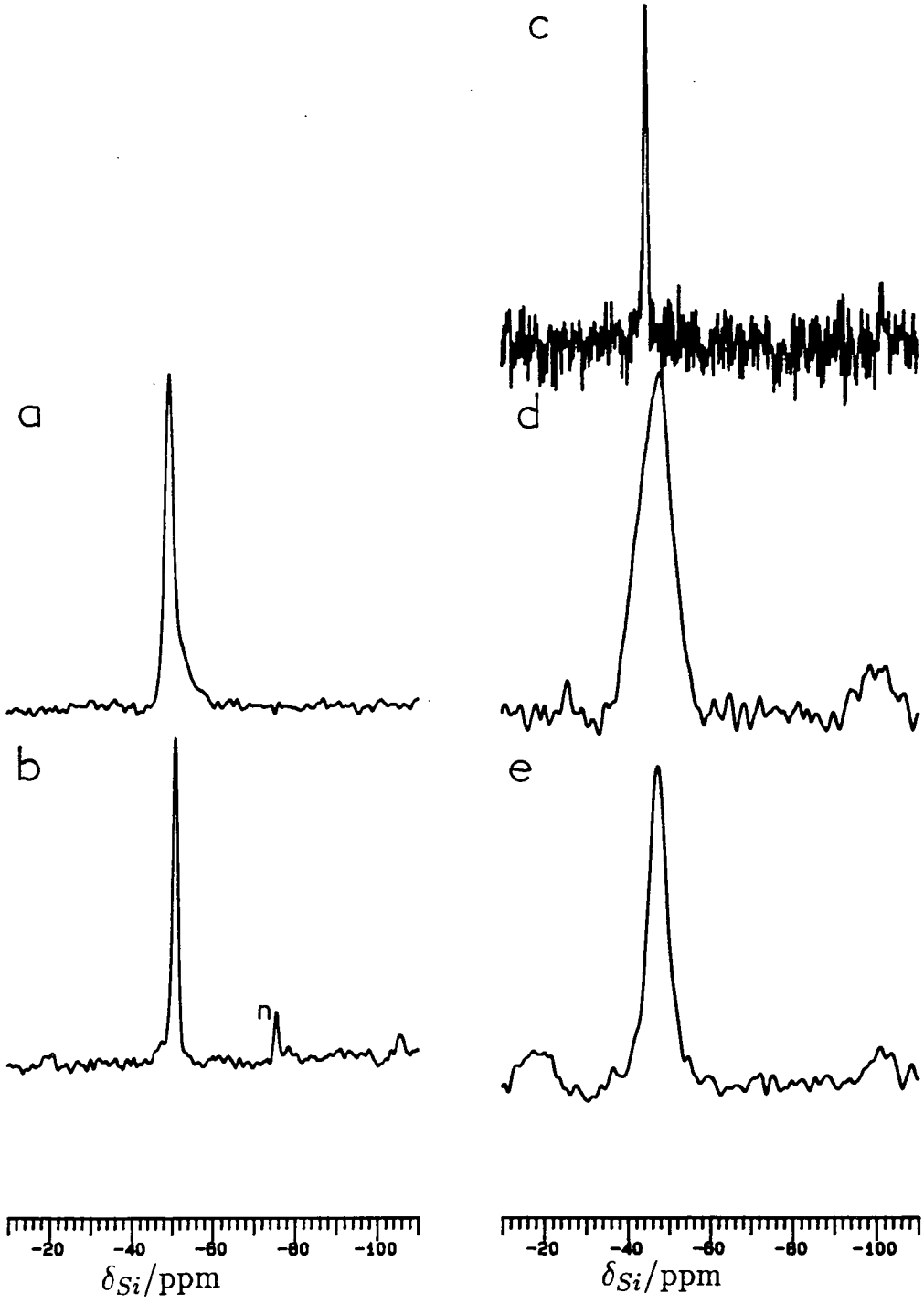

$LiSi_2N_3$ and LiSiON is surprisingly small: 1–2 ppm for substitution of a single oxygen for nitrogen in the n.n. coordination sphere. The correlation of Figure 6.2.10 suggests that a shift of > 10 ppm would be expected. This finding is in total agreement with the proposition discussed in Chapter 6, that in basically covalent structures, change in coordination environment is not the principal factor in determining chemical shift.

The chemical shifts observed from $MgSiN_2$ and $MgSiAlN_3$ are unremarkable, and consistent with the known Si n.n. environment and the structure type (covalent nitride).

$MgSiN_2$, $LiSi_2N_3$ and LiSiON all give very narrow ^{29}Si resonances, consistent with the fully ordered crystal structures of the phases. The ^{15}N enriched samples of $MgSiN_2$ and LiSiON gave spectra with very similar linewidths to the unenriched samples, indicating that, as before, unaveraged (^{29}Si,^{14}N) coupling is not responsible for significant line-broadening.

$MgSiAlN_3$ gives rise to a very broad ^{29}Si resonance, with line-broadening caused principally by chemical shift dispersion. This is in agreement with the crystal structure determination,[3] which proposes that Si and Al are fully disordered on the Si/Al sites. The ^{29}Si linewidth of 570 Hz (9.5 ppm) from sample 7.3 is the largest observed from a crystalline phase in this Thesis. It is clear from FWHH measurements of δ_{Si} that the two samples of $MgSiAlN_3$ (7.3 and 7.6) are of somewhat different compositions. A range of compositions for this phases has been proposed[3,4] as $MgSiN_2$—$MgSiAlN_3$—AlN, although the exact degree of homogeneity has not been determined.

7.3 Nitrogen–15 NMR

Nitrogen–15 NMR spectra are shown in Figure 7.3.1, and data were listed in Table 7.2.1. Marshall *et al.*[5] have reported δ_N for AlN of 64 ppm from an unenriched sample. All of the nitrogen chemical shifts for four-coordinate nitrogen in this Chapter are thus found to lie in the narrow range 45–77 ppm, essentially the same range as for [NSi_3] coordination outlined in Figure 6.3.3.

$MgSiN_2$ gives rise to two very narrow resonances with a 1:1 intensity ratio.

Figure 7.3.1 Nitrogen–15 MAS NMR Spectra of

(a) LiSiON (Sample 7.4) SF=30.4 MHz: PA=24^{O}; NT=62; RD=300 s; SR=2.90 kHz: AF=0.05 s.

(b) $MgSiN_2$ (Sample 7.5) SF=30.4 MHz: PA=23^{O}; NT=62; RD=300 s; SR=3.68 kHz.

(c) $MgSiAlN_3$ (Sample 7.6) SF=30.4 MHz: PA=30^{O}; NT=258; RD=300 s; SR=3.50 kHz; AF=0.01 s.

The shoulder on the spectrum of (a) is due to impurity Si_3N_4.

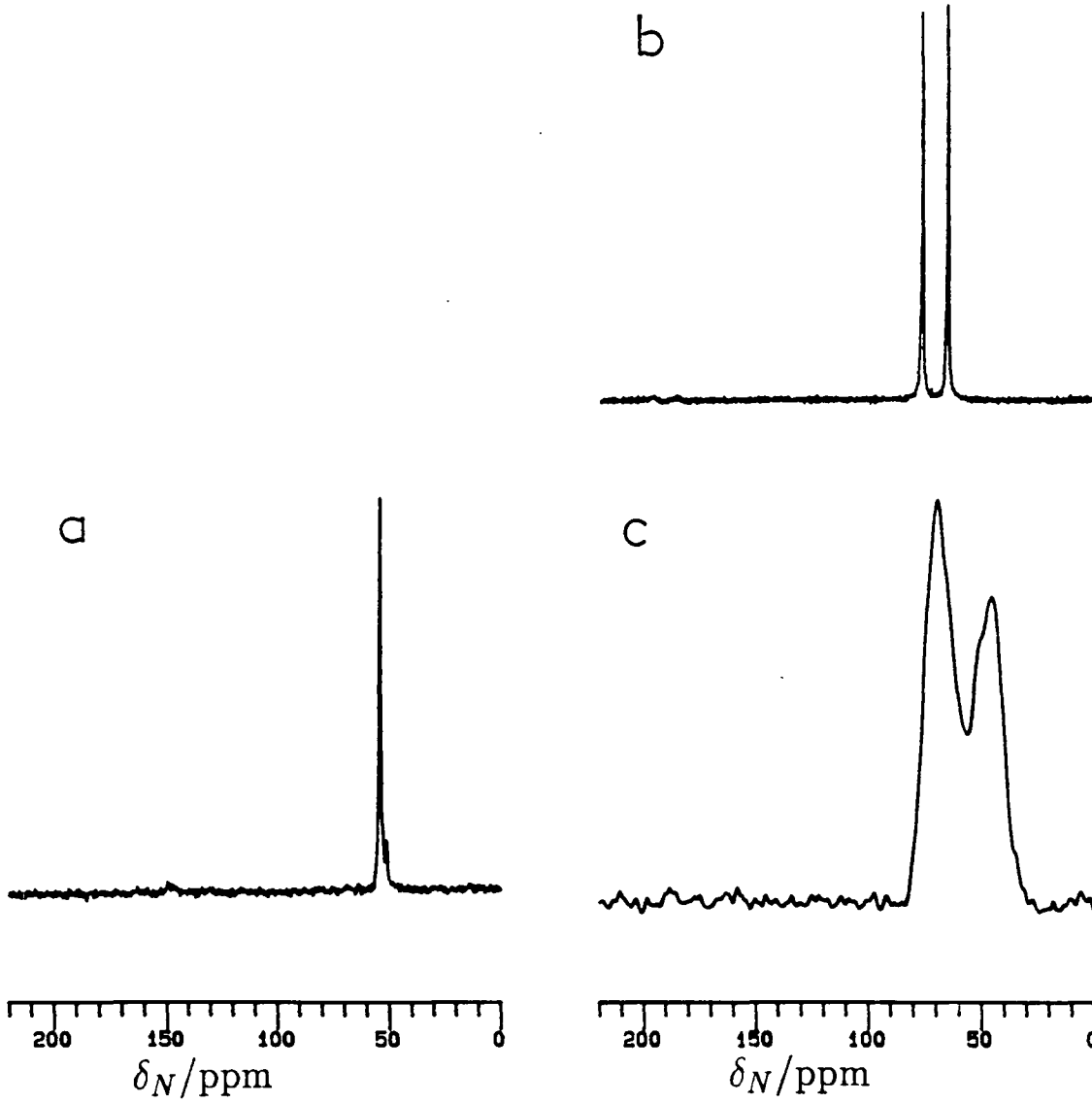

This corresponds with the crystal structure (see Section 3.1.5), in which nitrogen is present in two distinct [NSi_2Mg_2] environments. As in silicon nitrides, δ_N is seen to be extremely sensitive to changes in crystallographic environment. The resonances are both narrower than observed in silicon nitride and oxynitride, indicating a high degree of crystalline order.

The resonance from LiSiON is at a more negative shift than from $MgSiN_2$, and is as narrow. A similar shift in δ_N was observed in Si_2N_2O in comparison with Si_3N_4, indicating that n.n.n. coordination to oxygen may have a general deshielding effect.

The spectrum of $MgSiAlN_3$ is more difficult to account for. Two broad peaks of approximately equal intensity are observed, with some sub-structure in the peaks also apparent. The crystal structure indicates two nitrogen environment types: [NMg2(Si,Al)$_2$] and [NMg(Si,Al)$_3$], in a 1:2 ratio. One explanation of the spectrum is that the more intense peak, at 70.2 ppm is due to [NMg(Si,Al)$_3$],and the less intense peak, at 45.0 ppm to [NMg_2Si_2]. This would suggest that the phase contains rather less AlN than indicated by the formula, in agreement with the ^{27}Al NMR, which shows the presence of AlN in the sample. If the observed intensities are assumed quantitative, a 3:4 peak ratio then corresponds to a formula of $Mg_2Si_2AlN_5$. The broadness and structure of the resonances in this model are due to Si/Al disorder.

This interpretation is not fully consistent, however: it would lead one to expect that decreasing Mg coordination gives a more positive δ_N, yet the nitrogen chemical shift of AlN is 64 ppm, midway between the two observed resonances of $MgSiAlN_3$. The above model assumed that the number of Mg n.n. is the most important factor determining δ_N. It is not possible to argue that Si or Al n.n. coordination is the most important factor determining δ_N, because a single peak in the ^{15}N NMR would then be expected (assuming random Si/Al distribution). It is possible that the identity of n.n. atoms is not of importance, and that variations in bond angles and lengths are the major factors affecting δ_N in this phase.

Discussion

It has already been mentioned that nitrogen in tetrahedral (sp^3) and planar

Figure 7.4.1 Aluminium–27 MAS NMR spectrum of $MgSiAlN_3$ (Sample 7.6)
SF=78.2 MHz: PA=15°; NT=120; RS=1 s; Sr=10.10 kHz; AF=0.005 s.
No background subtracted.

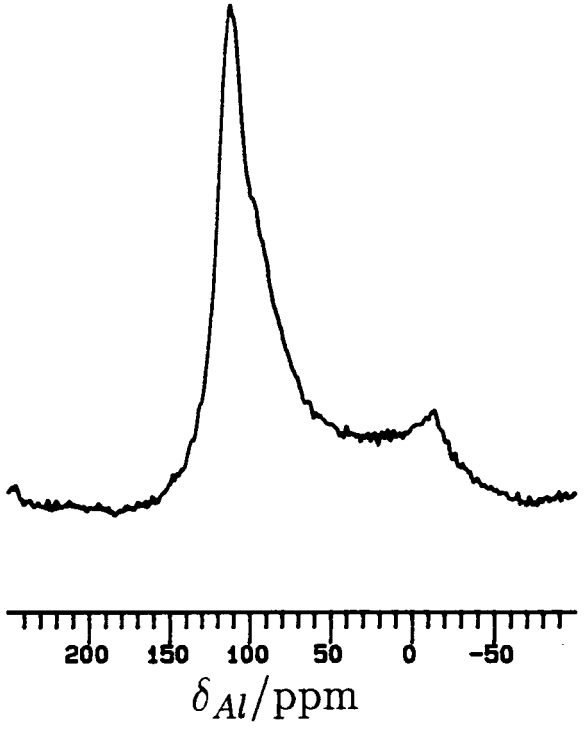

(sp^2) covalent coordination environments give rise to essentially indistinguishable chemical shifts, which are far removed from those from [NSi_2] environments, in which N is also coordinated to basically ionic moieties. This implies that the electron densities on the sp^2 and sp^3 nitrogens in covalent structures are very similar, and confirms that Li and Mg bond covalently in these materials. This is perhaps unsurprising, and is also found in ^{17}O NMR, but contrasts with ^{29}Si and ^{27}Al NMR, where 4- and 6-coordinate environments can be readily distinguished. It is concluded that δ_N provides an excellent measure of the degree of ionicity of a particular environment. A similar trend is found in solution-state ^{15}N NMR. Data from compilations by Mason,[6] show that δ_N(M≡N) lies in the range 350–750 ppm, whilst δ_N(M=NR) is in the range 200–400 ppm, and δ_N(M←NR_3) is in the range−50–+100 ppm.

7.4 Quadrupolar Nuclei

7.4.1 Aluminium-27 NMR

There have been several reports of the ^{27}Al MAS NMR spectrum of AlN. Early studies[5,7] reported δ_{Al}=110 ppm (ν_L = 78.2 MHz), but made no correction for quadrupole coupling. More recently, Dupree *et al.*[8] have reported an uncorrected shift of 113 ppm (ν_L = 93.93 MHz). Han *et al.*[9] report a corrected shift of 115 ± 1 ppm and $\chi_Q \approx 2.2$ MHz (for $\eta_Q = 0$) from measurements at $\mathbf{B_0}$ fields of 11.7 T and 8.45 T, but their error in χ_Q is large, given the stated errors in observed aluminium chemical shifts.

Hayashi *et al.*[10] have used ^{27}Al MAS NMR to characterise the hydrolysis of AlN by surface moisture, observing the growth of peaks in the region 0–10 ppm due to formation of $Al(OH)_3$, in which Al is 6-coordinate.

The spin-lattice relaxation behaviour of AlN was investigated at a Larmor frequency of 52.1 MHz. Two component relaxation was observed for the central transition, with a short component characterised by T_1=0.5(1) s, and a long component by T_1=5.2(5) s, in a 2:5 ratio. This behaviour could be caused by surface effects, but is most likely caused by the effect of the other energy levels, which can cause multiexponential decay.

Figure 7.4.2 Lithium–7 NMR spectra of

(a) LiSiON (Sample 7.1) SF=77.8 MHz; PA=23^{O}; NT=16; RD=30 s. SR=3.12 kHz.

(b) $LiSi_2N_3$ (Sample 7.7) SF=77.8 MHz; PA=23^{O}; NT=16; RD=30 s; SR=3.24 kHz.

(c) LiSiON (Sample 7.1) SF=77.8 MHz; PA=45^{O}; NT=16; RD=30 s; static.

(d) $LiSi_2N_3$ (Sample 7.7) SF=77.8 MHz; PA=45^{O}; NT=16; RD=30 s; static.

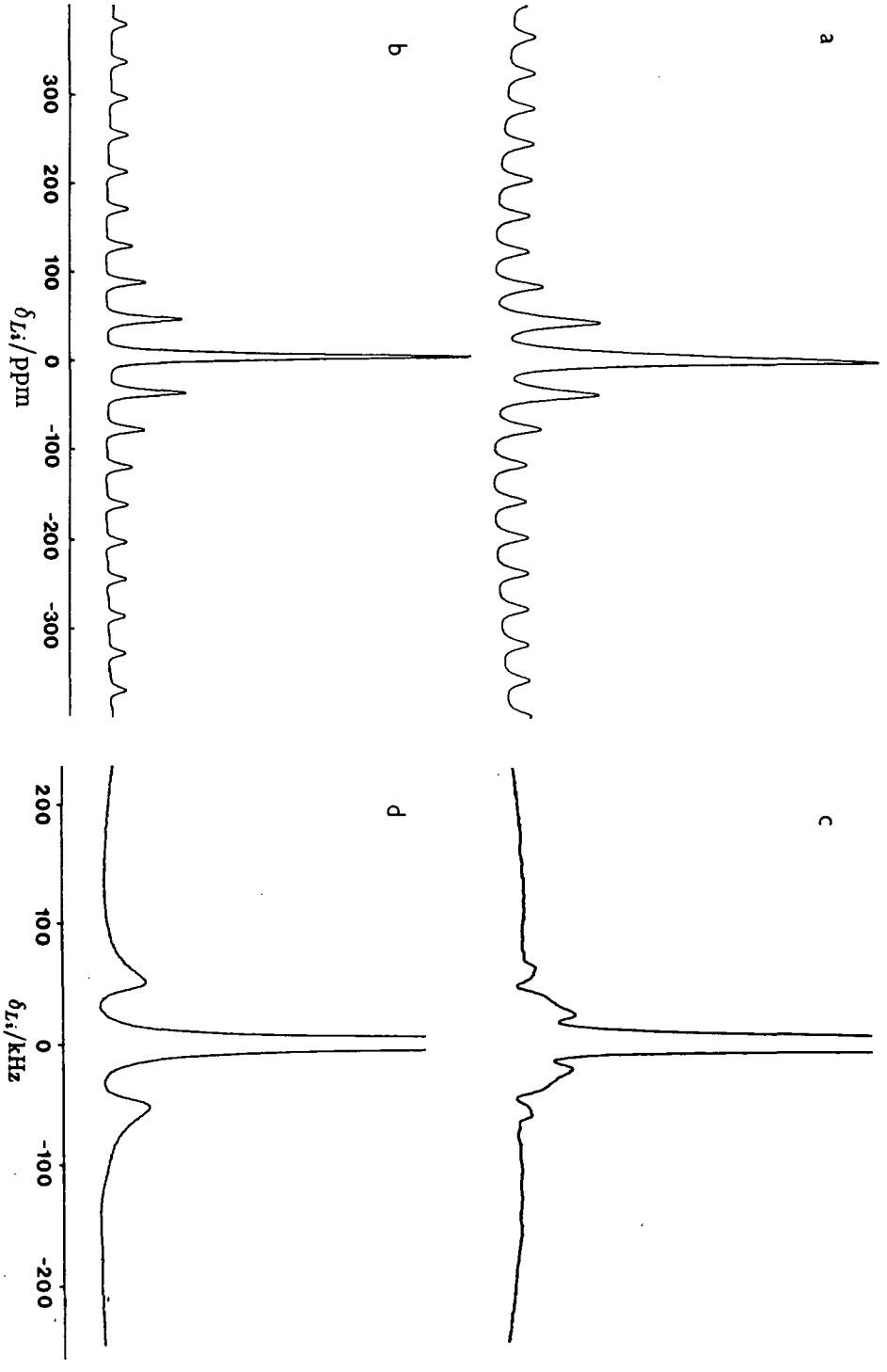

The ^{27}Al MAS NMR spectrum of $MgSiAlN_3$ (sample 7.6) is shown in Figure 7.4.1. The main peak, at 108 ppm is probably due to impurity AlN, but the shoulder at ~95 ppm is provisionally assigned to $MgSiAlN_3$, with an observed aluminium chemical shift characteristic of an $[AlN_4]$ environment.

7.4.2 Lithium–7 NMR

Samples of $LiSi_2N_3$ and LiSiON were examined by ^7Li MAS and static NMR, and the resulting spectra are shown in Figure 7.4.2. The ^7Li chemical shift range is known to be small,[11] and this is confirmed by the MAS spectra, which give $\delta_{Li}^{200} =$ 3.2 ppm for LiSiON, and $\delta_{Li}^{200} = 5.1$ ppm for $LiSi_2N_3$; with linewidths of ~600 Hz. These values of the chemical shifts are insignificantly different, and it seems unlikely that ^7Li MAS NMR can be used to characterise lithium environments.

The static spectra show well-resolved satellite peaks due to $(\pm\frac{3}{2}, \pm\frac{1}{2})$ transitions, which can be used to estimate values of χ_Q. The spectrum of $LiSi_2N_3$ shows satellite peaks at ±52 kHz, and the separation of these peaks corresponds to a value of $\chi_Q \sim 200$ kHz. The spectrum of LiSiON is more complex, and some of the satellite peaks may be due to the Li_2SiO_3 impurity. On this basis, the most intense pair of satellites give $\chi_Q \sim 90$ kHz, and the less intense pair give $\chi_Q \sim 250$ kHz. It seems that quadrupole coupling constants in ^7Li NMR could be used to characterise Li environments in a similar manner to studies on ^{17}O and other quadrupolar nuclei, but the factors which affect χ_Q cannot be discerned in such a narrow study.

REFERENCES

1. David, J.; Laurent, Y.; Lang, J. *Bull. Soc. Fr. Cristallogr.* **93**, 153–159 (1970).
2. David, J.; Lang, J. *C. R. Acad. Sci. Fr.* **261**, 1005 (1965).
3. Perera, D. S. Ph.D. Thesis, University of Newcastle upon Tyne, 1976.
4. Thompson, D. P. *Mat. Sci. For.* **47**, 21–42 (1989).
5. Marshall, G. L.; Harris, R. K.; Apperley, D. C.; Yeung, R. *Science of Ceramics* **14**, 347–352 (1987).
6. Mason, J. *Multinuclear NMR*; Mason, J. Ed.; Plenum, New York, 1987. Chapter 12.

7. Butler, N. D.; Dupree, R.; Lewis, M. H. *J. Mater. Sci. Lett.* **3**, 369–370 (1984).

8. Dupree, R.; Lewis, M. H.; Smith, M.E. *J. Appl. Cryst.* **21**, 109-116 (1988).

9. Han, O. H.; Timken, H. K. C.; Oldfield, E. *J. Chem. Phys.* **89**, 6046–6052 (1988).

10. Hayashi, S.; Hayamizu, K.; Yamamoto, O. *Bull. Chem. Soc. Jpn.* **60**, 761–762 (1987).

11. Akitt, J. W. Reference 6. Chapter 7.

Chapter VIII

α'– and β'–Sialon Ceramics

The structures of α'– and β'–sialons are closely related to those of α– and β–Si_3N_4, but there are many unresolved structural questions, notably the Si/Al and O/N ordering patterns.

8.1 Synthesis and Characterisation

Syntheses of samples are summarised in Table 8.1.1. Samples of α'–sialon were prepared by sintering appropriate mixes of $CaCO_3$ or Y_2O_3 with Al_2O_3, AlN and α–Si_3N_4. SiO_2 was not used in mixes because this tends to lead to larger weight losses. Sample 8.11 was prepared from sample 8.10 by addition of appropriate amounts of $CaCO_3$ and AlN. Calcium α'–sialons were prepared according to Patience,[1] using the mixes listed in Table 8.1.2. Starting compositions for yttrium α'–sialons were calculated including a correction for the oxygen content of α–$Si_3N_4$and AlN. Typically, weight losses of 5–8% were observed in synthesis of α'–sialons, in addition to that expected for loss of CO_2 from $CaCO_3$.

Table 8.1.2 Mixtures used in synthesis of Ca α'–sialons[1]

Mix			Estimated
$CaCO_3$	AlN	Si_3N_4	product composition
1	5	3	$Ca_{0.67}Si_{10}Al_2O_{0.67}N_{15.33}$
1	3	3	$CaSi_9Al_3ON_{15}$
2	2.5	3	$Ca_{1.5}Si_{8.5}Al_{3.5}O_{0.5}N_{15.5}$ + glass
3	2.5	3	$Ca_2Si_8Al_4N_{16}$

Considerable problems were encountered in the synthesis of ^{15}N–enriched β'–sialon samples. Direct sintering of mixtures of α–Si_3N_4, AlN and Al_2O_3 with small amounts (1–2$^w/_o$) of MgO to provide a liquid phase proved successful when using commercial α–Si_3N_4, but it proved impossible to grind synthetic α–$Si_3^{15}N_4$ to

Table 8.1.1 Synthesis of α'– and β'–sialons

Sample	Phase	Composition	Preparation					XRD analysis
			Mix	Furnace	Temp/°C	Time/h	Notes	
8.1	Ca α' I	$Ca_{0.67}Si_{10}Al_2O_{0.67}N_{15.33}$	A	C	1750	0.25		α'(s) AlN(tr)
8.2	Ca α' II	$CaSi_9Al_3ON_{15}$	A	C	1750	0.25		α'(s) AlN(vw)
8.3	Ca α' III	$Ca_{1.5}Si_{8.5}Al_{3.5}O_{0.5}N_{15.5}$	A	C	1750	0.25		α'(s) AlN(tr)
8.4	Ca α' IV	$Ca_2Si_8Al_4N_{16}$	A	C	1750	0.25		α'(s) AlN(tr)
8.5	Y α' I	$Y_{0.305}Si_{9.715}Al_{2.285}O_{1.37}N_{14.63}$	A	C	1750	1.0		α'
8.6	Y α' II	$Y_{0.365}Si_{9.455}Al_{2.545}O_{1.45}N_{14.55}$	A	C	1750	1.0		α'
8.7	Y α' III	$Y_{0.424}Si_{9.198}Al_{2.802}O_{1.53}N_{14.47}$	A	C	1750	1.0		α'
8.8	Y α' IV	$Y_{0.500}Si_{10.00}Al_{2.000}O_{1.50}N_{14.50}$	A	C	1750	1.0		α'(s) Melilite(w)
8.9	^{15}N Ca α' I	as 8.1	A	C	1750	0.25		α'
8.10	^{15}N Ca α' II	as 8.2	A	C	1750	0.25		α'
8.11	^{15}N Ca α' III	as 8.4	A	C	1750	0.25		α'(s) AlN(w)
8.12	β' I	Z=1					1	β'
8.13	β' II	Z=1.15					1	β'(vs) Al_2O_3(vw)
8.14	β' III	Z=1.9					1	β'
8.15	β' IV	Z=4					1	β'
8.16	β'	Z=3.3					2	β'(s) Al_2O_3(w) Aln(w)
8.17	^{15}N β'	Z=4	A	H	1700	1.0		β'(s) 15R(w)

Notes. 1: prepared D.P.T.; 2: prepared P.K.

Figure 8.1.1 a against c for β'–sialons (+), Y α'–sialons ($\triangle$) and Ca α'–sialons ($\oplus$).

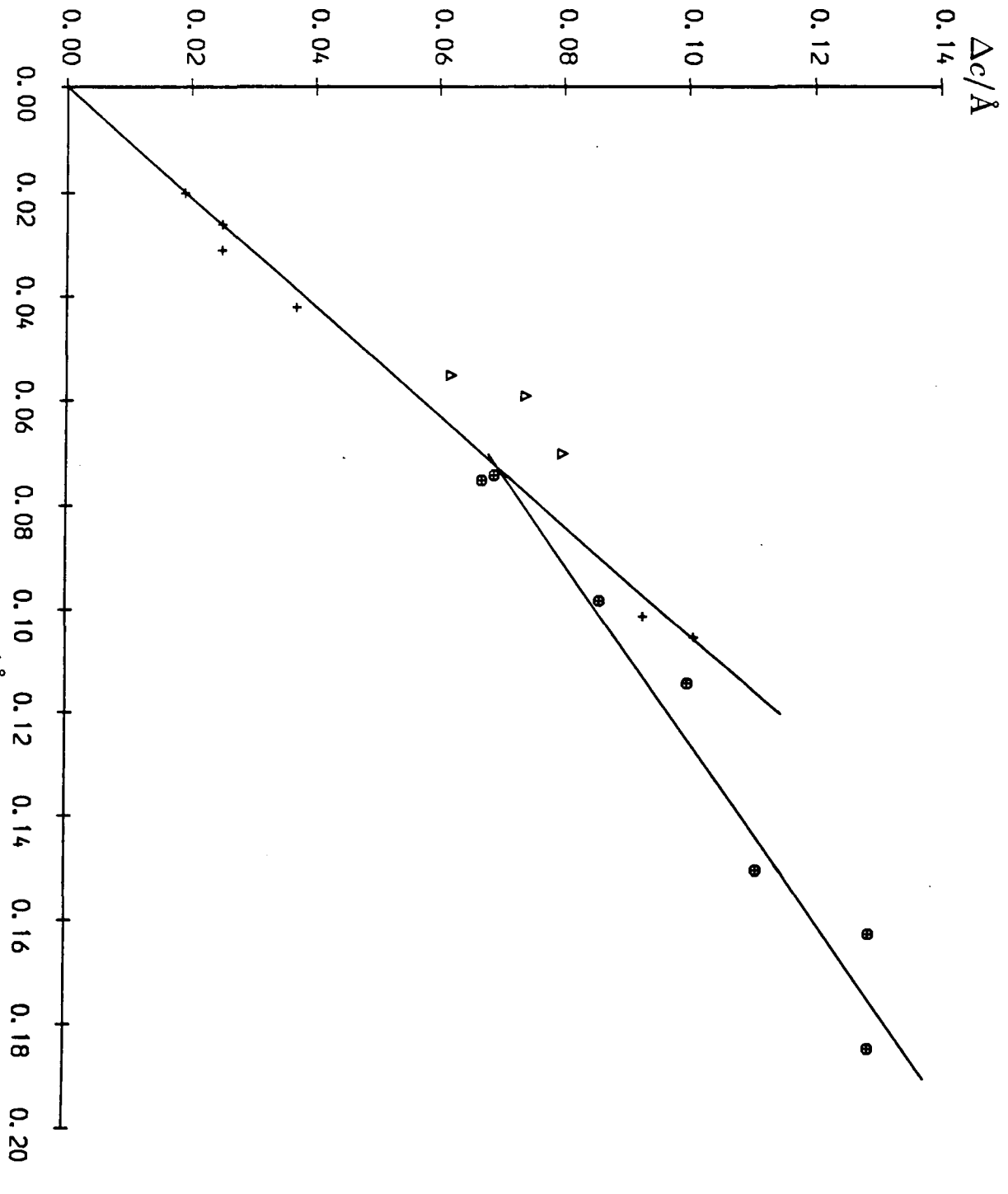

sufficiently small grain size: sinterings using this material always gave rise to very significant (> 10%) weight losses, and the product always contained α– and β–Si_3N_4, as well as β'–sialon with a range of Z values (as determined by powder XRD). Regrinding and resintering only led to further weight loss, and no homogenisation. A single sample of ^{15}N–enriched β'–sialon (Z=4) was prepared by hot-pressing a mixture of α–$Si_3^{15}N_4$, AlN and Al_2O_3. Hot-pressing has the effect of dramatically increasing the rate of solid-state reactions, but is generally undesirable for very small samples for MAS NMR because of pellet distortion, which can make sample recovery difficult, and extreme densification, which makes fine grinding without contamination problematic. All of the other samples of β'–sialon were prepared by other workers by hot-pressing.

Unit cell dimensions of all of the samples involved in this Chapter were measured and refined, and are listed in Tables 8.1.3 and 8.1.4. Comparisons of data for β'–sialons with Equation 3.1.1 shows that the Z values quoted in Table 8.1.1 are in some cases only approximate. Deviations can be caused by weight losses and incomplete reaction (e.g. samples 8.13, 8.16).

Cell dimensions are plotted in Figure 8.1.1 as functions of the deviation of a and c from the values of the parent phases: α–Si_3N_4 (a = 7.753 Å, c = 5.623 Å) and β–Si_3N_4 (a = 7.603 Å, c = 2.906 Å). The data for β'–sialons are as expected: Δa and Δc are found to be linked by the relationship

$$(\Delta c/\text{Å}) = -0.002 + 0.957(\Delta a/\text{Å}) \qquad r = 0.998 \qquad 6 \text{ points}$$

in close agreement with that predicted from Equation 3.1.1:

$$\Delta c = 0.900\Delta a$$

The data for the α'–sialons are not at all in agreement with previous reports of unit cell dimensions of α' phases. Jack[2] proposed the relationship

$$\Delta c = 0.889\Delta a$$

from measurements on Li, Ca and Y α'–sialons, but it is clear that such a relationship does not hold for either the Ca or Y phases studied in this Chapter. There

Table 8.1.3 Cell dimensions for α'–sialons (all hexagonal unit cells)

M	Sample	a/Å	c/Å	Δa/Å	Δc/Å
Ca	8.1	7.827	5.692	0.074	0.069
Ca	8.2	7.851	5.709	0.098	0.086
Ca	8.3	7.903	5.734	0.150	0.111
Ca	8.4	7.937	5.752	0.184	0.129
Ca	8.9	7.828	5.690	0.075	0.067
Ca	8.10	7.867	5.726	0.114	0.100
Ca	8.11	7.915	5.752	0.162	0.129
Y	8.5	7.808	5.685	0.055	0.062
Y	8.6	7.812	5.697	0.059	0.074
Y	8.7	7.823	5.703	0.070	0.080
Y	8.8	7.823	5.703	0.070	0.080

Table 8.1.4 Cell dimensions and calculated Z values for β'–sialons (all hexagonal unit cells)

Sample	Z	a/Å	c/Å	Δa/Å	Δc/Å	Z_a	Z_c
8.12	1.00	7.629	2.931	0.026	0.025	0.89	0.93
8.13	1.15	7.623	2.925	0.020	0.019	0.69	0.70
8.14	1.90	7.645	2.943	0.042	0.037	1.42	1.37
8.15	4.00	7.704	2.999	0.101	0.093	3.39	3.44
8.16	3.30	7.634	2.931	0.031	0.025	1.07	0.93
8.17	4.00	7.708	3.007	0.105	0.101	3.52	3.74

Note: Z values in second column based on synthetic data, in final two columns calculated from Equation 3.1.1.

Figure 8.2.1 ^{29}Si MAS NMR spectra of α'–sialons

(a) sample 8.1 (Ca) SF=59.6 MHz; PA=23^{O}; NT=119; RD=300 s; SR=3.96 kHz; AF=0.01 s

(b) sample 8.2 (Ca) SF=59.6 MHz; PA=23^{O}; NT=162; RD=300 s; SR=3.96 kHz; AF=0.01 s

(c) sample 8.3 (Ca) SF=59.6 MHz; PA=23^{O}; NT=134; RD=300 s; SR=3.95 kHz; AF=0.01 s

(d) sample 8.4 (Ca) SF=59.6 MHz; PA=23^{O}; NT=164; RD=300 s; SR=4.00 kHz; AF=0.01 s

(e) sample 8.7 (Y) SF=59.6 MHz; PA=26^{O}; NT=79; RD=300 s; SR=3.35 kHz; AF=0.01 s

(f) sample 8.11 (Ca) SF=59.6 MHz; PA=90^{O}; ST; SR=3.33 kHz; AF=0.01 s

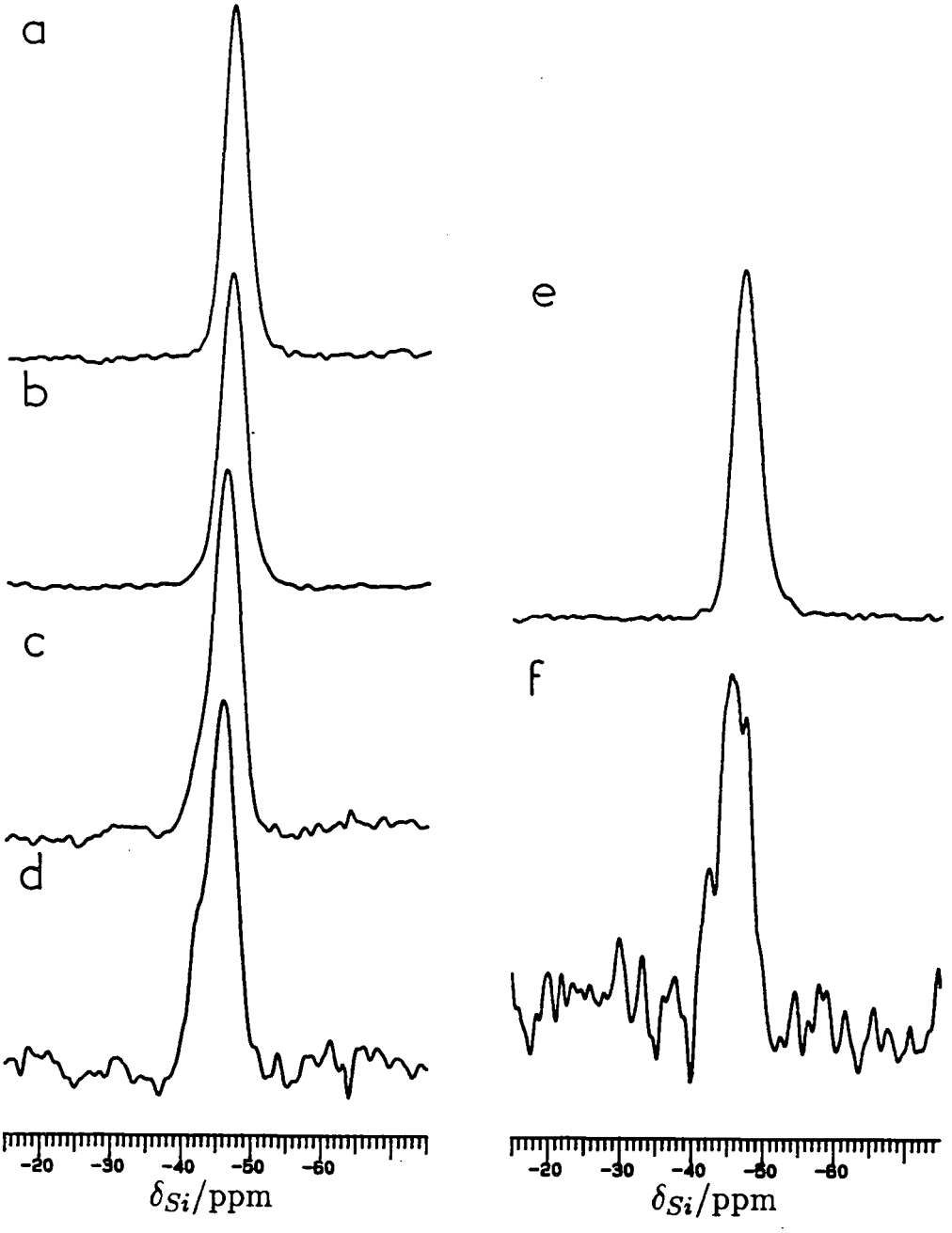

are too few data points to make a full analysis of the Y phases, but for the Ca phases, the relationship

$$(\Delta c/\text{Å}) = 0.027 + 0.584(\Delta a/\text{Å}) \qquad r = 0.980 \qquad 7 \text{ points}$$

is found to apply. This equation (see Figure 8.1.1) does not pass through the origin. This suggests that, unlike in the β'–sialons, a small structural distortion is occurring on moving from α–Si_3N_4 to the substituted α' phases. This assertion is supported by the fact that in neither the Y nor the Ca system does the homogeneity of the phases extend to Si_3N_4 (see for example Figure 3.1.11). In contrast, in the β'–sialons, such an homogeneity range does exist. It seems likely that a certain number of large cations are required in the interstices to stabilise the α' structure. Thompson[3] has reviewed the distorting effect of large cations on the α–Si_3N_4 structure: it is likely that these distortions are also at least partially responsible for the extra stability of the α' phase.

It can be seen from Tables 8.1.3 and 8.1.4 that much larger changes in a and c occur on substitution of Al for Si in α' than in β' phases. This is because the oxygen content of α'–sialons is much lower, and the Al—N bond length is much greater (1.87 Å) than Al—O (1.75 Å).

8.2 Silicon–29 NMR

8.2.1 α'–Sialons

Silicon–29 data are summarised in Table 8.2.1, and representative spectra are shown in Figure 8.2.1. All chemical shifts are found to lie in the very narrow range -47.4–-45.5 ppm, indicating that the silicon environments in all of the phases are very similar. Linewidths are found to lie in the range 230–300 Hz, which means that the splitting of the peaks because of crystallographic inequivalence cannot be observed.

In all of the phases, the N/O ratio is at least 9:1, and therefore the majority of silicon atoms are coordinated only to nitrogen. In addition, PSCR predicts that Si will preferentially bond to N, and Al to O. It might be expected, nevertheless, that some $[SiON_3]$ coordination environments would be present in at least some of

Table 8.2.1 NMR data on α'– and β'–sialons

Phase	Sample	Silicon–29		Nitrogen–15		Aluminium–27	
		δ_{Si}/ppm	FWHH/Hz	δ_N/ppm	FWHH/Hz	δ_{Al}^{300}	FWHH/Hz
Ca α' I	8.1	−46.8	230			98	3700
Ca α' II	8.2	−46.6	250			93	4800
Ca α' III	8.3	−46.0	260			111	sh
						89	3200
Ca α' IV	8.4	−45.5	320			111	1500
						90	sh
Y α' I	8.5	−47.4	240			98	3400
Y α' II	8.6	−47.3	250			109	4900
Y α' III	8.7	−47.3	250			111	3400
Y α' IV	8.8	−47.3	250				
^{15}N Ca α' I	8.9	−46.7	250	59.6	460		
^{15}N Ca α' II	8.10	−46.8	290	62.1	600		
^{15}N Ca α' III	8.11	−45.8	330	65.6	300		
β' Z=1	8.12	−48.3	175			110	1000
						~ 80	sh
β' Z=1.15	8.13	−48.9	160				
β' Z=1.9	8.14	−48.1	200			111	1300
						61	4000
β' Z=4	8.15	−46.8	260			111	1200
						58	3000
						9.4	1500
β' Z=3.3	8.16	−48.3	200				
^{15}N β' Z=4	8.17	−46.4	300	69	sh	63	3200
				49	600	10	sh

Figure 8.2.2 (a) a, and (b) c against δ_{Si} for Ca α'–sialons. α–Si_3N_4 (average) is also marked ($\oplus$).

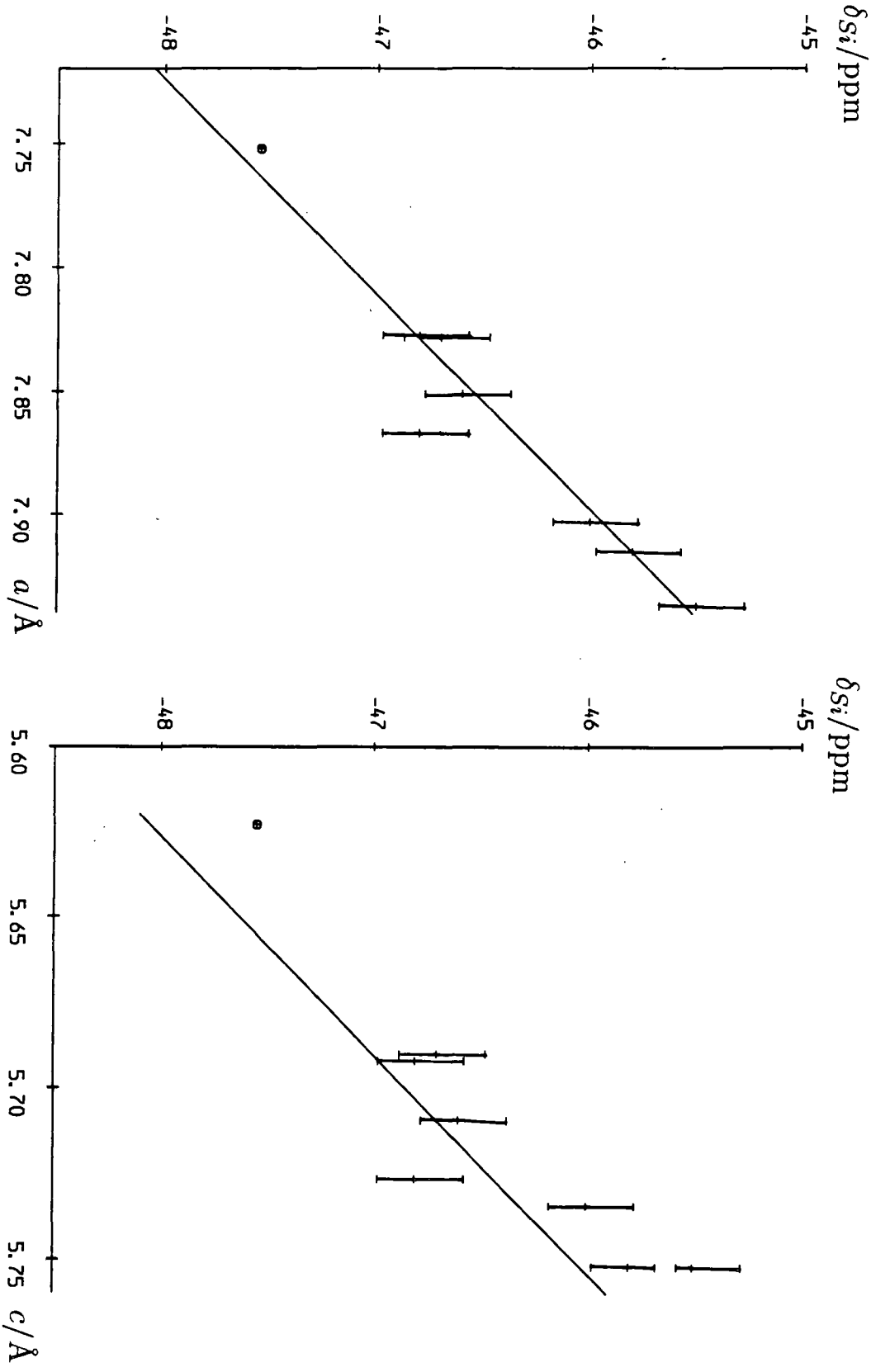

the samples. No evidence for any low-frequency peaks was seen in any of the ^{29}Si spectra: as might be predicted from electronegativity considerations. This result will be further discussed below.

It is apparent from Tables 8.1.3 and 8.2.1 that, despite the small range in δ_{Si} in the seven Ca α'-sialons studied, δ_{Si} does tend to become more positive as Al is incorporated and the cell dimensions increase. δ_{Si} is plotted against a and c in Figure 8.2.2. The correlation between the variables is striking, if shallow, and is approximately linear. It is described by the equations:

$$(\delta_{Si}/\text{ppm}) = -137.7 + 11.6(a/\text{Å}) \qquad r = 0.94 \qquad 7 \text{ points} \qquad (8.2.1a)$$

$$(\delta_{Si}/\text{ppm}) = -151.9 + 18.5(c/\text{Å}) \qquad r = 0.86 \qquad 7 \text{ points} \qquad (8.2.1b)$$

In each case, the point corresponding to sample 8.10 is found to lie well off the line for the other six points, and removing this point from the correlation analysis improves the reliability index to 0.98 for a, and 0.97 for c. The explanation for this single result probably lies in the sample inhomogeneity: the resonance is also broader than might be expected. α–Si_3N_4 was not included in the correlation.

The most surprising fact about this correlation is that δ_{Si} is found to become less negative as the oxygen content is increased, in contrast to previous experience (see for example Figure 6.2.9).

The correlation between δ_{Si} and cubic sodalite (Equation 3.2.2) shows that δ_{Si} becomes more negative in that system as a increases. This was related to increases in Si–O–M bond angle, which is well known to lead to more negative δ_{Si} (Section 3.2.2.1). Such a straightforward explanation is not apparent in the α' systems. Data in Table 8.2.1 suggests that the FWHH increases as a and c increase. This is most likely caused by Si/Al disorder at the n.n.n. sites. Increasing the number of Al in the n.n.n. sites should lead to a high-frequency shift because of increased shielding of Si caused by the lower electronegativity of Al (Figure 3.2.2). The reason why n.n. oxygen does not lead to a substantial negative shift is not clear, but may be related to the fact that (N—Si) and (O—Al) are isoelectronic. Substitution of (N—Si) by (O—Al) might thus lead to a negligible change in δ_{Si} if the groups have similar electronegativities. Only when (N—Si) is replaced by (N—Al) would

Figure 8.2.3 ^{29}Si MAS NMR spectra of β'–sialons

(a) Z=1 (sample 8.12) SF=59.6 MHz; PA=23^{o}; NT=218; RD=120 s; SR=3.19 kHz; AF=0.01 s

(b) Z=1.9 (sample 8.14) SF=59.6 MHz; PA=23^{o}; NT=500; RD=120 s; SR=3.15 kHz; AF=0.01 s

(c) Z=4 (sample 8.15) SF=59.6 MHz; PA=23^{o}; NT=430; RD=120 s; SR=3.03 kHz; AF=0.01 s

(d) Z=4 (sample 8.17) SF=59.6 MHz; PA=27^{o}; NT=82; RD=300 s; SR=3.38 kHz; AF=0.01 s

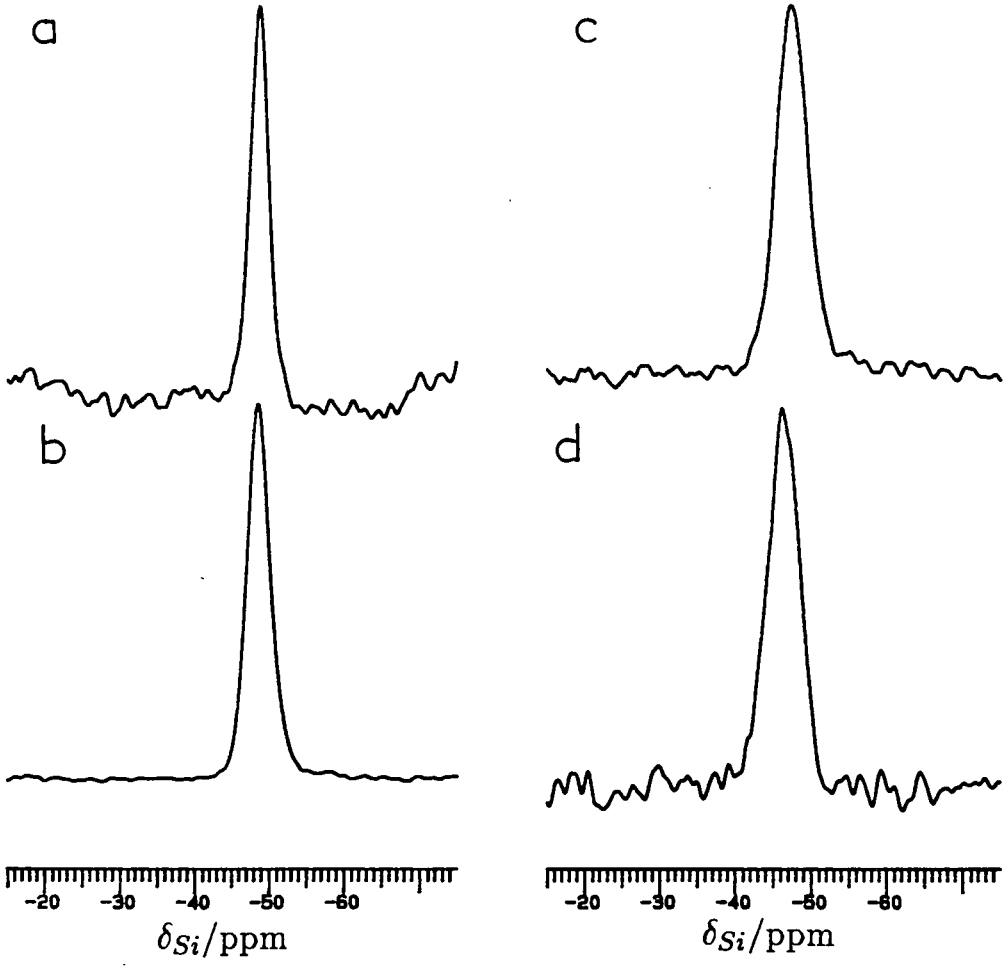

a change in δ_{Si} then occur. PSCR predicts that O will be preferentially bonded to Al, and in β'–sialons there is always an excess of Al over O, so coordination of Si to O will always be accompanied by substitution of Al at n.n.n. sites.

No correlation was attempted involving the yttrium α'–sialons, because the much shorter homogeneity range means that not enough well-spaced points can be obtained, but it is again clear that increased oxygen content of the phase does not result in a more negative chemical shift, and it is assumed that similar factors are at work in these phases as in the calcium system.

8.2.2 β'–Sialons

In an early study, Dupree *et al.*[4] reported the ^{29}Si MAS NMR spectra of β'–sialons with Z=1, 2 and 4. They observed that δ_{Si} remained unchanged at -48 ± 0.5 ppm throughout the series, and noted an increase in FWHH from 1 ppm (80 Hz at ν_L = 79.5 MHz) for β–Si_3N_4, to 3.5 ppm (280 Hz) for Z=1 and 5.5 ppm (440 Hz) for Z=4. They argue[5] that this implies that Si is bonded directly only to N, and not to O.

The ^{29}Si NMR data for the phases examined in this study are listed in Table 8.2.1, and typical spectra are illustrated in Figure 8.2.3. The chemical shifts and linewidths are found to lie in very narrow ranges: -46.4 to -48.9 ppm and 160 to 300 Hz. δ_{Si} is plotted against unit cell constant a (a very similar result is found for c) in Figure 8.2.4, and regression analysis gives the correlations:

$$(\delta_{Si}/\text{ppm}) = -238.5 + 24.91(a/\text{Å}) \qquad r = 0.984 \qquad 6 \text{ points} \qquad (8.2.2a)$$

$$(\delta_{Si}/\text{ppm}) = -124.6 + 25.71(c/\text{Å}) \qquad r = 0.984 \qquad 6 \text{ points} \qquad (8.2.2b)$$

β–Si_3N_4 (a = 7.603 Å, c = 2.906 Å) was not included in either correlation, and it is clear form Figure 8.2.4 that the line does not pass through the point corresponding to β–Si_3N_4: both of Equations 8.2.2 predict δ_{Si}=-49.0 ppm. This, plus the relatively large scatter in points at lower a and c, suggest that δ_{Si} is sensitive to sample inhomogeneity, particularly at low Al/O content.

As with the correlations for α'–sialons, the exact form is of less importance than the general trend. The correlation for the β'–sialons is found to go in the

Figure 8.2.4 a against δ_{Si} in β'–sialons

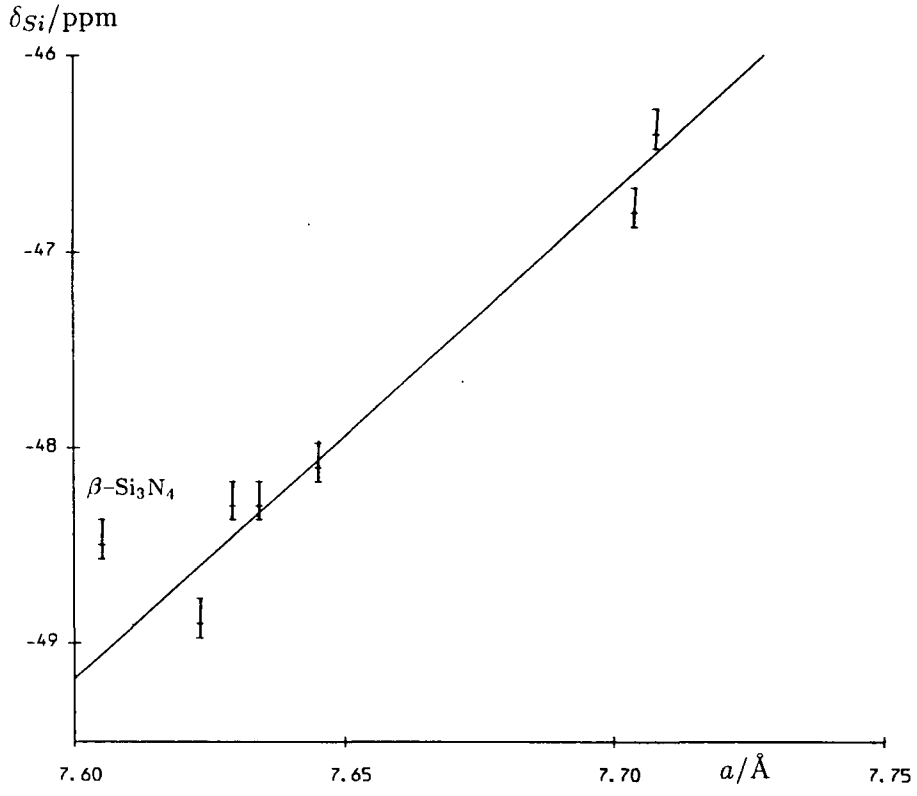

Figure 8.2.5 The ordering scheme in β'–sialon proposed by Dupree *et al.*[5]

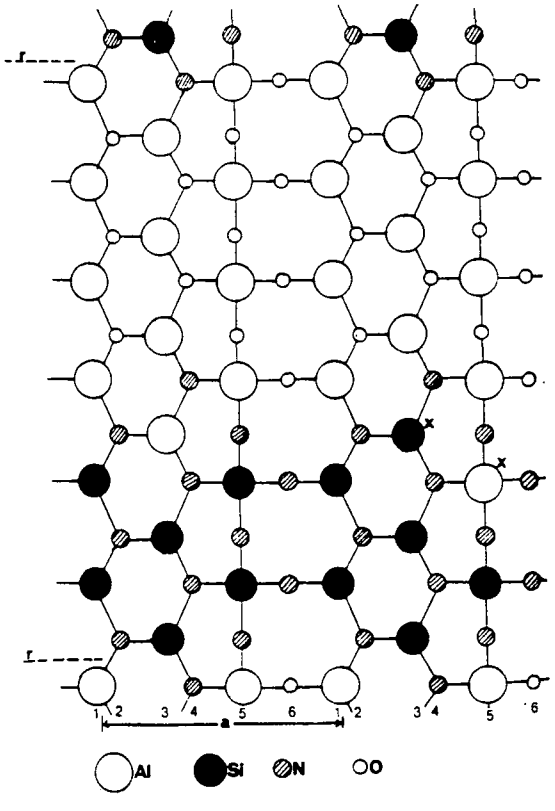

same direction as for the α'–sialons: the "wrong" direction for increased oxygen content. FWHH is also found to increase with level of substitution.

The oxygen content of β'–sialons is large (up to $50^a/o$ anion for Z=4), and it seems highly unlikely that no silicon is present in $[SiON_3]$ and $[SiO_2N_2]$ environments, even with the operation of PSCR, yet no low-frequency peaks are ever observed in the ^{29}Si NMR. The ordering scheme of Dupree *et al.*[5] (Figure 8.2.5) based on ^{29}Si and ^{27}Al NMR results seems unlikely (and is not in agreement with neutron diffraction studies), because regions so rich in Al and O would be expected to be unstable with respect to Al_2O_3; and also much broader XRD lines would be expected because of the highly ill-defined, and spatially variable dimensions of the unit cell. It is more likely that Si does occur in $[SiON_3]$ and $[SiO_2N_2]$ environments, but that these environments, plus $[SiN_4]$, give rise to almost identical chemical shifts, for similar reasons to those proposed above for the α'–sialons: coordination of O at n.n. level is invariably associated with Al at n.n.n. level.

The correlations described by Equations 8.2.1 and 8.2.2 are of similar sensitivity. It is therefore not unreasonable to propose that the explanations are the same: in general, changes in δ_{Si} are caused principally by an excess replacement of Si by Al in the n.n.n. environment over N to O substitution at n.n. level. This effect also leads to changes in a and c for reasons outlined above, and would be expected to give rise to a small positive shift in δ_{Si} in β'–sialons, because Al content increases more rapidly than O content as Z increases, and thus a net imbalance of Al can build up.

8.2.3 Discussion

Three systems have been examined in this Thesis in which substantial isomorphous substitution of Al–O for Si–N can occur: α'– and β'–sialons, and La new phase. In each of these systems, the ^{29}Si MAS NMR spectra are found to be basically unaltered on substitution, except that lines are broadened due to disorder, despite the often substantial increases in oxygen content. The same effect has also recently been observed in O'–sialons.[6] δ_{Si} is thought to be basically unchanged because substitution of N by O at n.n. level does not lead to a significant change in overall electron distribution, because of attendant substitution of Si by Al at n.n.n. level.

Figure 8.3.1 ^{15}N MAS NMR spectra of

(a) Ca α' (sample 8.9) SF=30.4 MHz; PA=90^{o}; NT=3; RD=3600 s; RD=14400 s: SR=3.66 kHz; AF=0.005 s

(b) Ca α' (sample 8.10) SF=30.4 MHz; PA=26^{o}; NT=258; RD=300 s; SR=3.32 kHz; AF=0.005 s

(c) Ca α' (sample 8.11) SF=30.4 kHz; PA=24^{o}; NT=148; RD=300 s; SR=3.30 kHz; AF=0.005 s

(d) β'-sialon (sample 8.17) SF=30.4 MHz; PA=24^{o}; NT=226; RD=300 s; SR=3.45 kHz; AF=0.005 s

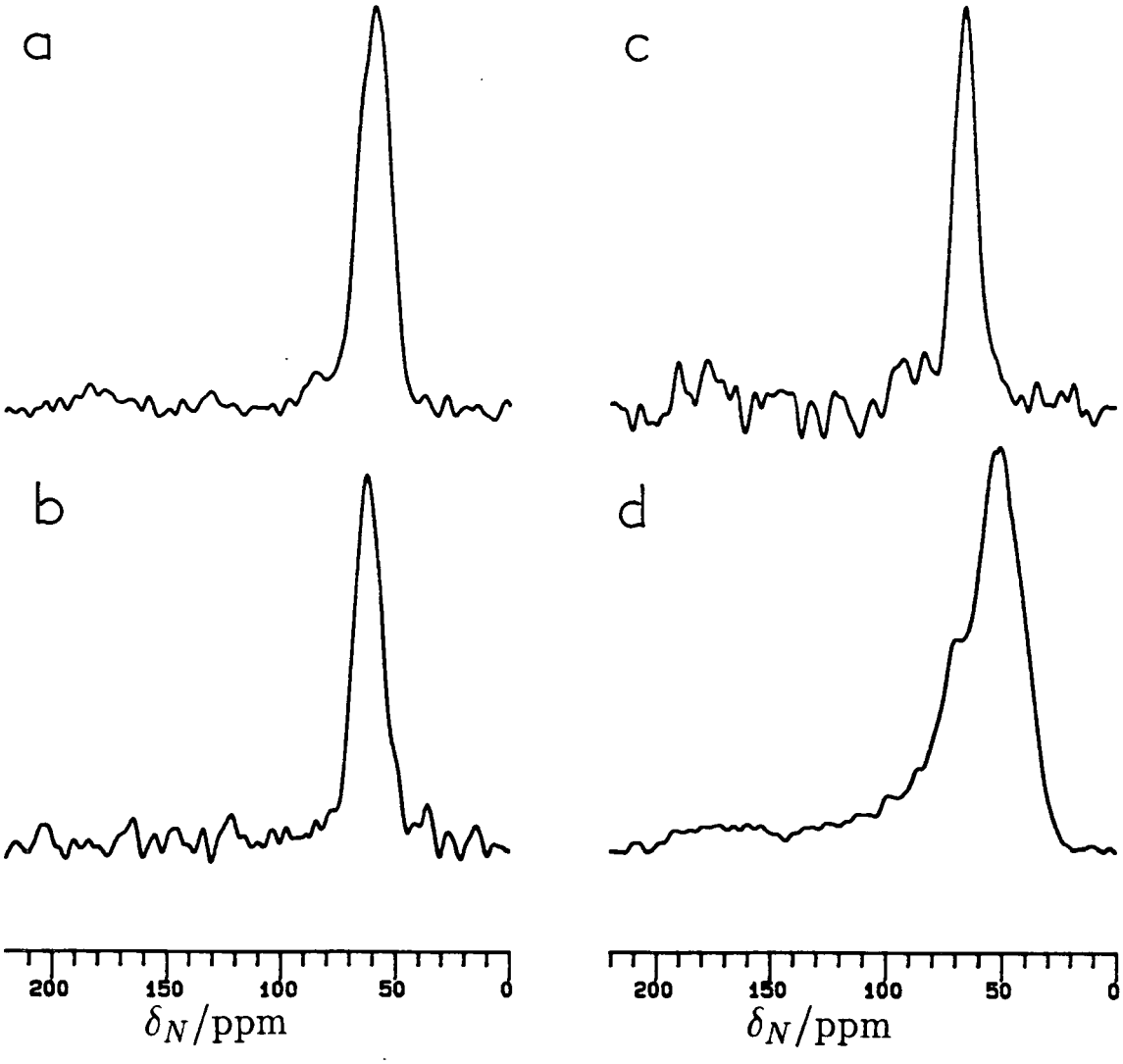

This theory is supported by consideration of the small changes in δ_{Si} with a or c in α'– and β'–sialons, but the fact that isomorphous substitution occurs at all is also relevant. For example, that the structure of β–Si_3N_4 remains unchanged when replacing even $50^a/_o$ N by O **must** imply that the electron distribution in the covalent framework is substantially unaltered, and retains homogeneity on substitution: otherwise the phase would not be expected to be stable with respect to disproportionation (e.g. to β–Si_3N_4 + AlO_xN_y). It is, however, changes in electron distribution which ultimately also give rise to changes in δ_{Si}. If no such change in distribution occurs, then δ_{Si} would be expected to remain roughly constant.

These observations could be generalised: in any system in which isomorphous substitution can occur within a covalent framework, it is to be expected that chemical shifts will remain substantially unaltered, whatever the extent of substitution. Ionic materials would not be expected to follow this rule, because their structures are determined principally by packing considerations, and electron distribution is much less important. Systems which might be examined to test further this rule include $Be_{1+x}Si_{1-x}O_xN_{2-x}$ (Figure 3.1.15), and individual sialon polytypoids, although in none of these phases is the range of homogeneity as great as in the β'–sialons. Silicates and zeolites way well provide intermediate cases, since bonding is generally partially ionic.

8.3 Nitrogen–15 NMR

8.3.1 α'–sialons

A series of three isotopically enriched calcium α'–sialons were examined by ^{15}N MAS NMR. The spectra are shown in Figure 8.3.1, with data listed in Table 8.2.1. The chemical shifts lie in a very narrow range ($\sim$ 6 ppm), as found in the ^{29}Si study. The lines are all broad, but, surprisingly, the sample with the highest Al content (8.11) gives rise to by far the sharpest signal. This suggests that the nitrogen is in a more uniform n.n. environment in this sample; it is likely that as the Al content is increased, there is a tendency towards $[NSi_2Al]$ coordination, which can be fully satisfied in sample 8.11, which has a proposed α' composition of $Ca_2Si_8Al_4N_{16}$. In the other two samples, coordination would then have to be mixed $[NSi_3]$ and $[NSi_2Al]$, leading to broader overall resonances. It is expected

Figure 8.3.2 (a) a, and (b) c against δ_N for Ca α'–sialons. An average value for α–Si_3N_4 is also shown ($\oplus$).

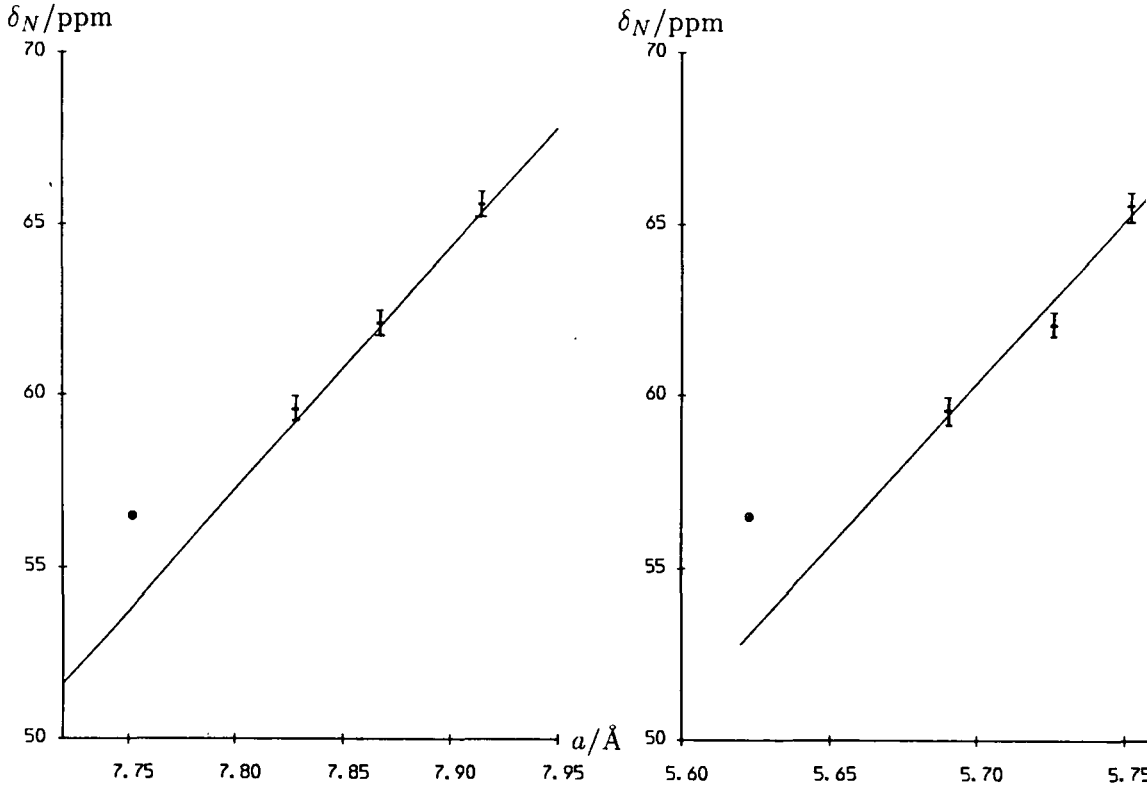

Figure 8.3.3 Deconvolution of the ^{15}N spectrum of β'–sialon (sample 8.17) shown in Figure 8.3.1(d).

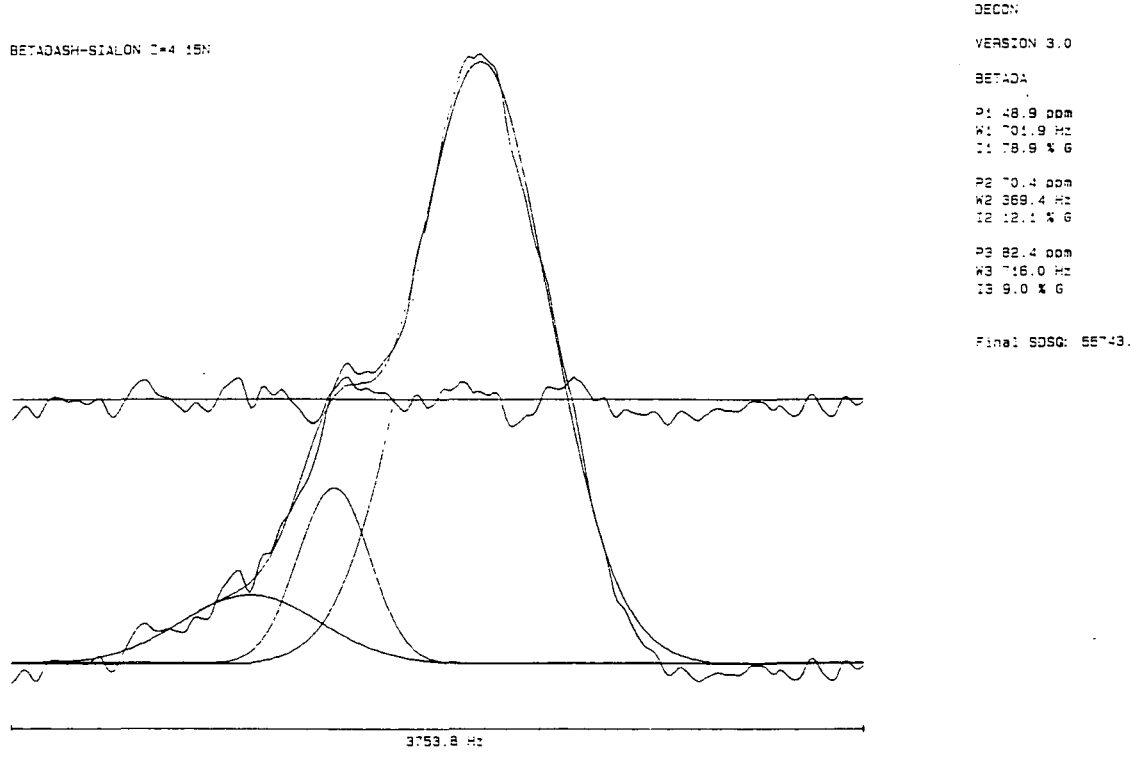

that some [NAl_2Si] and [NSi_3] environments are present in sample 8.11, but the amount is probably small.

δ_N is plotted against unit cell dimensions in Figure 8.3.2. Even though only three points were available, a linear correlation is seen, defined by the equations:

$$(\delta_N/\text{ppm}) = -481.5 + 69.1(a/\text{Å}) \qquad r = 0.999 \qquad 3 \text{ points} \qquad (8.3.1a)$$

$$(\delta_N/\text{ppm}) = -481.7 + 95.1(c/\text{Å}) \qquad r = 0.982 \qquad 3 \text{ points} \qquad (8.3.1b)$$

Neither equation includes the average value of δ_N for α–Si_3N_4: 56.5 ppm (assuming a 3:3:1:1 weighting of the four peaks). The lines clearly do not pass through this point, but below it. This is possibly because oxygen preferentially occupies the 2(a) and 2(b) sites, as in β'–sialons (Section 3.1.3). The correlation would then be expected to extrapolate to a point of lower δ_N at the cell dimension of α–Si_3N_4. Part of the correlation could also be caused by changes in relative occupation of the sites on substitution, since they cannot be resolved in the ^{15}N NMR.

The direction of the correlation is the same as that of δ_{Si}, indicating that both Si and N are shielded slightly on substitution. Changes in δ_N are probably caused by changes in n.n. environment, where substitution of Si by Al would be expected to lead to shielding of N because of the slightly lower electronegativity of Al (assuming no compensating changes in n.n.n. environment). It is clear, however, that the electron distribution seen by the N nucleus is only slightly altered on isomorphous substitution, as postulated in the previous section.

8.3.2 β'–sialon

Only one spectrum of a ^{15}N–enriched β'–sialon was obtained, from a phase with Z=4 (from starting composition). The spectrum is shown in Figure 8.3.1.

Comparison with the spectrum of β–$Si_3^{15}N_4$ (Figure 5.3.2) shows that resonances corresponding to both nitrogen sites (2(b) and 6(c)) can still be resolved, although the spectrum is much broadened. The chemical shift of the major component, 49 ppm, is not significantly shifted with respect to β–Si_3N_4, despite the high level of substitution, and this is to be compared with the results from the α'–sialons, where more significant shifts were observed. The reason is probably

Figure 8.4.1 ^{27}Al MAS NMR spectra of α'–sialons (background subtracted)
(a) sample 8.1 (Ca) SF=78.2 MHz; PA=15^{O}; NT=700; RD=1 s; SR=10.10 kHz; AF=0.005 s
(b) sample 8.2 (Ca) SF=78.2 MHz; PA=15^{O}; NT=700; RD=1 s; SR=10.30 kHz; AF=0.005 s
(c) sample 8.3 (Ca) SF=78.2 MHz; PA=15^{O}; NT=700; RD=1 s; SR=10.50 kHz; AF=0.005 s
(d) sample 8.4 (Ca) SF=78.2 MHz; PA=15^{O}; NT=700; RD=1 s; SR=10.55 kHz; AF=0.005 s

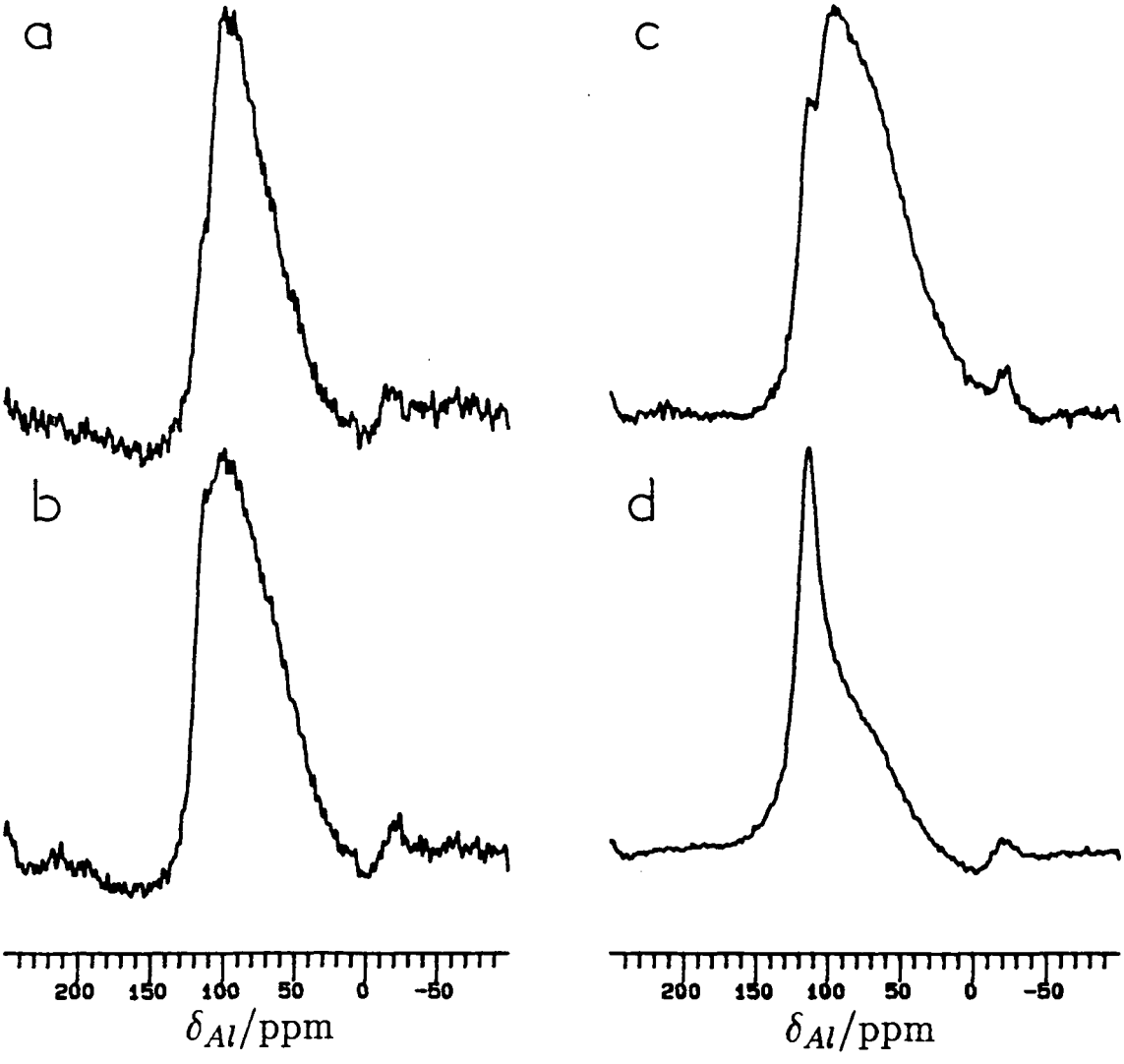

that O in the n.n.n. coordination sites is reducing the electron-donating effect of n.n Al in β'–sialon. The oxygen content of α' phases is much lower than that of β'–sialons.

The results of neutron diffraction studies of β'–sialons, discussed in Section 3.1.3, show that oxygen is more likely to occupy 2(b) than 6(c) sites. In an attempt to test this finding, the ^{15}N spectrum of β'–sialon was deconvoluted (Figure 8.3.3). Three peaks were needed for an acceptable fit: δ_N=48.9 ppm, FWHH=700 Hz, 78.9%; δ_N=70.4 ppm, FWHH=370 Hz, 12.1%; δ_N=82.4 ppm, FWHH=715 Hz, 9.0%. The peak at 82.4 ppm cannot be assigned with certainty, but is probably due to 15R sialon polytypoid, which is present in the β' sample. The ratio of N in 6(c) to 2(b) sites is thus calculated as 6.5:1, assuming that the spectrum is quantitative, and that no signal due to 15R sialon is contained under the main peaks. This compares with a 7:1 ratio calculated by Gillott *et al.*[7] for a material of essentially identical unit cell dimensions, by neutron diffraction. ^{15}N MAS NMR thus confirms the accepted model of O/N site occupancy discussed in Section3.1.3.

Deconvolution also gives an accurate value of δ_N for the 2(b) nitrogen of 70.4 ppm, very close to the observed 68.7 ppm from β–$Si_3^{15}N_4$. This resonance is also twice as narrow as the lower-frequency peak, and this may be due to a non-random Si/Al distribution.

8.4 Aluminium–27 NMR

8.4.1 α'–sialons

^{27}Al MAS NMR spectra were obtained on some Ca and Y α'–sialons, and results are listed in Table 8.2.1, with spectra shown in Figure 8.4.1. All spectra show that only tetrahedral aluminium is present in samples. Many of the spectra (notably of samples 8.4 and 8.7) show sharper components with δ_{Al}^{300}~111 ppm which can be assigned to impurity AlN, and also a broader component with δ_{Al}^{300} in the range 90–100 ppm, assigned to the α' phase. The precise value of δ_{Al}^{300} seems to decrease as cell dimension is increased, in contrast to the finding for δ_N and δ_{Si}, but exact correlations were not attempted because the broad resonance meant that the error in δ_{Al}^{300} was as much as ±5 ppm, and also because of the difficulty in knowing whether all of the aluminium was being seen or whether some

Figure 8.4.2 ^{27}Al MAS NMR spectra of β'–sialons (background subtracted)
(a) Z=1 (sample 8.12) SF=78.2 MHz; PA=15^{O}; NT=700; RD=1 s; SF=10.17 kHz; AF=0.005 s
(b) Z=1.9 (sample 8.13) SF=78.2 MHz; PA=15^{O}; NT=700; RD=1 s; SF=10.40 kHz; AF=0.005 s
(c) Z=4 (sample 8.15) SF=78.2 MHz; PA=15^{O}; NT=700; RD=1 s; SF=10.37 kHz; AF=0.005 s
(d) Z=4 (sample 8.17) SF=78.2 MHz; PA=15^{O}; NT=700; RD=1 s; SF=10.29 kHz; AF=0.005 s

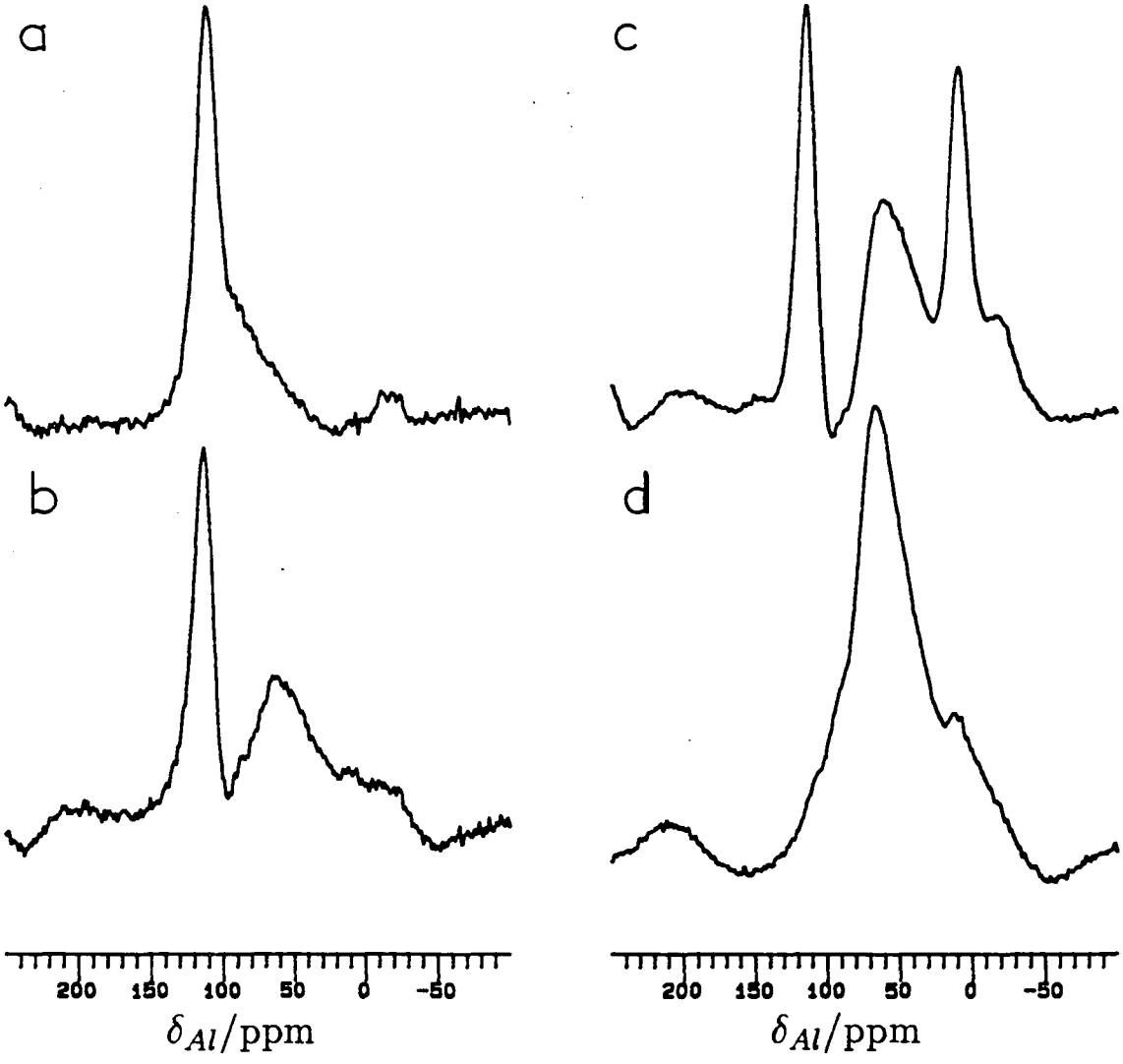

was in environments which give rise to excessively broad resonances due to second order quadrupolar coupling. Because of the latter difficulty, it is also difficult to rationalise the details of the spectra with known or postulated structures.

8.4.2 β'–sialons

Dupree *et al.*[5] have studied a series of β'–sialons (Z=1, 2, 4) by ^{27}Al MAS NMR. They show by use of only a 4 μs dead time delay that a great deal of the aluminium is present in environments giving rise to extremely broad resonances. The narrower resonances remaining after increasing the dead time are assigned to [AlN_4] (δ_{Al}^{360}=103–109 ppm), and [AlO_4] (δ_{Al}^{360}=66 ppm). A small peak due to octahedral aluminium is also observed. The authors conclude that peaks due to mixed aluminium oxynitride coordination environments are not observed in the longer dead time transformations. The authors do not state the AlN content of the β'–sialon samples examined.

Four β'–sialon samples were examined in this study, and spectra are shown in Figure 8.4.2, with data listed in Table 8.2.1. The features of the spectra of samples 8.12, 8.14 and 8.15 are similar to those seen by Dupree *et al.* The octahedral peak from sample 8.15 is assigned to Al_2O_3. It is not clear, however, from the spectra, that the peaks at 110–113 ppm are not due to impurity AlN, and indeed in the spectrum of sample 8.17 no such peak is observed, suggesting either that peaks in this region are due to impurity AlN, or that sample 8.17 is of a particularly high homogeneity in comparison with sample 8.15, which has similar unit cell dimensions.

It is clear that further studies involving preparation of a range of β'–sialons of different Z values, preferably by a variety of routes, are required to understand fully these results, and to rationalise them in terms of known or postulated structures. One feature of the spectra is striking however: δ_{Al}^{300} is around 30 ppm lower in β' than in α'–sialons. This is consistent with the higher oxygen content of the β' phase.

It will be of interest to determine whether δ_{Al} can be correlated with unit cell dimensions, and how deep or shallow this correlation is. Higher-field studies (say

at 500 MHz) would aid this study by minimising broadening and field-dependent shifts caused by second order quadrupolar coupling.

REFERENCES

1. Patience, M. M. Ph.D. Thesis, University of Newcastle upon Tyne, 1983.
2. Jack, K. H. *Progress in Nitrogen Ceramics* Riley, F. L. Ed., NATO ASI Ser. E. Martinus Nijhoff: The Hague. **65**, 45–60 (1983).
3. Thompson, D. P. *Mat. Sci. For.* **47**, 21–42 (1989).
4. Dupree, R.; Lewis, M. H.; Leng-Ward, G.; Williams, D. S. *J. Mater. Sci. Lett.* **4**, 393–395 (1985).
5. Dupree, R.; Lewis, M. H.; Smith, M. E. *J. Appl. Cryst.* **21**, 109–116 (1988).
6. Sjöberg, J. Unpublished data.
7. Gillott, L.; Cowlam, N.; Bacon, G. E. *J. Mater. Sci.* **16**, 2263–2268 (1981).

Figure 9.1.1 The 6H′ and 12H phase field (M:X=6:7)[2]

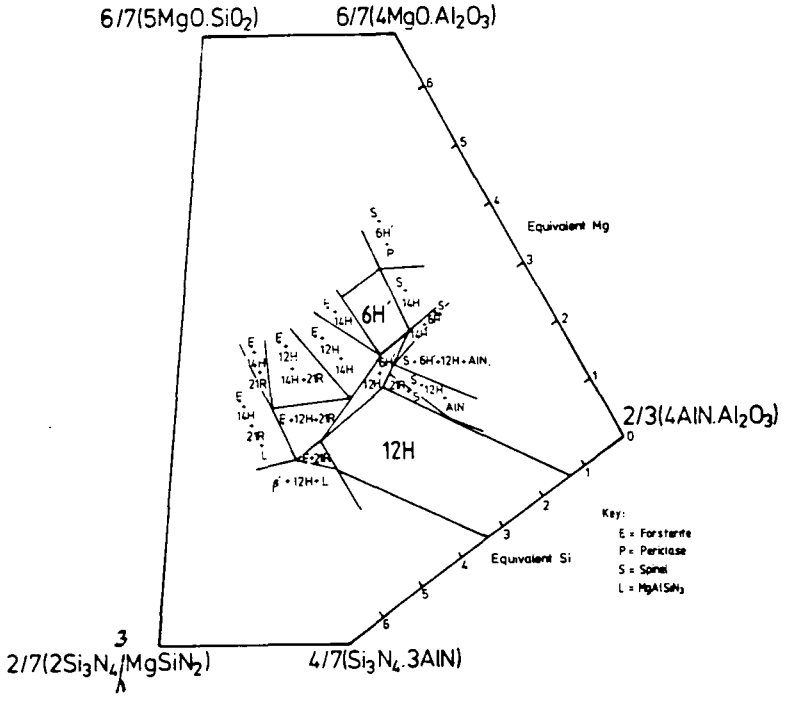

Figure 9.1.2 Be–Si–O–N samples

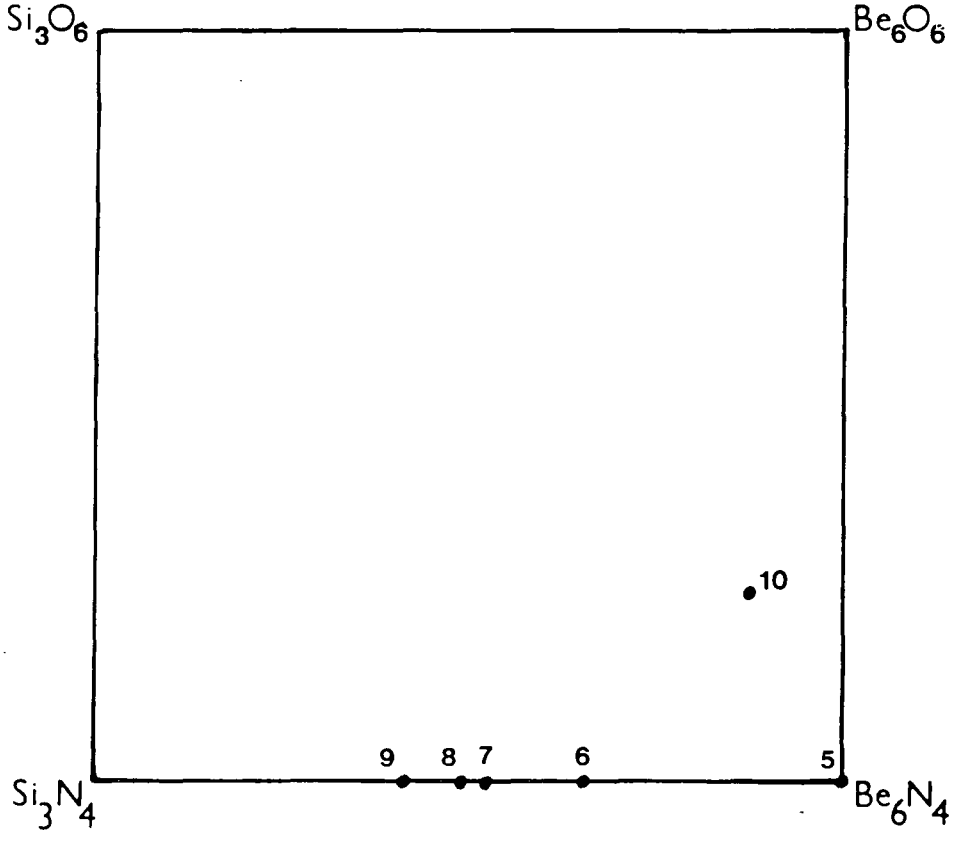

Chapter IX

Polytypoid Phases

The sialon polytypoids were discussed in Section 3.1.3, and it is clear that there are many unresolved issues in the structures of these phases, including the stacking order of the layers, and the Si/Al and O/N ordering schemes. They were therefore considered excellent candidates for a multinuclear magnetic resonance study. Two Mg–Si–Al–O–N polytypoids (6H′ and 12H), and the 15R Si–Al–O–N phase were chosen for special investigation. ^{9}Be studies of a series of Be–Si–O–N polytypoids are also discussed in this Chapter.

9.1 Synthesis of Samples

9.1.1 Mg–Si–Al–O–N Polytypoids

6H′ and 12H polytypoids were prepared by sintering of mixes of MgO, α–Si_3N_4, AlN and Al_2O_3 for short times at 1700^oC. The synthesis of these phases was found to be extremely sensitive to many factors, with weight loss being a constant source of problems: initial attempts led to losses of $> 10^w/_o$. The 6H′ and 12H phase fields (Figure 9.1.1) are broad in the 6M:7X plane, but very narrow in directions not lying in the plane. Therefore, even small losses in weight were found to lead to formation of large amounts of other polytypoids, as well as other phases such as Mg_2SiO_4, $MgAl_2O_4$ and AlN. Weight losses were minimised by use of Al_2O_3 rather than SiO_2, careful milling, use of powder bed technology and addition of excess Al_2O_3.

(i) **Al_2O_3 versus SiO_2.** SiO_2 in starting mixes is often found to lead to large weight losses because of reaction with Si_3N_4 to give SiO + N_2 (Equation 5.2.1). Use of Al_2O_3 in preference to SiO_2 as a source of oxygen is found to reduce weight losses.

(ii) **Milling.** Weight losses could be reduced by ball-milling the Si–Al–O–N components of the mix for > 3 days in IPA using ZrO_2 balls to reduce particle size.

This Si–Al–O–N mix was then mixed with the correct amount of MgO (or $Mg^{17}O$). This process does not require milling. The main material found to require milling was AlN, so when preparing ^{15}N-enriched samples, α–$Si_3^{15}N_4$ was thoroughly mixed with Al_2O_3, MgO and pre-milled AlN in an agate pestle and mortar (ball-milling could not effectively be carried out on sub-gram quantities). The time taken in mixing these components was found to be critical in preparing materials of high purity.

(iii) **Powder bed technology.**[1] The major mechanism of weight loss in this system is thought to be[2] volatilisation of Si_3N_4 and MgO by reactions such as

$$3MgO + Si_3N_4 \longrightarrow 3SiO + 2N_2 + 3Mg \qquad (9.1.1)$$

The idea behind powder bed technology is to increase the vapour pressure of volatile species such as SiO and Mg in the reaction vessel, and thus oppose reactions such as Equation 9.1.1 by affecting the position of equilibrium. This is achieved by sintering the pellet in a mixture of BN, MgO and α–Si_3N_4. MgO and α–Si_3N_4 react in the powder bed to produce SiO and Mg vapours. This is found to allow the pellet components to react together without significant volatilisation. The BN acts an inert filler. A mix of $50^w/_o$ BN:$40^w/_o$ MgO:$10^w/_o$ α–Si_3N_4 was found to be optimum. In a typical run, a weight loss of around 60% of non-BN material would be observed, with weight loss in the pellet reduced to 0–2%. XRD photographs of the powder bed after sintering showed that all of the α–Si_3N_4 and most of the MgO had reacted. Some Mg_2SiO_4 (forsterite) was formed by reactions such as

$$12MgO + Si_3N_4 \longrightarrow 3Mg_2SiO_4 + 6Mg + 2N_2$$

(iv) **Excess Al_2O_3.** Addition of an extra $2^w/_o$ Al_2O_3(of total Al_2O_3 content) was found to reduce the yield of 21R and 14H polytypoids by reducing slightly the M:X ratio of the mix.

Despite the precautions listed above, formation of other polytypoids as impurities was found to be almost inevitable (Table 9.1.1). It was also found that

Table 9.1.1 Synthesis and analysis of polytypoid phases.

Sample	Phase	Composition	Preparation					XRD analysis
			Mix	Furnace	Temp/°C	Time/h	Notes	
9.1	12H	$SiAl_5O_2N_5$					1	
9.2	15R	$SiAl_4O_2N_4$					1	
9.3	6H′	$Mg_{2.71}Si_{1.02}Al_{2.27}O_{4.70}N_{2.30}$	B/A	C	1700	0.25	2,3	6H(s) 14H(w) MgO(tr) Mg_2SiO_4(tr)
9.4	12H	$Mg_{1.125}Si_{1.00}Al_{1.92}O_{2.15}N_{2.57}$	B/A	C	1700	0.25	2,3	12H(s) AlN(w)
9.5	4H	Be_3N_2					1	4H(m) 3C(m)
9.6	8H	$Be_{3.90}Si_{1.05}N_4$					1	8H(s) 15R(w)
9.7	21R	$Be_{3.12}Si_{1.44}N_4$					1	21R
9.8	27R	$Be_{2.93}Si_{1.54}N_4$					1	27R(vs) $BeSiN_2$ (w)
9.9	$BeSiN_2$	$Be_{2.50}Si_{1.75}N_4$					1	27R (m) $BeSiN_2$ (m)
9.10	8H	$Be_{5.22}Si_{0.39}O_{1.5}N_3$					1	8H(s) 9R(w)
9.11	15R	$SiAl_4^{17}O_2N_4$	A	H	1700	1.0		15R
9.12	27R	$SiAl_8^{17}O_2N_8$	A	H	1700	1.0		27R(s) 21R(m)
9.13	6H′	as 9.4, ^{15}N-enriched	A	C	1700	0.25	3	6H(s) 14H(w) Mg_2SiO_4(tr)
9.14	12H	as 9.5, ^{15}N-enriched	A	C	1700	0.25	3	12H(m) 21R(m)
9.15	6H′	as 9.4, ^{17}O-enriched	B/A	C	1700	0.25	2,3	6H(s) 14H(w) Mg_2SiO_4(tr)
9.16	12H	as 9.5, ^{17}O-enriched	B/A	C	1700	0.25	2,3	12H(s) AlN(w)
9.17	β'	Be–Mg–Si–Al–O–N					1	β'

Notes. 1: DPT; 2: SiAlON B, then MgO A; 3: Powder bed used.

the composition of fired pellets varied quite considerably from run to run, making preparation of isotopically enriched samples difficult. In one instance (sample 9.16), a particularly pure sample was formed, whereas in another (sample 9.14) a sample of very poor quality resulted.

9.1.2 Si–Al–O–N Polytypoids

When AlN-rich Si_3N_4–SiO_2–Al_2O_3–AlN mixes are sintered, no significant liquid phase forms, and thus reaction is slow, and large weight losses result (compare the Mg–Si–Al–O–N system, where a Mg–Si–O liquid forms). Samples of Si–Al–O–N polytypoids must therefore be prepared by hot-pressing. In this study, two ^{17}O-enriched polytypoids were prepared by hot-pressing AlN–$Si^{17}O_2$ compacts under the conditions listed in Table 9.1.1. Weight losses were negligible in the two runs reported in this Section. The sample of 15R sialon was found to be XRD pure, but the sample of 27R sialon was found to include significant amounts of 21R polytypoid.

Sialon samples prepared by other workers at Newcastle were also hot-pressed.

9.1.3 Beryllium-containing Samples

Beryllium-containing samples must be handled with extreme care because of the toxicity of beryllium. Samples of beryllium polytypoids were prepared under the direction of D. P.Thompson (Newcastle) and L. J. Gauckler (Stuttgart). Details of sample handling are given in Chapter 4, and compositions are shown in Figure 9.1.2.

9.2 Silicon–29 NMR

9.2.1 Previous Investigations

There have been several brief reports of ^{29}Si MAS NMR spectra of polytypoid phases. Klinowski *et al.*[3] reported the spectrum of a sample of 15R sialon which also contained 12H and 21R polytypoids, plus unreacted AlN. Two peaks were observed, at −36.0 and −48.1 ppm, in the intensity ratio 1:2. The authors assigned the peaks to silicon in a predominantly nitrogen environment.

Figure 9.2.1 ^{29}Si MAS NMR spectra of

(a) 15R sialon (sample 9.11) SF=59.6 MHz; PA=26^{O}; RD=300 s; NT=155; SR=3.40 kHz; AF=0.005 s

(b) 12H sialon (sample 9.1) SF=59.6 MHz; PA=27^{O}; RD=300 s; NT=180; SR=3.06 kHz; AF=0.007 s

(c) 27R sialon (sample 9.12) SF=59.6 MHz; PA=26^{O}; RD=300 s; NT=207; SR=3.25 kHz; AF=0.005 s

(d) 6H$'$ Mg-sialon (sample 9.15) SF=59.6 MHz; PA=27^{O}; RD=300 s; NT=185; SR=3.03 kHz; AF=0.01 s

(e) 12H Mg-sialon (sample 9.16) SF=59.6 MHz; PA=27^{O}; RD=300 s; NT=500; SR=3.20 kHz; AF=0.005 s

p=Mg_2SiO_4

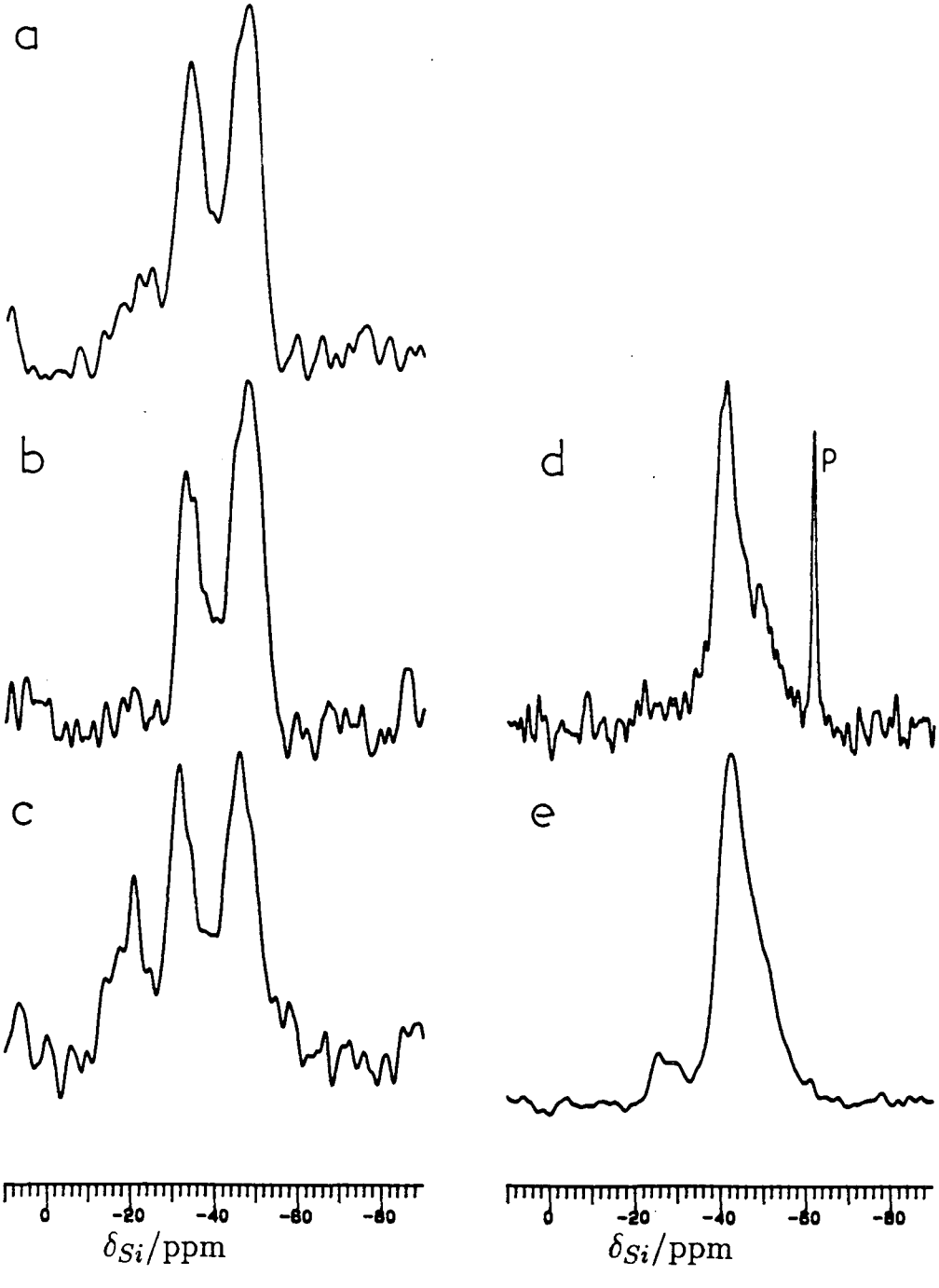

Marshall *et al.*[4] reported ^{29}Si chemical shifts for a series of three polytypoids: 12H (−30.0, −48.1 ppm); 15R(−34.7, −49.5 ppm) and 21R (−34.9,−49.4 ppm). No further details were given.

Apperley[5] has studied a series of Si–Al–O–N and Sc–Si–Al–O–N polytypoids by ^{29}Si MAS NMR. In the scandium series (12H and 15R), the intensity of the higher frequency ($\sim$ −34 ppm) peak is markedly reduced: in the 15R Si–Al–O–N polytypoid, a 2:1 peak ratio is found between peaks at −49.5 and −34.7 ppm, but in the scandium 15R, the ratio is closer to 4:1. If Sc is assumed to occupy octahedral sites, Al is then preferentially occupying sites giving a ^{29}Si peak at −34.7 ppm.

9.2.2 Si–Al–O–N Polytypoids

The ^{29}Si spectra of the polytypoids obtained in this study are shown in Figure 9.2.1, with data listed in Table 9.2.1. The 15R and 12H phases give shifts similar to those of Marshall *et al.*,[4] but the spectrum of the 15R polytypoid definitely shows the presence of a third peak with δ_{Si}=−22.0 ppm, which was not reported in the earlier study. No such peak was seen in the spectrum of the 12H polytypoid. Sample 9.12, which contains mainly 27R, plus some 21R gives a spectrum similar to those of the 15R and 12H phases, but with a much more pronounced high-frequency peak with δ_{Si}=−20.8 ppm.

The high-frequency peak observed from both 15R and 27R polytypoids has a chemical shift more typical of a silicon carbide (see Section 3.2.10), and is by far the least-negative shift observed in this study for a silicon oxynitride environment. Indeed, it was initially assumed to be due to a carbide impurity, but careful analysis of XRD photographs demonstrates that the samples contain no crystalline impurities apart from those listed in Table 9.1.1.

It has proved impossible to rationalise the spectra in terms of the structures of the phases because of the considerable uncertainties in the structural determinations and the complexity of the structures themselves. It is clear both from FWHH measurements and visual inspection that all peaks in the spectra are composite, and made up from silicon in a variety of environments.

Table 9.2.1 ^{29}Si and ^{15}N MAS NMR data on polytypoid phases.

sample	phase	Silicon-29			Nitrogen-15	
		δ_{Si}/ppm	FWHH/Hz	Intensity	δ_N/ppm	FWHH/Hz
9.1	12H (Si/Al/O/N)	−33.4	450	4		
		−47.7	530	7		
9.2	15R (Si/Al/O/N)	−21.0		1		
		−34.3	450	3		
		−47.0	500	3.5		
9.3	6H′ (Mg/Si/Al/O/N)	−42.0	300			
		−62.4[a]	25			
9.4	12H (Mg/Si/Al/O/N)	−41.9	600			
9.11	15R (Si/Al/O/N)	−22.0	485	1[b]		
		−35.3	440	3.6[b]		
		−47.8	515	5.4[b]		
9.12	27R (Si/Al/O/N)	−20.8		2		
		−31.5	300	3		
		−45.9	420	3		
9.13	6H′ (Mg/Si/Al/O/N)	−40.5	350		57.2	600
		−50.2	sh			
		−62.0[a]	25			
9.14	12H (Mg/Si/Al/O/N)	−42.5	600		61.5	650
9.15	6H′ (Mg/Si/Al/O/N)	−41.4	380			
		−49.3	sh			
		−62.0[a]	30			
9.16	12H (Mg/Si/Al/O/N)	−42.8	600			
9.17	21R (Be/Si/O/N)	−45.3	15			

Notes. (a) Mg_2SiO_4; (b) Determined by spectral deconvolution.

The structures of 12H and 15R phases were discussed in Section 3.1.3. From previous experience, it was predicted that aluminium would occupy the octahedral sites, and this is confirmed by the ^{29}Si NMR, which shows no peaks around -200 ppm, characteristic of [SiX_6]. The four coordinate sites, of which there are several, are then occupied by both Si and Al. Oxygen would be expected to coordinate principally to ionic (i.e. octahedral) aluminium, with nitrogen occupying the anion sites between layers of four coordinate metal.

It is possible[6] (see Section 10.1) to relate δ_{Si} to Si–X–Si bond angle in simple covalent silicon compounds without reference to the identity of X. Silicon in a wurtzite-type structure would, on this basis, be expected to give rise to $\delta_{Si} \sim -20$ ppm, because the Si–X–M bond angle is approximately 109°, as in SiC. Regions of the polytypoid structure are closely related to that of wurtzite, and it is therefore unsurprising that a high-frequency peak is seen in the ^{29}Si NMR of these phases, and that the intensity of this peak is greatest in the 27R polytypoid, which possesses the largest fraction of wurtzite-type layers. It is likely that deshielding is caused by coordination to more ionic non-metals, such as oxygen in layers directly adjacent to layers of octahedral aluminium; and to a lesser extent to occupation of layers with more open structures, in which Si/Al are shared between tetrahedra.

Consideration of the structures of 15R sialon determined by Thompson *et al.*[7] and Bando *et al.*[8] (Figure 3.1.4) leads to the conclusion that if the precise ordering of Si/Al is unimportant in determining δ_{Si}, then the structure of Bando *et al.*. is more likely to be correct because that of Thompson *et al.* possesses only two distinct Si/Al sites outside the octahedral layers (the structure was assumed centrosymmetric), but it is impossible to be sure about this conclusion because the relative effects of O/N coordination, Si–X–M bond angle, and the effect of shared layers, on δ_{Si} are not known. It is quite likely that neither structure is correct.

It is not clear why the 12H sialon, in which there are relatively more tetrahedral layers and less oxygen than the 15R phase, gives rise to a more negative average value of δ_{Si}, but the trend is reversed in going to the 27R phase. The most likely explanation is that the precise composition of the phases, which have considerable ranges of homogeneity parallel to a line of constant M:X ratio, has a profound effect on the relative occupation of sites by Si and Al. The Si–Al–O–N polytypoids are

certainly ripe for further ^{29}Si studies, including the preparation of polytypoids with varying composition within particular phase fields. Changes in relative peak intensities would probably help in assignment of peaks by consideration of the solid-state chemistry of isomorphous substitution.

9.2.3 Mg–Si–Al–O–N Polytypoids

Two polytypoids: 6H′ and 12H were examined by ^{29}Si MAS NMR, and the spectra are shown in Figure 9.2.1. The sharp peak in the spectrum of 6H′ is due to the presence of forsterite (Mg_2SiO_4, δ_{Si}=−61.9 ppm[9]) as a minor impurity. The structures of the two phases were shown in Figure 3.1.14, although it is likely that the stacking order in the phases may not be correct.

Both phases are more oxygen rich than the Si–Al–O–N polytypoids, particularly the 6H′ phase, which has no direct Si–Al–O–N analogue.

The 12H polytypoid shows only a single peak in the ^{29}Si NMR, in contrast to the spectrum of the isostructural Si–Al–O–N polytypoid, which clearly shows two peaks. The two spectra have, however, very similar centres of gravity. Thus, either a structural distortion is occurring when Mg is incorporated into the phase which causes the chemical shifts of the two environments to converge; or the increased oxygen content of the phase is having an variable and unclear effect on δ_{Si}. The former explanation seems much more likely, given the results from earlier chapters showing that in covalent materials n.n. coordination is unimportant in determining δ_{Si}, but the nature of the distortion is not known. The increased Si/Al ratio in the phase also means that the relative site occupancies may vary.

The 6H′ phase also shows one peak, with some structure, notably a low-frequency shoulder. It might be expected that the 6H′ phase would show a considerably more negative chemical shift because of its higher oxygen content. That this is not so is further evidence that bond angles and other structural parameters are the most important factors in determining δ_{Si} in covalent structures, because 6H′ and 12H have very similar structures (the diffraction patterns are very similar), but very different oxygen contents.

Figure 9.2.2 ^{29}Si MAS NMR spectrum of 21R Be–Si–O–N polytypoid
SF=39.8 MHz; PA=70^{o}; RD=1800 s; NT=34: SR=2.85 kHz; LB=0.01s

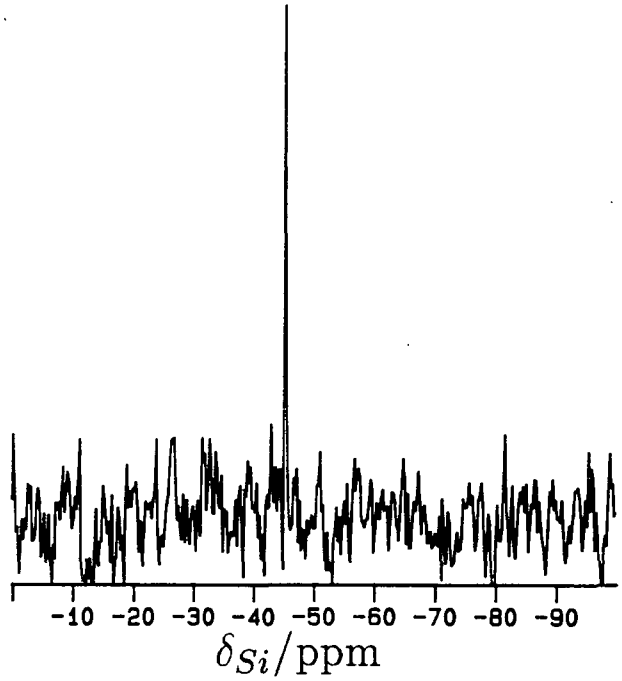

Figure 9.3.1 ^{15}N MAS NMR spectra of
(a) 6H$'$ Mg–sialon (sample 9.13) SF=30.4 MHz; PA=24^{o}; RD=300 s; NT=231; SR=3.25 kHz; AF=0.005 s
(b) 12H Mg–sialon (sample 9.14) SF=30.4 MHz; PA=24^{o}; RD=300 s; NT=142; SR=3.16 kHz; AF=0.005 s

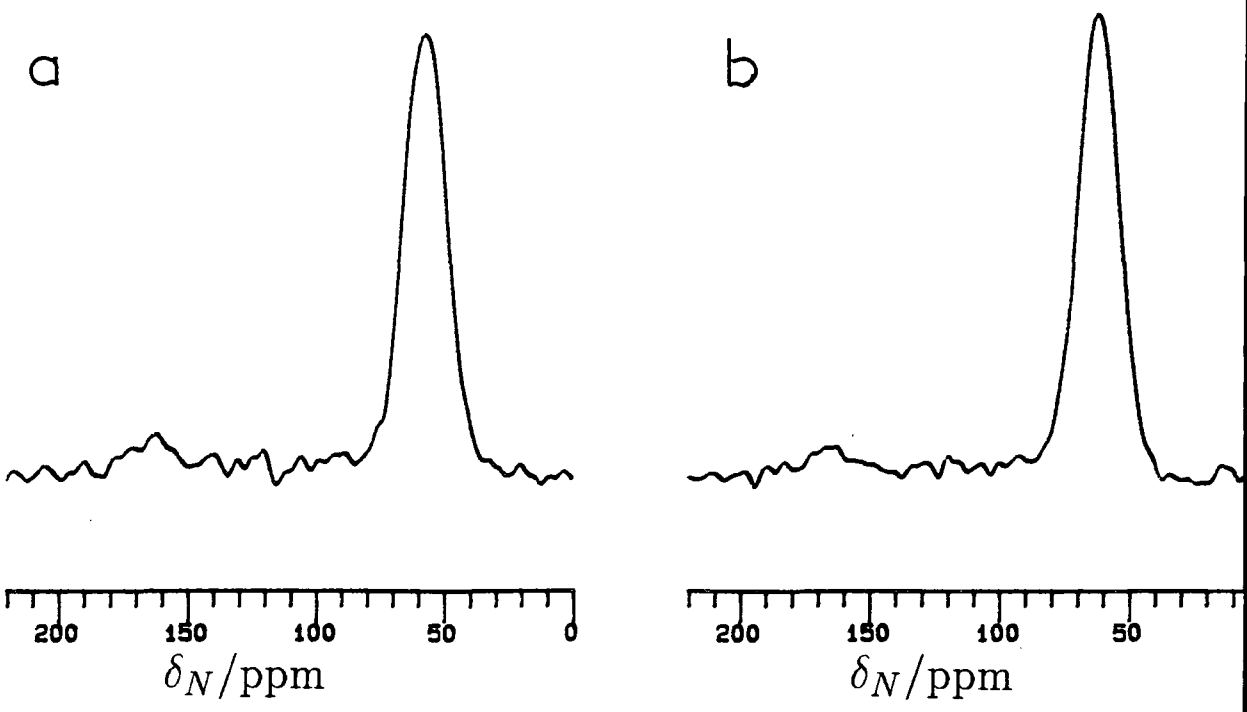

9.2.4 Be–Si–O–N Phases

A series of Be–Si–O–N phases was available, but it was found that the reduced sample volume resulting from the use of sealed capsules, plus the lower field necessary from safety considerations, meant that acquisition of ^{29}Si MAS NMR spectra from these phases was extremely time-consuming. A ^{29}Si spectrum was nevertheless obtained from the sample of 21R polytypoid (sample 9.7), although the signal-to-noise was extremely poor (Figure 9.2.2). The silicon chemical shift observed (−45.3 ppm) is typical of Si in an [SiN_4] environment. Most striking is the apparent narrowness of the resonance (15 Hz), but this figure must be treated with caution because of the poor signal-to-noise.

9.3 Nitrogen–15 NMR

Two ^{15}N-enriched Mg–Si–Al–O–N polytypoids were examined by ^{15}N MAS NMR. Spectra are shown in Figure 9.3.1, with data listed in Table 9.2.1. The two phases give virtually identical spectra. The chemical shifts observed are very similar to that for AlN (δ_N=64 ppm[4]), and the nitrogen environments are expected to be very similar to those in AlN, with N coordinated to four Si/Al atoms. The linewidths suggest a considerable degree of chemical shift dispersion due to a variety of environments.

9.4 Oxygen–17 NMR

Four samples were examined by ^{17}O NMR, and data are listed in Table 9.4.1. Spectra obtained at a Larmor frequency of 40.7 MHz are illustrated in Figure 9.4.1. Spectra obtained at 27.1 MHz were identical in feature, and are not shown. In no case was a significant field-dependent shift observed, and therefore all shifts recorded at 40.7 MHz are regarded as true values. It is concluded that χ_Q < 0.4 MHz in all phases. Linewidths are similar to those observed in the ^{15}N NMR study (Section 9.3), and are thus probably due principally to chemical shift dispersion.

It is clear from the spectra that within each series of two polytypoids, the ^{17}O spectra are virtually indistinguishable, but there is a significant shift in δ_O between Si–Al–O–N and Mg–Si–Al–O–N polytypoids. The chemical shift observed

Figure 9.4.1 ^{17}O MAS NMR spectra of

(a) 12H Mg–sialon (sample 9.16) SF=40.7 MHz: PA=23^{o}; RD=1 s; NT=2000; SR=6.60 kHz; AF=0.005 s

(b) 6H$'$Mg–sialon (sample 9.15) SF=40.7 MHz: PA=23^{o}; RD=1 s; NT=4800; SR=7.96 kHz; AF=0.005 s

(c) 15R sialon (sample 9.11) SF=40.7 MHz; PA=15^{o}; RD=1 s; NT=1200; SR=5.44 kHz; AF=0.005 s

(d) 27R sialon (sample 9.12) SF=40.7 MHz; PA=15^{o}; RD=1 s; NT=1600; SR=5.85 kHz; AF=0.005 s

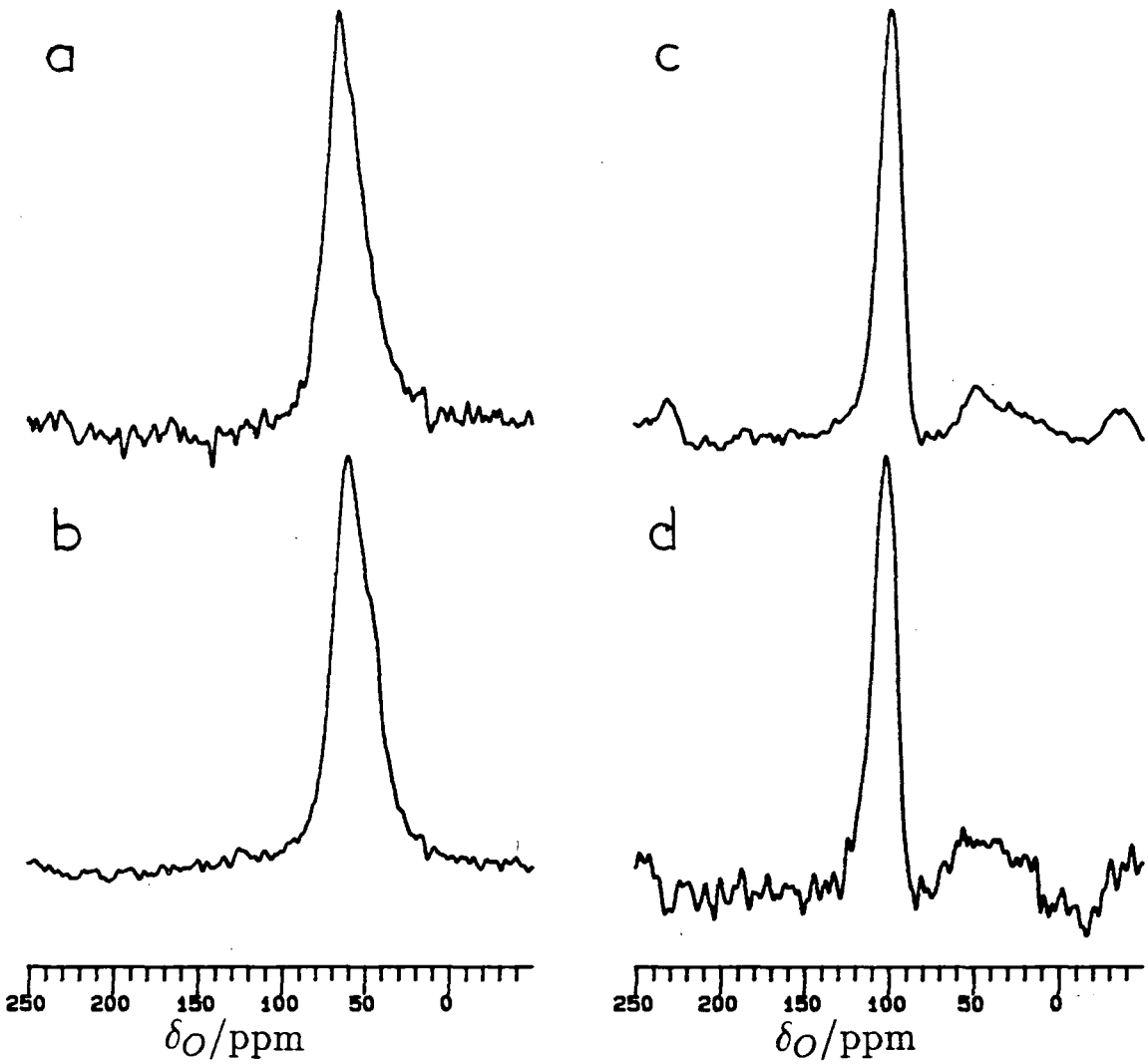

Table 9.4.1 ^{17}O MAS NMR of polytypoid phases.

Sample	phase	27.1 MHz		40.7 MHz	
		δ_O^{200}/ppm	FWHH/Hz	δ_O^{300}/ppm	FWHH/Hz
9.11	15R (Si/Al/O/N)	95	600	95	600
9.12	27R (Si/Al/O/N)	100	600	101	700
9.15	6H′ (Mg/Si/Al/O/N)	59	1000	59	1100
9.16	12H (Mg/Si/Al/O/N)	61	1050	65	1200

in the magnesium-containing phases is much closer to that observed from MgO (δ_O=47.4 ppm), in which oxygen is coordinated only to Mg. Structural considerations suggest that in the Mg polytypoids, oxygen will be mainly coordinated to Mg in six-coordinate layers (but see Section 9.5), whereas in the Si–Al–O–N phases, coordination is mainly to Al in the same six-coordinate layers. Mg^{2+} and Al^{3+} are, however, isoelectronic and have similar ionic radii, and it is therefore difficult to explain the difference in shifts between the two systems. It may be connected to the possible distortions in structure referred to in Section 9.2.3, and to the unusual oxygen environments in these phases.

9.5 Aluminium–27 NMR

Early ^{27}Al MAS NMR studies of polytypoid phases[3,10] showed that four and six coordinate aluminium could be readily distinguished, with six coordinate Al giving observed shifts of 2.3 or 13 ppm, with four coordinate Al at 108 or 110 ppm, assigned as [AlN_4] coordination. These studies have been extended by workers at Durham,[4,5] with similar findings, but all studies have demonstrated the need for very rapid sample rotation if spinning side-bands are not to cause severe problems in spectral interpretation. Spectra of five polytypoid phases were obtained at spin rates of 10–11 kHz in this study. Spectra are shown in Figure 9.5.1, with data summarised in Table 9.5.1. Intensity data are not important because of the problems of quantifying ^{27}Al spectra discussed in Chapter 2, and the problem of accurate background subtraction, but approximate peak areas do give an indication of relative numbers of environments. Small amounts of $MgAl_2O_4$ and Al_2O_3 could also lead to overestimation of the amount of octahedral aluminium.

Figure 9.5.1 ^{27}Al MAS NMR spectra of (no background subtracted)
(a) 12H sialon (sample 9.1) SF=78.2 MHz; PA=15^{O}; RD=1 s; NT=440; SR=10.60 kHz; AF=0.005 s
(b) 15R sialon (sample 9.11) SF=78.2 MHz; PA=15^{O}; RD=1 s; NT=700; SR=10.10 kHz; AF=0.005 s
(c) 27R sialon (sample 9.12) SF=78.2 MHz; PA=15^{O}; RD=1 s; NT=700; SR=10.10 kHz; AF=0.005 s
(d) 6H$'$ Mg–sialon (sample 9.15) SF=78.2 MHz; PA=15^{O}; RD=1 s; NT=120; SR=10.60 kHz; AF=0.005 s
(e) 12H Mg–sialon (sample 9.16) SF=78.2 MHz; PA=15^{O}; RD=1 s; NT=120; SR=10.56 kHz; AF=0.005 s

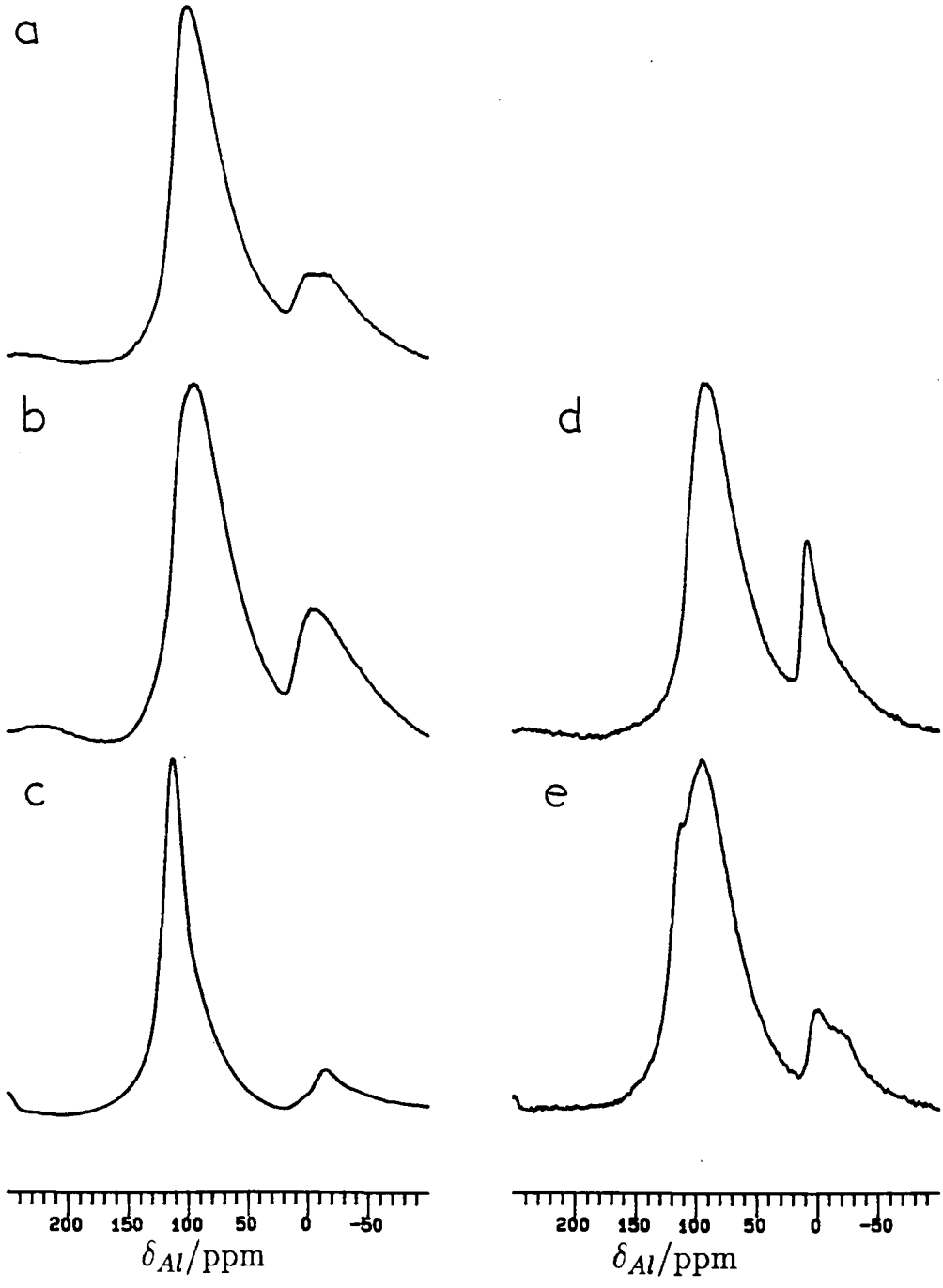

Table 9.5.1 ^{27}Al MAS NMR of polytypoid phases at 78.2 MHz.

Sample	phase	δ_{Al}^{300}/ppm	FWHH/Hz	Approx. Intensity
9.1	12H (Si/Al/O/N)	101	3500	4
		−8	4500	1
9.11	15R (Si/Al/O/N)	94	4000	3
		−6	4600	1
9.12	27R (Si/Al/O/N)	113	1800	
		?		
9.3	6H′ (Mg/Si/Al/O/N)	93	3700	4
		6	800	1
9.16	12H (Mg/Si/Al/O/N)	93	4400	4
		−1	1300	1

All the phases show a peak in the region 90–110 ppm, which is assigned to Al in a tetrahedral environment, with coordination principally to nitrogen. No splitting of the resonance is observed (contrast the ^{29}Si spectra presented in Section 9.2.2) due to the different tetrahedral environments, which must be occupied by Al as well as Si, and it must be assumed that the expected splitting is swamped by the broadening of resonances due to second order quadrupolar coupling. It is possible that higher-field studies would allow these environments to be resolved. The Mg-containing phases do not give significantly lower δ_{Al} values, despite the much higher oxygen content of these materials.

All of the phases except 27R Si–Al–O–N also show marked peaks in the region −10 to +10 ppm due to octahedral aluminium. In the case of 27R, it is assumed that the intensity of the peak is too small, compared to the relative amounts of tetrahedral and octahedral Al in the phase. It was expected that the intensities of the octahedral peaks from the Mg-containing polytypoids would be significantly reduced with respect to the Si–Al–O–N phases because of Mg preferentially occupying the octahedral sites. This is clearly not observed, and may either be due to Mg occupying tetrahedral sites (as in Mg–O–N polytypoids[7]) or to the effect of small amounts of $MgAl_2O_4$ impurity, which contains significant octahedral Al

Figure 9.7.1 ^{9}Be MAS NMR spectra of

(a) 27R polytypoid (sample 9.8) SF=28.1 MHz; PA=45^{O}; RD=1 s; NT=705; SR=1.24 kHz; LB=0.01 s

(b) $BeSiN_2$/27R (sample 9.9) SF=28.1 MHz; PA=45^{O}; RD=1 s; NT=404; SR=1.43 kHz; LB=0.01 s

(c) 8H polytypoid (sample 9.6) SF=28.1 MHz; PA=45^{O}; RD=1 s; NT=800; SR=1.31 kHz; LB=0.01 s

(d) 21R polytypoid (sample 9.7) SF=28.1 MHz; PA=45^{O}; RD=1 s; NT=2090; SR=1.20 kHz; LB=0.01 s

(e) Be_3N_2 (sample 9.5) SF=28.1 MHz; PA=45^{O}; RD=1 s; NT=2000; SR=1.10 kHz; LB=0.01 s

(f) 8H/9R polytypoids (sample 9.10) SF=28.1 MHz; PA=45^{O}; RD=1 s; NT=308; SR=1.33 kHz LB=0.01 s

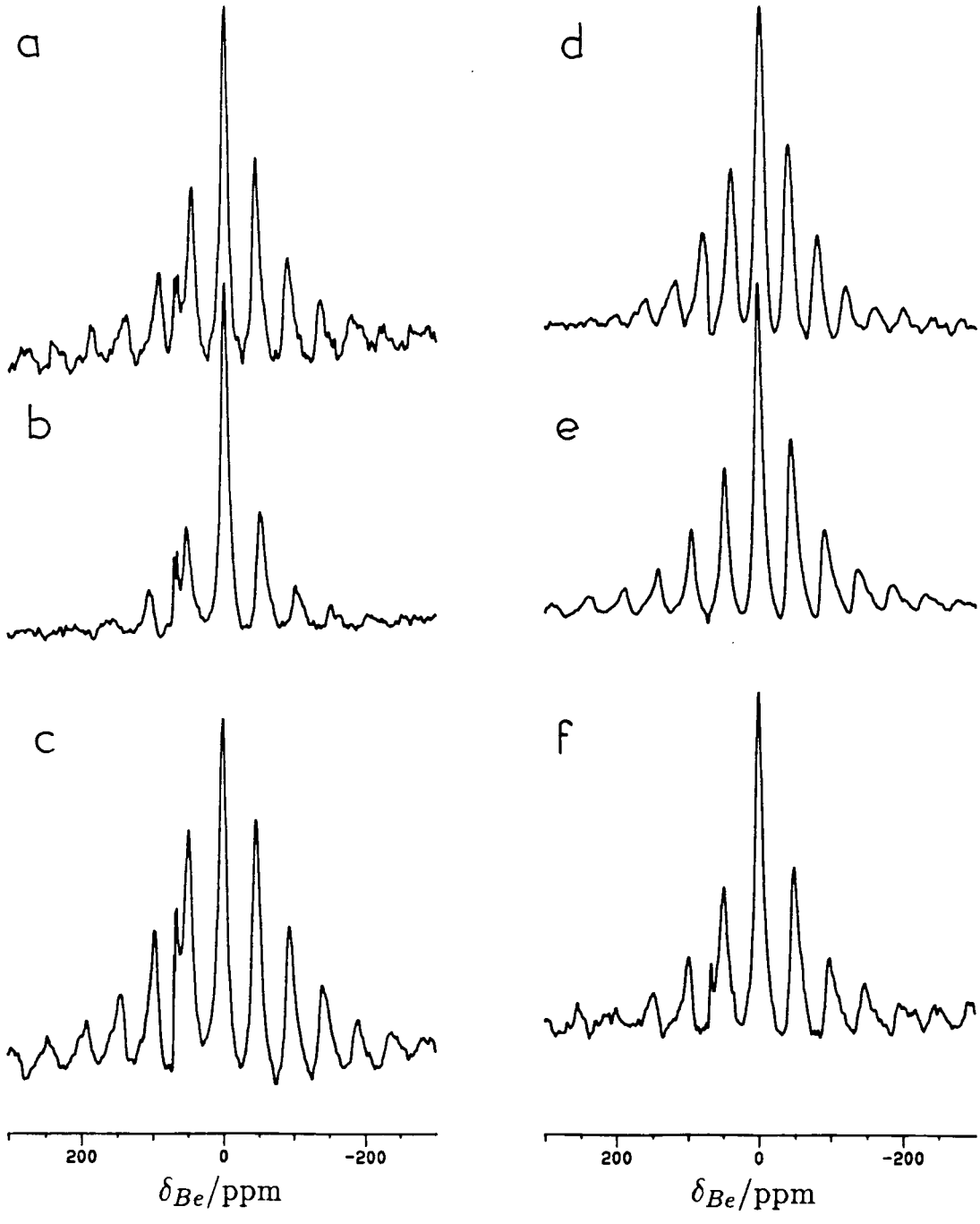

($\delta_{Al} \approx$ 0 ppm).

9.6 Discussion

A considerable amount of data was acquired on Si–Al–O–N and Mg–Si–Al–O–N polytypoids in the hope of resolving some of the structural issues relating to these phases, but it proved impossible to make many significant breakthroughs. The structures are complex, and also very different from any other phases studied, and it proved impossible to get any firm handles on the structures which would allow assignment of spectra. Two possible approaches could now be tried:

(i) Obtain accurate structural information on one of the phases using x-ray and probably neutron diffraction.This should allow the ^{29}Si spectrum to be assigned, and an understanding of the ^{15}N and ^{17}O spectra to be reached. Changes in these spectra on examining other phases should then allow a much greater amount of structural information on these phases to be obtained.

(ii) Studies of phase fields in which materials of very different composition are prepared could allow ^{29}Si spectra to be assigned, by consideration of the effect of changing composition on peak intensities.

9.7 Beryllium–9 NMR

A comprehensive ^{9}Be study of the Be–Si–O–N polytypoids was undertaken in the hope that ^{9}Be MAS NMR would prove of use as a structural tool. The ^{9}Be MAS NMR of six Be–Si–O–N samples plus a β'–Be–Mg–Si–Al–O–N phase are shown in Figure 9.7.1, referenced to 0.05 M $BeSO_4$ solution. Data are listed in Table 9.7.1. The ^{9}Be static NMR spectrum of sample 9.7 was obtained. It showed a broad featureless peak of width 5,500 Hz. No satellite peaks were observed.

The ^{9}Be spin-lattice and spin-spin relaxation times for sample 9.7 (21R) were measured using the methods outlined in Chapter 4. T_1 was determined as 20 ± 1 s (single component), and T_2 as 20±4 ms. Attempts to record a ^{9}Be nutation spectrum were unsuccessful, because of the presence of the spike at $\sim$ 70 ppm described in Chapter 4, which had a totally unacceptable distorting effect on the spectrum.

Table 9.7.1 ^{9}Be MAS NMR data at 28.1 MHz.

Sample	Phase	δ_{Be}^{200}/ppm	FWHH/Hz
9.5	Be_3N_2	−2	330
9.6	8H (Be/Si/N)	1	300
9.7	21R (Be/Si/N)	2	280
9.8	27R (Be/Si/N)	2	250
9.9	$BeSiN_2$/27R	2	250
9.10	8H (Be/Si/O/N)	2	300
9.17	β'	−1	

The MAS spectra obtained are almost indistinguishable. Linewidths of 250–330 Hz (9–12 ppm) make accurate determinations of δ_{Be}^{200} difficult. Values of χ_Q are also difficult to estimate, but FWHH measurements suggest that χ_Q is fairly constant throughout the series. Variable field measurements could not be made because of safety considerations. Spinning side-band manifolds extend to at least ±300 ppm in most spectra, putting a lower limit of 8.5 kHz on ν_Q, and 17 kHz on χ_Q. Müller[11] has demonstrated that for a spin–3/2 nucleus, a linewidth of $\sim (0.0301\chi_Q^2/\nu_L)$ can be attributed to second order quadrupolar broadening of the $(\frac{1}{2}, -\frac{1}{2})$ transition under MAS. This puts a maximum value of 530 kHz on the value of χ_Q for a FWHH of 300 Hz. The first figure ignores the possibility that ssbs are often not of significant intensity at the extremities of the manifold, and the latter figure that linebroadening can be due to other factors apart from quadrupolar coupling under MAS. If it assumed that ~ 100 Hz of linebroadening is due to other influences (including 50 Hz natural linewidth), then a value of χ_Q of 400 kHz is obtained. This would lead to a field-dependent shift of 5 ppm at 4.7 T. Such corrections have not been made.

This value can be compared with a value estimated from the static linewidth. If the linewidth is assumed to be solely due to second order quadrupolar broadening, then a FWHH of 5,500 kHz corresponds to χ_Q = 450 kHz. This result is again likely to be an overestimate, because of the many other influences on static linewidths.

Observed variations in δ_{Be}^{200} are small because they are caused principally by

changes in σ_d. A shift range of $\sim$ 4 ppm is observed in the series of compounds examined in this study. In the Be–Si–N phases (9.5–9.9), there is a small high-frequency shift as the silicon content of the phase increases, and the FWHH reduces by $\sim$ 25%, indicating a drop in χ_Q of 10–15%. Be n.n. coordination in all of these phases is [BeN_4], and therefore these changes must be caused by replacement of Be by Si at n.n.n. level, although the reason for this is not clear. One Be–Si–O–N polytypoid (sample 9.10) was also examined, and this sample, in which the Be n.n. environment is mixed oxynitride, gives a spectrum identical to that of the Si-rich Be–Si–N phases, indicating that increased O content at n.n. level has a similar effect to increased Si content at n.n.n. level. It must be reemphasised, however, that all of these effects are small in magnitude, and thus conclusions are difficult to make with certainty.

The above results can also be compared with those described in Section 3.2.6. The ^{9}Be chemical shift (uncorrected) is very similar to δ_{Be} for $[Be(NH_3)_4]^{2+}$ (2 ppm), suggesting that once shift corrections are made, the solid shifts are at significantly higher frequency than for a similar n.n. environment in solution. No allowance for n.n.n. differences has been made. Nearly all of the δ_{Be}^{200} values from the solids are also at significantly higher frequency than those observed for oxide and silicate phases (-0.6 to -4.0 ppm relative to $Be(H_2O)_4^{2+}$).

The β' sample (8.17) gives rise to a negative δ_{Be} value. It is assumed that the coordination environment is [BeN_4], but nothing is known about the distribution of Be, Mg, Si and Al in this phase.

The value of T_1 is surprisingly long for a quadrupolar nucleus, and indicates once again the problems associated with recording of spectra of any nuclei in ceramic samples.

The T_2 value measured using a rotation-synchronised CPMG sequence, indicates that the natural linewidth of a typical ^{9}Be resonance in a ceramic is 50 Hz. The CPMG sequence focuses quadrupolar broadening (probably including second order effects[12]), as well as chemical shift and dipolar effects, including chemical shift dispersion.

To conclude, the ^{9}Be shift range is found to be disappointingly small in ceramic

samples, but it is possible to discern that increasing Si n.n.n. coordination leads to a small high-frequency shift in δ_{Be}. If instrumental constraints could be overcome, it is possible that measurements of χ_Q might also provide structural information.

REFERENCES

1. Popper, P. *Progress in Nitrogen Ceramics*; Riley, F. L. Ed.; NATO ASI Ser. E; Martinus Nijhoff: The Hague. **65**, 187–210 (1983).
2. Buang, K. Ph.D. Thesis, University of Newcastle upon Tyne, 1979.
3. Klinowski, J.; Thomas, J. M.; Thompson, D. P.; Korgul, P.; Jack, K. H.; Fyfe, C. A.; Gobbi, G. C. *Polyhedron* **3**, 1267–1269 (1984).
4. Marshall, G. L.; Harris, R. K.; Apperley, D. C.; Yeung, R. R. *Science of Ceramics* **14**, 347–352 (1987).
5. Apperley, D. C. Internal Report, University of Durham, 1987.
6. Leach, M. J.; Harris, R. K.; Thompson, D. P. *Euro-Ceramics*; de With, G. Ed.; Elsevier: London, 1989. Volume 2. pp 140–144.
7. Thompson, D. P.; Korgul, P.; Hendry, A. Reference 1, pp 61–74.
8. Bando, Y.; Mitomo, M.; Kitami, Y.; Izumi, F. *J. Microsc. (Oxford)* **142**, 235–246 (1986).
9. Mägi, M.; Lippmaa, E.; Samoson, A.; Engelhardt, G.; Grimmer, A. -R. *J. Phys. Chem.* **88**, 1518–1522 (1984).
10. Butler, N. D.; Dupree, R.; Lewis, M. H. *J. Mater. Sci. Lett.* **3**, 469–470 (1984).
11. Müller, Von D. *Annal. der Physik (Leibzig)* **39**, 451–460 (1982).
12. Challoner, R. Ph.D. Thesis, University of Durham, 1989.

Figure 10.1.1 Plot of average Si–X–Si bond angle against δ_{Si} for a series of simple covalent Si compounds

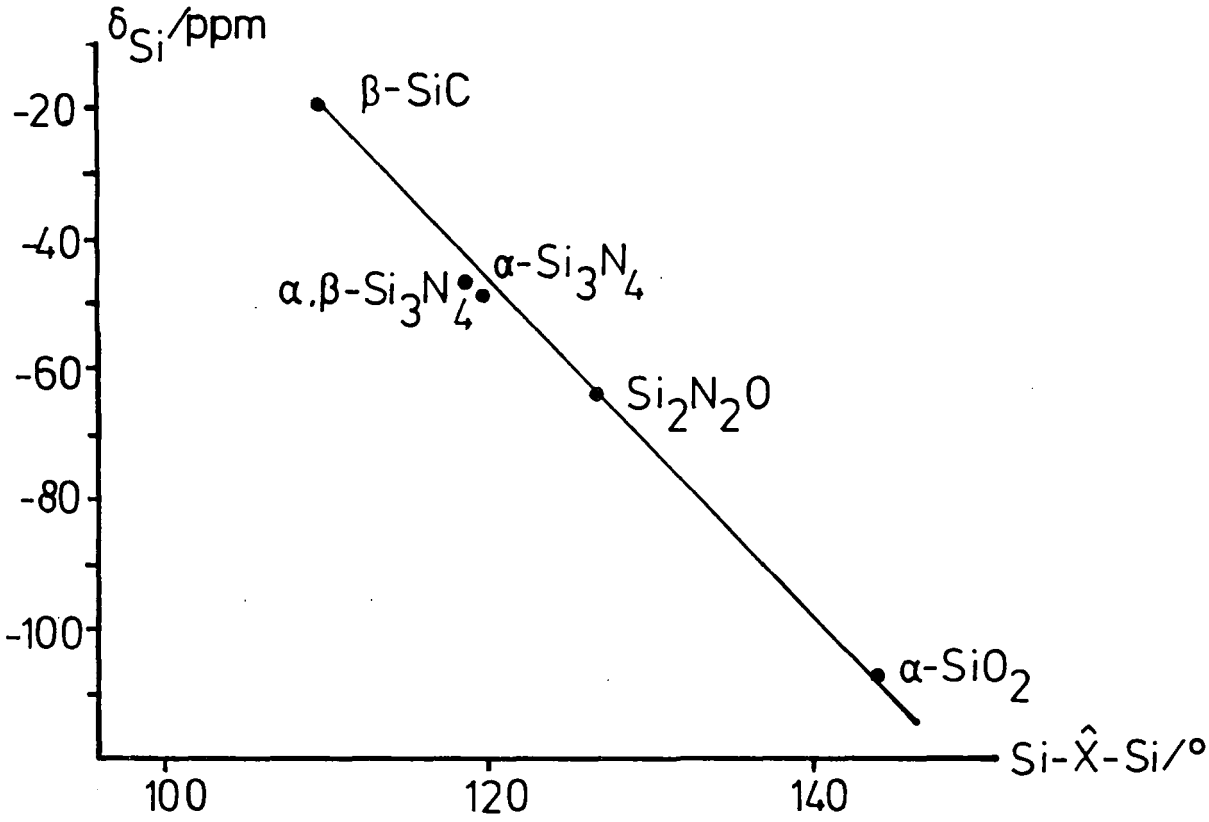

Chapter X

Conclusions

The aim of this brief chapter is to summarise the main findings of the study of a general nature, and make some suggestions for further work.

10.1 Silicon–29 NMR

A considerable volume of ^{29}Si data on a wide variety of phases has been acquired in the course of this study. Some of the results have confirmed the accepted notion that δ_{Si} is determined principally by n.n. coordination environment in sialon ceramics, but many others have suggested that other factors are also at work, particularly concerning materials in which bonding is principally covalent.

A clue as to how these other factors might be involved can be seen in Figure 10.1: a plot of δ_{Si} versus average Si–X–Si bond angle in a small range of simple binary and ternary covalent silicon compounds. Each Si—X bond is weighted equally in the case of Si_2N_2O. It must be stressed that no correction was made for the identity of X. This type of correlation is similar to that proposed by Sherriff and Grundy,[1] and discussed in Section 3.2.2.1, although the angle dependence is somewhat different. Magnetic anisotropy, and the hybridisation of the Si—X bonding orbital is therefore likely to be important in covalently bonded sialon materials. Attempts were made to extend the treatment of Sherriff and Grundy more exactly to the materials used for Figure 10.1, without success. Other phases did not fit into the correlation, probably because of the difficulties in defining and weighting different Si–X–M bond angles in complex phases, but it is clear from the discussion in Section 9.2.2 on sialon polytypoids that there is a connection between the very small Si–N–M bond angles in these phases and the less negative δ_{Si} values observed.

In phases in which bonding is primarily ionic, such as N–apatite, n.n. coordination is found to be very important in determining δ_{Si}, and correlations such as

that of Figure 6.2.10 are of potential use in determining the n.n. environment in phases of unknown structure.

In the majority of phases studied in this Thesis, accurate crystallographic information is not available, and therefore correlations such as Figure 10.1 and that of Sherriff and Grundy cannot be attempted. It is clear, however, particularly in phases such as new phase and $LaSi_3N_5$ that crystallographic environment is crucial in determining δ_{Si}. Studies of wurtzite materials and α'– and β'–sialons confirm this. Particularly important is the observation in β'–sialons and other phases that isomorphous substitution does not significantly affect δ_{Si}, and a possible explanation of this observation was described in Section 8.2.3. In these phases, as in the silicates analysed by Sherriff and Grundy, it seems likely that δ_{Si} can be related to crystallographically measurable parameters, without reference to the precise identity of the atoms.

The other important conclusion reached on factors affecting δ_{Si} concerned the identity of the counter-ion. Previous workers have not paid a great deal of attention to the effect of counter-ion in silicates or sialons, but it became clear in the course of the work on yttrium and lanthanum sialons that significant differences in δ_{Si} were occurring between the two cases. In addition, in materials such as $LaSi_3N_5$, the number of coordinating counter-ions is also important. These effects were discussed in relation to ^{17}O chemical shifts and cation polarisability in Section 6.2.3.

10.2 Nitrogen–15 and Oxygen–17 NMR

Preparation of isotopically enriched materials has proved extremely profitable in the information obtained from ^{15}N and ^{17}O NMR spectra. The most spectacular example was the critical help which the ^{15}N NMR spectrum of new phase provided in the determination of the crystal structure of this phase. It is anticipated that ^{15}N MAS NMR studies will also provide useful in determining the structures of other phases of unknown structure, such as the yttrium silicon nitrides.

The factors which affect δ_N and δ_O have been studied in detail. The most important factor is the ionicity of the nitrogen or oxygen bonds. This can be used to distinguish environments in materials such as the La–Si–O–N phases, where

coordination is mixed ionic/covalent. Thus [NSi_2] and [NSi_3], and O_{nb} and O^{2-} sites can easily be differentiated. The effect in ^{17}O NMR is found to depend on ionic radius of the counter-ion, as found in metal oxides[2] and silicates.[3] An explanation in terms of cation polarisability was outlined in Section 6.4, and should be equally applicable to ^{17}O or ^{15}N chemical shifts. Powerful evidence for this explanation was found in the ^{15}N NMR of the Mg and Li wurtzite phases, where δ_N was found to be much lower than in phases such as $LaSiO_2N$, despite coordination to metals of similar electronegativity.

10.3 Other Nuclei

^{27}Al, ^{139}La, ^{7}Li and ^{9}Be have all been examined in the course of this study, but none have proved of great use in structural work on sialon phases. ^{27}Al MAS NMR has proved useful in identifying 6– and 4–coordinate environments, but second order quadrupolar coupling has the unfortunate effect of further broadening resonances already broadened significantly by other influences. In no cases were individual environments resolved in a single phase, except where Al with more than one coordination number was present. It is probable that use of higher fields and rapid spin rates will allow a great deal of structural information ultimately to be deduced, particularly if an Al-free probe is also available.

^{7}Li and ^{9}Be are both easy to observe, but chemical shift measurements proved of very limited use because of the very slight shift ranges found, attributed to the fact that chemical shift is determined only by σ_d. More future is probably to be had in measurements of quadrupolar parameters. The same is also true of ^{139}La, where quadrupolar broadening is so great that no measurements of δ_{La} could be made.

10.4 Linewidth in Sialon Phases

A considerable variation in FWHH has been found in MAS spectra obtained in this Thesis, from 25 Hz for the ^{15}N resonance of Si_2N_2O to 5,000 Hz for the ^{27}Al resonance from U–phase. Many factors are at work, and a few of the most important are considered here, approximately in decreasing order of importance:

(i) Resonances from quadrupolar nuclei are seen to be significantly broader than

from spin–1/2 nuclei due to second order quadrupolar coupling. In general, nuclei with large quadrupole moments (e.g. ^{139}La) are found to give much broader resonances than those with small moments (e.g. ^{9}Be, ^{7}Li, ^{17}O). There are, however, some unexpected anomalies: ^{27}Al and ^{139}La have, for example, quite similar quadrupole moments, yet FWHH measurements are very different. Differences in e.f.g. must be important.

(ii) Chemical shift dispersion is seen to be crucial in determining linewidths for all nuclei. Its effect can be seen particularly clearly in the spectra of phases such as $MgSiAlN_3$, where Si/Al disorder leads to a 10 fold increase in FWHH over the closely related phase $MgSiN_2$, where no disorder occurs; and in the discrepancies in FWHH between samples of say β–Si_3N_4 reported in the literature. It is likely that most linewidth in excess of the narrowest observed (e.g. 50 Hz for ^{29}Si) is due to chemical shift dispersion, although unaveraged coupling may also be important in some cases. The two effects can in principle be differentiated by variable field studies. Some chemical shift dispersion is thought to be due to nuclei at surfaces, which also tend to have shorter T_1 times, enhancing the signal from these nuclei. Variable recycle delay experiments could, in principle, be used to investigate this effect.

(ii) Unaveraged dipole-quadrupole coupling is thought to be an important line broadening mechanism. An important finding in this Thesis is that (^{29}Si,^{14}N) coupling does not significantly contribute to the FWHH, but that (^{29}Si,^{139}La) and (^{15}N,^{139}La) probably do.

(iv) The effect of paramagnetic ions on linewidth in ceramic phases has not been investigated: all of the nitrogen-containing phases studied in this Thesis contain significant (up to 0.1%) quantities of iron, and the effects of this iron must be investigated. Preliminary investigations on CVD α–Si_3N_4 (which contains no paramagnetics) indicate that the iron has little effect on the ^{29}Si spectrum, except to increase the breadth of the ssb manifold. This is probably because the iron is present only at the grain boundary in this phase. In other phases this might not be the case.

(v) Natural linewidth can in theory be calculated from T_2 measurements, but these are not practicable on ^{29}Si or ^{15}N because of the long T_1 times. Linewidths

of < 5 Hz are sometimes recorded on silicates, and there is no reason to doubt that T_2 times are similar in sialons, although paramagnetic centres will also affect FWHH by altering T_2. For quadrupolar nuclei, natural linewidths of 50 Hz have been measured for ^{27}Al in AlN and ^{9}Be in a beryllium sialon.

10.5 Suggestions for Further Work

Many suggestions have already been made concerning preparation of further samples (e.g. polytypoids, Section 9.6), preparations of isotopically enriched materials (e.g. yttrium silicon nitrides, Chapter 6) and high-field studies on quadrupolar nuclei (*vide supra*). The other approach which could be taken is to apply new NMR techniques to sialons. Two possibilities are:

(i) Application of 2-D techniques to ^{29}Si (and possibly ^{15}N) NMR of sialons. The use of 2-D ^{29}Si COSY by Fyfe and co-workers has already been mentioned in Section 3.2.2. Isotopic enrichment in ^{29}Si would be necessary for such studies on sialons. It might then be possible to establish connectivities in materials such as polytypoids through this approach.

(ii) Use of DAS and DOR to improve resolution of spectra of quadrupolar nuclei has been referred to in Chapter 2. ^{27}Al NMR would particularly benefit from DOR, because it might allow aluminium environments to be identified by analogy to ^{29}Si NMR, if ^{29}Si-like linewidths could be achieved.

It must be clear from the work described in this Thesis that there are many structural issues concerning sialon materials which could be investigated using MAS NMR. Enough results have been obtained to demonstrate that time spent in such studies would not be wasted.

REFERENCES

1. Sherriff, B. L.; Grundy, H. D. *Nature* **322**, 819–822 (1988).
2. Turner, G. L.; Chung, S. E.; Oldfield, E. *J. Magn. Reson.* **64**, 316–324 (1985).
3. Timken, H. K. C.; Schramm, S. E.; Kirkpatrick, R. J.; Oldfield, E. *J. Phys, Chem.* **91**, 1054–1058 (1987).

Figure A.1 Representation of the Si–Al–O–N system

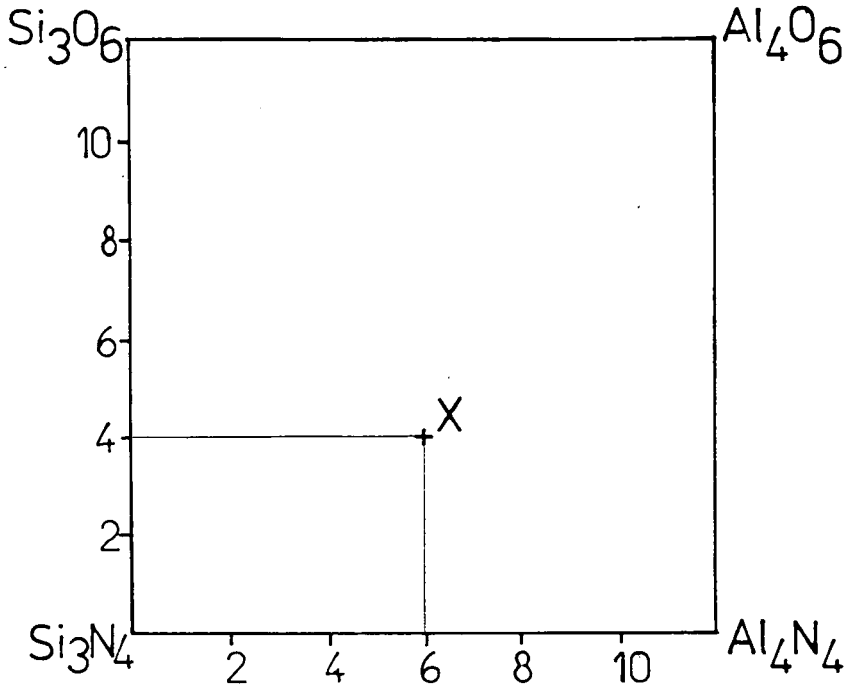

Figure A.2 Representation of the La–Si–Al–O–N system

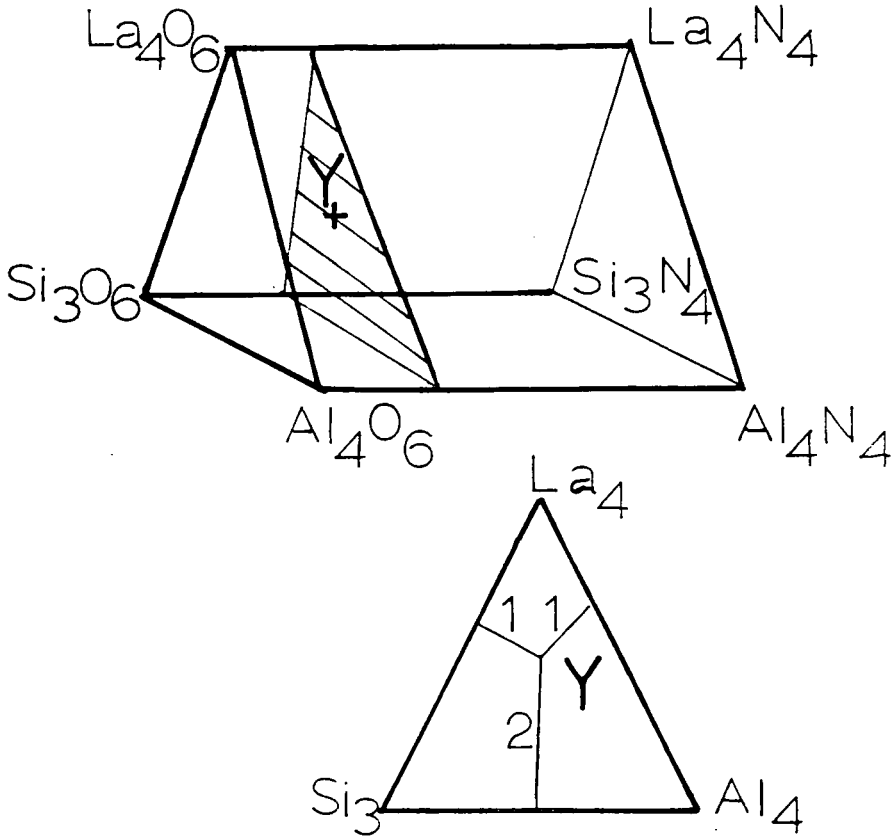

Appendix A

Representation of Four and Five Component Systems

Phase relationships in two and three component systems are commonly represented by standard two-dimensional phase diagrams. It is also possible to represent M_1–M_2–X_1–X_2 four component systems in two dimensions if the oxidation states of the four components remain constant, using a reciprocal salt diagram. In the diagram, the fraction of positive charge (assuming fully ionic bonding) in M_1 and M_2 is plotted along one axis, and the fraction of negative charge in X_1 and X_2 along the other axis. This allows a square phase diagram to be constructed. An example for the Si–Al–O–N system is shown in Figure A.1. Note that the corners represent binary oxides and nitrides.

Consider the point X. The x coordinate implies that equal positive positive charge is resident in Si and Al, and the y coordinate that 2/3 of negative charge is resident in N and 1/3 in O. This corresponds to a composition $Si^{6+}Al^{6+}O^{8-}N^{4-}$, or $(Si^{4+})_{\frac{3}{2}}(Al^{3+})_2(O^{2-})_2(N^{3-})_{\frac{8}{3}}$, or $Si_9Al_{12}O_{12}N_{16}$. To represent a known composition on the diagram, the process is simply reversed.

A M_1–M_2–M_3–X_1–X_2 system can be represented by incorporation of a third dimension to give a triagonal prism, see Figure A.2. The square faces are four component diagrams as in Figure A.1, and the triangular faces are standard three component phase diagrams except that compositions are again plotted in equivalents. Consider the point Y. This point lies on a plane parallel to the triangular faces which is 1/4 of the way from the oxide face to the nitride face, giving an anion composition $O^{9-}N^{3-}$. The projection of the triangular plane allows a cation composition of $La^{6+}Si^{3+}Al^{3+}$ to be deduced. This gives an overall composition of $La_2Si_{\frac{3}{4}}AlO_{\frac{9}{2}}N$.

This prismatic representation is rather unwieldy, so phase relationships are generally considered on sections through the prism, often with a constant M:X ratio (by atoms). These sections are generally not square, but no new principles are required for interpretation.

Appendix B

Referencing of ^{15}N NMR Spectra

There is no single, commonly accepted reference material for ^{14}N and ^{15}N NMR, unlike for most other commonly observed nuclei. No suitable internal reference material exists for solution-state NMR, because of the large solvent shifts observed in nitrogen NMR. Many external reference materials have been suggested for solution-state NMR, including NH_4NO_3 solutions of varying concentration (NH_4^+ or NO_3^- peaks), $NaNO_3(aq)$ and $NaNO_2(aq)$, but the large solvent shifts have led to the conclusion that a pure material is more suitable. Two materials have emerged as the most commonly accepted reference materials for solution-state NMR: $CH_3NO_2(l)$ and $NH_3(l,298\ K)$. Nitromethane has the advantage that it poses no practical difficulty in use, but possesses the perceived disadvantage that most chemical shift values are then negative. This has led to the use of liquid ammonia by many authors, despite the obvious practical difficulties. Mason[1] has listed the relative chemical shifts of the common nitrogen reference materials in solution.

The controversy over referencing has extended to the solid state. Authors have generally been content to reference to their own solid materials, bypassing the problem outlined above. Unfortunately, many different standards have been used, but the NH_4^+ peak from solid NH_4NO_3 is now beginning to become the norm for inorganic work, and has therefore been used throughout this Thesis. Table B.1 summarises the important nitrogen reference materials, and their relative chemical shifts.

Table B.1 Common nitrogen reference materials in the solution and solid states.

Material	form	δ_N/ppm*	examples
CH_3NO_2	*l*	0	1,2
NH_3	*l*,298 K	−380.2	3,4
NH_4NO_3	*s*	−358.2	5,6
NH_4NO_3	*s*	−4.8	7

*relative to nitromethane

REFERENCES

1. Mason, J. *Multinuclear NMR*; Mason, J. Ed.; Plenum, New York, 1987; pp 335–367.
2. Mason, J.; Mingos, D. M. P.; Schaefer, J.; Sherman, D.; Stejskal, E. O. *J. Chem. Soc. Chem. Commun.*, 444–446 (1985).
3. Levy, G. C.; Lichter, R. L. *Nitrogen–15 Nuclear Magnetic Resonance Spectroscopy*; Wiley: New York, 1979.
4. Chuang, I. D.; Hawkins, B. L.; Maciel, G. E.; Meyers, G. E. *Macromolecules* **18**, 1482–1485 (1985).
5. Bunker, B. C.; Tallant, D. R.; Balfe, C. A.; Kirkpatrick, R. J.; Turner, G. L.; Reidmeyer, M. R. *J. Am. Ceram. Soc.* **70**, 675–681 (1987).
6. Harris, R. K.; Leach, M. J.; Thompson, D. P. *Chem. Mater.* **2**, 320–323 (1990).
7. Harris, R. K.; Merwin, L. H.; Hägele, G. *Magn. Reson. Chem.* **27**, 470–475 (1989).

Epilogue

... and any chemistry student, faced by almost any treatise, should be aware that on one of those pages, perhaps in a single line, formula, or word, his future is written in indecipherable characters, which, however, will become clear "afterward": after success, error, or guilt, victory or defeat.

Primo Levi, The Periodic Table.

The Board of Studies in Chemistry at Durham University requires that each postgraduate research thesis contains a list of:

(i) all research colloquia and research seminars and lectures arranged by the Department of Chemistry and DUCS during the author's residence as a postgraduate student;

(ii) all research conferences attended and papers presentes by the author during the same period;

(iii) details of the postgraduate induction course.

Note: lectures attended in the Department of Mechanical, Materials and Manufacturing Engineering at Newcastle University are not listed in this section.

Conferences attended

(i) "Solid State Materials": Meeting of the ASSCG. Aberdeen, April 1988. Oral presentation: "High Resolution Solid-State NMR of Engineering Ceramics."

(ii) Ninth International NMR Meeting, University of Warwick, July 1989. Poster presentation: "High Resolution Solid-State Nuclear Magnetic Resonance Studies of Engineering Ceramics."

(iii) "Frontiers in High Resolution Solid State NMR Spectroscopy": RSC Faraday Division, London, November 1989.

(iv) "Solid State NMR: New Materials and New Techniques.": RSC Symposium, Warwick, September 1990. Oral presentation: "Nitrogen–15 and Oxygen–17 MAS NMR Studies of Nitrogen Ceramics."

Graduate symposia at Durham (1988, 1989) and Newcastle (1990) were also attended. At the last of these, an oral presentation was made: "Nitrogen–15 and Silicon–29 MAS NMR Studies of Nitrogen Ceramics."

Oral presentations on the work described in this Thesis have been given by Dr. D. P. Thompson at Materials Science conferences in Maastricht and Beijing.

Induction Course

1. Departmental organisation.
2. Safety matters.
3. Electrical appliances.
4. Chromatography etc.
5. Atomic absorptiometry and inorganic analysis.
6. Library facilities.
7. Mass spectroscopy.
8. NMR.

UNIVERSITY OF DURHAM

Board of Studies in Chemistry

COLLOQUIA, LECTURES AND SEMINARS GIVEN BY INVITED SPEAKERS
1ST AUGUST 1987 to 31st JULY 1988

BIRCHALL, Prof. D. (I.C.I. Advanced Materials) — 25th April 1988
Environmental Chemistry of Aluminium

BORER, Dr. K. (University of Durham Industrial Research Labs.) — 18th February 1988
The Brighton Bomb - A Forensic Science View

BOSSONS, L. (Durham Chemistry Teachers' Centre) — 16th March 1988
GCSE Practical Assessment

BUTLER, Dr. A.R. (University of St. Andrews) — 5th November 1987
Chinese Alchemy

CAIRNS-SMITH, Dr. A. (Glasgow University) — 28th January 1988
Clay Minerals and the Origin of Life

DAVIDSON, Dr. J. (Herriot-Watt University) — November 1987
Metal Promoted Oligomerisation Reactions of Alkynes

GRADUATE CHEMISTS (Northeast Polytechnics and Universities) — 19th April 1988
R.S.C. Graduate Symposium

GRAHAM, Prof. W.A.G. (University of Alberta, Canada) — 3rd March 1988
Rhodium and Iridium Complexes in the Activation of Carbon-Hydrogen Bonds

GRAY, Prof. G.W. (University of Hull) — 22nd October 1987
Liquid Crystals and their Applications

HARTSHORN, Prof. M.P. (University of Canterbury, New Zealand) — 7th April 1988
Aspects of Ipso-Nitration

HOWARD, Dr. J. (I.C.I. Wilton) — 3rd December 1987
Chemistry of Non-Equilibrium Processes

JONES, Dr. M.E. (Durham Chemistry Teachers' Centre) — 29th June 1988
GCSE Chemistry Post-mortem

JONES, Dr. M.E. (Durham Chemistry Teachers' Centre) — 6th July 1988
GCE Chemistry A Level Post-mortem

KOCH, Prof. H.F. (Ithaca College, U.S.A.) — 7th March 1988
Does the E2 Mechanism Occur in Solution?

LACEY, Mr. (Durham Chemistry Teachers' Centre) — 9th February 1988
Double Award Science

LUDMAN, Dr. C.J. (Durham University) — 16th December 1987
Explosives

McDONALD, Dr. W.A. (I.C.I. Wilton) — 11th May 1988
Liquid Crystal Polymers

MAJORAL, Prof. J.-P. (Université Paul Sabatier) — 8th June 1988
Stabilisation by Complexation of Short-Lived Phosphorus Species

MAPLETOFT, Mrs. M. (Durham Chemistry Teachers' Centre) — 4th November 1987
Salters' Chemistry

NIETO DE CASTRO, Prof. C.A. (University of Lisbon and Imperial College) — 18th April 1988
Transport Properties of Non-Polar Fluids

OLAH, Prof. G.A. (University of Southern California) — 29th June, 1988
New Aspects of Hydrocarbon Chemistry)

PALMER, Dr. F. (University of Nottingham) — 21st January 1988
Luminescence (Demonstration Lecture)

PINES, Prof. A. (University of California, Berkeley, U.S.A.) — 28th April 1988
Some Magnetic Moments

RICHARDSON, Dr. R. (University of Bristol) — 27th April 1988
X-Ray Diffraction from Spread Monolayers

ROBERTS, Mrs. E. (SATRO Officer for Sunderland) — 13th April 1988
Talk - Durham Chemistry Teachers' Centre - "Links Between Industry and Schools"

ROBINSON, Dr. J.A. (University of Southampton) — 27th April 1988
Aspects of Antibiotic Biosynthesis

ROSE van Mrs. S. (Geological Museum) — 29th October 1987
Chemistry of Volcanoes

SAMMES, Prof. P.G. (Smith, Kline and French) — 19th December 1987
Chemical Aspects of Drug Development

SEEBACH, Prof. D. (E.T.H. Zurich) — 12th November 1987
From Synthetic Methods to Mechanistic Insight

SODEAU, Dr. J. (University of East Anglia) — 11th May 1988
Durham Chemistry Teachers' Centre Lecture: "Spray Cans, Smog and Society"

SWART, Mr. R.M. (I.C.I.) — 16th December 1987
The Interaction of Chemicals with Lipid Bilayers

TURNER, Prof. J.J. (University of Nottingham) — 11th February 1988
Catching Organometallic Intermediates

UNDERHILL, Prof. A. (University of Bangor) — 25th February 1988
Molecular Electronics

WILLIAMS, Dr. D.H. (University of Cambridge) — 26th November 1987
Molecular Recognition

WINTER, Dr. M.J. (University of Sheffield) — 15th October 1987
Pyrotechnics (Demonstration Lecture)

UNIVERSITY OF DURHAM

Board of Studies in Chemistry

COLLOQUIA, LECTURES AND SEMINARS GIVEN BY INVITED SPEAKERS
1ST AUGUST 1988 to 31st JULY 1989

ASHMAN, Mr. A. (Durham Chemistry Teachers' Centre) — 3rd May, 1989
The Chemical Aspects of the National Curriculum

AVEYARD, Dr. R. (University of Hull) — 15th March, 1989
Surfactants at your Surface

AYLETT, Prof. B.J. (Queen Mary College, London) — 16th February, 1989
Silicon-Based Chips:- The Chemist's Contribution

BALDWIN, Prof. J.E. (Oxford University) — 9th February, 1989
Recent Advances in the Bioorganic Chemistry of Penicillin Biosynthesis

BALDWIN & WALKER, Drs. R.R. & R.W. (Hull University) — 24th November, 1988
Combustion: Some Burning Problems

BOLLEN, Mr. F. (Durham Chemistry Teachers' Centre) — 18th October, 1988
Lecture about the use of SATIS in the classroom

BUTLER, Dr. A.R. (St. Andrews University) — 15th February, 1989
Cancer in Linxiam: The Chemical Dimension

CADOGAN, Prof. J.I.G. (British Petroleum) — 10th November, 1988
From Pure Science to Profit

CASEY, Dr. M. (University of Salford) — 20th April, 1989
Sulphoxides in Stereoselective Synthesis

CRESSEY & WATERS, Mr. D. & T. (Durham Chemistry Teachers' Centre) — 1st February, 1989
GCSE Chemistry 1988: "A Coroner's Report"

CRICH, Dr. D. (University College London) — 27th April, 1989
Some Novel Uses of Free Radicals in Organic Synthesis

DINGWALL, Dr. J. (Ciba Geigy) — 18th October, 1988
Phosphorus-containing Amino Acids: Biologically Active Natural and Unnatural Products

ERRINGTON, Dr. R.J. (University of Newcastle-upon-Tyne) — 1st March, 1989
Polymetalate Assembly in Organic Solvents

FREY, Dr. J. (Southampton University) — 11th May, 1989
Spectroscopy of the Reaction Path: Photodissociation Raman Spectra of NOCl

GRADUATE CHEMISTS, (Polytechs and Universities in North East England) — 12th April, 1989
R.S.C. Symposium for presentation of papers by postgraduate students

HALL, Prof. L.D. (Addenbrooke's Hospital, Cambridge) — 2nd February, 1989
NMR - A Window to the Human Body

HARDGROVE, Dr. G. (St. Olaf College, U.S.A.) — December, 1988
Polymers in the Physical Chemistry Laboratory

HARWOOD, Dr. L. (Oxford University) — 25th January, 1988
Synthetic Approaches to Phorbols Via Intramolecular Furan Diels-Alder Reactions: Chemistry under Pressure

JÄGER, Dr. C. (Friedrich-Schiller University GDR) — 9th December, 1988
NMR Investigations of Fast Ion Conductors of the NASICON Type

JENNINGS, Prof. R.R. (Warwick University) — 26th January, 1989
Chemistry of the Masses

JOHNSON, Dr. B.F.G. (Cambridge University) — 23rd February, 1989
The Binary Carbonyls

JONES, Dr. M.E. (Durham Chemistry Teachers' Centre) — 14th June, 1989
Discussion Session on the National Curriculum

JONES, Dr. M.E. (Durham Chemistry Teachers' Centre) — 28th June, 1989
GCSE and A Level Chemistry 1989

LUDMAN, Dr. C.J. (Durham University) — 18th October, 1988
The Energetics of Explosives

MACDOUGALL, Dr. G. (Edinburgh University) — 22nd February, 1989
Vibrational Spectroscopy of Model Catalytic Systems

MARKO, Dr. I. (Sheffield University) — 9th March, 1989
Catalytic Asymmetric Osmylation of Olefins

McLAUCHLAN, Dr. K.A. (University of Oxford) — 16th November, 1988
The Effect of Magnetic Fields on Chemical Reactions

MOODY, Dr. C.J. (Imperial College) — 17th May, 1989
Reactive Intermediates in Heterocyclic Synthesis

MORTIMER, Dr. C. (Durham Chemistry Teachers' Centre) — 14th December, 1988
The Hindenberg Disaster - an Excuse for Some Experiments

NICHOLLS, Dr. D. (Durham Chemistry Teachers' Centre) — 11th July, 1989
Demo. "Liquid Air"

PAETZOLD, Prof. P. (Aachen) — 23rd May, 1989
Iminoboranes XB≡NR: Inorganic Acetylenes?

PAGE, Dr. P.C.B. (University of Liverpool) — 3rd May, 1989
Stereocontrol of Organic Reactions Using 1,3-dithiane-1-oxides

POLA, Prof. J. (Czechoslovak Academy of Sciences) — 15th June, 1989
Carbon Dioxide Laser Induced Chemical Reactions - New Pathways in Gas-Phase Chemistry

REES, Prof. C.W. (Imperial College London) — 27th October, 1988
Some Very Heterocyclic Compounds

REVELL, Mr. P. (Durham Chemistry Teachers' Centre) — 14th March, 1989
Implementing Broad and Balanced Science 11-16

SCHMUTZLER, Prof. R. (Technische Universitat Braunschweig) — 6th October, 1988
Fluorophosphines Revisited - New Contributions to an Old Theme

SCHROCK, Prof. R.R. (M.I.T.) — 13th February, 1989
Recent Advances in Living Metathesis

SINGH, Dr. G. (Teesside Polytechnic) — 9th November, 1988
Towards Third Generation Anti-Leukaemics

SNAITH, Dr. R. (Cambridge University) — 1st December, 1988
Egyptian Mummies: What, Where, Why and How?

STIBR, Dr. R. (Czechoslovak Academy of Sciences) — 16th May, 1989
Recent Developments in the Chemistry of Intermediate-Sited Carboranes

VON RAGUE SCHLEYER, Prof. P. (Universitat Erlangen Nurnberg) — 21st October, 1988
The Fruitful Interplay Between Calculational and Experimental Chemistry

WELLS, Prof. P.B. (Hull University) — 10th May, 1989
Catalyst Characterisation and Activity

UNIVERSITY OF DURHAM

Board of Studies in Chemistry

COLLOQUIA, LECTURES AND SEMINARS GIVEN BY INVITED SPEAKERS 1ST AUGUST 1989 TO 31ST JULY 1990

ASHMAN, Mr. A. (Durham Chemistry Teachers' Centre) — 11th October, 1989
The National Curriculum - an update

BADYAL, Dr. J.P.S. (Durham University) — 1st November, 1989
Breakthoughs in Heterogeneous Catalysis

BECHER, Dr. J. (Odense University) — 13th November, 1989
Synthesis of New Macrocylic Systems using Heterocyclic Building Blocks

BERCAW, Prof. J.E. (California Institute of Technology) — 10th November, 1989
Synthetic and Mechanistic Approaches to Ziegler-natta Polymerization of Olefins

BLEASDALE, Dr. C. (Newcastle University) — 21st February, 1990
The Mode of Action of some Anti-tumour Agents

BOLLEN, Mr. F.(Formerly Science Advisor, Newcastle LEA) — 27th March, 1990
Whats's New in Satis, 16-19

BOWMAN, Prof. J.M. (Emory University) — 23rd March, 1990
Fitting Experiment with Theory in Ar-OH

BUTLER, Dr. A. (St. Andrews University) — 7th December, 1989
The Discovery of Penicillin: Facts and Fancies

CAMPBELL, Mr. W.A. (Durham Chemistry Teachers' Centre) — 12th September, 1989
Industrial catalysis - some ideas for the National Curriculum

CHADWICK, Dr. P. (Dept. of Physics, Durham University) — 24th January, 1990
Recent Theories of the Universe (with Reference to National Curriculum Attainment Target 16)

CHEETHAM, Dr. A.K. (Oxford University) — 8th March, 1990
Chemistry of Zeolite Cages

CLARK, Prof. D.T. (ICI Wilton) — 22nd February, 1990
Spatially Resolved Chemistry (using Natures's Paradigm in the Advanced Materials Arena)

COLE-HAMILTON, Prof. D.J. (St. Andrews University) — 29th November, 1989
New Polymers from Homogeneous Catalysis

CROMBIE, Prof. L. (Nottingham University) — 15th February, 1990
The Chemistry of Cannabis and Khat

DYER, Dr. U. (Glaxo) — 31st January, 1990
Synthesis and Conformation of C-Glycosides

FLORIANI, Prof. C. (University of Lausanne, Switzerland) — 25th October, 1989
Molecular Aggregates - A Bridge between homogeneous and Heterogeneous Systems

GERMAN, Prof. L.S. (USSR Academy of Sciences - Moscow) — 9th July, 1990
New Syntheses in Fluoroaliphatic Chemistry: Recent Advances in the Chemistry of Fluorinated Oxiranes

GRAHAM, Dr. D. (B.P. Reserch Centre) — 4th December, 1989
How Proteins Absorb to Interfaces

GREENWOOD, Prof. N.N. (University of Leeds) — 9th November, 1989
Novel Cluster Geometries in Metalloborane Chemistry

HOLLOWAY, Prof. J.H. (University of Leicester) — 1st February, 1990
Noble Gas Chemistry

HUGHES, Dr. M.N. (King's College, London) — 30th November, 1989
A Bug's Eye View of the Periodic Table

HUISGEN, Prof. R. (Universität München) — 15th December, 1989
Recent Mechanistic Studies of [2+2] Additions

IDDON, Dr. B. (Univeristy of Salford) — 15th December, 1989
Schools' Christmas Lecture - The Magic of Chemistry

JONES, Dr. M.E. (Durham Chemistry Teachers' Centre) — 3rd July, 1990
The Chemistry A Level 1990

JONES, Dr. M.E. (Durham Chemistry Teachers' Centre) — 21st November 1989
GCSE and Dual Award Science as a starting point for A level Chemistry - how suitable are they?

JOHNSON, Dr. G.A.L. (Durham Chemistry Teachers' Centre) — 8th February, 1990
Some aspects of local Geology in the National Science Curriculum (attainment target 9)

KLINOWSKI, Dr. J. (Cambridge University) — 13th December 1989
Solid State NMR Studies of Zeolite Catalysts

LANCASTER, Rev. R. (Kimbolton Fireworks) — 8th February, 1990
Fireworks - Principles and Practice

LUNAZZI, Prof. L. (University of Bologna) — 12th February, 1990
Application of Dynamic NMR to the Study of Conformational Enantiomerism

PALMER, Dr. F. (Nottingham University) — 17th October, 1989
Thunder and Lightning

PARKER, Dr. D. (Durham University) — 16th November, 1989
Macrocycles, Drugs and Rock 'n' roll

PERUTZ, Dr. R.N. (York University) — 24th January, 1990
Plotting the Course of C-H Activations with Organometallics

PLATONOV, Prof. V.E. (USSR Academy of Sciences - Novosibirsk) — 9th July, 1990
Polyfluoroindanes: Synthesis and Transformation

POWELL, Dr. R.L. (ICI) — 6th December, 1989
The Development of CFC Replacements

POWIS, Dr. I. (Nottingham University) — 21st March, 1990
Spinning off in a huff: Photodissociation of Methyl Iodide

RICHARDS, Mr. C. (Health and Safety Executive, Newcastle) — 28th February, 1990
Safety in School Science Laboratories and COSHH

ROZHKOV, Prof. I.N. (USSR Academy of Sciences - Moscow) — 9th July, 1990
Reactivity of Perfluoroalkyl Bromides

STODDART, Dr. J.F. (Sheffield University) — 1st March, 1990
Molecular Lego

SUTTON, Prof. D. (Simon Fraser University, Vancouver B.C.) — 14th February, 1990
Synthesis and Applications of Dinitrogen and Diazo Compounds of Rhenium and Iridium

THOMAS, Dr. R.K. (Oxford University) — 28th February, 1990
Neutron Reflectometry from Surfaces

THOMPSON, Dr. D.P. (Newcastle University) — 7th February, 1990
The role of Nitrogen in Extending Silicate Crystal Chemistry